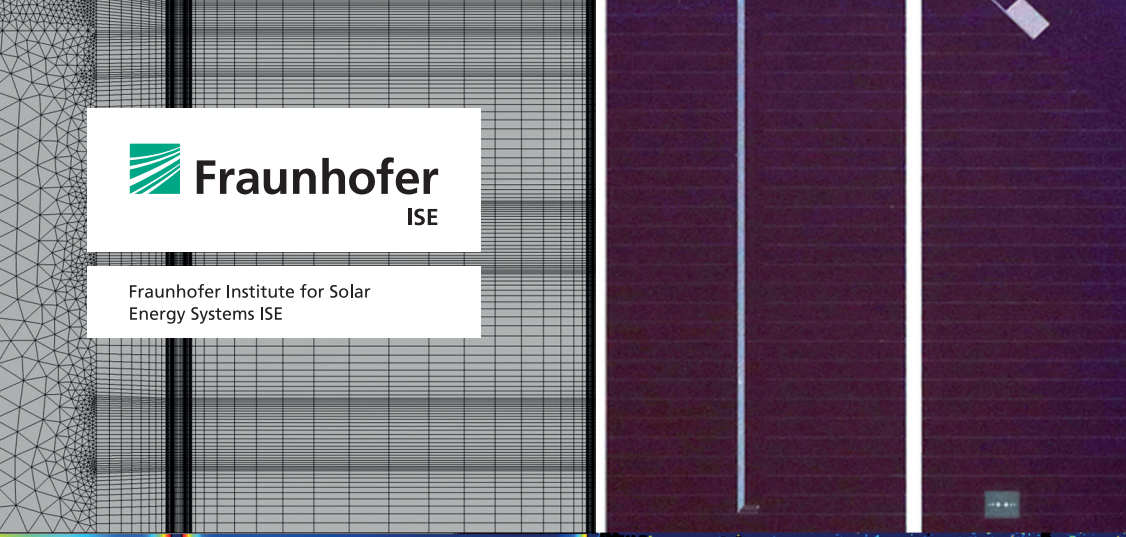

Fraunhofer ISE

Fraunhofer Institute for Solar Energy Systems ISE

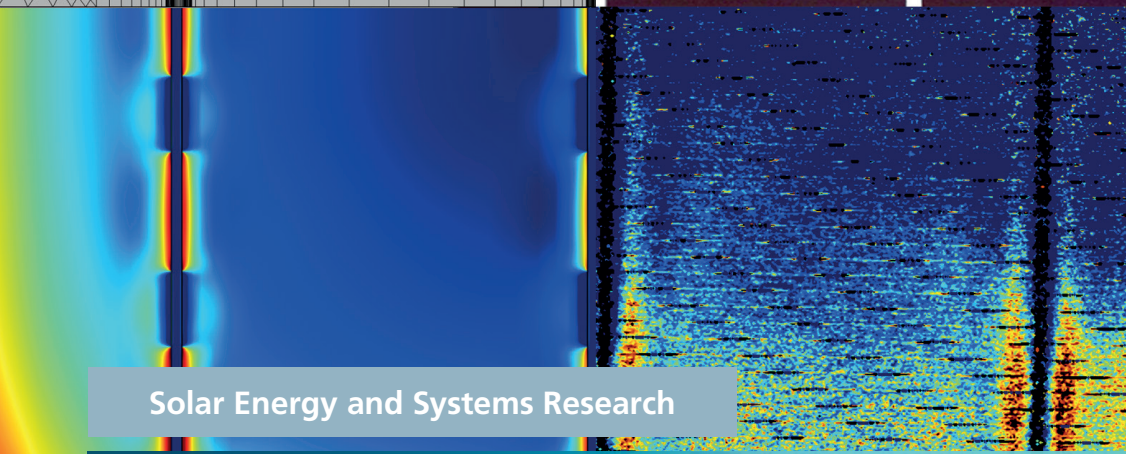

Solar Energy and Systems Research

# Thermomechanical Design Rules for the Development of Photovoltaic Modules

**Andreas Joachim Beinert**

Karlsruhe Institute of Technology

**Fraunhofer Verlag**

Fraunhofer Institute for Solar Energy Systems ISE

SOLARE ENERGIE- UND SYSTEMFORSCHUNG /
SOLAR ENERGY AND SYSTEMS RESEARCH

# Thermomechanical Design Rules for the Development of Photovoltaic Modules

Andreas Joachim Beinert

Fraunhofer Verlag

Contact:
Fraunhofer Institute for
Solar Energy Systems ISE
Heidenhofstrasse 2
79110 Freiburg
Germany
Phone +49 761/4588-5150
info@ise.fraunhofer.de
www.ise.fraunhofer.de

Cover illustration: © Fraunhofer ISE

Bibliographic information of the German National Library:
The German National Library has listed this publication in its Deutsche Nationalbibliografie; detailed bibliografic data is available in the internet at www.dnb.de.
ISSN: 2512-3629
ISBN: 978-3-8396-1808-0

D 90

Zugl.: Karlsruhe, KIT, Diss., 2021

Book Series: »Solare Energie- und Systemforschung / Solar Energy and Systems Research«

Print and finishing:
Fraunhofer Verlag, Mediendienstleistungen

This book was printed with chlorine- and acid-free paper.


Nobelstrasse 12
70569 Stuttgart
Germany
verlag@fraunhofer.de
www.verlag.fraunhofer.de

is a constituent entity of the Fraunhofer-Gesellschaft, and as such has no seperate legal status.

Fraunhofer-Gesellschaft zur Förderung
der angewandten Forschung e.V.
Hansastrasse 27 c
80686 München
Germany
www.fraunhofer.de

# Thermomechanical Design Rules for the Development of Photovoltaic Modules

Zur Erlangung des akademischen Grades eines

**Doktors der Ingenieurwissenschaften (Dr.-Ing.)**

von der KIT-Fakultät für Maschinenbau des
Karlsruher Instituts für Technologie (KIT)

angenommene

## Dissertation

von

*Andreas Joachim Beinert, M.Sc.*

Tag der mündlichen Prüfung: 8. Dezember 2021

| | |
|---|---|
| Hauptreferent: | apl. Prof. Dr.-Ing. Jarir Aktaa |
| Korreferent: | Prof. Dr.-Ing. Robert Stieglitz |
| Vorsitz: | Prof. Dr.-Ing. Thomas Böhlke |

The work of this dissertation at
**KIT-Department of Mechanical Engineering,**
**Institute for Applied Materials**


was conducted at
**Fraunhofer Institute for Solar Energy Systems ISE**


and funded by a PhD-scholarship of
**Cusanuswerk**

# I Abstract

Stress in solar cells plays a crucial role in the reliability of photovoltaic (PV) modules. The influences on stress are as diverse as the number of different materials in a PV module and become more and more complex with the growing variety of PV modules for different applications. The aim of this work is to derive a set of thermomechanical design rules to support and accelerate future PV module developments. For this purpose, three methods are developed and applied:

1. Thermomechanical finite element method simulations of PV module designs (FEM).
2. µ-Raman spectroscopy of laminated solar cells (µ-Raman).
3. Solar cell integrated stress sensors (*SenSoCell®*).

Furthermore, the concept of specific thermal expansion stiffness: $\hat{E}_\alpha = E \cdot \alpha \cdot A_j \cdot h$ is introduced. The product of the Young's modulus $E$, the coefficient of thermal expansion $\alpha$, the joint area $A_j$ and the materials height $h$ is a measure of how much thermal strain one material can induce in another.

The basis of the 15 Thermomechanical Design Rules is a comprehensive parameter sensitivity study of different PV module components and material properties. The study is carried out by FEM simulations and supported by experimental validations. For this purpose, a 3D-FEM model is developed, which models the PV module geometry in detail from busbar and ribbons up to the frame including the adhesive and realistic mounting conditions. The FEM simulation covers the soldering, lamination and mechanical load at various temperatures. A special focus is placed on singularities, which occur around the busbars and ribbons due to their geometric shape. The stress intensification by this model singularity is reduced by excluding the area within 50 µm around the busbar in the stress evaluation.

Confocal µ-Raman spectroscopy of planar silicon surfaces is extended to textured solar cell surfaces by adapting the measurement procedure and determining a new conversion coefficient ($\Sigma$ = -(1.19 ± 0.07) rel. $cm^{-1}$/GPa). The measurement procedure is successfully applied to single-cell laminates, which enables for the first time a spatially resolved µ-Raman stress measurement on solar cells after soldering and lamination. The FEM simulations performed along with the measurements agree well within the measurement uncertainty.

The idea of solar cell integrated stress sensors is to measure stress directly in the solar cell itself and hence to eliminate the interference with other PV module materials, as it may occur e.g. for foil strain gauges. Silicon based piezoresistance sensors are well known in the field of microelectronics. This work successfully transfers the principle to solar cell wafer by using only photovoltaic production technologies. In the development phase, different sensor designs are developed. The design with a sensitivity $S_\sigma$ of (-47.41 ± 0.14) %/GPa is subsequently implemented on a solar cell wafer. Two of such *SenSoCells*® (Sensors integrated in Solar Cells) are integrated into a PV module at different positions. The stress of the *SenSoCells*® is successfully measured during an experimental Mechanical Load Test. With a deviation of 4 MPa at 2400 Pa load, the geometric nonlinear FEM simulation agrees well with the measured stress.

# II Zusammenfassung

Für die Zuverlässigkeit von Photovoltaikmodulen spielt die mechanische Spannung eine wichtige Rolle. Die Einflüsse auf die mechanische Spannung sind so vielfältig wie die Anzahl verschiedener Modulmaterialien und sie werden durch die stetig wachsende Vielfalt an PV-Modulen für unterschiedlichste Anwendungen immer komplexer. Das Ziel dieser Arbeit ist es daher einen Satz von Thermomechanischen Designregeln herzuleiten, um zukünftige PV-Modulentwicklungen zu unterstützen und zu beschleunigen. Dazu werden drei Verfahren entwickelt und angewendet:

1. Thermomechanische Finite-Elemente-Simulationen von PV-Moduldesigns (FEM).
2. µ-Raman-Spektroskopie von eingebetteten Solarzellen (µ-Raman).
3. Solarzellen-integrierte Spannungssensoren (*SenSoCell*®).

Zudem wird das Konzept der spezifischen Wärmeausdehnungssteifigkeit $\hat{E}_\alpha = E \cdot \alpha \cdot A_\mathrm{j} \cdot h$ eingeführt. Das Produkt des E-Moduls $E$, thermischen Ausdehnungskoeffizienten $\alpha$, Kontaktfläche $A_\mathrm{j}$ und Materialdicke $h$ wird als Maß dafür verwendet, wie viel thermische Dehnung ein Material in einem anderen induzieren kann.

Die Basis der 15 Thermomechanischen Designregeln ist eine umfassende Parametersensitivitätsstudie von verschiedenen PV-Modul Komponenten und Materialeigenschaften, welche mit FEM-Simulationen durchgeführt und durch experimentelle Validierungen unterstützt wird. Hierfür wurde ein dreidimensionales FEM-Modell entwickelt, welches die PV-Modulgeometrie detailgetreu modelliert, beginnend bei den Busbars und Zellverbindern bis zum Rahmen inklusive Rahmenkleber unter Berücksichtigung realistischer Montage-Randbedingungen. Die FEM-Simulation umfasst die Solarzellverschaltung, Modullamination und mechanische Last bei verschiedenen Temperaturen. Ein besonderer Fokus wird auf die Singularitäten gelegt, welche um die Busbars herum auf Grund deren Geometrie entstehen. Die hieraus resultierende Spannungsüberhöhung wird dadurch reduziert, dass ein Bereich von 50 µm um den Busbar herum bei der Auswertung der mechanischen Spannung nicht berücksichtigt wird.

Die konfokale µ-Raman-Spektroskopie auf planaren Siliciumoberflächen wird auf texturierte Solarzellenoberflächen erweitert, indem das Messverfahren angepasst und ein neuer Umrechnungsfaktor bestimmt wird ($\Sigma$ = -

(1.19 ± 0.07) rel. $cm^{-1}$/GPa). Das Messverfahren wird im Rahmen dieser Arbeit erfolgreich auf Einzell-Laminate angewandt, so dass die mechanische Spannung erstmals nach Verlöten und Lamination ortsaufgelöst auf der Solarzelle gemessen werden kann. Die Messwerte stimmen im Rahmen der Messunsicherheit sehr gut mit den durchgeführten FEM-Simulationen überein.

Die Idee der Solarzellen-integrierten Sensoren ist es, die mechanische Spannung direkt in den Solarzellen zu messen und damit viele Nachteile üblicher mechanischer Verfahren zu vermeiden, wie z.B. bei Dehnungsmesstreifen die Wechselwirkungen mit anderen PV-Modulmaterialien. Siliciumbasierte piezoresistive Sensoren sind in der Mikroelektronik wohlbekannt. Diese Arbeit überträgt das Prinzip erfolgreich auf Solarzellenwafer, wobei ausschließlich Herstellungstechnologien aus der Photovoltaik zur Anwendung kommen. In der Entwicklungsphase werden zunächst verschiedene Designs entwickelt. Das Design mit einer Sensitivität $S_\sigma$ von (-47.41 ± 0.14) %/GPa wird dann in einen Solarzellenwafer implementiert. Zwei solcher *SenSoCells*® (Sensors integrated in Solar Cells) werden an zwei Positionen in ein PV-Modul integriert. Die mechanische Spannung der *SenSoCells*® wird erfolgreich während eines experimentellen Mechanischen Belastungstests gemessen. Mit 4 MPa Abweichung bei 2400 Pa Oberflächenlast, stimmt die geometrisch nichtlineare FEM-Simulation sehr gut mit der gemessenen mechanischen Spannung überein.

# III Content

# 1 Introduction

## 1.1 Motivation

To achieve the targets of the Paris Agreement [Unit15] and most importantly to keep the global warming below 1.5 °C to 2 °C relative to the pre-industrial level, we need to master a unprecedented energy-system transition [Roge16]. One potential scenario to keep the global warming well below 2 °C is developed by Shell [Shel18]. As Figure 1.1 demonstrates, solar energy is the most important piece in this so-called Sky scenario. It predicts that with 111 PWh/a solar energy will cover 40 % of the worldwide primary energy in 2100. Comparing this to the currently annually produced 1.7 PWh, shows the dimension of this needed transition.

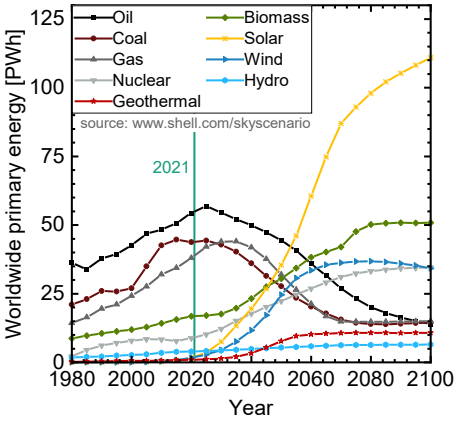


**Figure 1.1:** Worldwide primary energy production since 1980. The simulated prediction is the so called Sky scenario by Shell [Shel18]. It is a scenario of an energy mix, which keeps the global warming well below 2 °C.

To achieve such an immense solar energy production, not only the efficiency of photovoltaic (PV) modules but also the reliability is one important factor. Although PV module manufactures nowadays offer a linear performance warranty of up to 25 years and sometimes even higher [Rodr18], there are still failures seen in the field. Also, the fast price decay [ITRP20] and the resulting attempt to reduce the material costs generate new challenges with regard to the reliability. Every change in a PV modules bill of material requires intensive and time con-

suming testing and re-engineering. Although reliability tests are part of the certification procedure, some effects only appear in the field or in extended tests. The reason is that the certification tests are designed in a way to test one impact only, e.g. either temperature or mechanical load but not the combination. However, as it will be shown in this work, it is often the combination of several impact which is critical. Some of the most common failures are defective by-pass diodes, solar cell cracks, potential induced degradation (PID) and discoloration of the encapsulant [Könt17]. Some of them originate from a not optimized module design and material choice, some are related to incorrect handling and installation. This shows the need for a deeper understanding of the thermomechanics of PV modules and a set of general thermomechanical design rules. This work focusses on solar cell cracks, which is the dominating failure induced by high thermomechanical tensile stress [Kaul14, Könt11]. They can account for PV module degradation rates of up to 8 % relative power loss per year [Könt17]. Power loss again accounts for a higher levelized cost of electricity (LCOE) of the PV system, i.e. a more expensive energy transition. The thermomechanical design rules developed in this work target a longer PV module lifetime and thus to a lower LCOE and a faster energy transition.

## 1.2 Objectives

The objective of this work is a detailed and systematic investigation of the thermomechanical processes in conventional crystalline silicon PV modules and therefore to gain a deeper understanding of the PV modules thermomechanics. Based on which, thermomechanical design rules are derived, with the aim of reducing the stress in solar cells, induced by external mechanical loads.

To investigate the thermomechanical stress within the solar cells a combination of finite element method (FEM) simulations and experimental methods are used. The FEM simulations determine crucial influences on the thermomechanical stress by a parameter sensitivity study. Experimental methods validate the FEM simulations.

Since only a few methods for stress measurement in laminated solar cells exist, one major part of this work is the development of reliable stress measurement methods. Two paths are followed: A non-invasive method which allows measurements without contact to the sample and no special sample preparation. With the drawback, that a field of view to the sample is needed during loading conditions. Since this is not the case in some experiments, the second path is an invasive method using a PV module inserted sensing probe. Usually that modifies

the thermomechanical behavior. Therefore, a method is developed, which reduces the influence to a minimum.

## 1.3 Conventional PV Module Design

Within this Section, the conventional PV module design is briefly described. For a more detailed description it is referred to the literature like [Krau06, Quas15, Wirt16].

A conventional PV module consists of five layers, the frontglass, the solar cells embedded in two layers of encapsulant and a backsheet (Figure 1.2). The silicon solar cells are interconnected by solder coated copper ribbons connecting the top of one solar cell with the back of the next one. In over 60 % of the industrial modules, six of such strings with ten solar cells are interconnected in series to form a 60-cell module with a size of about 1×1.6 m² [ITRP20]. However, there is a trend to more solar cells, like 72 (1×2 m²) and to use half-cells instead of full-cells. The frontglass is usually a tempered low-iron soda-lime glass with a high transmittance. Above 65 % of the solar cells are made of monocrystalline silicon with a trend to above 80 % [ITRP20]. The most common encapsulant material with a market share of over 90 % is the copolymer Ethylene-vinyl acetate (EVA). Most backsheets are multilayered, with a Polyethylene terephthalate (PET) core layer. The combination with Polyvinylidene difluoride (PVDF) is with over 50 % the most common one followed by Polyvinyl fluoride (PVF) with around 25 %. [ITRP20]

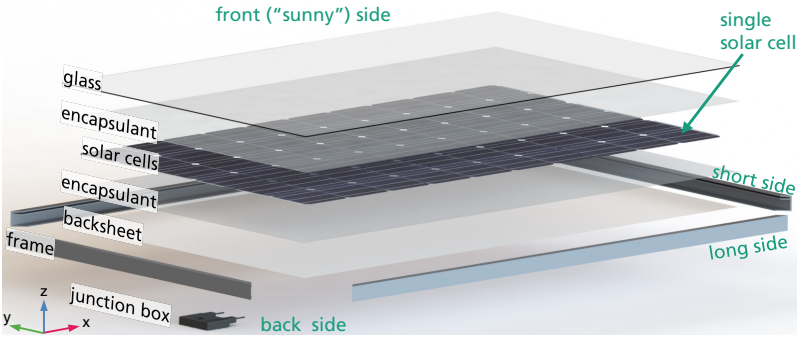


**Figure 1.2:** Structural setup of a conventional PV module with 60 crystalline silicon solar cells.

The PV module is produced in a lamination process at around 150 °C [Krau06, Quas15, Wirt16], in which the laminate is formed. Afterwards, the junction box for external electrical connection and the frame for mounting and stability are attached. In this work, the term laminate defines the sandwich of front-, backsheet, encapsulant and solar cells after lamination. The term PV module defines a laminate including a mounting structure, like a frame. The vast majority of silicon PV modules are built with the setup shown in Figure 1.2 or a slight variation of it, like a glass instead of a backsheet [ITRP20]. The latter one is referred to glass-glass modules.

## 1.4 Thermal Expansion Stiffness

High tensile stress may result in solar cell cracks. These cracks affect on one hand the electrical performance of the solar cells. On the other hand they can induce further failures like snail trails [Dola16], which again reduce the power output. With up to 8 % relative power loss per year [Könt17], solar cell cracks can severely affect the PV module power. In the following a broad overview of the origin of thermomechanical stress within PV modules is given.

Within this work, the phrase thermal stress refers to stress originating from thermal loads, i.e. temperature changes. The phrase mechanical stress refers to stress originating from mechanical loads. Finally, thermomechanical stress refers to stress originating from combined thermal and mechanical loads.

Thermal stress is observed whenever the PV module undergoes temperature changes due to the mismatch of the coefficients of thermal expansion (CTE) of the single layers. Examples are cooling down after lamination from 150 °C to room temperature and day-night as well as summer-winter operating temperature changes. Thermal stresses can be divided in two effects: One which arises from the CTE mismatch of the laminate materials with the reference temperature being the lamination temperature. The second effect arises from the interaction of the mounting structure, like an aluminum frame, with the laminate. Here, the CTE mismatch is between the mounting structure and the laminate. Since the mounting structure is usually attached to the laminate at room temperature, the reference temperature of the PV module is room temperature.

Mechanical stress occurs when the PV module is exposed to external mechanical loads like wind or accumulation of snow. Since this usually happens at temperatures different from the reference temperatures, this mechanical stress

superposes with thermal stress. Therefore, the origin of a PV modules stress is mostly thermomechanical.

To characterize materials according to their potential to induce thermal stress, the coefficient of thermal expansion $\alpha$ alone has a limited significance. For example, the encapsulant EVA has a relatively high CTE of 270 $10^{-6}K^{-1}$ but due to the low Young's modulus $E$ of 7.9 MPa, it acts as a buffer for the solar cells. Therefore, Carroll e*t al.* [Carr76] introduced the so called thermal expansion stiffness $E_\alpha$ for PV modules as the product of Young's modulus $E$ and coefficient of thermal expansion $\alpha$:

$$E_\alpha = E \cdot \alpha \,. \tag{1}$$

This work extends the concept of thermal expansion stiffness by introduction of two extended factors, which incorporate the materials geometric shape. The first factor, called volumetric thermal expansion stiffness $\bar{E}_\alpha$, is meant for a global description of the PV modules thermomechanics, for example the curvature after lamination due to the different expansion behavior of the PV module materials. Therefore, the volumetric thermal expansion stiffness $\bar{E}_\alpha$ is defined as the thermal expansion stiffness $E_\alpha$ multiplied volume $V$ of the inspected material:

$$\bar{E}_\alpha = E_\alpha \cdot V. \tag{2}$$

Table 1.1 shows these properties at room temperature for materials used in a conventional PV module. According to the thermal expansion stiffness $E_\alpha$, the ribbon has the highest impact on thermal stress of solar cells. However, due to the small volume of the ribbon, this is a highly local influence occurring only around the ribbon itself. This is represented by the low value of the volumetric thermal expansion stiffness $\bar{E}_\alpha$. In a more global perspective, the frontglass dominates the thermal behavior of the PV module with the highest volumetric thermal expansion stiffness $\bar{E}_\alpha$. Solar cells show a high thermal expansion stiffness $E_\alpha$, however due to their much smaller size, the impact on the global behavior is limited. Hence, the material with the second strongest influence is the backsheet. The extremely low thermal expansion stiffness value of EVA, shows its property as buffer layer at room temperature. Its volumetric thermal expansion stiffness $\bar{E}_\alpha$ is just slightly larger than the one of the much smaller solar cells.

As this discussion shows, thermomechanical stress within a PV module is complex. Because of the different layer dimensions and the corresponding influence on other layers, it has to be distinguished between local and global effects. The small PV module components might have a high, but only local impact. For local effects the volumetric thermal expansion stiffness $\bar{E}_\alpha$ is not a reasonable

measure. Therefore, the second factor introduced in this work, called specific thermal expansion stiffness $\hat{E}_\alpha$, is a refinement of the volumetric thermal expansion stiffness $\bar{E}_\alpha$ by taking only the joining surface area $A_\mathrm{j}$ and materials height $h$ rather than the whole volume into account. It describes how much thermal force a material can apply to another material in direct contact:

$$\hat{E}_\alpha = E_\alpha \cdot A_j \cdot h. \tag{3}$$

Figure 1.3 illustrates the difference exemplarily for a PV module glass. For the discussion of the stress within the solar cell, the specific thermal expansion stiffness $\hat{E}_\alpha$ will be used. When discussing the influence on the entire PV module, the volumetric thermal expansion stiffness $\bar{E}_\alpha$ is used.

The international standard for design qualification and type approval, IEC 61215 [Inte16], which defines a test sequence PV modules have to pass, considers the thermal and mechanical stress in its test procedures separately. Thermal stress is tested by the "thermal cycling test" (TC), which defines at least 200 temperature cycles between -40 °C and +85 °C. Mechanical stress is tested with "Static Mechanical Load Test" (ML), which defines a minimum homogenous load of 2400 Pa [Inte16]. A second standard, which covers inhomogeneous snow loads (IML) [Inte20], also considers the mechanical load only at room temperature. Therefore, there is no test procedure for the combination of thermal and mechanical stresses.

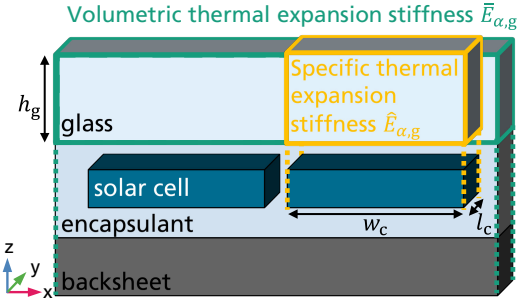


**Figure 1.3**: Illustration of the volume taken into account for the volumetric (green box) and specific (yellow box) thermal expansion stiffness on the example of glass with regard to the solar cell, not to scale

**Table 1.1**: Young's modulus $E$, coefficient of thermal expansions $\alpha$, the product of them $E_\alpha$ and the volumetric thermal expansion stiffness $\bar{E}_\alpha$ taken to the dimensions of the reference PV module (section 3.3) of the PV module layers at room temperature, [a]: provided by manufacturer, [b]: measured.

| Layer | Material | Young's Modulus $E$ [GPa] | Coeff. of thermal expansion $\alpha$ [$10^{-6}K^{-1}$] | Therm. exp. stiffness $E_\alpha$ [kPa $K^{-1}$] | Vol. therm. exp. stiffness $\bar{E}_\alpha$ [Pa $m^3$ $K^{-1}$] |
|---|---|---|---|---|---|
| Frontglass | Soda-Lime Glass | 74[a] | 9 [a] | 666 | 3529 |
| Encapsulant | EVA | 0.0085[b] | 270 [Eitn11c] | 2.3 | 1.7 |
| Solar Cell | Cz-Silicon | 130 [Wies12] | 2.62 [Lyon77] | 340 | 1.5 |
| Backsheet | TPT | 3.5 [Eitn11a] | 50.4 [Eitn11a] | 176 | 102 |
| Busbars | Silver | 7 [Kohn07] | 10 [Rend16a] | 70 | 0.0002 |
| Ribbon | Copper | 70 [Wies12] | 17 [Wies12] | 1190 | 0.05 |

## 1.5 Structure of the Work

This work is based on three different approaches to determine stress in solar cells: one approach consists in numerical simulations by the finite element method, two approaches are to validate the simulations experimentally:

1. µ-Raman spectroscopy.
2. Solar cell integrated sensors.
3. FEM simulations.

The development of these three approaches is separately discussed throughout the entire work. Accordingly, each chapter is structured regarding to them.

Chapter 1 introduces the framework within this work and its objectives (Section 1.2). It also introduces the conventional PV module design (Section 1.3) and the specific thermal expansion stiffness $\hat{E}_\alpha$ (Section 1.4).

Chapter 2 is a concise overview of the state of the research.

Chapter 3 describes the approach and used methods within this work.

Chapter 4 comprises the main results and findings of this work. First, it shows the results of the developed experimental stress determination methods (Sections 4.1 and 4.2). Followed by results of the investigation of singularities in the FEM model as well as the validation by mechanical load tests in Section 4.3. The following Sections show the stress within the PV module: Section 4.4 describes the stress from PV module production and comprises the μ-Raman measurements as well as FEM simulations. Section 4.5 describes stresses originating from mechanical load as well as temperature differences by FEM simulations. The last Section 4.6 within Chapter 4 shows the results of a comprehensive parameter sensitivity study.

Chapter 5 discusses the results, again first the development of the stress determination methods in Section 5.1, followed by the discussion of influences on the stress within the solar cells in Section 5.2. Within this section thermomechanical design rules are derived, which are summarized in Section 5.3.

Finally, Chapter 6 summarizes the work and gives an outlook.

# 2 State of the Research

In this chapter, the state of research is discussed on the basis of the most relevant publications. Since this work covers different areas, with each having a broad spectrum of publications, the discussed references are chosen to give an overview of the relevant scientific achievements in each area.

The basis for today's PV technology was developed in the *Flat-Plate Solar Array Project* [Call86], which was started in 1975 and conducted by the *Jet Propulsion Laboratory*. In this 10-year research project, it was investigated how photovoltaics developed for space applications can be transferred for terrestrial use. Although todays PV modules have a different design, the technology is still strongly influenced by the eight reports covering different components of PV modules [Brig86, Call86, Cudd86, Gall86, Leip86, Lutw86, McGu86, Ross86]. An important aspect was degradation of PV modules and factors influencing it. The influences of stress in solar cells for example was investigated by parameter variations of a FEM model simulating a temperature change of 100 K [Carr76]. From these results also first design rules were derived. However, the investigated PV module design differs from today's conventional design (see Section 1.3) in two aspects: 1. As back layer an Aluminum substrate was used. 2. No encapsulant was used between substrate and solar cells. Instead, solar cells were adhered to the substrate by an adhesive. Also, for most parameter variations, the front cover was neglected. Therefore, today only the design rule for encapsulants is applicable. It recommends thermally soft encapsulant, i.e. encapsulants with a low thermal expansion stiffness $E_\alpha$. Although, most of the design rules themselves are not applicable anymore, the methodology is still valid. Nevertheless, no other publications covering general thermomechanical design rules explicitly could be found. Since this work focuses on thermomechanical design rules, the following Sections cover the state of the research regarding thermomechanical stress in solar cells within a PV module.

## 2.1 Thermomechanical Stress

Degradation of PV modules is still a subject of research [Ferr12, Jord13, Jord16, Könt16, Könt17], where mechanical stability is one important aspect [Könt11, Ping09]. There are several publications focusing on thermomechanics, e.g. [Diet10, Eitn11a, Eitn11b, Eitn11c, Krae14, Krae15, Lee11, Lee12, Pagg13b,

Thak12] and on mechanical loads, e.g. [Aßmu17a, Aßmu17b, Lee13, Mick11, Mülh13, Sand13, Schn17, Suzu18]. The most relevant publications will be briefly introduced below. Mostly, the focus is just on one part of the PV module, like ribbons [Krae13] or different metallization layouts [Diet13b].

Mickiewicz *et al.* [Mick11] have shown on 9-cell laminates that the drastic increase of EVA's Young's modulus at temperatures below 0 °C leads to an increase in cracks in the solar cells during mechanical load. Even though Mühlhöfer *et al.* [Mülh13] found, that the higher stiffness of the encapsulant at low temperatures results in a lower bending, they confirmed Mickiewicz observations also for 60-cell modules.

Gabor *et al.* [Gabo16] compared different PV modules setups and mounting structures in mechanical load. They found that reducing the strain gradients reduces the amount of cell cracking. Also, they showed that solar cells in glass-glass modules are exposed to very low stresses due to the position in the neutral axis.

## 2.1.1 Experimental Stress Determination

Experimental methods for determination of stress within PV modules can be divided into non-invasive and invasive methods, as depicted in Figure 2.1. In the following, methods which are relevant for this work are summarized, for more details it is referred to literature, like [Shar08]. For each method examples of application on solar cells are given. The two methods used in this work, µ-Raman spectroscopy and piezoresistive stress sensors, are covered in more detail.

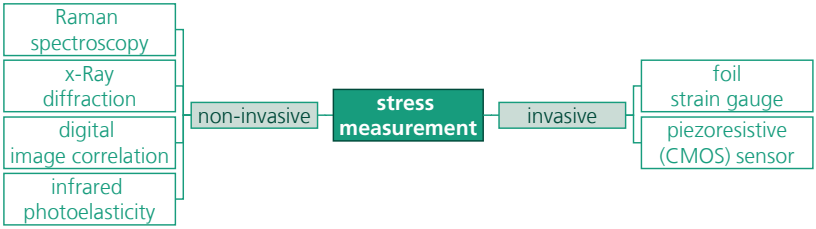


**Figure 2.1** Overview of experimental stress determination techniques relevant for PV modules.

### 2.1.1.1 Non-Invasive Stress Determination

Most non-invasive stress measurement methods comprise methods utilizing the interaction of any kind of electromagnetic waves with matter. The advantage of such methods is that usually they do not require a special sample preparation.

The limiting requirement for such methods is the need of a direct field of view from the radiation source to the detector, which is not possible for all setups.

Eitner *et al.* [Eitn09, Eitn10b] used the digital image correlation with two CCD stereo cameras to measure the cell gap displacement of a three-cell PV laminate from thermal loading. An accuracy of 1 µm was achieved and the method was used to validate a FEM model.

Wong *et. al* [Wong97] used Infrared (IR) photoelasticity to measure the stress in solar cells due to silicon oxide and aluminum layers. Zheng *et al.* [Zhen02] used phase stepping to obtain the magnitude and orientation of stress in solar wafers. Since IR photoelasticity is a transmissive method, application in PV modules is only possible, if all materials are IR transparent.

Another optical stress measurement method is X-ray microdiffraction, which has been established in recent years. There are two different approaches in the literature:

1. The measurement of deflection by a laboratory X-ray setup, called X-ray topography: Meng *et al.* [Meng16, Meng18] applied the method to quantify the bending and stress of a 31.8×31.8 mm² solar cell due to lamination. Since the stress is obtained from the deflection measurement, X-ray topography is limited to processes involving a deflection.
2. Microdiffraction using a synchrotron X-ray source: Budiman *et al.* [Budi14] apply the method to measure the stress of a 125×125 mm² back-contact solar cell within a PV laminate with a transparent backsheet. Due to limited penetration depth, the measurement has to be performed through the backsheet and requires a synchrotron X-ray source. Nevertheless, the same group used the method to investigate stress after soldering and lamination in a 125×125 mm² back-contact solar cell [Tipp17] as well as the influence of two different encapsulants on stress after lamination [Hand17]. Recently, the method was transferred to multicrystalline solar cells by the same group [Tipp19].

**Raman Spectroscopy**

Raman spectroscopy is a well-established method for stress determination in the field of microelectronics [Anas70, Gane70, Loud64, Wolf96a]. It allows spatially resolved measurement of stress without a mechanical contact to the sample, which is explained in detail in Section 3.1. In the following, some examples for the application in the field of photovoltaics are given. However, there was no

work about the application of Raman spectroscopy in laminated solar cells within a PV module available at the start of this thesis.

Gundel *et al.* [Gund11a, Gund11b] used µ-Raman spectroscopy to identify stress from laser-induced doping. They measured in cross sections of floatzone silicon solar cells. Within the same group first attempts were taken to incorporate surface topology of silicon solar cells for a more accurate measurement of doping concentration [Hein12, Hein14]. These works were the foundation of the measurement procedure developed within this work. Also on cross sections of monocrystalline silicon wafers, Schmid [Schm10] measured stress from different metallization pastes. She experimentally determined the Raman peak position of the investigated samples as (520.44 ± 0.05) $cm^{-1}$ and the correlation of the Raman peak shift to stress for a <100> surface as (300 ± 30) MPa/$cm^{-1}$ using a 3-point-bending setup. Mühleisen *et al.* [Mühl15] measured the stress around the busbar end from solar cell interconnection on the surface of multicrystalline solar cells. They used 520.5 $cm^{-1}$ as the silicon reference peak value and conversion factors from literature. From the same group, Neumaier *et al.* [Neum16] used the same method to measure stress in mono- and multicrystalline solar cell strings. They did not take different crystal orientations in multicrystalline solar cells and the structure pyramids of monocrystalline solar cells (see Section 3.1) into account. Therefore, their results scatter significantly. A more thorough investigation of the effect of multicrystalline solar wafers was done by Pogue *et al.* [Pogu18]. They used Raman spectroscopy and photoelasticity to measure residual stress within grains and on grain boundaries from casting and wire sawing. Using polarized µ-Raman spectroscopy, they resolved each crystal in the multicrystalline silicon wafer individually. The polarized µ-Raman spectroscopy was established by Becker *et al.* [Beck07]. Popovich *et al.* [Popo11] also investigated residual stress in multicrystalline solar cells in the different production steps from wire sawing until metallization. They used different monocrystalline conversion factors from literature for cross-sectional and surface samples independent on grain crystal orientation.

#### 2.1.1.2 Invasive Stress Determination

Invasive methods require a special sample preparation or modification with the benefit, that no field of view is necessary. Therefore, they can be used in a wider range of applications than non-invasive methods. However, the drawback of the sample preparation is that it often modifies and interacts with the investigated effects.

One of the conventional techniques for the measurement of stress in laminates are foil strain gauges [Ifju08]. These utilize the dependence of the resistance on strain. A metal is usually attached to a carrier foil in a meander style. However, in PV modules they are rarely used because of several disadvantages [Eitn10b]. For example, the strain gauge adheres to the encapsulant as well as the solar cell, therefore the strain in the gauge cannot be appointed to one layer specifically, which is particularly a drawback for thermal stress. In addition, inserting the strain gauge into the laminate usually requires a special sample preparation, which modifies its thermomechanical properties. Nevertheless, Hirschl *et al.* used strain gauge rosettes to measure strain in a one-cell PV laminate during lamination and subsequent thermal cycles [Hirs12]. They concluded that the deviation of the measurement to a FEM simulation originates from the anisotropic material behavior of the encapsulant.

**Piezoresistive Stress Sensors**

The piezoresistive effect of semiconductors, like silicon, is well known [Kand82, Kand91, Smit54]. It correlates a strain to a resistance change, which allows the measurement of strain within the semiconductor itself. First sensors were developed by Edwards, Spencer *et al.* [Edwa83, Spen81]. Since then silicon based piezoresistive stress sensors play an important role in the field of microelectronics [Gree88, Jaeg94], there are several text books covering different aspects, for example [Doll13, Shar08, Swee93, Trän14, Völk06]. In research, the applications range from the investigation of process steps [Lemk11] to analysis of the electronic packaging [Bitt91, Suhl01]. Especially the investigation of the stresses applied by the packaging to all kind of sensors is in the focus of many publications, as indicated by the review of Barlian *et al.* [Barl09]. Further applications are pressure and force sensors [Barl09]. The majority of today's piezoresistive stress sensors are complementary metal–oxide–semiconductor (CMOS) based sensors [Barl09]. Often they consist of a set of four sensors, connected in a Wheatstone bridge configuration [Gies11].

However, so far there are no applications using solar cell production processes and implementations on silicon solar cells or even within PV modules known.

## 2.1.2 Finite Element Modelling of PV Modules

The finite element method offers the possibility to assess the full physical state of the PV module. Since this is a huge advantage compared to the experimental

stress determination, FEM simulations are a convenient alternative to experiments. However, due to the large aspect ratio of the planar dimensions to height, FEM modelling of PV modules requires an enormous computational effort for absolute values, which also have to be validated. Therefore, just with the improvement and price decline of simulation hardware in recent years, the use of mechanical FEM simulations increases. In the following, the most relevant works are summarized.

Eitner *et al.* [Eitn11a, Eitn11b, Eitn11c] investigated the thermomechanical stress after lamination at 150 °C and one temperature cycle to -40 °C of a frameless 60-cell glass-foil PV laminate without ribbons systematically. For each PV module component, they have investigated the materials with regard to the material model. They conclude that except of the EVA, all components can be simulated using linear elastic material models. For EVA they propose a generalized Maxwell model with 26 arms [Eitn10a]. They found the third principal stress $\sigma_{III}$ in the solar cells of the glass-foil laminate at -40 °C between -14.4 MPa and -84.4 MPa. Their model was validated using a minimized 2D FEM model of a three cell string where the cell gap displacement was compared to a measurement with a digital image correlation [Eitn09, Eitn10b].

Dietrich *et al.* [Diet10] investigated the influence of the height of solar cells and EVA on the stress from thermal cycling and mechanical load from 4-point bending of a frameless PV laminate consisting of one 5-cell string. Both parameters strongly influence the bending of the laminate. They found that the highest stress occurs at the end of the busbar. For all materials linear elastic material models were used. The FEM model was validated by measuring the deflection in a 4-point bending test. In further works, they showed that the aluminum back side metallization has no significant influence on stress in solar cells and extended the FEM model to a 60 cell PV module including a frame [Diet14]. The FEM model includes ribbons on the solar cells but not in the cell gaps. With the 60-cell model, they simulated lamination and 2400 Pa mechanical load, where a line mounting along either the long or short side is used [Diet12]. With the same FEM model, they showed that non-uniform load leads to a different stress distribution and consequently the mounting type plays an important role [Diet13a].

Linholm *et al.* [Lind20] investigated the solder joint fatigue in thermal cycling on a framed 72-cell module, which includes busbars and ribbons in a submodel. Except of the solder, for which an Anand's viscoplastic creep model was used, all materials were linear elastic. Glass-foil modules induce higher strains than glass-glass modules and also EVA than polyolefin. The higher accumulated plastic work

within EVA modules is attributed to its lower Young's modulus in the investigated temperature range.

Paggi *et al.* [Pagg13a] proposed multi-scale numerical model of a PV module, which also covers the grain structure of a multicrystalline solar cell. In the global, model a frameless 60-cell PV laminate without ribbons was simulated using the assumption of small deflections. In the sub model, only one solar cell was modelled in full detail, including the polycrystalline microstructure. This sub model also includes fracture mechanics to compute crack patterns, which are then used to compute electrically inactive areas and their impact on the electrical performance of the solar cell.

Aßmus *et al.* [Aßmu17a] derived approximations for different non-uniform and non-orthogonal load distributions. They used the extended layerwise theory approach to model a 60-cell PV laminate without ribbons and without a frame with linear elastic materials. With the same FEM model, they investigated different geometrical aspect ratios according to their deflection [Aßmu17b].

Schicker *et al.* [Schi14] showed that if the frame is not considered explicitly, the used boundary conditions have a significant influence on the deformation of the module and the stress of the solar cells.

Hartley *et al.* [Hart20] focused on realistic screw-mounting conditions of a 60-cell PV module without ribbons. They considered the friction between the PV module frame and the supporting beam as well as the screw. Also, corner connectors were considered with friction to the frame. They used latin hypercube sampling and the comparison to mechanical load tests up to 2400 Pa to find realistic friction coefficients. The model assumes geometric linearity with linear elastic isotropic materials. Within two standard deviations of the mean, determined by the latin hypercube sampling, the simulation matches the measurements within the uncertainty. The identified the frontglass and the rubber inlay as components with the highest influence on the deflection.

Krämer *et al.* [Krae15] showed that stress in solder bonds of 60-cell glass-glass frameless PV laminates exposed to thermal cycles is significantly higher compared to glass-foil PV laminates. They also compared the accumulation of plastic creep strains in back-contact PV modules to conventional glass-backsheet and glass-glass modules [Krae13, Krae14]. According to their simulation, the value in conventional solder joints is half the value of back-contact modules and for both interconnection technologies higher in glass-glass modules than in glass-backsheet modules. In both studies, for the solar cells, EVA and glass linear

elastic models were used for all other material bilinear elastoplastic material models. The FEM model was not validated.

Owen-Bellini *et al.* [Owen17a, Owen17b] simulated thermal cycling of mini-laminates with six solar cells incorporating a viscoelastic EVA model. They found compressive stress in the solar cells and shear stress in the ribbons.

Lee *et al.* [Lee11] developed a non-validated FEM model of a 60-cell framed PV module without ribbons using linear elastic material models. The FEM model covers lamination and subsequent thermal stress caused by the temperature distribution in operation. According to the FEM simulation the maximum first principal stress $\sigma_I$ in the solar cells is 29 MPa. With the same FEM model, they simulated a maximum first principal stress $\sigma_I$ of 106 MPa at a homogeneous mechanical load of 5400 MPa [Lee13].

Li *et al.* [Li19] performed a comparative study of busbar solar cells and smart wire interconnection technology (SWCT) solar cells. The FEM simulation covers soldering, lamination, transport and subsequent static and dynamic mechanical loading as well as thermal cycling. As materials they used temperature dependent linear elastic and for the copper ribbons elastoplastic models. The frame was represented by fixed constraints on the module edges. According to their non-validated simulations, the stress in solar cells is lower for SWCT modules than for busbar modules for all investigated loads. For busbar solar cells, dynamic loading induces slightly higher stress in the solar cells than static loading.

Rendler *et al.* [Rend16a, Rend16b] simulated the soldering process. They chose a solar cell stripe as a symmetry element and used bilinear elastoplastic material models for the copper ribbon. The FEM simulation was validated by the deflection of a single-side soldered solar cell stripe [Rend15]. They found the maximum first principal stress $\sigma_I$ in the extension of the busbar.

Lai *et al.* [Lai13] conducted a parameter study of the soldering process, comparing different geometry parameters, on a single solar cell. The FEM modell used bilinear plastic material and elastoplastic material models. They also found the maximum residual stress in the extension of the busbar. The stress increases for a decrease of solar cell thickness as well as for an increase in ribbon thickness and width. They performed a plausibility check by measuring the bow of a soldered solar cell, which was smaller than the simulated one. They extended the FEM model by crack simulations to take the singularity at the ribbon end into account. The evaluation of the stress intensity factors confirmed the previous findings of the stress dependence [Lai14].

Shiin *et al.* [Shin18] investigated the influence of soldering and the flattening of the solar cell during lamination. They performed a parameter study for the number of busbars, solar cell thickness and different solder alloys on a single solar cell. The flattening process during lamination was simulated by an applied pressure. According to their non-validated simulation, the residual soldering stress slightly decreases by the flattening process.

Song *et al.* [Song18] used a two dimensional FEM model to simulate the stress during soldering and the different phases of lamination. They modelled the cross-section of three three-busbar solar cells as a representation of the cross-section through the short symmetry plane of a 66-cell PV module. They used linear elastic, temperature dependent material models for all materials except of the copper ribbons, which were modelled elastoplastically. The melting of the encapsulant was modelled by using a temperature dependent Young's modulus. According to the non-validated FEM simulation, the highest stress in the solar cells occurs in the pressure ramping up phase during lamination.

Knausz *et al.* [Knau15] showed that the process parameters in the encapsulant production and later in lamination have a significant influence on the thermal expansion behavior of the foils.

#### 2.1.2.1 Handling Singularities

Stress singularities of sharp corners are well known in the literature, one of the first who described the singularity of angular corners of plates was Williams [Will52]. England [Engl71] found that the boundary conditions have a strong influence on the singularity and determine its type. Also, the geometry strongly influences the magnitude of the singularity. Sinclair extended the mathematical framework [Sinc99, Sinc00]. Several works have investigated similar singularities and found that a typical behavior is the proportionality to $r^{-\lambda}$ with $r$ being the distance to the singularity and $\lambda$ the eigenvalue also called order of the singularity [Koto06, Mayl12, Sinc04a, Sinc04b]. With the establishment of the finite element method, singularities were investigated using FEM. Whitcomb *et al.* [Whit82] revealed that the finite element method is not able to describe the stress in two mesh elements adjacent to the singularity correctly because the stress tensor is not symmetric at the position of a stress discontinuity or singularity. Apart for the two adjacent mesh elements, the stress can be determined correctly by FEM. Therefore, by minimizing the size of the first two mesh elements, the influence of the singularity can be localized to a small area. Levy [Levy91] confirmed these findings.

Suganuma *et al.* [Suga84] discovered that in a ceramic-metal joint the maximum stress of the singularity decreases with interlayer thickness.

Munz *et al.* [Munz92] discovered that for thermal loading, the stress near the singularity is independent of its order. In a later work on ceramic-metal joints with an interlayer Munz *et al.* [Munz95] discovered that close to the singularity the stress is dominated by the interface of the interlayer with the ceramic/metal. Beyond a critical distance, the influence of the interlayer vanishes and only the properties of the ceramic and metal determine the stress. Between these two regions there is a transition zone and far away from the singularity, the stress is not related to the ceramic-metal joint anymore. The stress magnitude calculated by FEM close to the edge depends on the material parameters of the layers. For small differences it converges to a finite value, for large differences it tends to infinity.

Alam *et al.* [Alam09] investigated intermetallic compounds of solder joints by FEM. They concluded that due to the asymmetry of the elastic and plastic properties there might be always a singularity at the interface between solder and the intermetallic compound.

Since the FEM-modelling of solar cells is a relatively new topic, there are just a few authors covering the handling of singularities in the FEM models, apart from fracture mechanical approaches. Rendler *et al.* [Rend19] are among the first mentioning how the singularities are treated. They chose the approach to neglect the mesh element adjacent to the singularity according to Whitcomb *et al.* [Whit82]. Hsiao *et al.* [Hsia19] modified the geometry by introduction fillets to avoid the singularities at the regions of interest.

# 3 Stress Determination Methods in Encapsulated Solar Cells

The basis of thermomechanical design rules is a detailed understanding of stresses within a PV module. In module production process residual stress is build up, which is mainly compressive and locally tensile, e.g. at the end of the busbars. Therefore, it is important to consider these stresses when investigating stress from external loads, like mechanical or thermal loads. For a fundamental understanding it is desirable to consider residual stress from production and stress from external loads separately. This option is provided by the finite element method. Additionally, it gives the possibility to examine the stress globally, hence to identify locations of highest stress. Moreover, it allows to split the stress tensor in its components to obtain a comprehensive understanding. In this work a three-dimensional FEM model of a PV module is built in the commercial software *COMSOL Multiphysics v5.4* and *v5.5* (see Section 3.3). The FEM model simulates a rudimental soldering process followed by the lamination., then a frame is added to the laminate and the stress from the production is transferred and used as an initial stress state. Finally, mechanical load at temperatures from -40 °C to +85 °C is simulated as well as purely thermal load with the same temperatures. Crucial material parameters, like the temperature dependent Young's modulus of the encapsulant are measured by a dynamic mechanical analyzer (*DMA 242 C* by *Netzsch*). The remaining parameters are taken from literature. The FEM model is validated experimentally. Finally, parameter variation studies are conducted to investigate influences of material properties and geometric dimensions.

As a brittle material, silicon solar cells can fail under tensile stress. Therefore, tensile stress is converted into a probability of cell fracture $P_f$ using the two parameter Weibull distribution considering size effect (see Section 3.3.3.1).

For the validation of the FEM model stress measurement methods, which are applicable in a laminate structure are identified. Since only a few methods for the stress or strain measurement in PV modules exist so far, a focus is put on the improvement of existing and development of new methods. Two approaches are used: a non-invasive and invasive. The non-invasive stress measurement utilizes the dependence of the Raman scattering on the strain in silicon (see Section 3.1). The µ-Raman spectroscopy is widely used in the field of microelectronic, also

some applications on silicon solar cells are reported. However, so far the surface topology of silicon solar cells have not been taken into account. Also, no application on laminated solar cells within a PV module are reported. Therefore, a methodology which considers the surface topology of monocrystalline silicon solar cells is developed. This method is then transferred to laminated solar cells, taking the frontglass and encapsulant into account. The developed method is used to measure residual stress after soldering and lamination in PV laminates. The measurement results are compared to the FEM simulation and accordingly the FEM simulation is validated by them.

So far, no invasive stress measurement method exists, which measures the stress in the solar cell directly. Foil strain gauges for example, which are attached to the solar cell surface are in the interface between the solar cell and the encapsulant. Thus, they measure a superposition of the strain within the solar cell and the encapsulant. Therefore, an attempt to integrate a stress sensor into the silicon solar cell is made. Different sensor designs are developed, which utilize the piezoresistance of highly doped silicon by measuring the resistance of a local highly doped sensing part (see Section 3.2). Along with the sensor design, the processing is developed and the sensors are produced at the Fraunhofer ISE. The developed solar cell integrated stress sensors are used to validate the FEM model by measuring the stress during mechanical load.

## 3.1 µ-Raman Spectroscopy

µ-Raman spectroscopy is a method for stress determination in the field of microelectronics. Hence, it is well understood for planar silicon surfaces and different crystal orientations. However, for silicon solar cells there are two differences: 1. the surfaces are textured and 2. in a PV module, the solar cells are encapsulated and covered by a frontglass. Consequently, the measurement procedures described in the literature are not applicable. To develop a measurement procedure for laminated textured solar cells, first the influence of the texturing and afterwards of frontglass as well as encapsulant are investigated. In the following the general measurement set-up (Section 3.1.2) followed by the developed measurement procedure (Section 3.1.3) is described.

The content of this Section as well as corresponding results have been published in the journal *Solar Energy Materials and Solar Cells* [Bein19]. The method development has been a collaboration with Andreas Büchler. He conducted the µ-Raman measurements, while my task has been conversion into stress as well as the silicon pyramid FEM simulation.

### 3.1.1 Relation of Strain and Raman Signal

The Raman spectroscopy measures the phonon energy in a crystal by the inelastic scattering of light [Rama53, Smek23]. Using a laser for excitation, the scattering spectra shows several peaks. The most prominent is the Rayleigh peak, which is generated by light with the same wavelength as the laser and results from elastic scattering. The peak is flanked by two strong peaks that are equidistant on an energy scale to the Rayleigh peak. These peaks are related to an inelastic scattering process of photons that involves annihilation or generation of lattice vibrations (phonons). Therefore, the photons causing these peaks, either absorb (Stokes peak) or release (Anti-Stokes peak) energy in the scattering process, as depicted in Figure 3.1. The Stokes peak is called Raman peak for a one-phonon generation. The energetic gap between Rayleigh peak and Raman peak equals the phonon energy. Commonly, the frequency scale, represented by the wavenumber, is used rather than the energy scale and normalized to the position of the Rayleigh peak. Then the position of the Raman peak, which follows the shape of a Lorentzian distribution, defines the Raman wavenumber. If the excitation laser is focused onto the sample in a micrometer range, it is commonly referred to as µ-Raman.

Mechanical strain induces distortions in the crystal lattice and thus a shift of the Raman wavenumber. For planar surfaces it can be shown that there is a linear correlation between strain and shift of the Raman wavenumber [Anas70, Wolf96a].

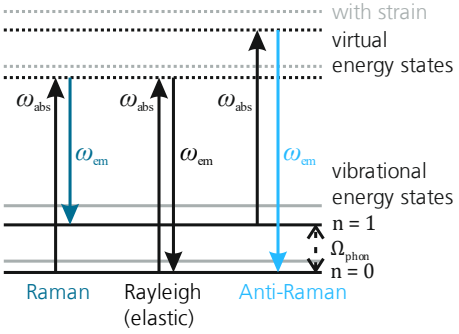


**Figure 3.1:** Schematic energy-level diagram of the Raman shift; $\omega_{abs}$: wavenumber of absorbed photon, $\omega_{em}$: wavenumber of emitted photon and $\Omega_{phon}$: wavenumber of excited phonon state. The shift due to strain is indicated by the grey lines; not to scale; modified after [Bein19].

## 3.1.2 Measurement Set-up

The used µ-Raman spectrometer consist of a confocal microscope with an x-y translation sample stage, a Si-CCD detector and a fiber coupled Nd:YAG laser of 532 nm wavelength for the Raman excitation. The laser has a penetration depth in silicon of about 1 µm. The spot diameter of the focused beam is about 0.5 µm. The laser power is set to 1 mW. The measurements are performed in scanning mode, which allows for subsequent measurements of several spectra along a defined line or within a defined area. An algorithm fits each Raman peak in the measured spectra by a Lorentzian function. The fit parameter of the center of the Lorentzian is used as the measurement result for the Raman wavenumber. A 3-point bending stage can be placed on the x-y stage to apply a well-defined stress in silicon (see Figure 3.2).

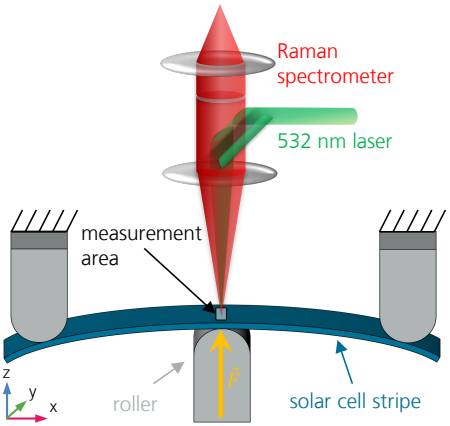


**Figure 3.2:** Sketch of the 3-point bending setup within the µ-Raman spectrometer to measure on the vertex. The setup can be tilted to measure on the cross-section, not to scale, modified after [Bein19].

## 3.1.3 Measurement Procedure

### 3.1.3.1 Determination of Conversion Factor for Textured Surfaces

Due to potassium hydroxide (KOH) etching, the surface of monocrystalline silicon solar cells exhibits randomly distributed pyramids with (111) flanks. A typical pyramid size is in-between 3-5 µm. The (100) surface is only exposed in the valleys between the pyramids. Therefore, the light is mainly scattered and emitted on

(111) surfaces. On the other hand, the lattice deformation and the phonon vibrations happen also in the (100) plane. Therefore, the phonon vibrations, i.e. the stress sensing, and the photon back scattering may happen in different crystal planes. Additionally, the stress distribution within the texture pyramids on the stretched solar cell is inhomogeneous. Using a simple FEM simulation of one silicon square-based pyramid (base: 5×5 µm², height: 5 µm, Figure 3.3, material properties Table 3.2), which edge is displaced on its base, the stress distribution within the texture pyramids is simulated. If the base of the pyramid is stretched, tensile stress appears all over the volume close to the base. In comparison on the upper part of the pyramid the two flanks that are parallel to the direction of the stretch show tensile stress, while the two flanks perpendicular to the stretch show compressive stress (see Figure 3.3). With an increasing displacement of the base, the tensile stress in the flanks parallel to the deflection increases close to the base. However, close to the tip, compressive stress increases. Thus, the variation of the stress magnitude along the surface near the bulk increases, as well as the magnitude of the average (tensile) stress.

Since the spot-size of the used laser is small compared to the pyramid size, µ-Raman spectroscopy resolves the inhomogeneous stress distribution within the texture pyramids. This means that µ-Raman measures tensile and compressive stress on the surface of solar cell stripes, depending on the laser beam position on the pyramid. The following consequences from the simulation are relevant for the formulation of a measurement procedure on textured surface on a silicon bulk that is under tensile stress:

1. Volume close to the pyramid tips is mainly in compressive stress.
2. Volume close to the pyramid base is mainly in tensile stress.
3. Seen from top-view perspective, the area fraction of tensile stress is large compared to the compressive stress volume along the pyramid tip. Thus, if the Raman frequencies within an area bigger than the pyramid size are averaged the influence of tensile stress dominates.
4. Since tensile and compressive stress increase with increasing deflection, the variation of measured Raman frequencies in such an area increases.

For the experimental verification it is referred to [Bein19, Büch17]. As the results in Figure 3.3 show, the induced stress in the bulk leads to different stress values in the pyramid. Therefore, the measurement values depend on the used optics, more precisely on the depth of focus compared to the pyramid height. A high numerical aperture (NA) lens allows for spatially resolved analyses of the local stress distribution, as the depth of the confocal plane is small with respect

to the pyramid texture height. A low NA lens detects light from the whole pyramidal shaped surface, as the whole texture lies within the confocal plane. Consequently, a low NA objective is used for textured surfaces.

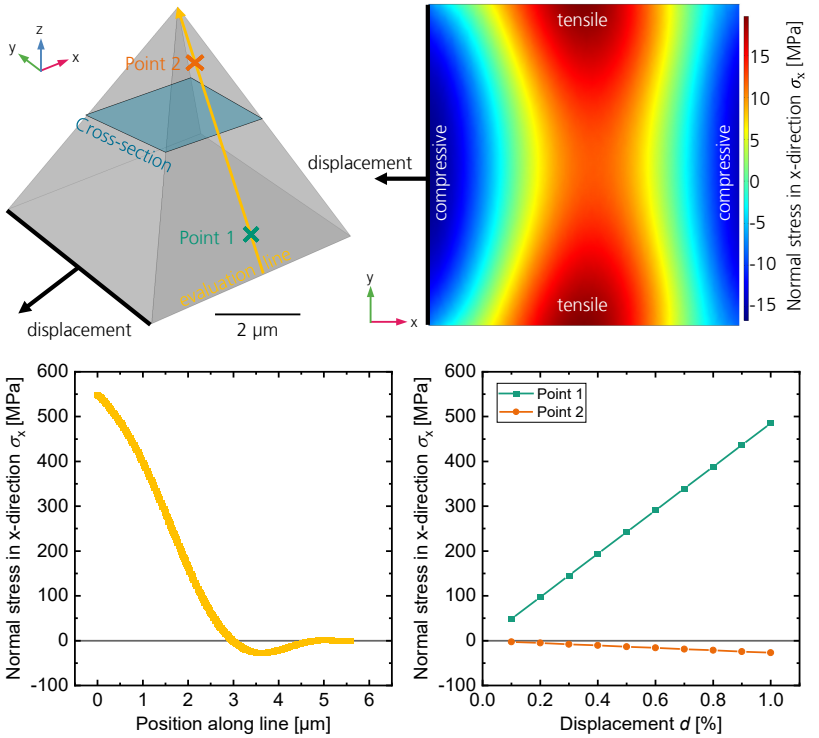


**Figure 3.3:** *Top left*: sketch of a simulated silicon pyramid. Top *right:* normal stress in x-direction in the cross-section of the pyramid (indicated in petrol) that results if the base edge is displaced in the direction indicated by the black arrows. Both modified after [Bein19]. *Bottom left*: normal stress in x-direction along the evaluation line (indicated in yellow); *Bottom* right: normal stress in x-direction at the two evaluation points (indicated in green and orange).

To determine a conversion coefficient for textured silicon surfaces, identically processed industrial crystalline silicon solar cells are split into stripes of 10×1 cm². The Young's modulus is determined measuring the force-deflection-curve of 20 stripes on a universal testing machine *zwicki Z0.5 TN* with an identical 3-point bending stage to the one in the µ-Raman spectrometer. For these probes, the maximum stress on the surface of the solar cell strip at the vertex is determined in dependence of the deflection within the linear elastic limit (Figure 3.4).

Using the 3-point bending stage within the µ-Raman setup, the Raman spectra on the surface of the textured solar cell stripes at the vertex position is measured for different deflections. The bending set-up has been installed to induce tensile stress on the measured surface. For each deflection 1000 Raman spectra are measured within an area of 10×30 µm², that is small compared to the sample size but large in respect to the surface texture pyramids. The distribution of the 1000 evaluated Raman frequencies for each deflection is summarized in histograms (see Figure 3.4, right). Finally, the distribution in the histograms is fitted with a Gaussian function. The mean of the Gaussian is used as the measurement result for the average Raman wavenumber at the respective deflection and the variance of the Gaussian as a measure for the variation. For each deflection, the peak shift is plotted in respect to the reference measurement (measurement at no deflection) in Figure 3.5 right. Until 10 mm, the average peak-shift is a linear function of the deflection. For higher deflections, the function becomes nonlinear due to sliding.

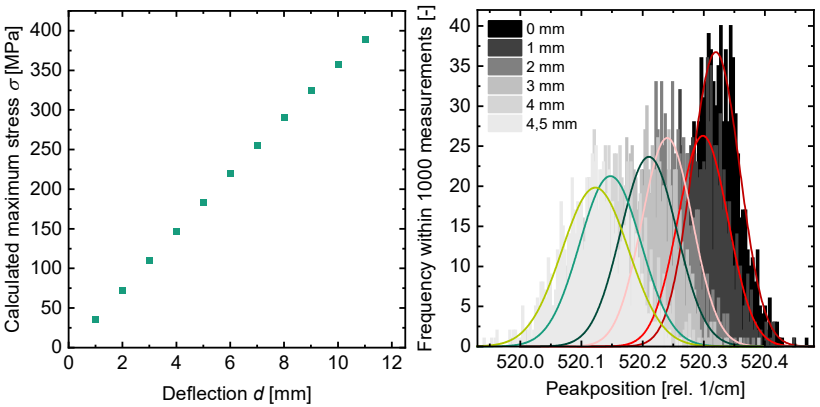


**Figure 3.4:** *Left*: Calculated maximum stress values in the vertex of a 10×1 cm² solar cell stripe for different deflections in 3-point bending test. *Right:* Measured distributions of Raman frequencies for different deflections in 3-point bending test. Each histogram is fitted with a Gaussian. Both modified after [Bein19].

To determine the conversion coefficient, for each deflection the calculated maximum stress is plotted versus the average peak shift of the 1000 measurements. By a linear regression, the slope of the line was obtained, which defines the conversion coefficient $\Sigma$.

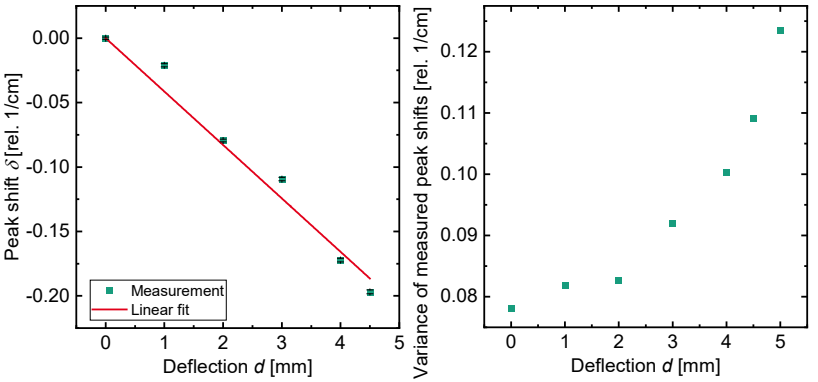


**Figure 3.5:** *Left:* Average peak shift for each deflection in 3-point bending test compared to the reference measurement; please note, that the error bars are too small to be visible. *Right*: Gaussian variance of the measured Raman peak shift for each deflection in 3-point bending test. Both modified after [Bein19].

### 3.1.3.2 Influence of Frontglass

To investigate the influence of the frontglass of a module on the stress determination via µ-Raman spectroscopy, a glass sheet (height: 3.2 mm) is placed between a solar cell stripe (10×1 mm²) on the bending stage and the microscope lens. Since the confocal microscope focusses on the silicon surface, light interaction with the glass sheet is not measured by the µ-Raman Spectrometer. Thus, any residual stress from lamination does not impact the measurement. However, the optical losses (reflection and absorption) have to be compensated by increasing the laser intensity, which is adjusted to induce a Raman peak intensity of approximately equal height with and without glass. For several deflections the same sample is measured 1000 times in an area of 10×30 µm² at the same spot with and without the glass sheet. The peak shifts are plotted in histograms and the Gaussian fits of the obtained distributions for 0.5 mm and 1 mm deflection are compared.

### 3.1.3.3 Laminated Solar Cells

To determine the thermomechanical stress from each module production step on the sunny side of the solar cell, twelve single-cell laminates have been built using industrial processes. Monocrystalline three busbar solar cells, with continuous busbars on the front and six solder pads on the back (see Figure 3.7 and Table 3.2 for the material specifications) are used. Since the residual stress would be relieved by crack formations, the solar cells are controlled for cracks by

electroluminescence imaging (EL) after soldering and lamination. Figure 3.6 illustrates the performed investigations after each production step.

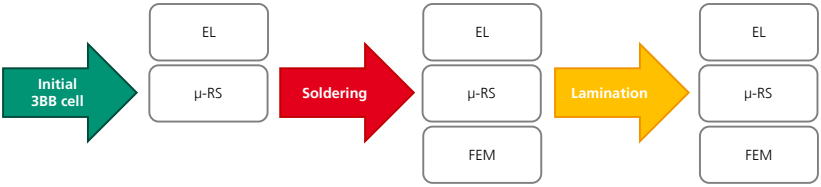


**Figure 3.6:** Schematic flowchart of the conducted measurements and simulations after each module production step. EL: Electroluminescence imaging, µ-RS: µ-Raman spectroscopy, FEM: Finite element modelling. Modified after [Bein19].

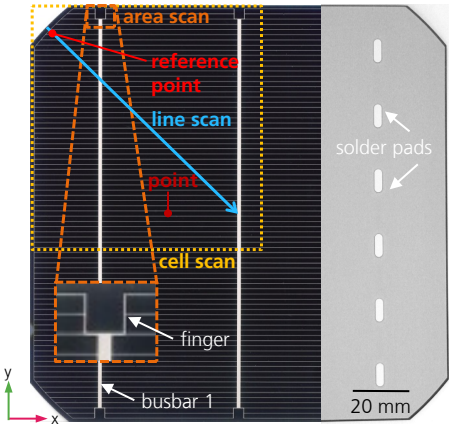


**Figure 3.7:** Investigated solar cell layout with the positions of µ-Raman measurements. The area scan is additionally enlarged in the insertion. The back side is overlaid on the right.

Temperature influences the Raman peak-position but the measurement set-up did not allow an accurate control of the solar cell temperature. Therefore, a measurement procedure that is invariant to changes in the solar cell temperature has been used. A reference wafer position, that has the lowest stress change during processing, is defined. This reference position is measured before and after each µ-Raman measurement on the actual region of interest. The stress in the region of interest is then determined based on the average difference of the Raman peak position detected in the measurements on the reference wafer position and the measurements within the region of interest. The corner of the solar cell is used as reference position, since it is expected to be the wafer position with the lowest stress [Eitn11a]. This and all other used measurement locations are depicted in Figure 3.7. To capture the overall residual stress, a measurement

in the center of the solar cell between two busbars is performed after each production step. The measurement position is labeled by "point" in Figure 3.7. The reference and actual stress measurement consist of 1000 single measurements distributed within an area of 10×30 µm² with an integration time of 0.01 s.

### Metallization and Soldering

In order to determine the residual stress from the cell production processes, like metallization, the stress on the solar cell before soldering has been measured. Solar cells come with a small bow but are flattened in the lamination process, therefore, the metallized and soldered solar cells have been flattened by covering it with a glass sheet, used for module production. The metallized solar cells are measured additionally without a glass sheet to determine the stress induced by the flattening.

For the soldering of the solar cell, the semi-automated contact-soldering platform *SOMONT CONSOL,* which contacts both sides of the solar cell simultaneously, has been used. The temperature of the hotplate on the solar cells backside is set to 175 °C, while the solder tip on the sunny side to 235 °C with a contact time of 3 s. After the soldering and EL inspection, the residual stress of the flattened solar cell is recorded.

### Lamination

The soldered solar cells are then laminated using a conventional module setup, with two layers of commercially available low UV-cut-off Ethylene-vinyl acetate (EVA), a trilayer composite Tedlar-Polyethylene-Tedlar (TPT) backsheet and a frontglass. A maximum lamination temperature of 160 °C is used. After the lamination process, the residual stress is measured again at the same position as the soldered cell. Additionally, a quarter of the solar cell is scanned, labelled by "cell scan" in Figure 3.7. Here, the Raman signal is measured each 200 µm in x and y direction on an area of about 85×85 mm², which sums up to 180,625 measurement positions. To reduce the measuring time, only 10 Raman spectra are measured at each position. The obtained peak positions are fitted with a Gauss-function. To overcome the thermal drift during the long measurement, three characteristic positions (indicated in Figure 4.15) have measured before and, as a control, also after the area scan. With these values the peak shift due to temperature is determined and the area scan values are shifted accordingly. A second area scan at the end of the busbar is performed, labelled by "area scan" in Figure 3.7, measuring the Raman signal again 10 times every 20 µm on an area of about

6×6 mm², which sums up to 129,600 measurement positions. The thermal drift correction is also applied.

For the line scan, 1000 Raman spectra have been recorded each 50 µm along the diagonal of the solar cell, labelled with line scan in Figure 3.7. This results in 1000 measurement positions. Afterwards a mean over 35 neighboring points has been drawn and then the peak shift has been converted into stress. Since the line scan is much faster than the area scan, no thermal drift correction is required.

### 3.1.4 Stress Components Measured by µ-Raman

De Wolf [Wolf96a] showed that depending on the crystal orientation of the silicon surface different modes of the Raman signal are observed. On textured surfaces the (111) plane dominates, while also (100) planes might be present. Additionally, the Raman wavenumber shift depends on the crystal plane in which phonons propagate, which is the (100) plane and not the plane of main absorption and emittance for textured surfaces. Therefore, it is not straight forward to determine which Raman modes are involved in the scattering process on textured surfaces. Conveniently, for the determination of the conversion coefficient, there's no need to know which crystal planes are involved in the Raman scattering, because it correlates a measured peak shift to a measured stress. However, in order to compare the FEM simulation described in Section 3.3.4.1 to the µ-Raman measurements, the stress components detected by µ-Raman spectroscopy must be known. In the FEM simulation, the surface texture is not considered and the solar cell has a planar (100) surface. For such a (100) surface only the third Raman mode is observed. The modes represent the eigenvalues $\lambda$ of the secular equation [Anas70, Gane70]:

$$\begin{vmatrix} p\varepsilon_x + q(\varepsilon_y + \varepsilon_z) - \lambda & 2r\varepsilon_{xy} & 2r\varepsilon_{xz} \\ 2r\varepsilon_{xy} & p\varepsilon_y + q(\varepsilon_x + \varepsilon_z) - \lambda & 2r\varepsilon_{yz} \\ 2r\varepsilon_{xz} & 2r\varepsilon_{yz} & p\varepsilon_z + q(\varepsilon_x + \varepsilon_y) - \lambda \end{vmatrix} = 0\,, \tag{4}$$

where $\varepsilon_{ij}$ are the components of the strain tensor and $p$, $q$ and $r$ are the phonon deformation potentials, which are material constants for constant temperatures. According to FEM simulations it can be assumed that for the investigated loading cases, soldering and lamination, $\varepsilon_{xz}$ and $\varepsilon_{yz}$ are negligible and equation (4) simplifies to

$$\begin{vmatrix} p\varepsilon_x + q(\varepsilon_y + \varepsilon_z) - \lambda & 2r\varepsilon_{xy} & 0 \\ 2r\varepsilon_{xy} & p\varepsilon_y + q(\varepsilon_x + \varepsilon_z) - \lambda & 0 \\ 0 & 0 & p\varepsilon_z + q(\varepsilon_x + \varepsilon_y) - \lambda \end{vmatrix} = 0\,. \tag{5}$$

From this, the third eigenvalue ($\lambda_3$) is obtained as:

$$\lambda_3 = q\varepsilon_x + q\varepsilon_y + p\varepsilon_z\,. \tag{6}$$

Since only the third one is observed during Raman measurements, $\lambda_1$ and $\lambda_2$ are not shown here. According to De Wolf [Wolf96a], this eigenvalue corresponds to the third Raman mode:

$$\Delta\omega_3 = \omega_3 - \omega_{3,0} \approx \frac{\lambda_3}{2\omega_{3,0}} \tag{7}$$

$$\Rightarrow \Delta\omega_3 \approx \frac{\lambda_3}{2\omega_{3,0}} = \frac{1}{2\omega_{3,0}}\left(q\varepsilon_x + q\varepsilon_y + p\varepsilon_z\right), \tag{8}$$

with $\omega_{3,0}$ being the stress free and $\omega_3$ being the shifted wavenumber of the third Raman mode. Therefore, the wavenumber shift can be related to the stress components using the inverse constitutive equation $\vec{\varepsilon} = \boldsymbol{S} \cdot \vec{\sigma}$, with the inverse 6×6 elasticity tensor $\boldsymbol{S}$ and the strain vector $\varepsilon$. Please note that tensors are printed in bold:

$$\begin{pmatrix} \varepsilon_x \\ \varepsilon_y \\ \varepsilon_z \\ 0 \\ 0 \\ 2\varepsilon_{xy} \end{pmatrix} = \begin{pmatrix} S_{11} & S_{12} & S_{12} & 0 & 0 & 0 \\ S_{12} & S_{11} & S_{12} & 0 & 0 & 0 \\ S_{12} & S_{12} & S_{11} & 0 & 0 & 0 \\ 0 & 0 & 0 & S_{44} & 0 & 0 \\ 0 & 0 & 0 & 0 & S_{44} & 0 \\ 0 & 0 & 0 & 0 & 0 & S_{44} \end{pmatrix} \cdot \begin{pmatrix} \sigma_x \\ \sigma_y \\ 0 \\ 0 \\ 0 \\ \sigma_{xy} \end{pmatrix}. \tag{9}$$

It is assumed, that $\sigma_z$, $\sigma_{xz}$ and $\sigma_{yz}$ are negligible, as confirmed by the FEM simulations for the investigated load cases. With equations (8) and (9) it follows:

$$\Delta\omega_3 \approx \frac{1}{2\omega_{3,0}}(q(S_{11} + S_{12}) + pS_{12})\left(\sigma_x + \sigma_y\right). \tag{10}$$

Equation (10) corresponds to the result from De Wolf [Wolf96a] for a biaxial and a uniaxial stress. Therefore, the conversion coefficient holds for all investigated load cases. From equation (10) it follows that Raman scattering on a (100) surface measures a superposition of the normal stress in x- and y-direction. In the literature [Wolf96a] it is common to define the stress as:

$$\sigma = \frac{1}{2}(\sigma_x + \sigma_y). \tag{11}$$

Consequently, when comparing FEM simulation results to µ-Raman measurements, the stress is evaluated according to equation (11).

## 3.2 Solar Cell Integrated Stress Sensor

In the previous chapter, µ-Raman spectroscopy has been introduced as a method for stress determination. Since it is based on the interaction of an electromagnetic wave with an atom in a crystal lattice causing lattice vibrations, which in turn perturb the other electron shells, the measurement has to be performed with a special, darkened setup and usually in a laboratory. Consequently, in-situ measurements are very challenging for this method. To overcome these issues, a piezoresistive stress sensor, which is integrated into the silicon solar cell wafer has been developed in this work. It measures stress in the solar cell itself without interfering with it.

After a successful development phase, described in Section 3.2.1, the chosen sensor has been implemented into a solar cell wafer and used for the validation of the FEM model, which is described in Section 3.3.4.2.

### 3.2.1 Development

The sensor is based on the piezoresistance effect of doped silicon similar as in sensor applications in the field of microelectronics [Gies10, Gies11, Spen81, Suhl01]. The method is transferred to p-type monocrystalline silicon solar cell wafers and lab-scale silicon solar cell production technologies are used. The stress sensor is realized as a rectangular piezoresistive resistor using high local n-doping by ion-implantation and subsequent silver metallization, as depicted in Figure 3.8. The same process is used to generate local passivated contacts in silicon solar cells. To shield the sensor from the electrons generated in the adjacent silicon, a highly p-doped shielding guard-ring (set to ground in the characterization measurements) is implemented around the sensor.

Since silicon based piezoresistive stress sensors are well known in the field of microelectronics, it is referred to textbooks like [Doll13, Lau93, Trän14, Völk06] for a detailed description.

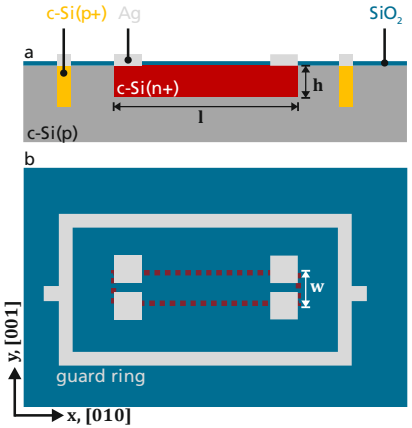


**Figure 3.8**: Schematic drawing of a piezoresistive stress sensor integrated in solar cells. a: Cross-sectional view, the sensor consists of a highly n-doped area within the p-doped substrate and a highly p-doped shielding guard-ring. Both are contacted by Ag metallization. b: Top view: the p-doped area of the shielding is hidden by the metallization. The dotted line indicates the shape of the piezoresistive sensor part, which is hidden by the $SiO_2$ layer. Not to scale, modified after [Bein20a].

### 3.2.1.1 Piezoresistance of Silicon

This Section gives an overview of the piezoresistance effect of n-doped silicon focusing on the physics needed for the sensor development. If not further specified, the content is based on the textbooks of Doll *et al.* [Doll13], Tränkler *et al.* [Trän14] and Völklein *et al.* [Völk06].

The resistance $R_{\sigma,0}$ of a rectangular sensor depends on the sheet resistance $R_{\square}$ of the n-doped layer, its length $l$ and width $w$:

$$R_{\sigma,0} = R_{\square}\frac{l}{w}. \tag{12}$$

If an external stress is applied to the sensor, the change of resistance $\Delta R_{\sigma}$ can be expressed in first order approximation by the piezoresistive tensor $\boldsymbol{\pi}$, which also reflects the anisotropy of silicon [Suhl01]:

$$\Delta\vec{R}_{\sigma} = R_{\sigma,0}\,\boldsymbol{\pi}\,\vec{\sigma}\,, \tag{13}$$

with $\vec{\sigma}$ being the stress vector in the so-called Voigt notation.

For a uniaxial stress, which is the case for a four-point bending test, the stress vector $\vec{\sigma}$ has one component $\sigma_{\mathrm{x}}$ and equation (13) reduces to

$$\Delta R_\sigma = R_{\sigma,0}\, \pi_{11} \sigma_x \,. \tag{14}$$

By correlation an external stress to a resistance change, this relation defines the sensitivity $S_\sigma$ of a piezoresistive sensor:

$$S_\sigma = \pi_{11} = \frac{\Delta R_\sigma}{R_{\sigma,0}\, \sigma_x}. \tag{15}$$

The piezoresistive coefficient $\pi_{11}$ depends on the temperature $T$ and the charge carrier density $N$, which can be described by the dimensionless factor $P$ [Kand91].

$$\pi_{11}(T,N) = \pi_{11,ref}\, P(T,N)\,, \tag{16}$$

where $\pi_{11,\mathrm{ref}}$ is the piezoresistive coefficient at room temperature and a given charge carrier density $N_{\mathrm{ref}}$. With equations (12) and (16), the change in resistance $\Delta R_\sigma$ due to a uniaxial stress becomes

$$\Delta R_\sigma = R_\square \frac{l}{w}\, \pi_{11,ref}\, P(T,N)\, \sigma_x \,. \tag{17}$$

Hence in addition to stress the resistance change $\Delta R_\sigma$ is influenced by the sheet resistance $R_\square$, the aspect ratio $a = l/w$, the charge carrier density $N$ and the temperature $T$. The latter dependence vanishes for sufficiently high charge carrier densities ($\gg 10^{20}$ cm$^{-3}$) [Kand91]. From these parameters different design variations is derived in the next Section.

### 3.2.1.2 Design Development

With equation (17) the geometric dimension of the piezoresistive sensor is derived. The resistance $R_{\sigma,0}$ is chosen in a way that the resulting current for an applied voltage of 1 V is in the range of micro- to milliampere. The sheet resistance $R_\square$ is set to a target value of 100 $\Omega/sq$. Also, the width $w$ is set to a target value of 30 µm. Therefore, the variables in equation (17) are reduced to two, the length $l$ and the charge carrier density $N$. For the length $l$ three different values are chosen to obtain resistance values for $R_{\sigma,0}$ of 500 Ω, 1000 Ω and 5000 Ω. For the charge carrier density $N$ two values are chosen. This gives a total of six different design variations, which are shown in Table 3.1.

The sensors were produced by the group *Innovative Cleanroom Technologies* at Fraunhofer ISE on p-type float zone etched silicon solar wafers with a specific resistance of 1 Ωcm and a thickness of 250 µm. On each wafer, 40 sensors are placed in a way that the wafer can be cut into stripes of 10×100 mm$^2$ containing four sensors. The sensors are aligned along the [010]-axis of the (100)-Wafer.

Due to the cubic crystal-structure of Silicon, the [010] direction is equal to the [001] and [100].

**Table 3.1**: Design variations of the piezoresistive stress sensor.

| Variation | Charge carrier density $N$ [cm$^{-3}$] | Aspect ratio $a$ [-] | Length $l$ [µm] | Width $w$ [µm] | Resistance $R_{\sigma,0}$ [Ω] |
|---|---|---|---|---|---|
| S.1 | $1 \times 10^{19}$ ($N^+$) | 5 | 150 | 30 | 500 |
| S.2 | $1 \times 10^{19}$ ($N^+$) | 10 | 300 | 30 | 1000 |
| S.3 | $1 \times 10^{19}$ ($N^+$) | 50 | 1500 | 30 | 5000 |
| S.4 | $5 \times 10^{19}$ ($N^{++}$) | 5 | 150 | 30 | 500 |
| S.5 | $5 \times 10^{19}$ ($N^{++}$) | 10 | 300 | 30 | 1000 |
| S.6 | $5 \times 10^{19}$ ($N^{++}$) | 50 | 1500 | 30 | 5000 |

Figure 3.9 shows the process flow with the relevant process parameters. The first process step is the boron (B) implantation for the shield guard-ring. A boron dose of $5\times10^{15}$ cm$^{-2}$ is used with an annealing at 1050 °C (80 min, $O_2$ atmosphere). In the second step the phosphorous (P) implantation takes place. Two different doses are used:

a) $5.25\times10^{14}$ cm$^{-2}$ with an annealing at 1050 °C (80 min, $O_2$ atmosphere), labeled $N^+$.
b) $9\times10^{14}$ cm$^{-2}$ with an annealing at 950 °C (30 min, Ar atmosphere), labeled $N^{++}$.

In the last step the metal is evaporated (e-gun). The metallization consists of a stack of titanium, palladium, silver with layer thicknesses of 50, 50 and 1000 nm respectively. For all structures, a positive photoresist is used in photolithography. All implantations as well as the evaporation are done on a beamline implanter (*VIISta HC, Applied Materials*). For annealing a *centrotherm* tube furnace is used.

The doping profiles are analyzed using electrochemical capacitance-voltage measurements (ECV), see Figure 3.9 right. For the $N^+$-profile a charge carrier surface density of $1\times10^{19}$ cm$^{-3}$ and for the $N^{++}$-profile a surface density of $5\times10^{19}$ cm$^{-3}$ is measured.

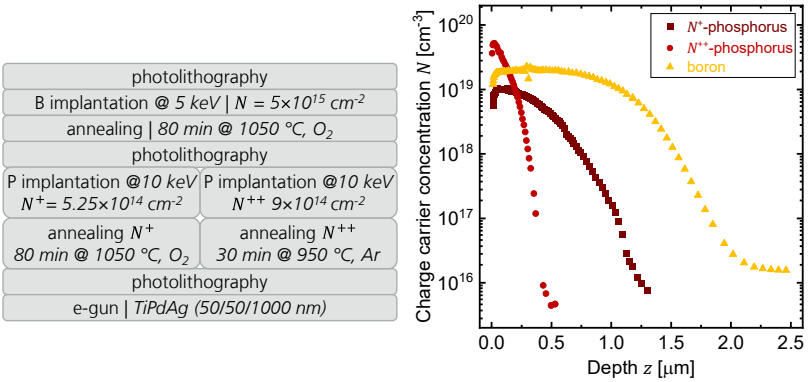


**Figure 3.9:** *Left:* Process flow of stress sensor fabrication. P: phosphorus, B: boron, e-gun: electron beam physical vapor deposition, TiPdAg: titanium, palladium, silver. *Right:* with ECV measured doping profiles of $N^+$ (dark red) and $N^{++}$ (red) profile of the piezoresistor and the boron profile of the shield guard-ring (green). Both modified after [Bein20a].

### 3.2.1.3 Sensitivity

The relation of the measured resistance change to the stress within the sensor is called sensitivity $S_\sigma$, is determined by a four-point bending characterization. For this, the wafers are split into single stripes of 10×100 mm$^2$ using a laser. Each stripe contains four different sensor variations. The current-voltage characteristics is measured for two sensors at a time. The distance of the four-point bending supports is set so that both sensors are exposed to the same stress. For a more detailed description of the used four-point bending bridge it is referred to [Beck15]. In pretests, it is found that the sensor stripes fracture at around 90 MPa, therefore the test range is limited to 65 MPa and subdivided into 13 load steps. At each load step the current at an applied voltage of 1 V is measured by an electrical four-wire measurement. From the data, the change of resistance $\Delta R_\sigma$ is calculated relative to the load of 0 MPa. The relative resistance change $\Delta R_\sigma / R_{\sigma,0}$ is then plotted over the uniaxial stress $\sigma_{xx}$ (see Figure 4.3). Finally, the sensitivity $S_\sigma$ of the sensor, which corresponds to the piezoresistive coefficient $\pi_{11}$ is evaluated by performing a linear fit according to equation (15):

$$S_\sigma = \frac{\Delta R_\sigma}{R_{\sigma,0}\,\Delta\sigma_x}. \tag{18}$$

Between 10 and 19 sensors of each design variation are characterized.

#### 3.2.1.4 Laminate Integration

Of the chosen sensor design a wafer stripe is laminated using a conventional PV module setup (Figure 3.10), with a 14.7×10.5×0.01 cm³ glass, EVA and a TPT backsheet. The resistance change $\Delta R_\sigma$ during a three-point bending test to failure is measured and interconverted to stress using the sensitivity determined in Section 4.2.1.1.

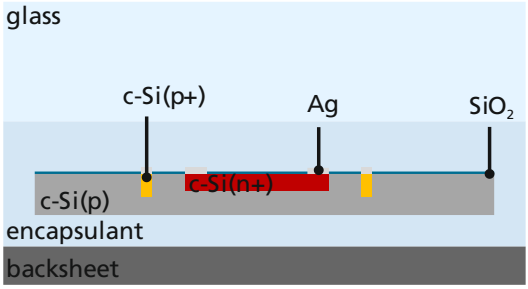


**Figure 3.10:** Setup of the laminated sensor stripe. A standard glass-foil setup is used with EVA as encapsulant and a 1 mm thin glass, not to scale.

### 3.2.2 Stress Sensors Integrated in Solar Cells "*SenSoCell*"

To measure stress within solar cells of a fullsize module during mechanical load the developed stress sensors are implemented on a solar cell wafer to be integrated into the PV module production. Accordingly, the samples should have the size of the solar cells within the used PV module, which have an edge length of 156 mm. The exact setup is described in Section 3.3.4.2. However, it has been turned out that with the available equipment the processes on such wafer sizes has not achieve the needed quality and stability, for example the photosensitive coating used in the photolithography, can not be applied with a homogenous thickness. Therefore, the sensors are integrated on the wafers used before with an edge length of 125 mm. Figure 3.11 shows the schematic design as well as a picture of a *SenSoCell*. The wafer is aligned so that the [010]-direction correspond to the x-axis in the FEM model and the [001]-direction to the y-axis. The flat defines the bottom right corner as depicted in Figure 3.11. A pair of the chosen sensor design S.5 is implemented at six different positions of the solar cell wafer. At each position one sensor is aligned along the x-axis and one along the y-axis. Since the stress sensor has a temperature dependence a temperature sensor is developed simultaneously and also implemented in the *SenSoCell* (see Figure 3.11). The temperature sensor is a resistance thermometer utilizing the

resistance temperature coefficient $\alpha_T$ of the silver metallization. It is used to determine the solar cell temperature exactly. Details about the temperature sensor can be found in the appendix B. Additionally, a capacitance moisture sensor is developed. It utilizes the moisture dependence of the encapsulant itself. As electrodes silver metallization is used. However, since the focus of the work is on thermomechanics, the moisture sensor is not further discussed.

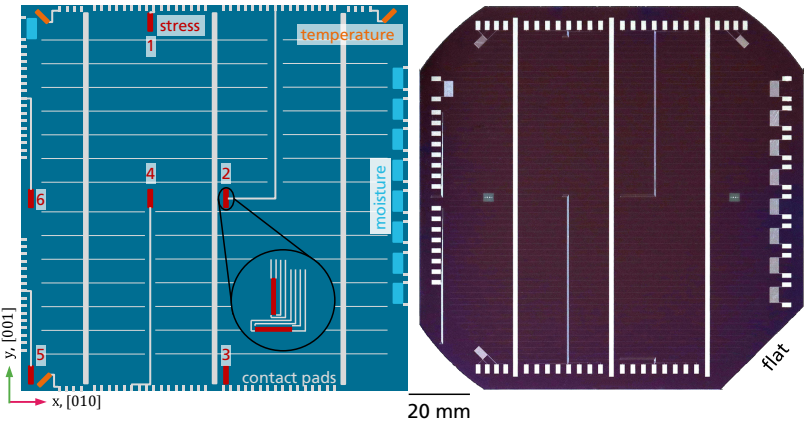


**Figure 3.11:** *left:* schematic layout of a cell with integrated piezoresistive stress (red), temperature (orange) and moisture (blue) sensors, not to scale, modified after [Frau20]. At each position of the stress sensor, two sensors perpendicular to each other are implemented as indicated by the insert. The stress sensors are numbered in clockwise direction, starting with the top left sensor. *Right:* picture of a *SenSoCell* used in the validation experiments.

The *SenSoCell* is produced with the same processes described above (Section 3.2.1.2). For the temperature and moisture sensor only the last two process steps in Figure 3.9 are applied (see also Figure B.6.4 in appendix B.1). Also for the busbar and finger metallization these process steps are used with the difference, that the $SiO_2$ layer is opened before to establish an electrical contact to the silicon bulk.

### 3.2.2.1 Sensitivity of *SenSoCell*

The Sensitivity of the stress sensors is verified by 4-point bending on three samples of sensor pair 6 (Figure 3.11). The 4-point bending test is conducted according to DIN SPEC91351:2017-04 [DIN 17] on a *zwicki Z0.5 TN* by *ZwickRoell* using a 50 N force gauge. The roller distance is set to 40 mm and 80 mm with a pre load of 1 N and a speed of 0.05 mm/s. In order to prevent fracturing, the maximum stress is set to the same value of 65 MPa as for the sensor stripes. The

resistance of the stress sensor is measured by a four-wire configuration using the datalogger *Agilent 34970A* with a 20-channel relay multiplexer *Agilent 34901A*. Each sample is measured 10 times consecutively. Equivalent to Section 3.2.1.3, the sensitivity $S_\sigma$ is determined for each sensor direction by plotting the relative resistance change $\Delta R_\sigma/R_{\sigma,0}$ over the uniaxial stress $\sigma_\mathrm{x}$ and performing a linear fit. The mean is drawn over the 10 measurements of each sample and then over three samples.

### 3.2.2.2 Stress Components Measured by *SenSoCell*

In Section 3.2.1.1 the assumption of a uniaxial stress is made, which holds for the case of 4-point bending. The stress in a laminated solar cell is mostly biaxial, thus above derived relation between the resistance change $\Delta R_\sigma$ and the stress $\sigma$ does not hold anymore. More generally, the piezoresistance consists of the longitudinal and transversal effect, which are defined by the orientation of the stress to the electric field $\vec{E}$:

- Longitudinal: $\sigma_\mathrm{i} \parallel \vec{E}$,
- Transversal: $\sigma_\mathrm{i} \perp \vec{E}$.

Due to the low sensor height, the electrical field component along the sensor height is negligible. Therefore, equation (13) can be written as:

$$\Delta R_\sigma = R_{\sigma,0}\,(\pi_l \sigma_l + \pi_t \sigma_t), \tag{19}$$

with $\pi_\mathrm{l}$ and $\pi_\mathrm{t}$ being the longitudinal and transversal piezoresistive coefficients and $\sigma_\mathrm{l}$ and $\sigma_\mathrm{t}$ the longitudinal and transversal stress components. As opposed to uniaxial stress state in a biaxial state, the resistance change is influenced not by just one stress component but both. In the following, relations for each sensor orientation are derived.

$$\sigma_x \parallel \vec{E} \; and \; \sigma_y \perp \vec{E}, \tag{20}$$

$$\pi_l = \pi_x \; and \;\; \pi_t = \pi_y, \tag{21}$$

$$\sigma_l = \sigma_x \;\; and \;\; \sigma_t = \sigma_y. \tag{22}$$

Similarly, for the stress sensor aligned along the y-axis it is:

$$\sigma_y \parallel \vec{E} \; and \;\; \sigma_x \perp \vec{E}, \tag{23}$$

$$\pi_l = \pi_y \; and \;\; \pi_t = \pi_x, \tag{24}$$

$$\sigma_l = \sigma_y \;\; and \;\; \sigma_t = \sigma_x. \tag{25}$$

For lightly ($10^{16}$ cm$^{-3}$) n-doped silicon, the literature value of piezoresistive coefficient along [100] are $\pi_l = -102\ 10^{-11}$Pa$^{-1}$and $\pi_t = 53.4\ 10^{-11}$Pa$^{-1}$ [Smit54]. This allows the assumption:

$$\pi_l = -2 \cdot \pi_t. \tag{26}$$

With this, the resistance change $\Delta R_\sigma$ (equation (19)) becomes:

$$\Delta R_\sigma = R_{\sigma,0}\, \pi_l \left(\sigma_l - \frac{1}{2}\sigma_t\right). \tag{27}$$

Inserting the relations (20), (21) and (24), (25) gives the resistance change $\Delta R_\sigma$ for the sensor along the x-axis and y-axis:

$$\Delta R_{\sigma,x} = R_{\sigma,0,x}\, \pi_l \left(\sigma_x - \frac{1}{2}\sigma_y\right), \tag{28}$$

$$\Delta R_{\sigma,y} = R_{\sigma,0,y}\, \pi_l \left(-\frac{1}{2}\sigma_x + \sigma_y\right). \tag{29}$$

Now, adding the resistance changes of both sensor orientations results in the following relation between the measured resistance change and the stress within the solar cell:

$$\frac{1}{\pi_l}\left(\frac{\Delta R_{\sigma,x}}{R_{\sigma,0,x}} + \frac{\Delta R_{\sigma,y}}{R_{\sigma,0,y}}\right) = \frac{1}{2}(\sigma_x + \sigma_y). \tag{30}$$

This relation is used for the validation of the FEM model by using the sensitivity $S_\sigma$ determined in Section 4.2.1.1 for the longitudinal piezoresistive coefficient $\pi_l$.

## 3.3 Finite Element Modelling of PV Modules

After a short introduction to the finite element method, the challenges of FEM modelling of PV modules are described followed by the approach used to handle these challenges. Finally, the developed FEM model is presented.

### 3.3.1 Finite Element Method

The finite element method is a numerical method to solve physical problems that are mathematically formulated as partial differential equations (PDE). As opposed to an analytical solution, the problem is split into a set of problems, by splitting the geometry into a mesh of finite elements. For each mesh element integration points are defined on which the problem is solved numerically by using mostly

polynomial shape functions. The accuracy of the solution increases with the degree of the polynomial function as well as with the number of mesh melements. However, both comes with an increase of unknown coefficients in the PDEs, called degrees of freedom (DoF) of the system, which again increases the computational effort, i.e. solution time and needed memory. Therefore, FEM modelling is always a trade-off between an accurate solution and minimizing DoF. In the following the most fundamental equations will be given, for a more detailed description it is referred to literature like [Eitn11c, Hart07, Klei12, Wagn17].

For the mathematical description of structural mechanics problems, first the constitutive equations, which describe the relation between stress and strain, have to be defined. Here, a linear elastic isotropic material is assumed for simplicity. Then for a three-dimensional problem, the Hooke's law is:

$$\vec{\sigma} = \boldsymbol{C} \cdot \vec{\varepsilon}, \tag{31}$$

with the elasticity matrix $\boldsymbol{C}$:

$$\boldsymbol{C} = \frac{E}{(1+\nu)(1-2\nu)} \begin{pmatrix} 1-\nu & \nu & \nu & 0 & 0 & 0 \\ \nu & 1-\nu & \nu & 0 & 0 & 0 \\ \nu & \nu & 1-\nu & 0 & 0 & 0 \\ 0 & 0 & 0 & \frac{1-2\nu}{2} & 0 & 0 \\ 0 & 0 & 0 & 0 & \frac{1-2\nu}{2} & 0 \\ 0 & 0 & 0 & 0 & 0 & \frac{1-2\nu}{2} \end{pmatrix}, \tag{32}$$

where $\nu$ is the Poisson's ratio and $E$ the Young's modulus. For materials with a cubic crystal symmetry, as it is the case for silicon, the elasticity matrix $\boldsymbol{C}$ can also be expressed by the three elastic constants $C_{11}$, $C_{12}$ and $C_{44}$, which are specified later in Section 3.3.2.1:

$$\boldsymbol{C} = \begin{pmatrix} C_{11} & C_{12} & C_{12} & 0 & 0 & 0 \\ C_{12} & C_{11} & C_{12} & 0 & 0 & 0 \\ C_{12} & C_{12} & C_{11} & 0 & 0 & 0 \\ 0 & 0 & 0 & C_{44} & 0 & 0 \\ 0 & 0 & 0 & 0 & C_{44} & 0 \\ 0 & 0 & 0 & 0 & 0 & C_{44} \end{pmatrix}. \tag{33}$$

In equation (31), the stress and strain are written as vectors in the Voigt notation:

$$\vec{\sigma} = \begin{pmatrix} \sigma_{xx} \\ \sigma_{yy} \\ \sigma_{zz} \\ \tau_{xy} \\ \tau_{yz} \\ \tau_{zx} \end{pmatrix} \quad \text{and} \quad \vec{\varepsilon} = \begin{pmatrix} \varepsilon_{xx} \\ \varepsilon_{yy} \\ \varepsilon_{zz} \\ \gamma_{xy} \\ \gamma_{yz} \\ \gamma_{zx} \end{pmatrix}. \tag{34}$$

The strain again is the partial derivative of the displacement vector $\vec{u} = (u, v, w)^{\mathrm{T}}$:

$$\vec{\varepsilon} = \boldsymbol{D} \cdot \vec{u}\,, \tag{35}$$

with the differential-operator-matrix $\boldsymbol{D}$:

$$\boldsymbol{D} = \begin{pmatrix} \partial x & 0 & 0 \\ 0 & \partial y & 0 \\ 0 & 0 & \partial z \\ \partial y & \partial x & 0 \\ 0 & \partial z & \partial y \\ \partial z & 0 & \partial x \end{pmatrix}. \tag{36}$$

Equations (31) and (35) fully describe elastostatic problems together with the balance of forces:

$$\boldsymbol{D}^T \cdot \vec{\sigma} - \vec{p} = 0\,, \tag{37}$$

where the vector $\vec{p} = \left(p_{\mathrm{x}}, p_{\mathrm{y}}, p_{\mathrm{z}}\right)^{\mathrm{T}}$ incorporates the external loads.

Inserting Equation (35) in Equation (31) and again in Equation (37) describes the balance of forces by the displacement vector $\vec{u}$:

$$\boldsymbol{D}^T \cdot (\boldsymbol{C} \cdot \vec{\varepsilon}) = \boldsymbol{D}^T \cdot (\boldsymbol{C} \cdot (\boldsymbol{D} \cdot \vec{u})) = \vec{p}, \tag{38}$$

To determine stress for a certain external load $\vec{p}$, the displacement vector $\vec{u}$ has to be computed by solving this differential equation. Usually, no analytic solution exists and an approximation method has to be used. Here, the variational formulation is used, which is based on the principal of virtual work. It states that an elastic body is in equilibrium if the internal virtual work is equal to the external virtual work:

$$\delta W_{\mathrm{i}} = \delta W_{\mathrm{a}}. \tag{39}$$

We focus on the made approximation of the displacement vector $\vec{u}$ by the product of the row matrix $\boldsymbol{G}$ with the displacement of each node $\vec{d}$:

$$\vec{u} = \boldsymbol{G} \cdot \vec{d}\,. \tag{40}$$

With this, the principal of virtual work can be expressed by one linear system

$$\boldsymbol{K} \cdot \vec{d} = \vec{f}\,, \tag{41}$$

which is the basic function of the finite element method. The vector $\vec{f}$ incorporates all external forces of the physical problem, which are set as boundary conditions. The element stiffness matrix $\boldsymbol{K}$ contains the material parameters and models.

Building the linear system (41) is often very time and memory consuming. There are two approaches to solve the problem: direct and iterative. For the direct approach, which is used within this work, a common method is the LU-factorization, which decomposes the Matrix $\boldsymbol{K}$ into an upper $\boldsymbol{U}$ and a lower triangular matrix $\boldsymbol{L}$:

$$\boldsymbol{K} = \boldsymbol{L}\boldsymbol{U}\,. \tag{42}$$

Due to the triangular shape of these matrixes the linear system (41) is easy to solve. This approach is robust but associated with a large computational effort.

Less computational resources are needed for the iterative approach. Here the solution of $\vec{d}$ is approximated starting from a trial function $\vec{d}_{\mathrm{t}}$. After the first iteration, the trial function is slightly modified and then the linear system is solved again. The iterations go until the difference between the $(n-1)$ and $n$-th solution is smaller than a given deviation threshold margin. This method relies on the convergence of the trial function to the "real" solution, which either might not occur due to a bad choice of the trial function or a local optimum is found instead of the global. Therefore, the iterative approach is less stable.

### 3.3.2 FEM Model of a 60-Cell PV Module

The DoF and hence computational effort increases with number of mesh elements a geometry is separated in. At the same time, mesh elements should have an aspect ratio of planar dimensions to height between one and 20 for an accurate solution. Since the aspect ratio of solar cell length (156.75 mm) to height (0.18 mm) is 867, a very fine mesh is required for an accurate solution. For very thin structures, an alternative to 3D elements is the use of plate or shell elements. Here, thin layers are modelled as a 2D structure and stress along height is calculated using assumptions, e.g. that there are no significant changes perpendicular to the plane or only a linear stress gradient. Due to this assumption, plate or shell elements are not applicable to PV modules, because especially the encapsulant has significant changes along the height. Therefore, only 3D elements are used within this work. Since all layers of the laminate are rectangular, the use of a

rectangular mapped mesh which is extruded over the height is a convenient choice. The resulting hexahedral mesh is the most efficient mesh for rectangular structures and leads to more robust solutions. Since the stress in the solar cells is the main focus of this work, the solar cell mesh must be fine rnough to resolve the stress. Therefore a mesh sensitivity study is conducted below (Section 3.3.2.3). The stress in the front- and backsheet plays a minor role, therefore it is sufficient to resolve the displacement correctly and a coarser mesh can be used. This is realized by splitting the PV module into two fully coupled components, as depicted in Figure 3.12:

1. The interconnected solar cell matrix embedded in the encapsulant.
2. The front- and backsheet connected to the frame with a rubber inlay.

The geometry is build up starting with the backsheet from the symmetry planes with the origin of the coordinate system being on the back side of the backsheet at the crossing of the symmetry planes, as indicated in Figure 3.12. All simulations performed in this work, the same coordinate system is used. Also all figures use this coordinate system.

To further reduce the computational effort assumptions and simplifications are made:

- The twofold symmetry of the PV module is utilized by modelling a quarter PV module (see Figure 3.14). In fact the PV module is not perfectly symmetric along the long side, because the ribbons go from the top of one cell to the back of the next cell. However, the inaccuracy by assuming a symmetry is negligible.
- The rounded edges of pseudo-square wafers are neglected by modelling the solar cells as full-square wafer.
- The front side finger and back side aluminum metallization is neglected, since it has no significant influence [Diet14].
- A linear elastic temperature dependent material model is used for the encapsulant.
- The solder coating (a few micrometers) of the ribbon is neglected and a linear elastic material behavior is used for copper.
- The composite nature of the backsheet is neglected by modelling it as one single layer instead of typically three composite layers. The material properties are measured for the composite, therefore an effective material model is used.
- The frame geometry is simplified by reducing it to rectangular elements and neglecting details with no influence on the mechanical behavior.

- The mounting of the frame to the supporting structure is modelled by a fixed constraint at the typical contact area on the bottom of the frame.
- A stationary linear analysis with a linear approximation for the strain is used.

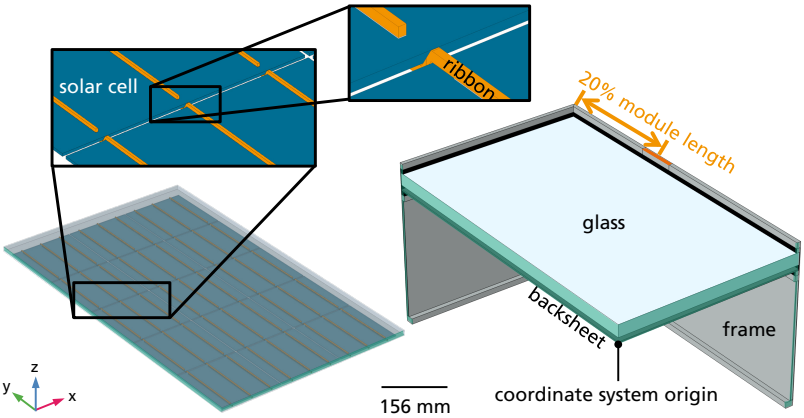


**Figure 3.12:** Geometric representation of the reference PV module. *Left:* component 1: the solar cell matrix embedded in the encapsulant with a detail-view of the cell gap (inserts). *Right:* component 2: the front- and backsheet with the frame. The symmetry planes are highlighted in green. The origin of the coordinate system is on the back side of the backsheet where the symmetry planes cross. The contact area on the frame top is highlighted in orange. Z-direction 10× enlarged.

The FEM model covers a simplified soldering process, lamination and mechanical load at different temperatures. The stress tensor from each study is transferred to the subsequent study, as further explained in Section 3.3.2.2.

In the following the developed FEM model of a 60-cell PV module is described starting with the used material models for each material. Secondly, the simulation studies with used boundary conditions are introduced. Finally, the discretization into a FEM mesh is explained.

### 3.3.2.1 Material Models and Characterization

Table 3.2 shows for each PV module layer/component the used material and corresponding material properties in the FEM simulation of the reference module. In the following for each material the chosen parameters are discussed.

**Table 3.2:** Material properties and layer height of the module materials used in the reference FEM model, *: provided by manufacturer, †: measured, see Figure 3.13.

| Component | Material | Height $h$ [mm] | Density [g cm$^{-3}$] | Young's modulus $E$ [GPa] | Poisson's ratio $\nu$ [-] | CTE $\alpha$ [$10^{-6}$ K$^{-1}$] |
|---|---|---|---|---|---|---|
| Frontglass | soda-lime glass | 3.2 | 2.53* | 74* | 0.24* | 9* |
| Encapsulant | EVA | 0.45 | 0.96 [Eitn11a] | *T*-dep.† | 0.4 [Eitn11a] | 270 [Eitn11a] |
| Solar Cell | Cz-Silicon | 0.18 | 2.329 [Eitn11a] | Elasticity matrix [Gree88] | | *T*-dep. [Robe81, Robe82] |
| Backsheet | TPT [Eitn11a] | 0.35 | 2.52 | 3.5 | 0.29 | 50.4 |
| Busbars | Silver | 0.014 | 10.5* | 7 [Kohn07] | 0.37* | 10 [Rend16a] |
| Ribbon | Copper | 0.2 | 8.7* | 70 [Wies12] | 0.35* | 17 [Wies12] |
| Frame | Aluminum [Hayn14] | varying | 2.7 | 70 | 0.33 | 23 |
| Rubber inlay | Rubber | 1.15 | 0.067* | 0.0074* | 0.3* | 769* |

### Glass

The glass used for PV modules is a soda-lime float glass with a very low iron content to reduce absorption and thereby increase transmission. The mechanical properties of glass are taken from the literature [Duff94, Munz01]. Below its glass transition temperature $T_G$ of 550 °C [Duff94] glass has a purely elastic behavior. The material parameters used in this work are provided by the manufacturer *f* | *solar* of the used soda-lime float glass *f* | *solarfloat*.

### Encapsulant

The most used encapsulant in PV modules is EVA, which shows viscoelastic properties [Eitn10a]. Eitner proposed the use of a generalized Maxwell model with 26 Maxwell arms [Eitn11c] and showed in FEM simulations of the cell gap change within one thermal cycle, that this gives the most accurate representation of the experimental data. However, in the used Software *COMSOL Multiphysics*, each Maxwell arm adds five additional degrees of freedom per mesh node. For the proposed generalized Maxwell model of Eitner, this corresponds to 133 DoF per mesh node, instead of three. Within this work it has been attempted to create a new generalized Maxwell model, with less Maxwell arms. Due to the complexity

of the material behavior, the number of Maxwell arms could only be reduced to 20 Maxwell arms, which still corresponds to 103 DoF per mesh node. The implementation in an FEM simulation of lamination has shown that the stress value at room temperature converges to the value using a temperature dependent material model. However, the computation time and used memory increases drastically. Therefore, a temperature dependent Young's modulus is used in order to allow for extensive parameter variations within a reasonable computation time.

The temperature dependent Young's modulus is extracted from dynamic mechanical measurements at 1 Hz in the range from -100 °C to +160 °C using the *DMA 242 C* by *Netzsch*. Figure 3.13 shows the obtained data for the EVA *STR PHOTOCAP 15585*, which is used as a reference, and one experimental thermoplastic Polyolefin (TPO), used in the material variation study.

### Solar Cell

Silicon solar cells exhibit a cubic symmetric material behavior. The linear elastic properties are expressed by the elasticity matrix $\boldsymbol{C}$ (see equation (33)). Due to the cubic crystal symmetry, three values are enough to fully describe the elasticity matrix $\boldsymbol{C}$. The values taken from the literature [Gree88] are: $C_{11}$=164.8 GPa, $C_{12}$=63.5 GPa and $C_{44}$=79.0 GPa. The coefficient of thermal expansion $\alpha$ is temperature dependent [Robe81, Robe82] and is $2.62\times10^{-6}$ $K^{-1}$ at 25 °C.

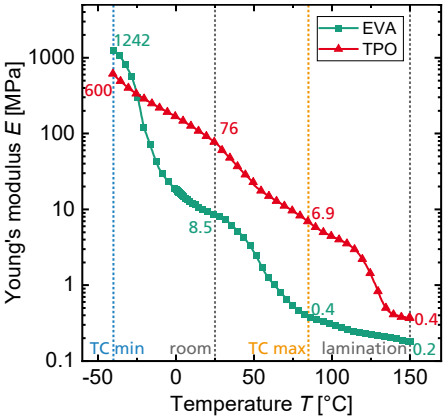


**Figure 3.13:** Measured temperature dependent Young's modulus at 1 Hz of two encapsulants. For clarity not all data points are shown, the line is a guide to the eye.

**Backsheet**

Most backsheets are multi-layer materials with usually three layers. Typically, the inner layer is by far the thickest and therefore the outer layers have a minimal impact on the thermomechanics of the PV module. Therefore, the backsheet is simplified to just one layer with an effective linear elastic material model. The material parameters of the used backsheet *Isovoltaic Icosolar 2442* are documented in the literature [Eitn11a]. This backsheet has a PET core with PVF outer layers. For other backsheet used in the parameter variation, tensile tests on a universal testing machine *zwicki Z0.5 TN* by *ZwickRoell* are performed to determine the Young's modulus at room temperature.

**Busbars and Ribbon**

The busbars consist of a screen printed and tempered silver paste, the ribbons of solder coated copper. Since the solder coating of the ribbons is thin compared to the copper core, the ribbons are simplified to pure copper. To reduce the computational effort, a linear elastic material behavior is used instead of a plastic, which holds for strains below 1 % [Wies09]. It is noteworthy, that the Young's modulus of ribbons is due to the fabrication process lower than for conventional bulk copper [Wies09]. Also, for the silver paste, the assumption of a linear elastic material model is taken to reduce the computational effort.

**Frame**

The frame is made of extruded aluminum. It is assumed that the strains within the frame stay in the elastic regime. Accordingly, the frame is modelled by a linear elastic material model, with data taken from the literature [Hayn14].

#### 3.3.2.2 Studies

Figure 3.14 illustrates the simulated processes and how they are implemented as simulation studies. Each step is introduced in the following subsections. For all studies static simulations are performed.

**Soldering**

Prior to the lamination a simplified soldering process is simulated to consider the stress from soldering in the subsequent processes. For this simulation step only the solar cells with busbars and the ribbons are considered. A homogeneous temperature distribution is assumed and the cooling down from the solder solidification temperature of 179 °C to room temperature is simulated in one single step. To suppress rigid body motion and at the same time simulate the flattening

of the strings during the lamination process, the out-of-plane translation is suppressed (roller constraint) on the back side of each ribbon. Additional roller conditions are placed on the side of the first ribbon in the first solar cell of a string and on the cross-section of the ribbons in the short symmetry plane.

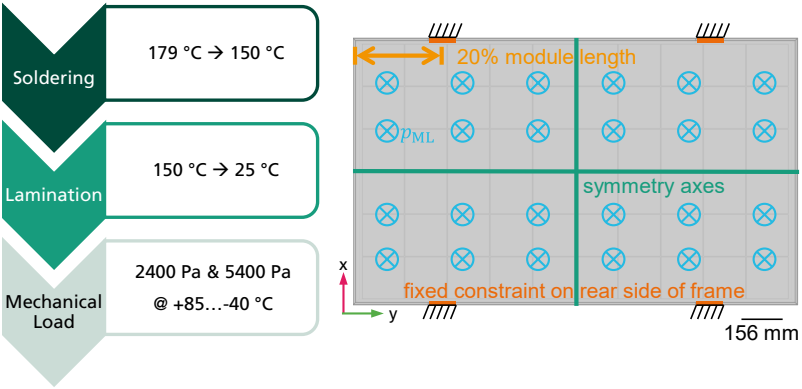


**Figure 3.14:** *left*: Processes covered by the FEM model. From each study, the stress tensor is transferred as input condition to the next study. Due to the use of linear elastic material models, the soldering process is simulated to the lamination temperature, rather than 25 °C. *Right*: Boundary conditions used in the mechanical and thermal load study steps. The orange rectangles indicate the position of the fixed constraints on the bottom side of the frame and the green lines the symmetry axes. The constant pressure normal to the glass front side is indicated by the light blue ⊗. Modified after [Bein20b].

### Lamination

In the lamination process, all laminate materials are considered. It is assumed that the materials can deform independently from each other until the cross-linking of the EVA starts at 150 °C. Therefore, the stress relief in the soldered solar cells prior the cross-linking is considered by transferring the soldering stress tensor at 150 °C, rather than at room temperature, to the lamination simulation step. A homogeneous temperature distribution is assumed for all materials and the cooling down from the lamination temperature to 25 °C is simulated in a single step by setting the reference temperature to 150 °C. The resulting stress tensor is then transferred to the (thermo-)mechanical load simulation step. Translational symmetry conditions are placed on all surfaces in the symmetry planes (see Figure 3.14). The front side of the frontglass is constrained by a roller to suppress the rigid body motion and additionally simulate the flattening of the laminate when the frame is attached.

**(Thermo-)mechanical Load**

For the simulation of mechanical and thermal load, a frame is added to component 2 (see Figure 3.12). The mounting of the frame on a rack is simulated by applying fixed constraints on the bottom side of the long side of the frame. The distance to the edge is 20 % of the module length, as shown in Figure 3.14. This corresponds to model 3 in [Schi14] and is widely used for industrial PV modules.

In this simulation step, the mechanical, thermal as well as the combination – thermomechanical – loads are simulated. For this purpose, a thermal strain constraint is applied to all layers with a reference temperature of 25 °C, which is the temperature at which the frame is attached to the laminate. A homogeneous temperature distribution is assumed. The mechanical load is then simulated by setting the module temperature $T_{\mathrm{mod}}$ to 25 °C. The mechanical load is applied as a constant pressure normal to the surface $p_{\mathrm{ML}}$ on the front side of the frontglass. Loads of 2400 Pa and 5400 Pa are simulated. To simulate mechanical load at different temperatures, the module temperature $T_{\mathrm{mod}}$ is varied under the previous loads. And to simulate thermal loads, the applied mechanical load $p_{\mathrm{ML}}$ is set to 0 Pa while the module temperature $T_{\mathrm{mod}}$ is varied between -40 °C and 85 °C.

### 3.3.2.3 Mesh

For both components, hexahedral mesh elements with a quadratic serendipity shape function are used. Where hexahedral elements are not applicable, also prisms, four-sided pyramids and tetrahedra are used. Table 3.3 shows the number of mesh elements used for each mesh type and the next Subsection covers mesh sensitivity studies for crucial domains.

**Table 3.3:** Number of elements used for the different type of mesh elements in both components.

| | Hexahedra | Prisms | Pyramids | Tetrahedra |
|---|---|---|---|---|
| Component 1 | 824,724 | 1,428,484 | 8,640 | 987,939 |
| Component 2 | 98,520 | - | - | - |

In component 1, the focus is put on the mesh of the solar cell in order to resolve the stress exactly. To build an efficient mesh with a minimum of nodes, a high node distance is chosen at locations of low stress gradients, which is then decreased with increasing stress gradients. The maximum node distance of 5.2 mm is determined in the mesh sensitivity study below. Due to the rectangular

shape, hexahedral elements are used. The next critical domains, which require a fine mesh, are the busbars and ribbons. These are the smallest layers in component 1 and are enclosed by the encapsulant for which the hexahedral mesh from the solar cell is continued with three elements in the thickness. To avoid more mesh elements in the encapsulant but allow a fine hexahedral mesh element in the rectangular busbar and ribbon, a mesh transition zone of the ribbon width is introduced. Within this zone prisms are used for the transition from the fine hexahedral mesh of the busbar and ribbon to the coarser encapsulant mesh. The last critical point is the crimp of the ribbon in the cell gap, where the ribbon goes from the top of one cell to the bottom of the next. The crimp itself is meshed with prisms, while for the transition zone tetrahedra are used. Figure 3.15 shows these different mesh elements in a detailed view along with the mesh of the whole component 1.

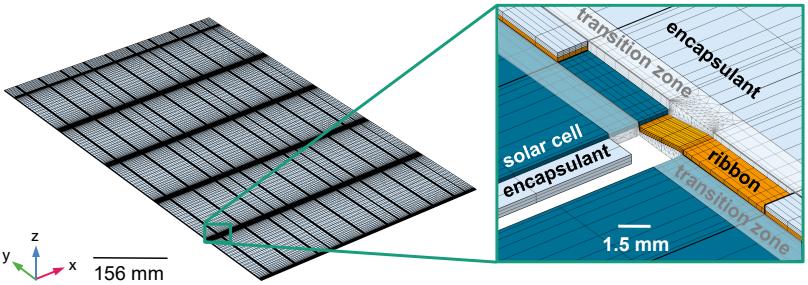


**Figure 3.15**: Mesh of component 1 (embedded solar cell matrix). The insert (same coordinate system) shows a mesh detail at the position where the ribbon (orange) goes from the front of one solar cell (blue) to the back of the next. The encapsulant (light blue) is removed partially to allow a view on the solar cell and ribbon.

Figure 3.16 shows the mesh wo component 2, which consists of rectangular domains without any enclosures. Accordingly, solely hexahedral mesh elements are used. The backsheet and frontglass are meshed with a maximum node distance of 10.4 mm. For the frame a finer mesh is used, with a focus on the inlay to allow a correct deformation of the inlay as well as the frame.

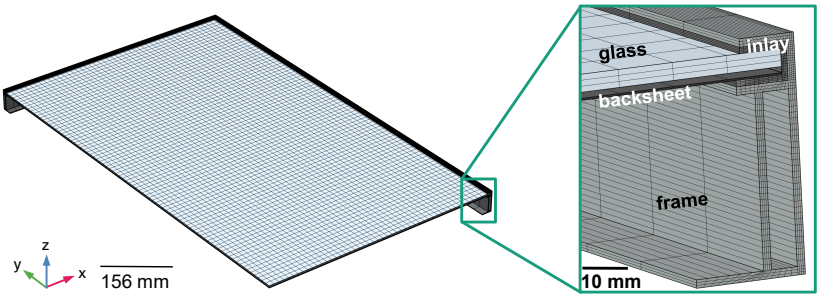


**Figure 3.16**: Mesh of component 2 (frame with front- and backsheet). The insert shows a detailed view of the frame with inlay.

### Mesh Sensitivity Study

A mesh sensitivity study is carried out to identify a suitable mesh, which yields reasonable results and uses as little resources as possible. The study is carried out in three subsequent steps. Firstly, the sensitivity of the minimum third principal stress $\sigma_{\mathrm{III}}$ in the lamination study step as well as the maximum first principal stress $\sigma_{\mathrm{I}}$ at 5400 Pa in the mechanical load study step on the number of elements in the solar cells is investigated. Secondly, the sensitivity of the maximum first principal stress $\sigma_{\mathrm{I}}$ at 5400 Pa on the number of elements in the frame is investigated. In order to focus on the solar cell and to reduce the computational effort, busbar and ribbons are not yet included in the FEM model for these two studies. Thirdly, the sensitivity of the maximum first principal stress $\sigma_{\mathrm{I}}$ at the end of the busbar at 5400 Pa on the number of elements in busbar and ribbons is investigated. Figure 3.17 shows that below 30 elements along the solar cell edge the stress values change significantly. Therefore, at least 30 elements are used per solar cell edge, which corresponds to 2700 elements per solar cell or a node distance of 5.2 mm.

Figure 3.18 shows that below 90 mesh elements along the frame length, the maximum first principal stress $\sigma_{\mathrm{I}}$ in the solar cells decreases significantly but shows no significant change above. Therefore 90 elements are chosen, which corresponds to an average node distance of 9.5 mm. On the long side of the frame, the mesh elements become finer with a ratio of the node distance to the next element (element ratio) of three towards the fixed constraint at the clamping position. At the short side of the frame, 30 equidistant elements are used.

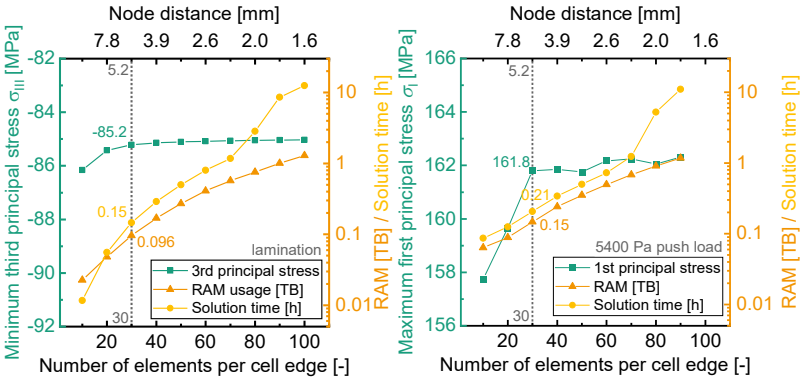


**Figure 3.17**: Mesh sensitivity study for the number of elements on the solar cell edge. The left axis shows the extrema of the principal stresses (green) in the solar cells and the right axis the needed RAM (orange) and solution time (yellow). The grey dotted line indicates the chosen number of elements. *Left:* for lamination. *Right:* for 5400 Pa in mechanical load.

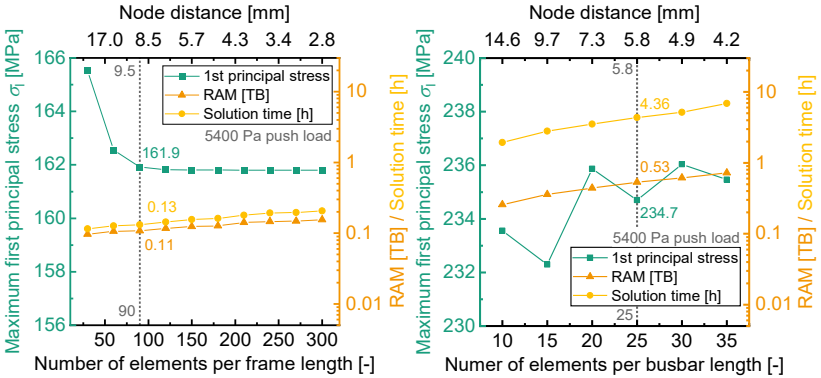


**Figure 3.18**: Mesh sensitivity study with the maximum first principal stress $\sigma_I$ (green, left axis) in the solar cells at 5400 Pa in mechanical load and the needed RAM (orange, right axis) and solution time (yellow, right axis). The grey line indicates the chosen number of elements. *Left:* The maximum first principal stress $\sigma_I$ in the solar cells for the frame length. *Right*: The maximum first principal stress $\sigma_I$ at the end of the busbar for the number of elements along the busbar length (y-diection).

Figure 3.18 shows the sensitivity of the maximum first principal stress $\sigma_I$ at the busbar end position on the number of elements per busbar length. Here the stress shows an oscillating convergence to a value of around 235 MPa. The oscillation most likely originates from singularities which arise at the busbar corners. 25 mesh elements are chosen, which corresponds to an average node distance

along the y-axis of 5.8 mm with a smaller distance towards the edge with an element ratio of seven. For the width (not shown) five elements (0.3 mm node distance) are chosen. For the stress between the busbars, both numbers of elements don't have a significant influence.

#### 3.3.2.4 Parameter Sensitivity Study

To gain a deeper understanding of the thermomechanics in the PV module and as a basis for the thermomechanical design rules, two different parameter sensitivity studies are carried out with the developed FEM model:

1. Variation of the PV module and solar cell size and format (see Table 3.5 and Figure 3.19).
2. Variation of the used materials (see Table 3.6, Table 3.7 and Table 3.8).

For the first variation, the focus is on size effects. Rendler *et al*. [Rend19] showed that the maximum tensile stress from the solder joint occurs at the end of the busbar. If the busbar end has a distance larger than 8 mm to the cell edge, the maximum tensile stress is independent of the solder joint length. This implies that for the performed variations - assuming the same metallization layout for all variations - the contribution of the solder joint to the total stress is approximately constant. Accordingly, to study the influence of the size effects, the ribbons and busbars can be neglected, which reduces the computational effort significantly. For the second variation, the full FEM model is used. For both variations, the reference setup is a glass-foil PV module with 60 full format 156.75×156.75 mm² solar cells, a cell gap of 3 mm and the material properties given in Table 3.2. The total size is 1.664×0.997 m², all dimensions are listed in Table 3.4. In the following, the two parameter sensitivity studies are explained.

**Table 3.4:** Dimensions of the 60-cell PV module reference FEM model (without symmetry).

| | **Frontglass** [mm] | **Encapsulant** [mm] | **Solar cell** [mm] | **Backsheet** [mm] | **Busbars** [mm] | **Ribbon** [mm] |
|---|---|---|---|---|---|---|
| Length $l$ | 1,664 | 1,664 | 156.75 | 1,664 | 151.25 | 151.25 |
| Width $w$ | 997 | 997 | 156.75 | 997 | 1.5 | 1.5 |
| Height $h$ | 3.2 | 0.45 | 0.18 | 0.35 | 0.014 | 0.2 |

To investigate size effects the number of solar cells, solar cell size and solar cell format are varied independently from each other with the parameters shown in Table 3.5. The influence on size is sketched to scale in Figure 3.19. Each configuration is simulated as a glass-foil and a glass-glass setup (Figure 3.20). For

the glass-glass setup, the backsheet is replaced by glass, with the front and back glass having a thickness of 2 mm. Please note, that both setups have a frame for a better comparability. The variation of the number of solar cells is composed of an increase of the number of strings (6, 8, 10) per module and an increase of the number of solar cells per string (10, 12, 14).

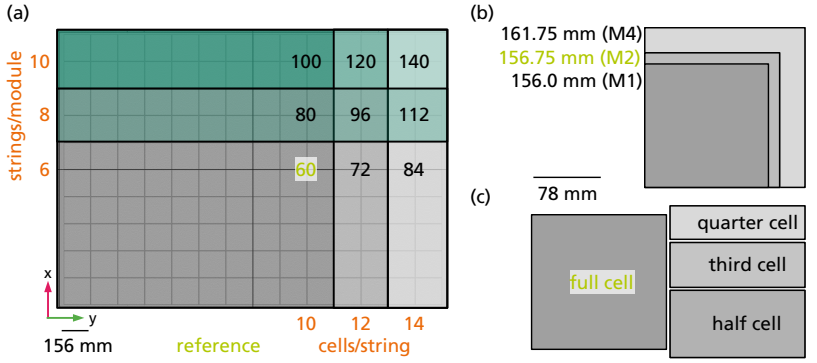


**Figure 3.19:** Illustration of the size sensitivity study; a: module sizes for the different number of solar cells per module. The grey shading indicates the increase in cells per string and the green shading indicates the increase in strings per module; b: solar cell sizes and c: solar cell formats. The reference value is printed in light green.

**Table 3.5:** Parameters varied for the investigation of size effects. The reference parameters are underlined. All Parameters are simulated for glass-foil and glass-glass modules.

| **Parameter** | **Values** | | | | | | | | |
|---|---|---|---|---|---|---|---|---|---|
| **Number of cells** | 60 | 72 | 84 | 80 | 96 | 112 | 100 | 120 | 140 |
| strings | 6 | 6 | 6 | 8 | 8 | 8 | 10 | 10 | 10 |
| cells/string | 10 | 12 | 14 | 10 | 12 | 14 | 10 | 12 | 14 |
| **Cell size [mm]** | 156.00 (M1) | | | 156.75 (M2) | | | 161.75 (M4) | | |
| **Cell format** | full | half | | third | | | quarter | | |

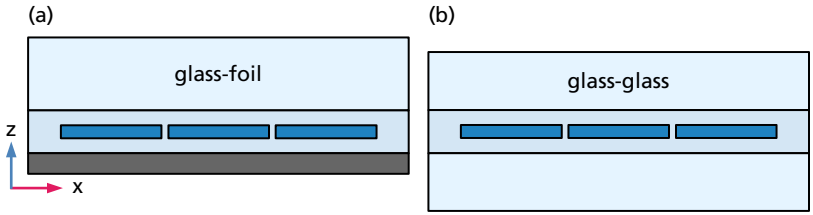


**Figure 3.20:** Schematic illustration of glass-foil (a) and glass-glass (b) module setups, not to scale.

The second parameter variation is again separated in three different variations:

i. A dependent variation of crucial material parameters of a glass-foil PV module (Table 3.6).
ii. An independent variation of crucial material parameters and layer height of a glass-foil PV module (Table 3.7).
iii. An independent variation of the front- and backsheet material and height of a symmetric "glass-glass" PV module setup (Table 3.8).

The ranges of the parameters are chosen to be within realistic materials.

The dependent material parameter variation is supposed to investigate the influence of the Young's modulus $E$ and the CTE $\alpha$ of the PV module layers. In this variation only glass-foil modules are considered. The frontglass CTE is varied in a range representing values of borosilicate and soda-lime glass as well as polycarbonate. For the encapsulant two different measured temperature dependent Young's moduli are used (see Figure 3.13). For the backsheet the Young's moduli of particularly soft, normal and stiff backsheets are used as well as the CTEs of possible other backsheet materials, like soda-lime glass or polycarbonate.

**Table 3.6:** Material parameters used in the dependent parameter variation of glass-foil modules. The reference parameters are underlined; †: measured, see Figure 3.13.

| **Frontglass** | **Encapsulant** | **Backsheet** | |
|---|---|---|---|
| **CTE $\alpha$** [$10^{-6}$ $K^{-1}$] | **Young's modulus $E$** [GPa] | **Young's modulus $E$** [GPa] | **CTE $\alpha$** [$10^{-6}$ $K^{-1}$] |
| 3 | T-dep (TPO) † | 0.410 | 9 |
| <u>9</u> | <u>T-dep (EVA) †</u> | <u>3.5</u> | <u>50.4</u> |
| 65 | | 6.36 | 65 |

In the independent parameter variation, the focus is mainly on the height of the frontglass, encapsulant and the solar cell. Here, also only glass-foil modules are considered. Additionally, the Young's modulus of the encapsulant is varied between the measured values at -40 °C, 25 °C and +150 °C. At last, the material of the frame is varied between Aluminum, stainless steel and wood.

**Table 3.7:** Parameters used in the independent parameter variation of glass-foil modules. The reference parameters are underlined; †: measured, see Figure 3.13; □: see Table 3.9.

| Frontglass | Encapsulant | | Solar Cell | Frame |
|---|---|---|---|---|
| **Height** [mm] | **Height** [µm] | **Young's modulus $E$** [MPa] | **Height** [µm] | **Material** |
| 2 | 250 | 1242† | 80 | Aluminum□ |
| 3.2 | 450 | 8.5† | 120 | Steel□ |
| 4 | 600 | 0.2† | 180 | Wood□ |
| | 800 | | | |

In the last variation, the symmetric PV module setup of a glass-glass setup is investigated. The height of the front- and backsheet is varied and the soda-lime glass is replaced by much lighter polycarbonate.

**Table 3.8:** Parameters used in the independent variation for symmetric PV modules. The reference parameters are underlined; □: see Table 3.9.

| Front- and backsheet material | Height [mm] |
|---|---|
| Soda-lime glass□ | 1 |
| Polycarbonate□ | 2 |
| | 3.2 |

**Table 3.9:** Material parameters of materials used in the parameter sensitivity study. *: provided by manufacturer.

| Material | Density | Young's modulus $E$ | Poisson's ratio $\nu$ | CTE $\alpha$ |
|---|---|---|---|---|
| | [g/cm$^{-3}$] | [GPa] | [-] | [10$^{-6}$ K$^{-1}$] |
| soda-lime glass | 2.53* | 74* | 0.24* | 9* |
| Polycarbonate | 1.2* | 2.35* | 0.37* | 65* |
| Aluminum [Hayn14] | 2.7 | 70 | 0.33 | 23 |
| Stainless Steel [Kuch07] | 7.9 | 200 | 0.3 | 16 |
| Wood [Kuch07] | 0.538 | 12.3 | 0.29 | 3.8 |

### 3.3.3 Evaluation of Stress and Strain

Due to the rectangular busbars, singularities at the end of the busbars overestimate the stress strongly. The approach of Whitcomb *et al.* [Whit82] to neglect

adjacent mesh elements is used and extended. This approach has the disadvantage, that the stress from solar cell interconnection is relevant for the cell fracture probability. Therefore, special attention has to be paid on how much is excluded. The aim is to find a good balance between considering the stress from interconnection and excluding singularities. To define the areas to be neglected, the singularity is investigated in the reference FEM model. First the areas to be neglected are defined as the area of the busbar plus an additional margin of size $\delta$ around, as depicted in Figure 3.21. Different margin sizes are investigated between 12.5 µm $\leq \delta \leq$ 5 mm, with the same number of mesh elements. The stress in the extension of the busbar, starting at its corner is evaluated on the backside of the solar cell along a line indicated by the yellow arrow in Figure 3.21.

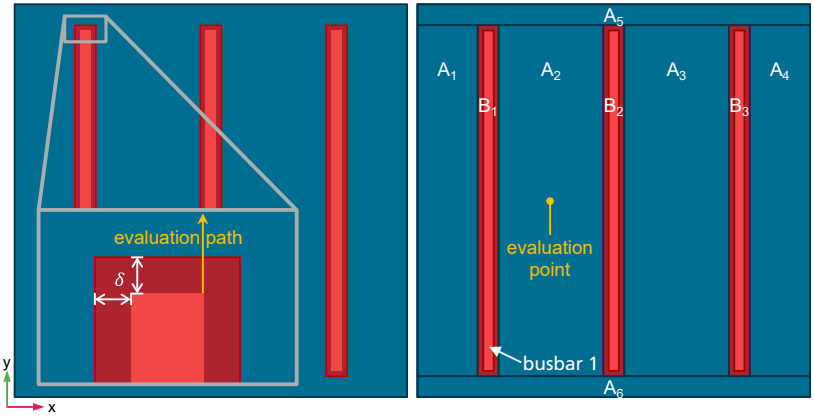


**Figure 3.21:** *Left:* sketch of the non-evaluated box around the busbar with the distance between the busbar and the box edge $\delta$, the yellow arrow indicates the line along which the stress is evaluated. *Right:* Segmentation of the solar cell into surfaces for the evaluation of maximum values. The dark red areas $B_1$-$B_3$ around the busbars are not evaluated to exclude singularities. All other values (not maxima) are evaluated at the indicated evaluation point; not to scale.

The detailed results are presented in Section 4.3.1. However, in order to describe how the stress and strain are evaluated, the overall result of the singularity investigation is anticipated here: the margin size is chosen to be 50 µm, i.e. the mesh elements within 50 µm around the busbar are ignored for the evaluation of the stress and strain. This defines three areas, labelled with $B_1$-$B_3$ in Figure 3.21, which are excluded from the evaluation. For practical reasons, the remaining part of the solar cell is segmented into six rectangular areas, labelled with $A_1$-

$A_6$ in Figure 3.21. Because singularities have a minor impact on stress integration, the probability of cell fracture $P_f$, which is introduced in the following, is evaluated on the whole solar cell surface.

Silicon solar cells have statistically distributed micro-cracks with varying lengths between 10-15 µm, which originate from the wafer and solar cell processing [Möll05]. As a brittle material, Silicon follows linear elastic fracture mechanics. Since the micro-cracks are usually perpendicular to the surface, silicon solar cells fail in loading mode I, i.e. tensile stress in the surface plane [Munz01]. For a triaxial stress, it is common to use the first principal stress $\sigma_I$ as a tensile stress equivalent. The principal stresses are the invariants of the stress tensor. It is a convention to sort the invariants according to their values, where the largest value is appointed to the first principal stress $\sigma_I$ and the lowest to the third principal stress $\sigma_{III}$. Because the third principal stress $\sigma_{III}$ often has negative values, it is the compressive stress equivalent. The second principal stress $\sigma_{II}$ usually has values around zero and therefore is not relevant [Gros17]. For the analysis of the FEM results, the first and third principal stress are used, depending on if tensile or compressive stress is dominant. Both values are evaluated in the solar cell in the center of the module. The highest stress usually occurs in the center of the solar cell. Since the middle busbar of the three busbar solar cell is in the center, the stress is evaluated between the first and second busbar, as indicated by the evaluation point in Figure 3.21. For both also, the largest value on the front and back side of all solar cells is evaluated in the areas $A_1$-$A_6$ by taking the maximum of the first principal stress $\sigma_I$ and the minimum of the third principal stress $\sigma_{III}$ respectively. Additionally, the Weibull distribution considering the size effect is used to convert the maximum of the first principal stress $\sigma_I$ into a probability of cell fracture $P_f$. In the following first the general Weibull distribution is introduced and then applied to silicon solar cells. When describing the general Weibull distribution, the wording probability of failure is used, while for solar cells, the probability of cell fracture is used. This distinction is done because a crack in a laminated solar cell does not necessarily result in a failure of the solar cell.

#### 3.3.3.1 Weibull Distribution

Due to the above mentioned statistically distributed micro-cracks of silicon solar cells, they do not have a well-defined fracture stress but a statistical fracture probability. In the literature the Weibull distribution [Weib39] is often used to describe the probability of failure $P_f(\sigma)$ for silicon [Bagd03]. In the following the two-parameter Weibull distribution is given, for the details and the derivation it is referred to literature, like [Munz01, Weib39, Weib51].

The probability of failure $P_f(\sigma)$ depends on the characteristic fracture stress $\sigma_\theta$ and the Weibull modulus $m$:

$$P_f(\sigma) = 1 - exp\left(-\left(\frac{\sigma}{\sigma_\theta}\right)^m\right). \tag{43}$$

The Weibull modulus $m$ is also called shape factor of the distribution. A high value corresponds to a steep gradient of the probability function $P_f(\sigma)$ on a double logarithmic scale. This is the case for a homogeneous defect distribution, because all samples fracture at similar stress. In contrast to an inhomogeneous defect distribution, which corresponds to a low $m$-value. Here, the samples fracture at very different stress values depending on the defect severity in the stressed area. The characteristic fracture stress $\sigma_\theta$ is defined as the stress at which 63.2 % of the specimens would fail.

Above distribution is only valid for a unit volume with a homogenous stress distribution. To take the stressed size and inhomogeneous stress distributions into account equation (43) has to be expressed by an integral over the volume. However, since solar cells fracture due to surface defects, a surface integral $dA$ over the area stressed in tension is sufficient:

$$P_f(\sigma) = 1 - exp\left(-\int\left(\frac{\sigma(x,y)}{\sigma_0}\right)^m dA\right), \tag{44}$$

where $\sigma_0$ is the geometry independent Weibull scale factor. The stress distribution $\sigma(\mathrm{x},\mathrm{y})$ can be written as a constant stress value $\sigma$, which depends on the applied load and a dimensionless geometric stress shape function $g(\mathrm{x},\mathrm{y})$:

$$\sigma(x,y) = \sigma \cdot g(x,y)\,. \tag{45}$$

With equation (45), the negative exponential in equation (44) becomes:

$$\int\left(\frac{\sigma(x,y)}{\sigma_0}\right)^m dA = \left(\frac{\sigma}{\sigma_0}\right)^m \int g^m(x,y)\,dA\,. \tag{46}$$

The integral is called the effective area $A_{\mathrm{eff}}$:

$$A_{eff} = \int g^m(x,y)\,dA\,. \tag{47}$$

Hence, the probability of cell fracture in equation (44) becomes:

$$P_f(\sigma) = 1 - exp\left(-A_{eff}\left(\frac{\sigma}{\sigma_0}\right)^m\right). \tag{48}$$

The effective area $A_{\mathrm{eff}}$ gives the relation between the Weibull scale factor $\sigma_0$ and the characteristic fracture stress $\sigma_\theta$:

$$\sigma_0 = A_{eff}^{1/m}\,\sigma_\theta\,. \tag{49}$$

**Cell Fracture Probabilities of Solar Cells**

There are several publications focusing on the strength of solar cells and how the manufacturing process influences it, e.g. [Bein05, Haas18, Kohn09, Pogu18, Röth15]. Table 3.10 gives an overview of selected Weibull parameters found in the literature for silicon wafer and cells. Comparing the values for wafer and solar cells reveals, that the production process reduces the characteristic fracture stress. No significant difference is found between monocrystalline (c-Si) and multicrystalline (mc-Si) silicon [Barr14, Kaul17] and between Al-BSF and PERC solar cells [Kaul17] (not shown in Table 3.10). However, the direction of the applied load on the backside of the solar cell has a significant influence. If the tensile stress is parallel to the busbars (BB), i.e. roller perpendicular to the busbars, the characteristic fracture stress $\sigma_\theta$ is reduced by 31 % compared to tensile stress perpendicular to the busbars [Kaul14]. In the same range the reduction for solar cell splitting using the laser scribing with cleaving (LSC) process is found. Here, the decrease depends on the scribing side. If the scribing side is under tension the reduction is up to 36 %, while the non-scribed side has a reduction of 10 %. A less harmful splitting process is the thermal laser separation (TLS), which shows no significant impact [Kaul18].

In the following, the probability of cell fracture $P_{\mathrm{f}}(\sigma)$ (equation (44)) is applied to solar cells within a PV module and an expression to convert measured or simulated stress into a cell fracture probability is derived. As described in the previous paragraph, the probability of cell fracture depends on the surface under stress. For solar cells within a PV module, the stress on the front (sunny) and back side is usually in the same order of magnitude. Therefore, both surfaces have to be considered when calculating the probability of cell fracture:

1. Sunny side (S-F)
2. Back side (B-F)

The integral in the geometric dependent probability of failure $P_{\mathrm{f}}(\sigma)$ in equation (44) has to be drawn for each side and the exponent becomes the sum over these:

$$P_{\mathrm{f}}(\sigma) = 1 - \exp\left( - \sum_{\mathrm{i}} \int \left( \frac{\sigma(\mathrm{x},\mathrm{y})}{\sigma_{0,\mathrm{i}}} \right)^{m_{\mathrm{i}}} dA_{\mathrm{i}} \right), \tag{50}$$

with $\mathrm{i}$ = B-F, S-F. This expression corresponds to the determination of the effective area $A_{\mathrm{eff,i}}$ for each side individually, therefore equation (48) becomes:

$$P_{\mathrm{f}}(\sigma) = 1 - \exp\left( - \sum_{\mathrm{i}} A_{\mathrm{eff,i}} \left( \frac{\sigma}{\sigma_{0,\mathrm{i}}} \right)^{m_{\mathrm{i}}} \right). \tag{51}$$

In equation (47), the effective area $A_{\mathrm{eff}}$ is calculated by integration of the geometric stress shape function $g(\mathrm{x},\mathrm{y})$. Since solar cells fail under tensile stress, the maximum first principal stress $\sigma_{\mathrm{I,max}}$ is used as a failure criterion. Accordingly, the probability function in equation (51) is evaluated for $\sigma_{\mathrm{I,max}}$ and the geometric stress shape function is then the ratio of the first principal stress to its maximum:

$$g_{\mathrm{i}}(\mathrm{x},\mathrm{y}) = \frac{\sigma_{\mathrm{I}}(\mathrm{x},\mathrm{y})}{\sigma_{\mathrm{I,max}}}, \tag{52}$$

with the distribution of the first principal stress $\sigma_{\mathrm{I}}(\mathrm{x},\mathrm{y})$. Finally, the probability for a solar cell fracture within a PV module is:

$$P_{\mathrm{f}} = 1 - \exp\left( - \sum_{\mathrm{i}} A_{\mathrm{eff,i}} \left( \frac{\sigma_{\mathrm{I,max}}}{\sigma_{0,\mathrm{i}}} \right)^{m_{\mathrm{i}}} \right). \tag{53}$$

The Weibull parameters for the different sides are taken from Kaule *et al.* [Kaul18] (print bold in Table 3.10).

Please note, that the fracture probability expresses the likelihood of at least one crack in at least one solar cell within a PV module. It strongly depends on the maximum first principal stress $\sigma_{\mathrm{I,max}}$. As mentioned in the beginning of Section 3.3.3, the rectangular busbar shape overestimates the maximum stress strongly. Accordingly, the fracture probability is also overestimated in the parameter sensitivity study presented in Section 4.6.

**Table 3.10:** Overview of Weibull parameters for solar cells and wafer in the literature. All values are obtained from 4-point bending tests. c-Si: monocrystalline silicon; mc-Si: multicrystalline silicon; Al-BSF: Aluminum back-surface-field; BB: busbar; S: sunny side in tension; B: back side in tension; P: roller parallel to BB; C: roller perpendicular to BB; F: full cell; LSC: laser scribing with cleaving half cell; TLS: thermal laser separation half cell. bold: used in this work.

| **Publication** | **Specimen** | **Char. fracture stress $\sigma_\theta$** [MPa] | **Weibull modulus $m$** [-] | **Scale factor $\sigma_0$** [MPa·m$^2$] |
|---|---|---|---|---|
| Barredo *et al.* [Barr14] | mc-Si etched wafer 156×156×0,17 mm³ | 228.21 | 6.84 | 108.64 |
| | c-Si etched wafer 156×156×0.17 mm³ | 230.95 | 7.19 | 113.50 |
| | quasi mono etched wafer 156×156×0,167 mm³ | 223.83 | 5.22 | 84.25 |
| Schönfelder *et al.* [Schö07] | c-Si isotextured wafer 156×156×0.18 mm³ | 262 | 9 | 167 |
| Kaule *et al.* [Kaul14] | c-Si Al-BSF 3BB cell 156×156×0.2 mm³, SP-F | 197 | 14 | 140 |
| | c-Si Al-BSF 3BB cell 156×156×0.2 mm³, SC-F | 199 | 15 | 145 |
| | c-Si Al-BSF 3BB cell 156×156×0.2 mm³, BP-F | 242 | 14 | 172 |
| | c-Si Al-BSF 3BB cell 156×156×0.2 mm³, BC-F | 166 | 17 | 125 |
| Kaule *et al.* [Kaul18] | mc-Si Al-BSF 4BB 156×156 mm², BP-F | 180.0 | 6.9 | 91.1 |
| | mc-Si Al-BSF 4BB 156×78 mm², BP-LSC | 116.1 | 17.5 | 88.8 |
| | mc-Si Al-BSF 4BB 156×78 mm², BP-TLS | 176.4 | 7.9 | 97.3 |
| | mc-Si Al-BSF 4BB 156×156 mm², SP-F | 184.0 | 7.8 | 100.8 |
| | mc-Si Al-BSF 4BB 156×78 mm², SP-LSC | 166.4 | 8.7 | 97.0 |
| | mc-Si Al-BSF 4BB 156×78 mm², SP-TLS | 177.5 | 8.5 | 102.1 |

## 3.3.4 Validation

For the validation of the developed FEM model the two developed methods for stress measurement are applied. The µ-Raman spectroscopy is used to validate the FEM simulation of soldering and lamination. For the validation of the mechanical load simulation, the solar cell integrated stress sensors are used.

### 3.3.4.1 Raman Spectroscopy

In the results (Section 4.6.5, Figure 4.33), it will be shown that the size of the laminate has a minor influence on the stress after lamination. Therefore, the validation of the lamination model is done with a one-cell laminate, in order to reduce computational effort. Accordingly, the FEM model described above is reduced to one single solar cell with the dimensions in Table 3.11. The adapted FEM model is described in the following.

**Table 3.11:** Dimensions of the one-cell laminate built for the validation using µ-Raman spectroscopy.

| | **Frontglass** [mm] | **Encapsulant** [mm] | **Solar cell** [mm] | **Backsheet** [mm] | **Busbars** [mm] | **Ribbon** [mm] |
|---|---|---|---|---|---|---|
| Length $l$ | 177.23 | 177.23 | 156 | 177.23 | 145 | 150.7 |
| Width $w$ | 175.38 | 175.38 | 156 | 175.38 | 1.35 | 1.5 |
| Height $h$ | 4 | 0.4 | 0.18 | 0.35 | 0.014 | 0.2 |

The FEM model consists of two computation steps. The first step simulates soldering of solar cell by cooling down from the solder solidification temperature of 179 °C to room temperature. The second step simulates lamination by cooling down from 160 °C to room temperature. Linear elastic and temperature dependent material models are used, which are shown in Table 3.2. For the silicon solar cell an anisotropic material model is utilized. To mimic the production process of PV laminates, the residual soldering stress tensor is transferred to the computation of the lamination process. The residual stress from soldering is reduced during the heating up process before the lamination. Therefore, the stress tensor is transferred to the lamination model at lamination instead of room temperature. The laminates twofold symmetry is utilized by simulating a quarter of the single-cell laminate. Consequently, translational symmetry boundary conditions are placed at the symmetry surfaces. The model considers the silver front busbars

and back side pads, while the silver fingers and aluminum layer on the back side are not part of the model.

The mesh consists of mainly hexahedra with some prisms, for example at the pseudo-square corner of the solar cell. Each layer has at least three elements in the thickness with a maximum of five layers for the silicon solar cell, as depicted in Figure 3.22. In total the mesh consist of about 530,000 elements. The soldering and lamination is simulated by utilizing the thermal expansion with setting the stress free temperature to the solders solidification of 179 °C temperature and lamination temperature of 160 °C respectively. To prevent rigid-body displacement, a point fixed constraint is placed on the back side of the solar cell at the symmetry edge for the soldering process. Additionally, a the out-of plane translation is suppressed on the back side of the solar cell in the soldering simulation to simulate the flattening of the soldered solar cell for the µ-Raman measurements. In lamination, the frontglass is fixed at the symmetry point on the front side, which simulates, that the laminate cools down with the sunny side down. The initial stress in the solar cell before soldering is as a first approximation set to zero.

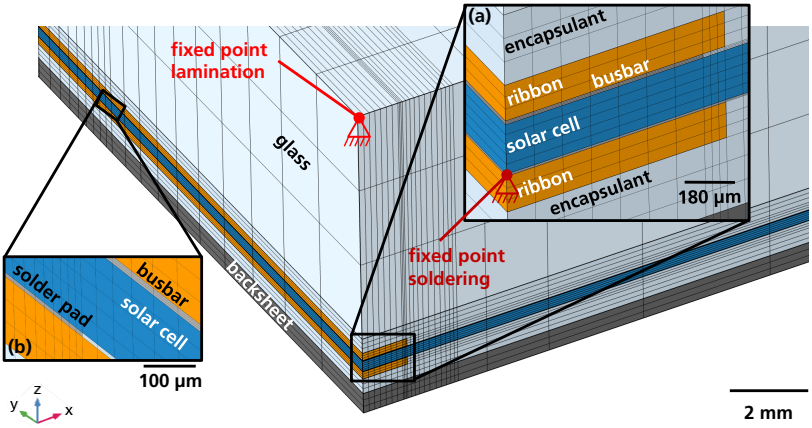


**Figure 3.22:** Symmetry corner of the laminate with the used mesh. The enlargement (a) shows the mesh in more detail. Enlargement (b) shows additionally a detail of the next solder pad, which is not present in (a). Modified after [Bein19].

### 3.3.4.2 Stress Sensors Integrated in Solar Cells "*SenSoCell*"

#### Module Setup and Production

From the initial FEM simulations (Figure 4.18) two characteristic positions of the stress distribution at mechanical load are identified. They are in the center of the module as well as at the corner. At these positions *SenSoCells* are integrated into the PV module for validation of the FEM simulation. The *SenSoCells* are placed so that the sensors are on the back side facing the backsheet. The other solar cells are interconnected in series by the automated tabber stringer *Rapid ONE* by *Somont* using 1.6×0.15 mm² interconnectors and 5×0.3 mm² crossconnectors.

Figure 3.23 shows the setup of the PV module produced for validation, which differs from the reference setup (described in Section 3.3.2) in the following points:

- The two SenSoCells are not electrically connected to the other solar cells and bypassed by cross-connectors. Accordingly, the FEM model without interconnectors is used in order to simplify the model geometry. It is verified (Appendix C, Figure C.6.6) that the influence of the interconnectors on the deflection is negligible.
- A different backsheet (Coveme dyMat PYE white, 218 µm height, Table 3.12) is used.
- A larger (1.7×1.0 m²) and different glass (Interfloat GMB Sina TT,Table 3.12) is used.
- A different frame is used as depicted in Figure 3.23 . In the parameter sensitivity study, a simplified geometry is used in order to use a hexahedral mesh. In the validation experiment, the frame is simulated in full detail.
- A different adhesive to join the frame to the laminate is used. The Young's modulus of the used *PV-804 Neutral Sealant* from *Dow Corning* is not available, therefore the value of the equivalent adhesive *PV-8080 Neutral Sealant* also from *Dow Corning* is used in the FEM simulation.
- Measurement values (not shown) for the position of the laminate within the frame are taken, rather than positioning it vertical symmetrical.
- Instead of a homogenous surface load, the vacuum suction cups of the mechanical load test stand are modelled by a 2D Gaussian load distribution (see equation (54) and Figure 3.25), which slightly decreases the deflection.

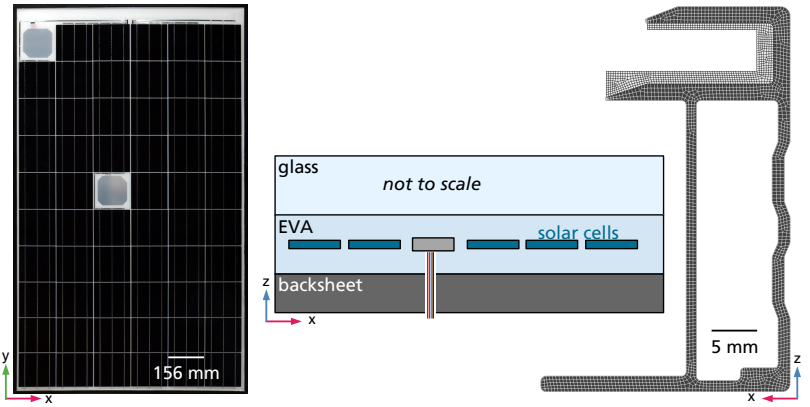


**Figure 3.23**: *left*: picture of one validation module. *Center*: cross section of the module illustrating the cabling through the backsheet, not to scale. *Right:* Cross-section with the mesh of the frame (dark grey) and asymmetric adhesive (light grey) used in the validation.

**Table 3.12:** Material properties and layer height of the module materials used in the validation FEM model which are different from the reference FEM model, *: provided by manufacturer, †: measured.

| **Component** | **Material** | **Height $h$** [mm] | **Density** [g cm$^{-3}$] | **Young's modulus $E$** [GPa] | **Poisson's ratio $\nu$** [-] |
|---|---|---|---|---|---|
| Frontglass | soda-lime glass | 3.2 | 2.5* | 73* | 0.24* |
| Backsheet | PET | 0.218 | 1.3* | 2.35† | 0.3* |
| Adhesive/inlay | silicone | varying | 0.067* | 0.00043* | 0.49* |

Three laminates are laminated using the hydraulic vacuum membrane-plate laminator *Bürkle YPSATOR122-5 HKV* with an evacuation time of 4 min, a pressing time of 8 min with 900 mbar and passive cooling at ambient temperature. After lamination a black anodized Aluminum (EN AW 6060 T6 - C35) frame with a height of 40 mm is attached to the laminates. The frame consists of four miter cut parts, which are connected with a corner connector depicted in Figure 3.24. During the framing the short frame parts with the preassembled corner connectors are pressed into the long parts. Simultaneously, the laminate is bonded to

the frame using the silicone *Dow PV-804* by *Dow Corning*. After framing, the PV modules are inspected for cell cracks by electroluminescence imaging.

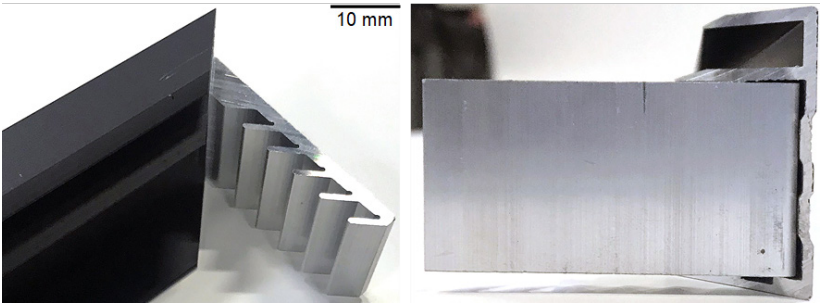


**Figure 3.24:** Preassembled frame corner connector pressed in the short side of the frame in diagonal view (*left)* and side view of the miter cut (*right*).

### Mechanical Load

The Mechanical Load Tests are conducted on a custom made pneumatic Mechanical Load Test stand, fulfilling the requirements of the IEC 61215 standard [Inte16]. The PV modules are mounted on a profile of 40 mm width by four 100 mm long frame clamps *Schletter 400440*. The center of the frame clamp has a distance of 34.2 mm (20 % frame length) to the frame corner. The load is applied by 32 vacuum suction cups, of which four are clustered in a square, as illustrated in Figure 3.25. The total load is the pressure of all vacuum cups averaged over the PV module area. The radius $r_{\mathrm{vc}}$ of the vacuum cups is 48 mm. The center-to-center distance between two vacuum cups is 21.5 cm along the long side (y-axis) of the module and 26.8 cm along the short side (x-axis). The distance to the module edge of the outer vacuum cups is 10 cm.

In the FEM model, the vacuum cups are represented by a 2D Gaussian distribution, which applies the normalized force equivalent $F_{\mathrm{n}}$ at the positions of the vacuum cups:

$$p(\mathrm{x},\mathrm{y}) = \frac{F_{\mathrm{n}}}{2\pi\left(\frac{r_{\mathrm{vc}}}{3}\right)^2} \sum_{\mathrm{i,j}}^{4,8} \exp\left(-\frac{\left(\mathrm{x}-\mathrm{pos}_{\mathrm{x,i,j}}\right)^2 + \left(\mathrm{y}-\mathrm{pos}_{\mathrm{y,i,j}}\right)^2}{2\left(\frac{r_{\mathrm{vc}}}{3}\right)^2}\right), \tag{54}$$

where $F_{\mathrm{n}}$ is the force equivalent to the surface load normalized to the number of vacuum cups, $\mathrm{i}$ is the index for the vacuum cup along the short side of the module and $\mathrm{j}$ for the long side, $\mathrm{pos}_{\mathrm{x,i,j}}$ and $\mathrm{pos}_{\mathrm{y,i,j}}$ are the $\mathrm{x}$ and $\mathrm{y}$ positions of the $\mathrm{i,j}$-vacuum cup. The surface integration of this distribution over the PV module area gives the applied surface load $p_{\mathrm{ML}}$. Figure 3.25 shows a picture of the

test stand and the corresponding load distribution in the FEM model according to equation (54).

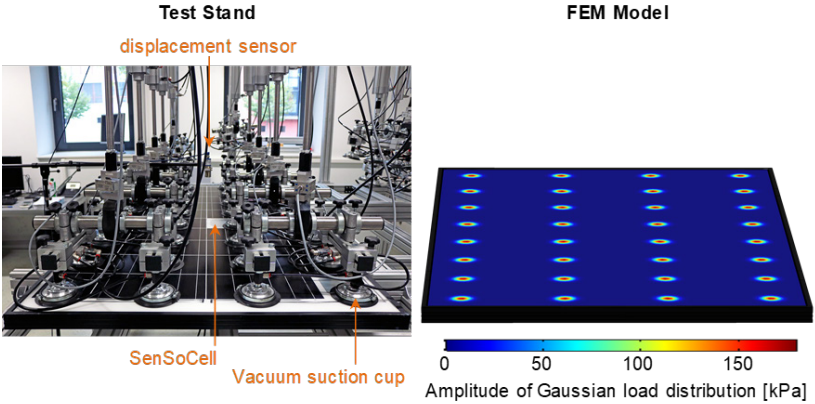


**Figure 3.25:** *left:* Picture of the Mechanical Load Test stand*; right:* Gaussian load distribution of the vacuum suction cups implemented in the FEM model.

The displacement of the module is measured by an optical displacement sensor in the center of the module. In the FEM model, the displacement is evaluated at the same position.

The tare load by the vacuum cups is approximately 500 Pa. This is compensated before the test, so that the displacement of the module is 0 mm. Then the load is applied continuously with about 15 Pa/s until 2400 Pa. To inspect the modules for new cell cracks by EL-imaging, the load is released. After the EL imaging, the modules are loaded again until 5400 Pa followed by EL-imaging.

The resistance of the *SenSoCells* is measured during the load test by a 4-terminal probe using an *Agilent 34970A* with a 20-channel relay multiplexer *Agilent 34901A*. The change relative to 0 Pa load is converted into a stress using the sensitivity $S_\sigma$ of (-47.41 ± 0.14) %/GPa determined in Section 4.2.1.1.

### Simplified Model

The validation experiments on the PV modules shows a significant deviation between measured and simulated deflection (see Figure 4.8, Section 4.3.2.1). To find the root cause of this deviation, a simplified geometry is investigated in order to reduce the degrees of freedom in the FEM simulation. The geometry is reduced to only the glass sheet with the frame and adhesive. The same material

and processes as for the PV module are used. Two such framed glass sheets are produced for two different experiments depicted in Figure 3.26:

1. The same Mechanical Load Tests as for the PV module are performed with a focus on the deformation of the frame corner and the frame clamp. Both are filmed during the whole test. Additionally to the Mechanical Load Test on the PV module, a second available displacement sensor is used to measure the displacement on the center of the short edge of the glass sheet.
2. Same as 1. but with support of the frame corner by two additional frame clamps and a diagonal mounting rail.

For both experiments, the FEM model is adapted to simulate the exact experimental setup. Additionally, sensitivity analyses are carried out on different parameters, like the laminate positioning within the frame, material properties of glass, adhesive and frame as well as different boundary conditions for the frame mounting.

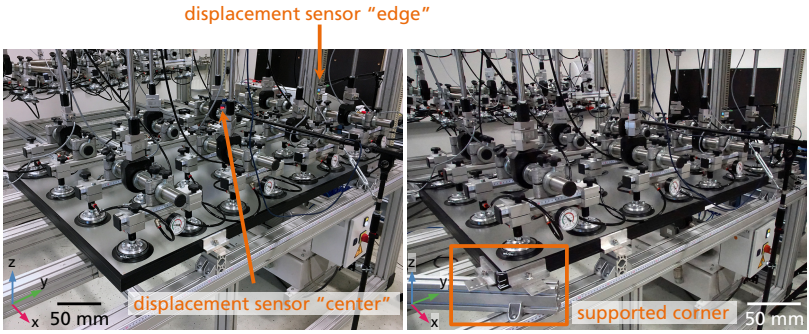


**Figure 3.26:** Setup of simplified validation experiment 1 on a framed glass sheet (*left*) and experiment 2 with supported frame corner (*right*).

# 4 Thermomechanical Stress in PV Modules

Sections 4.1 - 4.3 present the results of the developed stress determination methods. Their application on investigating the stress within solar cells is covered in Sections 4.4 - 4.6.

## 4.1 µ-Raman Measurement Technique

### 4.1.1 Conversion Coefficient

In order to obtain a conversion coefficient for the investigated monocrystalline silicon solar cells between the Raman peak shift and stress, the measured peak shift $\delta$ is plotted versus calculated maximum tensile stress at the same deflection in Figure 4.1. The slope defines the conversion coefficient $\Sigma$ and is obtained as: $\Sigma$ = -(1.19 ± 0.07) rel. cm$^{-1}$/GPa. Since the surface topology is very specific for each solar cell design, the conversion coefficient has to be determined for each solar cell design individually.

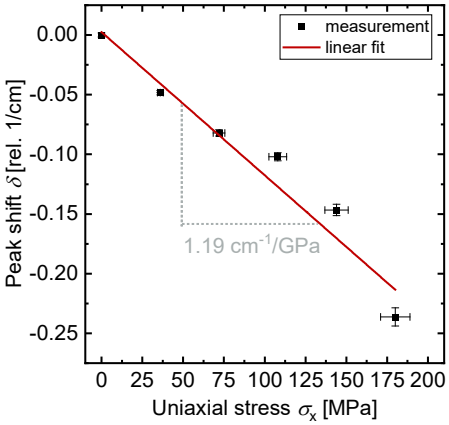


**Figure 4.1:** Measured average Raman peak shift $\delta$ versus maximum uniaxial tensile stress $\sigma_x$ at the same deflection in an identical 3-point bending stage. The red line is a linear fit to the data. Modified after [Bein19].

### 4.1.2 Influence of Frontglass

Figure 4.2 shows exemplarily the peak shift wavenumber within 1000 measurements as histograms for two different deflections. Each diagram shows measurement results obtained with and without glass. The difference in average peak position is (-0.001 ± 0.006) rel. $cm^{-1}$, which corresponds to a stress difference of (0.8 ± 5) MPa. Comparing the uncertainty of the difference in Raman peak position with and without glass to the obtained difference, shows that the uncertainty is six times larger and thus the glass sheet does not impede the µ-Raman measurement. Similar results are obtained for other 3-point bending deflections as well (not shown).

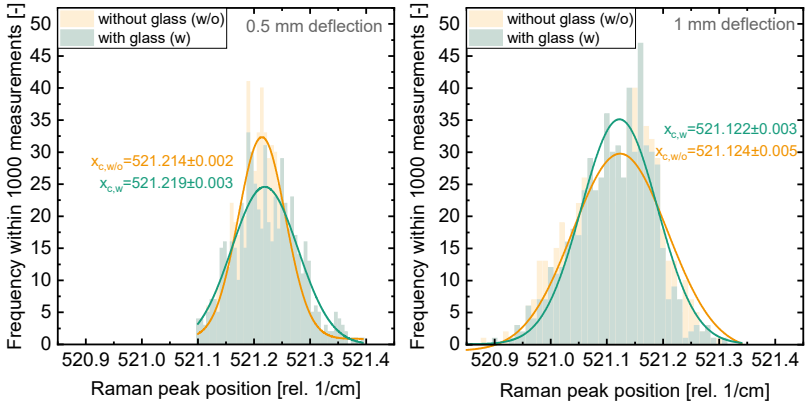


**Figure 4.2:** Distribution of measured Raman peak positions of the solar cell stripe for two different deflections in a 3-poinz bending stage (*left:* 0.5 mm, *right*: 1 mm) measured with and without glass sheet in front of the sample. Modified after [Bein19].

## 4.2 Solar Cell Integrated Sensor Calibration

### 4.2.1 Development

#### 4.2.1.1 Sensitivity

Figure 4.3 (left) exemplarily shows the relative resistance change of one sensor from variation S.5. As expected from equation (17), the resistance shows a linear dependence on the applied stress.

Sensitivities of all six design variations are depicted as box plots in Figure 4.3 (right). The sensitivity decreases with increasing aspect ratio $\alpha$ as well as with

increasing charge carrier density $N$. From equation (12) and (17) (Section 3.2.1.1), based on a linear approximation, the sensitivity $S_\sigma$ should be independent of both factors. However, silicon's piezoresistance is based on the electron and hole transport in which the charge carrier density $N$ plays a crucial role. The neglected higher-order terms, which can be found in [Doll13], incorporate charge carrier density $N$ as well as aspect ratio $a$. Therefore, the results show, that for a more precise description higher-order terms have to be considered. However, for the design phase of the sensors, the linear approximation is a good first order approach.

The best reproducibility is achieved with design variation S.5 ($a$ = 10/1, $N$ = 5×10$^{19}$ cm$^{-3}$) with a sensitivity $S_\sigma$ of (-47.41 ± 0.14) %/GPa. Therefore, this design is used for the laminate integration and is implemented in the *SenSoCell*.

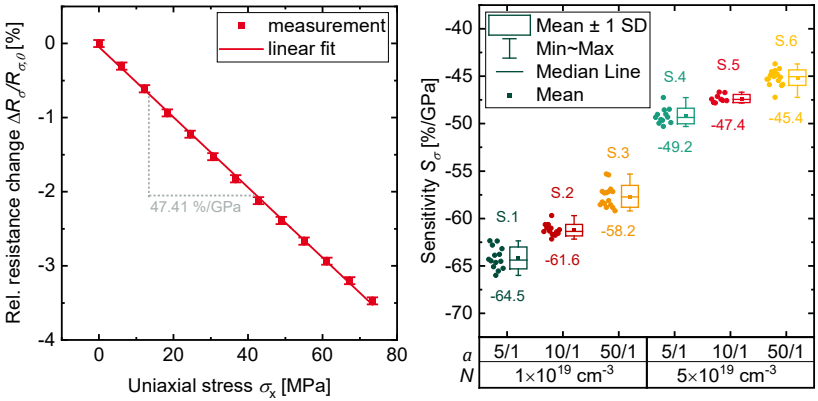


**Figure 4.3:** *Left:* Relative resistance change vs. uniaxial stress for one exemplary sensor from variation S.5. The solid red line is a linear fit to the data from which the sensitivity $S_\sigma$ is obtained. *Right:* Sensitivity box plot of the six different stress sensor variations. On the ordinate are the aspect ratio $a$ and the charge carrier density $N$. The box represents the standard deviation, the line within the box is the median and the square is the mean, the whiskers show the minimum and maximum values. Modified after [Bein20a].

### 4.2.1.2 Laminate Integration

Figure 4.4 shows the rel. resistance change and the corresponding calculated stress during 3-point bending test of the laminated sensor stripe. A linear correlation between deflection and relative change in resistance is obtained. The interconversion into stress reveals that the silicon stripe is in compressive stress. The step at around 0.6 mm deflection originates most likely from a sudden change of the resistance due to a small fracture in a solder joint or metallization.

The successful measurement of bending stress proves that the proposed sensor is capable to determine stress within a PV module setup.

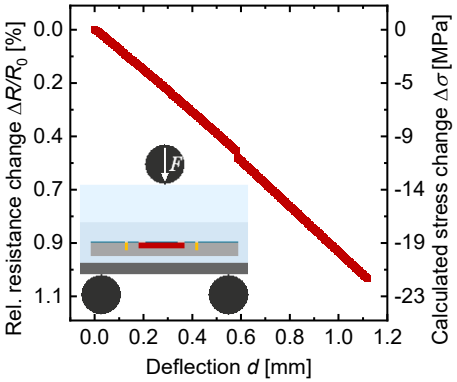


**Figure 4.4:** Stress measured in a laminated sensor stripe as a function of deflection $d$ in three-point bending. The stress is calculated from the relative resistance change $\Delta R_\sigma/R_{\sigma,0}$ using a sensitivity $S_\sigma$ of -47.41 %/GPa. The insert shows the three-point bending setup schematically. Modified after [Bein20a].

## 4.2.2 Sensitivity of *SenSoCell*

This Section presents measurements on the full solar cell wafer. Exemplarily, Figure 4.5 shows the relative resistance change $\Delta R_\sigma/R_{\sigma,0}$ for one of the tested *SenSoCell* sensor pairs along with the values of the sensor stripe shown in Figure 4.3 left. It seems like the *SenSoCell*'s resistance has a slight nonlinearity. However, in the range of values measured within this work, the linear fit is a reasonable description of the curves slope. The mean value of the longitudinal sensor over all tested *SenSoCell*s is (-47.3 ± 0.3) %/GPa. The difference of 0.11 %/GPa to the mean value of the corresponding sensor stripes is smaller than the error. Therefore, the sensitivity of the sensor stripes is also valid for the *SenSoCell*. The mean value of the transversal sensor over all tested *SenSoCell*s is (23 ± 0.6) %/GPa. In Section 3.2.2.2 the assumption is made, that the transversal sensitivity is the negative value of half the longitudinal sensitivity

$$S_{\sigma,\mathrm{t}} = -\frac{1}{2} S_{\sigma,\mathrm{l}}. \tag{55}$$

For the measured values it is:

$$S_{\sigma,\mathrm{t}} = -(0.49 \pm 0.01) \cdot S_{\sigma,\mathrm{l}}. \tag{56}$$

Therefore, the made assumption are reasonable.

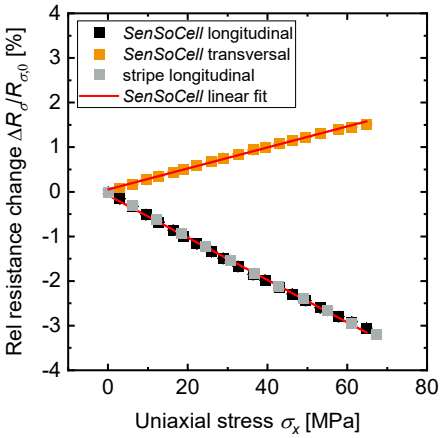


**Figure 4.5:** Relative resistance change vs. measured uniaxial stress for one exemplary *SenSoCell* sensor pair in longitudinal (black symbols) and transversal (orange symbols) direction as well as the sensor stripe shown in Figure 4.3 (grey symbols). The solid red line is a linear fit to the data from which the sensitivity $S_\sigma$ is obtained. Please note, that the error bars are too small to be visible.

## 4.3 Finite Element Model

As described in Section 3.3.3, the rectangular shape of busbars and ribbons intensifies the stress at the busbar end within the solar cells. Therefore, firstly the investigation of the singularity around the busbars is analyzed, followed by the validation of the simulation.

### 4.3.1 Singularity around Busbars

To find a good balance between the exclusion of stress singularities and considering the stress from interconnection in the evaluation, the singularity around the busbars is evaluated for the first simulation step, which is soldering, in order to avoid the superposition of several loads. The first principal stress $\sigma_\mathrm{I}$ along the evaluation path (Figure 3.21) is plotted for all investigated margin sizes in Figure 4.6. In the double-logarithmic representation, the stress curve changes its shape at around 50 µm away from the busbar end. A similar behavior is described by Munz *et al.* [Munz95] for a ceramic-metal joint with an interlayer. They found that the ceramic-interlayer interface influences the stress only to a certain distance. After this distance the stress is only influenced by the ceramic-metal interface, which also influences the stress magnitude in the first region. Transferred

to the silicon-ribbon joint with the metallization defined as interlayer, the curve can be divided into two regions:

1. < 50 µm: the silicon-metallization interface dominates the stress.
2. > 50 µm: the silicon-ribbon interface dominates the stress.

However, the silicon-ribbon interface influences also in region 1 the magnitude of the stress. Additionally, the insert in Figure 4.6 reveals a dependence of the stress on the mesh element size. Since each margin size has the same number of elements within the margin, an increase in margin size corresponds to a mesh element size increase. For margin sizes below 300 µm the stress curves depend on the margin size and are discontinuous at the margin border with a sudden stress increase. For 10 µm and 12.5 µm margin sizes, this is particularly well seen in Figure 4.6 highlighted by the grey circle. When going to large margin sizes ($\delta$ > 300 µm), there are less than two mesh elements within the first 50 µm, i.e. the influence of the silicon-metallization interface is limited to the first one or two mesh elements. Therefore, the stress resulting from the silicon-metallization interface is not resolved for margin sizes > 300 µm and the stress curve is independent of the margin size. While for lower margin sizes the strength of the silicon-metallization interface influence depends on the mesh element size.

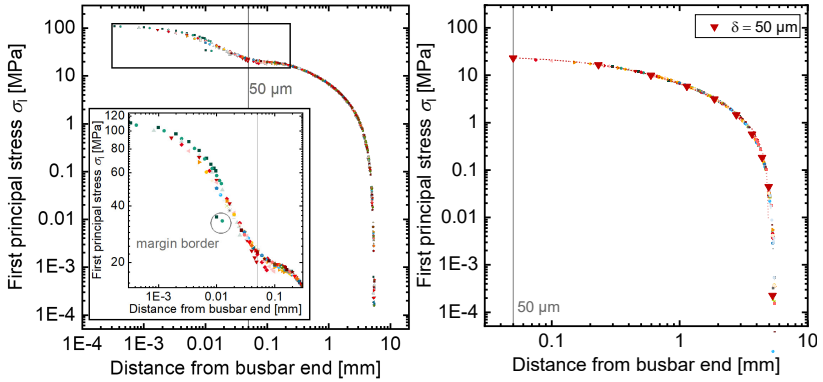


**Figure 4.6:** First principal stress $\sigma_I$ on the back side of the solar cells after soldering in double-logarithmic representation for all margin sizes (*left*) and outside the margins for margin sizes $\delta$ > 50 µm (*right*). The different margin sizes are indicated by different symbols and colors, the grey lines indicate the chosen margin size $\delta$ of 50 µm. The insert on the left is an enlargement of the black box. The grey circle highlights the discontinuity at the margin border exemplarily for the margin sizes $\delta$ 10 µm and 12.5 µm.

Evaluating the stress only outside the margins (Figure 4.6 (right)), i.e. in the areas $A_1$-$A_6$ (Figure 3.21), reveals that starting from a margin size of $\delta$ = 50 µm,

the curves are also independent of the margin size. Therefore, the first principal stress $\sigma_\mathrm{I}$ is independent of the mesh element size for margin sizes $\delta > 50$ µm and for distances larger than 50 µm away from the busbar end. Consequently, a margin size of 50 µm is the smallest margin size, which removes the influence of the FEM mesh and the silicon-metallization interface. Consequently, 50 µm are chosen as a margin size around the busbar in which the stress and strain are not evaluated.

However, the influence of the silicon-ribbon interface is still relatively strong, i.e. the singularity due to the rectangular shape of the busbar and ribbon is reduced by this approach but not completely removed, i.e. the obtained values for the stress are exaggerated compared to a realistic geometry with rounded edges.

Now, the maximum stress value is determined in the areas $A_1$-$A_6$ (Figure 3.21), but since the stress is integrated in the probability of cell fracture $P_\mathrm{f}$ the exaggeration might not be that crucial. To investigate this, the probability of cell fracture $P_\mathrm{f}$ of the center solar cell is compared for different approaches:

1. Evaluation on the whole cell area (A1-A6 and B1-B3);
2. Evaluation only on A1-A6;
3. Evaluation only on B1-B3;
4. Determining a singularity function for the stress curve within $B_1$-$B_3$ and evaluation of the probability of cell fracture $P_\mathrm{f}$ only within $B_1$-$B_3$.

The last approach is motivated by the observation, that the stress converges to a finite value when approaching the busbar end, although theoretically the stress should diverge to infinity when approaching a sharp edge [Sinc99, Sinc00, Will52]. Several works have investigated similar singularities and found that a typical behavior is the proportionality to $r^{-\lambda}$ [Koto06, Mayl12, Sinc04a, Sinc04b]. Therefore, what is called "singularity" before is not a "real" singularity in terms of this definition. The reason for the stress convergence might lie in the similar Young's moduli of the joint layers (see Table 3.2) [Munz95]. However, in Figure 4.6 it can be seen, that the stress curve has a linear part (in the double-logarithmic representation) between around 10 µm and 50 µm distance from the busbar edge, which is a $r^{-\lambda}$ behaviour. Accordingly, the stress behaves like a pure singularity in this range and by fitting a $r^{-\lambda}$ function to it, a singularity function can be obtained:

$$\sigma_\mathrm{I}(x) = \frac{s}{r^\lambda}, \tag{57}$$

with $s$ being a scale factor. Substituting this function into the geometric stress shape function (equation (52)) gives an expression for the probability of cell fracture $P_\mathrm{f}$ for a real singularity:

$$P_\mathrm{f} = 1 - \exp\left( -\sum_\mathrm{i} \int \left( \frac{s}{r^\lambda \, \sigma_{\mathrm{I,\,max}}} \right)^{m_i} dA_i \left( \frac{\sigma_{\mathrm{I,max}}}{\sigma_{0,\mathrm{i}}} \right)^{m_\mathrm{i}} \right) . \tag{58}$$

Therefore, approach 4 compares the probability of cell fracture $P_\mathrm{f}$ obtained from the FEM model (approach 3) to the probability of cell fracture $P_\mathrm{f}$ for a real singularity by evaluating equation (58) instead of (53) on the areas $B_1$-$B_3$.

Figure 4.7 shows the values of the four approaches. It is clearly visible, that the probability of cell fracture $P_\mathrm{f}$ is dominated by the stress within $B_1$-$B_3$ and that the stress exaggeration is much lower compared to a real singularity. Therefore, the evaluation of the probability of cell fracture $P_\mathrm{f}$ within $B_1$-$B_3$ results in exaggerated values compared to a realistic geometry with rounded edges. However, compared to a singular stress behavior, the value is much lower. Since the stress within $B_1$-$B_3$ is indeed relevant for the fracture probability, as a trade-off, the probability of cell fracture $P_\mathrm{f}$ is evaluated on the whole solar cell area ($A_1$-$A_6$ and $B_1$-$B_3$) using the maximum first principal stress $\sigma_\mathrm{I}$ determined only on $A_1$-$A_6$.

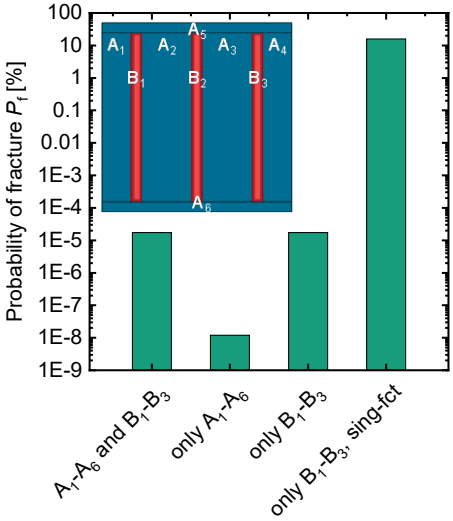


**Figure 4.7:** probability of cell fracture $P_\mathrm{f}$ for different evaluation approaches, please note that the y-axis is logarithmic to resolve the low values.

## 4.3.2 Validation of FEM Model

### 4.3.2.1 Deflection

As a first validation variable, the deflection of the PV module as a function of the applied mechanical load as depicted in Figure 4.8, is analyzed. The results show that the used linear approximation strongly overestimates the measured deflection, although it shows a linear behavior. At 2400 Pa the deviation is 28 mm (134 %) and at 5400 Pa 69 mm (161 %). Including geometrical nonlinearity in the simulation leads to a better agreement but also to a non-linear deflection curve which is in contrast to the measurement. Due to this different behavior, the deflection divergates for loads above 3000 Pa. At 2400 Pa the deviation is 0.6 mm (2.9 %) and at 5400 Pa 9.3 mm (21.7 %). Sensitivity analyses of different parameters and boundary conditions, showed now significant change in the curve shape. To find the root cause of the deviation, the parameters are reduced by using only a framed glass. With this the same Mechanical Load Test is performed. Due to technical problems in this experiment, the recording of data starts at the pre-load of the vacuum cups (~500 Pa). The result is depicted in Figure 4.9.

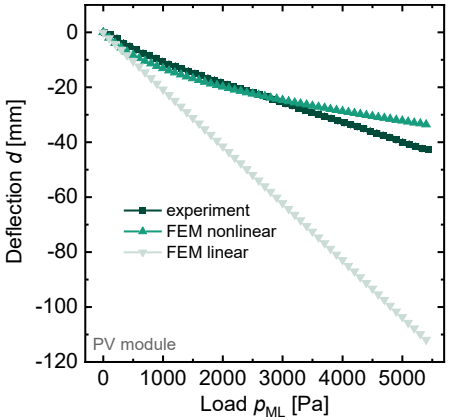


**Figure 4.8:** Mean measured deflection of the 3 validation modules (dark green) and FEM simulation with a geometric non-linear study (green) and linear study (light green). Please note, that the error bars of the measured deflection are too small to be visible.

The framed glass sheet shows the same behavior as the PV module with a larger overall deflection of up to 14 % at 5400 Pa. A second displacement sensor is available in this experiment to measure the deflection in the center of the short edge. At the edge, the experiment shows a slight non-linearity until about

1700 Pa and then a linear shape. Several sensitivity analyses of different parameters and boundary conditions show only a small influence on the FEM simulation outcome and had no significant influence on the deviation to the measurement.

The video analysis of the frame corner reveals that the long and short parts translate and rotate relative to each other above around 1000 Pa. Figure 4.9 illustrates this exemplarily at 5400 Pa load. After unloading the deformation remains, which is an indication for a plastic deformation of the corner connector and presumably of the frame wall. The findings of this experiment indicate that the linear deflection shape is due to the frame torsion, which amplifies the deflection. This hypothesis is tested by trying to suppress the frame torsion in the next experiment on a new framed glass sheet. Here, the frame corner is supported by two additional frame clamps (shown for one corner in Figure 3.26), which still allows to observe the corner. Figure 4.10 shows the outcome.

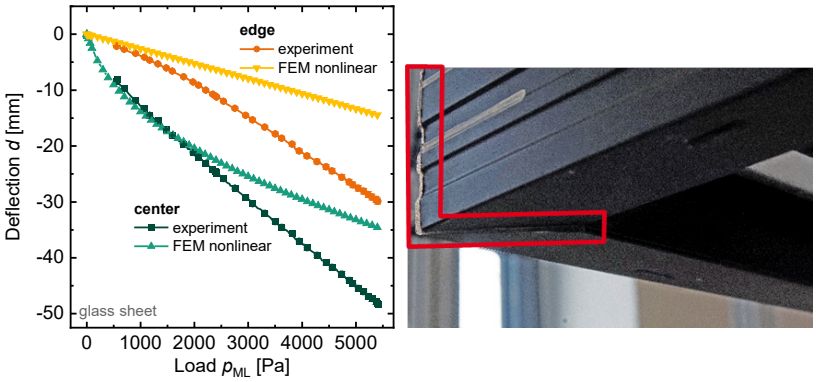


**Figure 4.9:** *Left:* Measured deflection of framed glass sheet in center (dark green) and edge (green) along with FEM results (center: orange, edge: yellow). Please note, that the error bars of the measured deflection are too small to be visible. *Right*: Translation and rotation of frame corner at 5400 Pa load, indicated by the red area.

Suppressing the frame torsion and translation leads to the expected nonlinear center deflection, with the FEM simulation having less than 2.2 mm deviation (above the pre-load of the vacuum cups). However, the video analysis reveals a small translation of the short relative to the long frame part, which shows no movement at the frame corner. The translation is almost completely reversible after unloading. Accordingly, there is only a small plastic deformation, maybe even none because the translation could originate from the tolerance between the corner connector and frame. Since the translation is on the short side of the frame, the deflection of the glass sheet edge is more affected than the center,

which explains the larger deviation between experiment and FEM simulation at the edge. Therefore, it is concluded that the deviation of the simulated to the measured deflection of the PV module originates from the frame torsion and translation.

The deviation could be reduced by including the corner connector in the FEM model. However, to significantly improve the accuracy, the FEM simulation has to include the plasticity of the corner connector and frame as well as the friction between both. This again increases the degrees of freedom and hence the computational resources immensely. Considering that the deviation is well understood and relatively small for loads below 3000 Pa, implementing the corner connector seems not reasonable.

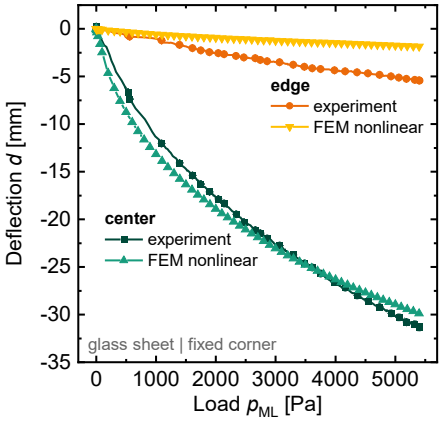


**Figure 4.10:** Measured deflection of the framed glass sheet with additionally supported frame corner in the center (dark green) and edge (green) along with FEM results (center: orange edge: yellow). Please note, that the error bars of the measured deflection are too small to be visible.

### 4.3.2.2 Stress

As a second validation variable, stress in the solar cells of the PV module tested without additional corner support, is analyzed. Firstly, the stress in the center *SenSoCell* is discussed, which is depicted in Figure 4.11. As expected from the deflection, the linear FEM simulation strongly overestimates the measured stress. The deviation is 19 MPa (88 %) at 2400 Pa and 49 MPa (122 %) at 5400 Pa. Until 1800 Pa, the geometric non-linear FEM simulation is in good accordance with the measured stress. The deviation above originates from the frame torsion and is 4 MPa (20 %) at 2400 Pa and 15 MPa (38 %) at 5400 Pa. Because the

stress follows the curvature $\vec{\kappa} = \Delta\vec{d}$, which has a steeper gradient than the deflection (see Appendix C, Figure C.6.7), the intercept of the measured and simulated stress is at lower loads compared to the intersection of measured and simulated deflection in Figure 4.8.

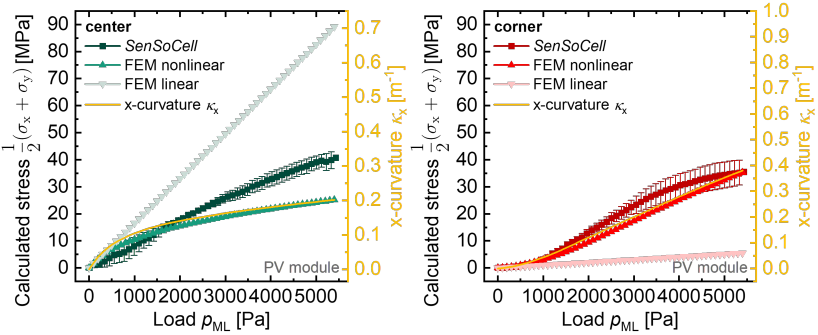


**Figure 4.11:** Stress calculated from resistance change of the *SenSoCell* within the PV module (dark colors) along with the nonlinear FEM simulation (normal colors) and linear FEM simulation (light colors) as well as the x-curvature from the geometric non-linear FEM simulation (right axis, yellow). *Left:* in the center *SenSoCell* (green). *Right:* in the corner *SenSoCell* (red).

Secondly, the stress in the corner *SenSoCell* is discussed. As opposed to the center, the linear FEM simulation strongly underestimates the stress. The deviation at 2400 Pa is 15 Pa (88 %) and 30 MPa (86 %) at 5400 Pa. The reason is the different deflection shape of a linear simulation. Figure 4.12 illustrates the spatial distribution of the deflection shape for the linear and geometric non-linear simulation. Because the direction of the applied force does not change with increasing load in the linear simulation, the displacement of the corners is underestimated. Whereas in the more realistic geometric non-linear simulation, the updating of the force direction with each load step leads to a more homogeneous and stronger displacement on the PV modules short edge as well as corner. The different displacement shape also affects the curvature $\kappa$ depicted for the geometric non-linear FEM simulation in Figure 4.13.

The two relevant curvatures are along x and y. The butterfly shaped x-curvature $\kappa_x$ shows that in the middle line of the short side (x-direction) the curvature is relatively small and that the curvature in the corner is in the same range as in the center cells. The y-curvature $\kappa_y$ is relatively small except at the short edge and corner. The reason is the stiffness of the frame corner, which leads to a high bending moment close to the corner. This together leads to a similar stress in the

corner and center solar cells, which overall is relatively low and does not lead to a significant amount of cell cracks in the EL-imaging (not shown).

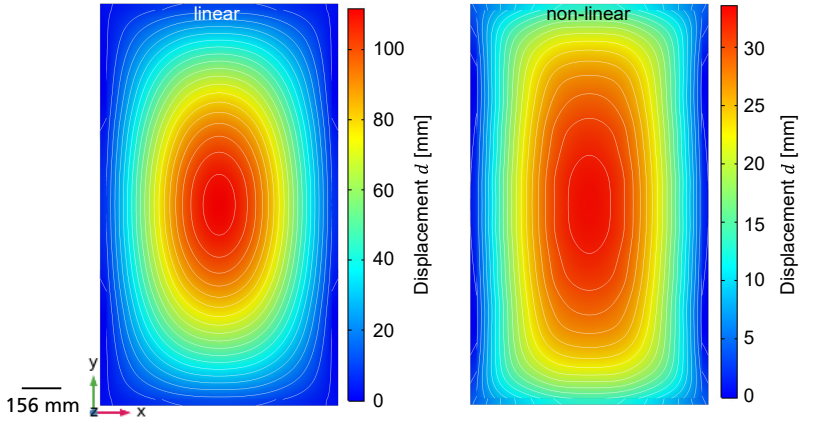


**Figure 4.12:** Deflection shape at 5400 Pa mechanical load of PV module of linear (left) and geometric non-linear FEM simulation (right). The displacement is plotted in the glass and frame, the white lines are equidistant lines of identical deflection.

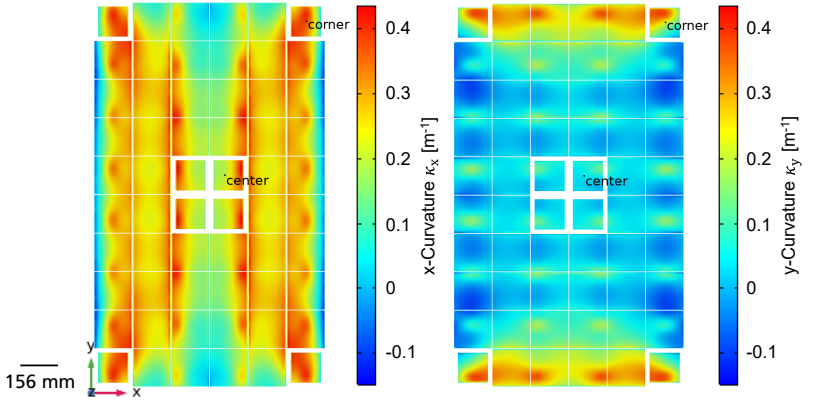


**Figure 4.13:** Simulated distribution of curvature of the solar cells at 5400 Pa load in x-direction (*left*) and y-direction (*right*). The positions of the sensors are indicated

Examining Figure 4.11 again, shows that the geometric non-linear FEM simulation is in reasonable accordance to the measured stress. The deviation at 2400 Pa is 4 Pa (26 %) and at 5400 Pa the deviation is smaller than the meas-

urement uncertainty. In contrast to the center, the frame torsion leads to a flattening of the stress curve above 3000 Pa because the frame torsion reduces the curvature increase.

To conclude the validation experiments, the relevant findings are summarized along with their implication for the FEM model and the parameter sensitivity study.

1. The long and short parts of the used frame translate and rotate relative to each other. This results in a linear PV module deflection as a function of applied load.
2. The FEM model assumes a perfect bonding of the frame parts.
3. The linear FEM simulation strongly overestimates deflection and stress in the center and underestimates stress in the corner.
4. The geometric non-linear FEM simulation underestimates deflection and stress in the center for high loads. In the corner the simulated stress it is in good accordance to measurements.
5. Good accordance exists between geometric non-linear FEM simulation and measurement for suppressed frame torsion for framed glass sheet.

Therefore, it is concluded that the deviation between the geometric non-linear FEM simulation and experiment originates from the differences in the frame bonding, which is specific for each frame. The purpose of this work is to obtain a general understanding of the PV modules thermomechanics and hence to develop a FEM model as general as possible. The approach of Hartely *et al.* [Hart20]to include the frame corner connector and its friction to the frame is too computational resource intensive when combined with geometric non-linearity, which is needed for higher loads. Accordingly, the assumption of perfectly bonded frame parts is kept.

Now, comparing the linear and geometric non-linear FEM simulation, above results clearly show that the geometric non-linear simulation reflects a more realistic description of the measurements. However, this comes with a huge increase in computational resources. For the validation model the geometric non-linear models needs twice the memory (518 GB instead 262 GB) and 91 times the solution time on a faster CPU (172 h instead of 1.9 h) compared to the linear model. Taking into account, that in the validation model the metallization and ribbons are neglected and only the mechanical load at one temperature instead of seven are simulated, the solution time of the linear model increases to 27 h. With a total of 72 parameter combinations carried out, the solution time of the geometric non-linear model is out of the scope for this work (7371 days instead

of 81 days for all parameters). Therefore, the strong deviation of the linear model is accepted in favor of a broader parameter variation and hence a broader insight in the thermomechanics of PV modules. This implies that the absolute values presented are strongly overestimated and only the relative values should be taken into consideration.

To conclude the validation experiments, the geometric linear simulation overestimates the measured results but the linear approximation is an efficient approach for a comparative identification of different influences and hence to gain a fundamental understanding of the PV module thermomechanics.

# 4.4 Stress from PV Module Production

## 4.4.1 Single-Cell Laminate

In this Section, the results of the μ-Raman spectroscopy measurements on single-cell laminates are presented along with the FEM simulation results.

### 4.4.1.1 Metallized Solar Cells

Table 4.1 summarizes the results of the point μ-Raman measurements on solar cell and module level. The measured shift of the Raman peak is depicted relative to the reference position at the solar cell corner along with the converted and simulated stress values. In the following, only the stress values will be discussed, which are additionally illustrated in Figure 4.14.

The larger contraction of the aluminum layer on the back side of the solar cell during cooling down leads to a small bow of the metallized solar cell. For the corresponding residual compressive stress on the surface of the metallized solar cell (-9.3 ± 1.0) MPa are measured. By covering it with a glass sheet the stress increases by -12 MPa to (-21 ± 2) MPa.

**Table 4.1:** Comparison of results of point μ-Raman measurements and FEM simulation between first and second busbar. Stress values are additionally illustrated in Figure 4.14.

| **Cell process step** | **Raman peak shift** [$10^{-3}$ rel $cm^{-1}$ ] | **Raman stress** [MPa] | **FEM stress** [MPa] | **FEM + initial stress** [MPa] |
|---|---|---|---|---|
| Metallized | 11.24 ± 0.15 | -9.3 ± 1.0 | 0 per def. | |
| Metallized flat | 24.8 ± 0.4 | -21 ± 2 | 0 per def. | -21 |
| Soldered flat | 31.4 ± 0.4 | -26 ± 3 | -1 | -22 |
| Laminated | 64 ± 2 | -53 ± 6 | -48 | -57…-69 |

### 4.4.1.2 Soldered Solar Cells

Due to the higher coefficient of thermal expansion (CTE) of copper, the ribbon contracts much stronger during the cooling down from the solidification temperature than the silicon solar cell. This induces a compressive stress on the solar cell, which is measured with (-26 ± 3) MPa on the flattened solar cell. Hence, the soldering process induces an additional compressive stress of -5 MPa (measured). From the FEM simulation of the soldering process a compressive stress difference between the reference and the measurement position of -1 MPa is obtained. To compare the values, the initial stress of the metallized solar cell and the flattened configuration needs to be considered for the simulation. Therefore, the measured initial stress of the flattened metallized solar cell is added to the FEM value, which leads to -22 MPa. This simple approximation leads to a good agreement between FEM simulation and the µ-Raman measurement. The difference originates most likely from the roller boundary condition on the back side of the solar cell in the FEM model.

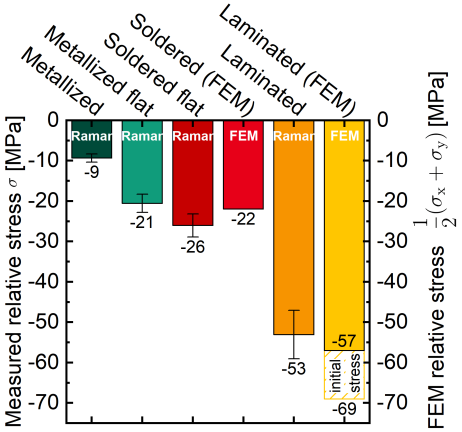


**Figure 4.14:** Relative stress $\sigma$ of all µ-Raman point measurements and relative stress $1/2(\sigma_x+\sigma_y)$ from the FEM simulation; the FEM values are a superposition of the residual stress of the metallized solar cell and the FEM result. The whiskers depict the uncertainty of the Raman values. Modified after [Bein19].

### 4.4.1.3 Laminated Solar Cells

#### Local Stress

During the lamination process, the EVA cross-links and thereby connects the solar cell to the frontglass and the backsheet. Since this takes place at elevated

temperatures, the solar cell compression after soldering is further increased during the cooling down after lamination by the higher contraction of the glass and backsheet compared to the solar cell. After lamination a residual compressive stress of (-53 ± 6) MPa is measured, which is an increase of -27 MPa compared to the residual soldering stress. From the FEM simulation, a residual compressive stress of -48 MPa (without initial stress) is obtained. In this case, the comparison to the measured stress is less straightforward, since the solar cell still exhibits a small bow after lamination [Meng18]. According to the FEM simulation, this bow is about 70 µm, which is smaller than the initial bow. Hence, the initial bow from metallization is not removed completely by lamination. Therefore, the actual initial stress is expected to be between the values of the non-flattened (minimum) and flattened metallized (maximum) solar cell. Accordingly, this range is represented by the shaded area in Figure 4.14 with the maximum compressive stress being the value of the FEM results after lamination plus the initial stress of the flattened solar cell as a shaded area. Additionally, the FEM simulation overestimates the stress, due to the used linear elastic material model for the encapsulant as indicated by Eitner *et al.* [Eitn11a, Eitn11b].

### Large Area Scan of a Quarter Laminate

Figure 4.15 shows the stress mapping relative to the reference point indicated in Figure 3.7 of a quarter solar cell within a laminate. Along with the µ-Raman stress map, Figure 4.15 shows the results from the FEM simulations of soldering and lamination, also indicating the stress at the characteristic positions. The presented relative stress from FEM simulations $(\sigma_x+\sigma_y)/2$ is shown relative to the reference point. Please note, that for the stress mappings, no initial stress is added to the FEM results, because no stress mappings are performed on metallized solar cells.

The finger metallization in the FEM model is neglected, which however, is visible in the µ-Raman stress map by thin dark lines. Since the metallization is not sensible for µ-Raman spectroscopy, no Raman peaks are detected. The lines are not continuous because the fingers are thinner than the used distance between two measurements. The discontinuous soldering on the back side of the solar cell is clearly visible in the FEM results by the areas of higher compressive stress, indicated by white dotted boxes in Figure 4.15, which represent the solder pads. In the µ-Raman stress map these areas are slightly visible. Both stress mappings show that apart from the corner and close to the busbar, the solar cell is under compression. The difference left of the busbar comes most likely from the neglected metallization in the FEM model and the thermal drift of the Raman signal.

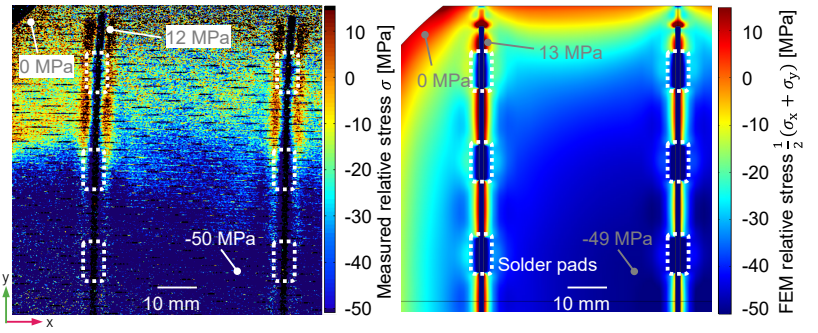


**Figure 4.15:** *Left* µ-Raman cell scan. The color code represents the interconverted stress relative to the reference point indicated in Figure 3.7. Black lines are metallization fingers and busbars, where no Raman spectra are measured. *Right:* Relative stress $(\sigma_x+\sigma_y)/2$ from FEM simulation of the same area. Please note, that metallization is not part of the FEM model. Dotted white boxes indicate the position of back side metallization pads. [Bein19]

Due to the textured surface, the µ-Raman stress map is quite noisy. As discussed above (Section 3.1.3.1), the pyramids have a highly inhomogeneous stress distribution, which is reflected by the variance of the Gaussian. With increasing stress, the variance increases parabolic-like (see Figure 3.5). For the stress maps, 10 spectra are measured for each pixel. Therefore, the mean of the Gauss fit has a limited accuracy, which can be increased significantly by taking more Raman spectra for each pixel. However, this comes with a drastic increase of the measurement time and also an active temperature control of the sample stage is required. Also, a mean of neighboring point can be drawn, as we do for the line scan in Figure 4.16.

The stress gradient over the diagonal of the laminated solar cell is shown in Figure 4.16. Both, the µ-Raman and the FEM results show a steady increase of the compressive stress from the corner to the center of the solar cell, with interruptions at the busbars, where the Raman measurements are not reliable. The highest relative compressive stress is measured in the center of the solar cell with µ-Raman spectroscopy as -50 MPa. The same value comes from the FEM simulation. Both values correlate with the point measurements presented above. From the corner of the cell to the first busbar the µ-Raman and FEM results show a very similar trend. Between the first and the second busbar the µ-Raman stress shows a steeper slope than the FEM stress. Presumably, the reason for the difference lies in the neglected back side aluminum metallization in the FEM model.

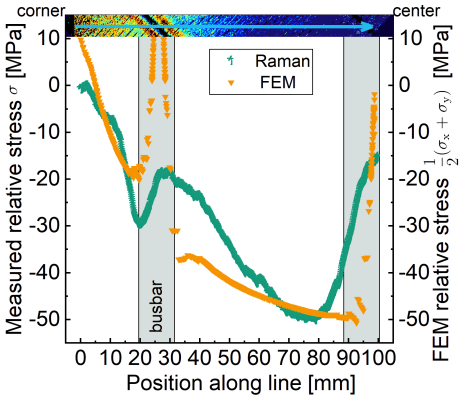


**Figure 4.16:** Relative stress $\sigma$ from µ-Raman measurement and relative stress $(\sigma_x+\sigma_y)/2$ from FEM simulation after lamination on the diagonal of the solar cell. The grey boxes indicate the position of the busbars. The insert on top is a guide to the eye showing the position along the line in Figure 4.15. Modified after [Bein19].

### Area Scan of the End of one Busbar

Figure 4.17 shows a detailed area scan of one busbar end after lamination. Here the µ-Raman stress mapping resolution is 10× the resolution of the cell scan in Figure 4.15, hence the fingers are fully resolved and visible by the thin dark lines. Also, the busbar and the ribbon, which is slightly overlaying, are visible.

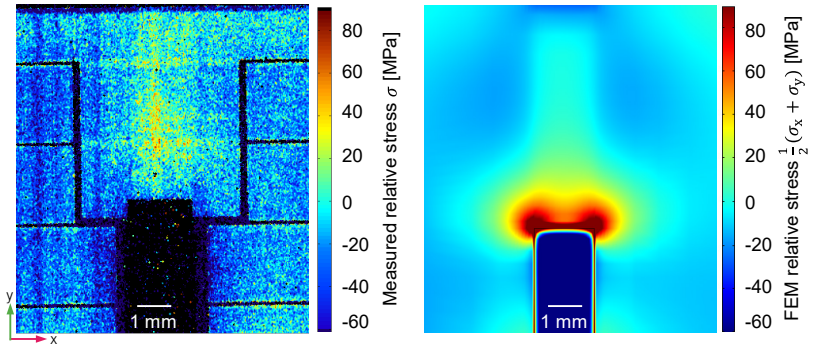


**Figure 4.17:** *Left:* µ-Raman area scan of the end of busbar. The color code represents the interconverted stress relative to the reference point indicated in Figure 3.7. The black lines are the metallization fingers and busbar/ribbon, where no Raman spectra are measured. *Right:* Relative stress $(\sigma_x+\sigma_y)/2$ from the FEM simulation of the same area. Please note, that the metallization is not part of the FEM model. [Bein19]

Please note that the rectangles at the end of the busbar lead to singularities in the FEM simulation which overestimate the absolute stress value in the circular

areas around the busbar end. Since this is a modelling artefact, the mapping is compared qualitatively. However, the overall shape of the stress distribution is valid. The stress of the µ-Raman measurements and the FEM simulation show a similar spatial distribution. The area of tensile stress in the extension of the busbar originates from the superposition of the overall compressive stress after lamination and from the local tensile stress due to the stronger contraction of the ribbon compared to the silicon cell in the soldering process.

### 4.4.2 60-Cell Module

Figure 4.18 left shows the third principal stress $\sigma_{III}$ after lamination on the rear side of solar cells within the 60-cell reference configuration.

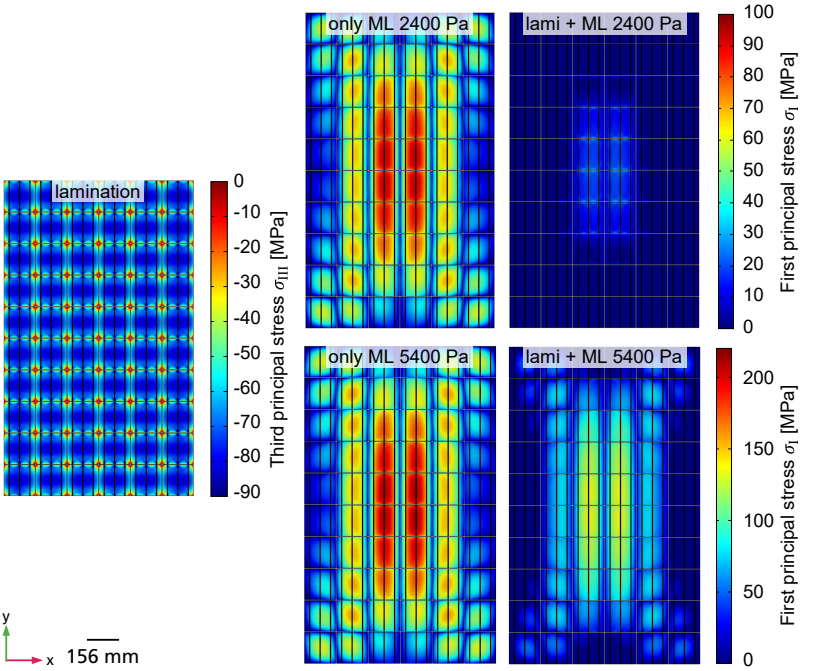


**Figure 4.18**: Simulated spatial stress distribution on the back side of the solar cells of the reference configuration; *left:* third principal stress $\sigma_{III}$ after lamination; *center*: first principal stress $\sigma_I$ at 2400 Pa (*top*) and 5400 Pa (*bottom*) push load, without transferring the lamination stress tensor to the mechanical load study; *right*: first principal stress $\sigma_I$ at 2400 Pa (*top*) and 5400 Pa (*bottom*) push load, with transferring the lamination stress tensor to the mechanical load study.

As the stress after lamination is dominated by the interaction of the solar cell with the front- and backsheet, the stress distribution of one solar cell within a 60-cell module is almost identical to the one of a single cell laminate. The value between the first and second busbar is -81 MPa. Please note, that this value is not directly comparable to above value for the single laminate, because different stress values are evaluated and above relative values are presented.

## 4.5 Stress from Mechanical Load

### 4.5.1 Stress of Reference Module

The push load in the Mechanical Load Test induces tensile stress in the solar cells. As mentioned in Section 4.4, after lamination the solar cells are in compression. Therefore, the residual compressive lamination stress partly compensates the tensile stress in mechanical load. The FEM model takes this into account by transferring the stress tensor from the lamination study to the mechanical load study. To demonstrate how effective the stress compensation is, in one simulation of the reference configuration the stress tensor is not transferred. Figure 4.18 shows the result of this simulation along with the stress after lamination and at mechanical load with the residual lamination stress.

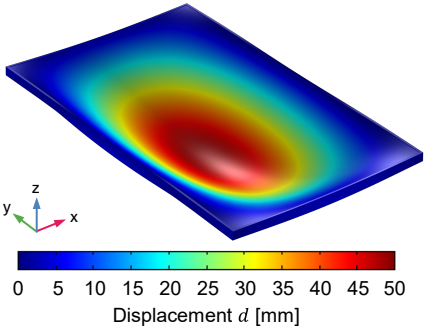


**Figure 4.19**: Simulated displacement distribution of the reference configuration at 2400 Pa push load.

If the stress tensor is not transferred, the first principal stress $\sigma_1$ follows the curvature indicated by the displacement field from the applied mechanical load shown in Figure 4.19. The highest stress occurs in the center cells and is around 90 MPa at 2400 Pa. After lamination the compressive stress in the solar cells is around -80 MPa. Now, when transferring the stress tensor from lamination, the

first principal stress $\sigma_{\mathrm{I}}$ vanishes almost completely and the dominating stress is compressive (not shown). Only in the center cells remains a low first principal stress. Increasing the load to 5400 Pa, increases the first principal stress $\sigma_{\mathrm{I}}$ in the solar cells. The stress distributions shape remains unchanged in the case without the residual lamination stress. The highest stress is again in the center cells with around 210 MPa. Transferring the lamination stress tensor, reveals that the tensile stress is also reduced but due to the higher stress level only compensated in a few cells. Therefore, the dominating stress is tensile in most of the solar cells.

### 4.5.2 Temperature Influence

All results in this and the next Sections are presented in fourfold graphics containing the most relevant quantities to explain the first principal stress $\sigma_{\mathrm{I}}$ and the corresponding probability of cell fracture $P_{\mathrm{f}}$ for the module at mechanical load, which are always in the top row. Two values of the first principal stress $\sigma_{\mathrm{I}}$ are shown: the maximum value, which is used to calculate the cell fracture probability $P_{\mathrm{f}}$, and the value between the busbars in the center cell (see Figure 3.21), which is independent of the interconnection and hence free from singularities. Please note, that due to the singularities from the rectangular busbar shape, the maximum first principal stress $\sigma_{\mathrm{I,max}}$ and accordingly the cell fracture probability $P_{\mathrm{f}}$ are overestimated. This results in cell fracture probabilities $P_{\mathrm{f}}$ of around 100 % for most of the investigated parameters. Also, the cell fracture probability $P_{\mathrm{f}}$ expresses the likelihood of at least one crack in at least one solar cell within the PV module and not how many cracks appear. Therefore, this does not necessarily imply that the solar cells would be strongly damaged. In the bottom row the third principal stress $\sigma_{\mathrm{III}}$ between the busbars of the center cell after lamination is shown as well as the deflection $d$ between the busbars of the center cell at mechanical load. All values evaluated between the busbars of the center cell are denoted by "center cell values" in the legends. The varied parameter is represented by the value itself on the ordinate and with the specific thermal expansion stiffness $\hat{E}_{\alpha}$ at 25 °C with respect to solar cell area.

The IEC 61215 [Inte16] test norm for PV modules specifies the temperature of the Mechanical Load Test as (25 $\pm$ 5) °C. However, most encapsulants and EVA particularly, have a temperature dependent Young's modulus $E$ (see Figure 3.13) and hence a temperature dependent specific thermal expansion stiffness $\hat{E}_{\alpha,\mathrm{e}}$. Figure 4.20 shows how this influences the behavior of the PV module in the mechanical load test at 2400 Pa and 5400 Pa as well as without load to investigate the pure temperature influence.

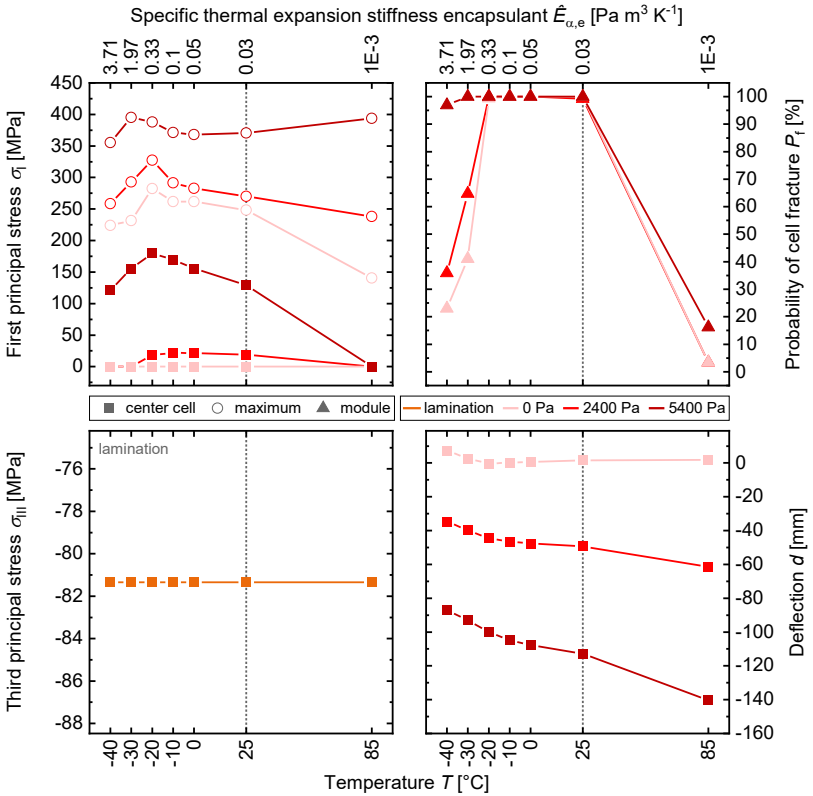


**Figure 4.20:** Temperature influence in mechanical load for the reference at 0 Pa (only temperature) (light red), 2400 Pa (red) and 5400 Pa (dark red). *Top row: left*: maximum value (open circles) and value between the busbars (filled squares) of the center cell of the first principal stress $\sigma_I$; *right*: corresponding probability of cell fracture (triangles); *bottom row: left*: third principal stress $\sigma_{III}$ after lamination; *right*: deflection. Please note, that the bottom ordinates depict temperature $T$ and the top ordinates the corresponding specific thermal expansion stiffness $\hat{E}_{\alpha,e}$.

Firstly, the pure temperature dependence (0 Pa) is discussed. The compressive stress after lamination dominates the overall stress at room temperature. Therefore, the first principal stress $\sigma_I$ between the busbars is negligible for all temperatures. However, the stronger contraction of the ribbon compared to the solar cell leads to a non-zero maximum tensile stress $\sigma_{I,max}$ at the end of the ribbon. When going from room temperature, where the frame is attached, to higher temperatures, the maximum tensile stress $\sigma_{I,max}$ decreases because the residual strain from lamination is reduced. When applying to lower temperatures, the

maximum tensile stress $\sigma_{\mathrm{I,max}}$ increases until -20 °C because of the stronger difference in contraction of the solar cell and ribbon. In this range until -20 °C, the specific thermal expansion stiffness $\hat{E}_{\alpha,\mathrm{e}}$ is relatively low which implies a low interaction of the solar cell with the front- and backsheet. Therefore, the stress from the stronger ribbon compression dominates. Around -20 °C EVA has a glass transition which increases the specific thermal expansion stiffness $\hat{E}_{\alpha,\mathrm{e}}$ and surpasses the value of the solar cell (1.5 Pa m$^3$ K$^{-1}$). Now, the coupling of the solar cell to the front- and backsheet is much stronger and additionally the compression of the encapsulant is no longer negligible. The ribbon is hindered in its contraction and therefore induces less stress in the solar cell. The reason is that the solar cell CTE $\alpha_{\mathrm{c}}$ is smaller than the frontglass CTE $\alpha_{\mathrm{fs}}$ but the ribbon CTE $\alpha_{\mathrm{r}}$ is larger ($\alpha_{\mathrm{c}} < \alpha_{\mathrm{fs}} < \alpha_{\mathrm{r}}$) and additionally, the ribbon is closer to the front-/backsheet. Furthermore, the solar cell is stronger compressed by the larger contraction of the front-/backsheet and encapsulant, which increases the compressive stress in the solar cell. This effect reduces the cell fracture probability $P_{\mathrm{f}}$ significantly.

Adding 2400 Pa push load increases the stress but the overall temperature dependence of all values is unchanged. This stress increase reveals the temperature dependence of the center cell first principal stress $\sigma_{\mathrm{I}}$ which arises from two effects: firstly, the deflection depends on the temperature: between -40 °C and -20 °C it increases due to the decrease in the encapsulants Young's modulus $E_{\mathrm{e}}$. After the glass transition around -20 °C the Young's modulus $E_{\mathrm{e}}$ decreases less and so the deflection increases also less. Around 80 °C, the EVA starts to melt, accordingly, the Young's modulus $E_{\mathrm{e}}$ decreases stronger again and the deflection increases also stronger. Secondly, the strain absorption of the EVA increases with decreasing Young's modulus $E_{\mathrm{e}}$, i.e. with increasing temperature. This decreases the bending stress as well as the thermal compressive stress. Therefore, the tensile stress peaks at -10 °C. Below, the tensile stress decreases due to the lower deflection and becomes simultaneously compensated by the stronger compressive stress. For higher temperatures, the increasing absorption of the bending strain becomes the dominating effect.

Lastly, increasing the push load to 5400 Pa further increases the stress and reveals another phenomenon: due to the increase of the bending strain absorption for lower Young's moduli of the encapsulant, the influence of the deflection on the solar cell strain vanishes in the center. Contrarily, the deflection increases for lower Young's moduli of the encapsulant. Therefore, the displacement of the

solar cells increases and accordingly the ribbons become stretched which increases the tensile stress at the interface to the solar cell.

## 4.6 Parameter Sensitivity Study

In the following, the results of the parameter sensitivity study are presented in the fourfold graphic introduced in the previous Section. Most graphics include results at 25 °C as well as -40 ° and 85 °C. However, the discussion will focus mainly on the 25 °C results, unless the results of the other temperatures are remarkably and not covered by the discussion of the general temperature dependence in Section 4.5.2. The results are subdivided by PV module layer and varied property.

### 4.6.1 Front/Back Cover

#### 4.6.1.1 Frontglass Height

In a glass-foil configuration, the frontglass is the supporting element of the PV module. Therefore, its height plays a crucial role for the stability in the mechanical load test. Figure 4.21 shows that for increasing glass height, the deflection decreases significantly. However, the lower slope exceeding 3.2 mm indicates that between 2 mm and 3.2 mm a critical value is reached. For much lower heights, the deflection will increase strongly, while for higher values, the deflection decreases much less. The same behavior is seen in the stress values. The maximum stress decreases with increasing glass height as well as the tensile stress between the busbars in the center cell, which becomes negligible for 4 mm glass. However, the change in cell fracture probability $P_{\mathrm{f}}$ is minimal, due to high maximum stress values.

Interestingly, the glass height has almost no influence on the third principal stress $\sigma_{\mathrm{III}}$ after lamination. Because the specific thermal expansion stiffness $\hat{E}_{\alpha}$ of glass is about 25 times the one of solar cells, the impact of the glass on the solar cell does not change significantly with increasing height (for $h_{\mathrm{fs}} \gg h_{\mathrm{c}}$). More relevant are the material properties of the front- and backsheet, which are presented in the next Subsection.

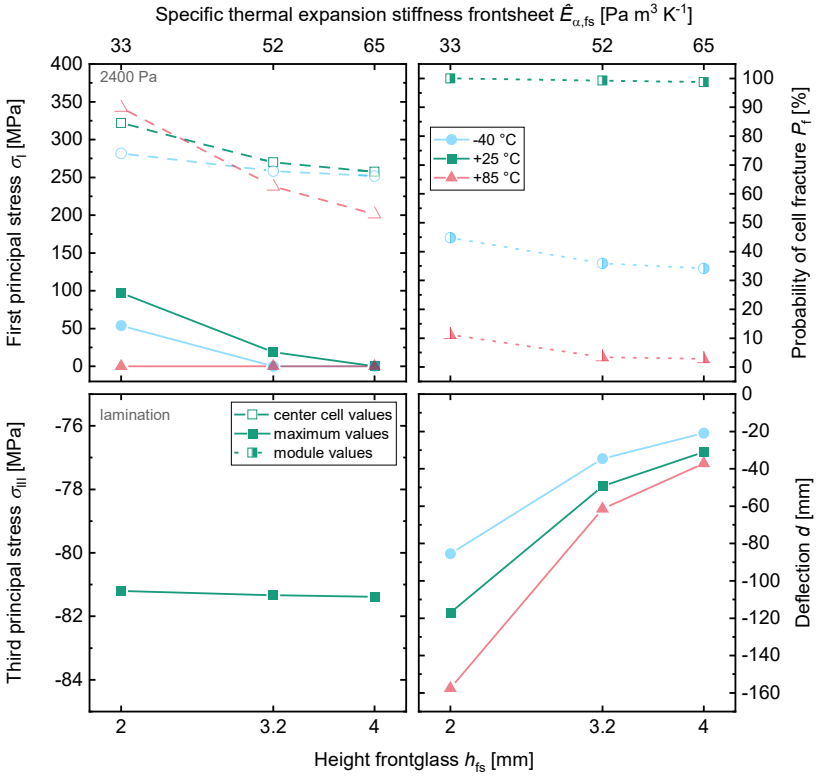


**Figure 4.21:** Results from frontglass height $h_{fs}$ variation at 2400 Pa push load for -40 °C (blue circles), +25 °C (green squares) and +85 °C (red triangles). *Top row: left*: maximum value (open symbols) and value between busbars of the center cell of the first principal stress $\sigma_I$; *right*: corresponding probability of cell fracture; *bottom row: left*: third principal stress $\sigma_{III}$ after lamination; *right*: deflection. Please note, that bottom ordinates depict height $h_{fs}$ and top ordinates the corresponding specific thermal expansion stiffness $\hat{E}_{\alpha,fs}$.

### 4.6.1.2 Material Properties

#### Frontsheet CTE

Due to the CTE-mismatch of front- and backsheet, the laminate has a bow after it is cooled down to ambient temperature after lamination, which increases for larger CTE differences. The investigated values represent different glass types as well as polycarbonate as a glass alternative. If the backsheet CTE (50.4×10$^{-6}$ K$^{-1}$) is larger than the frontsheet CTE ($\alpha_{bs} > \alpha_{fs}$), the laminate curvature is convex,

while a smaller backsheet CTE ($\alpha_{bs} < \alpha_{fs}$) yields a concave curvature, which is depicted in Figure 4.22.

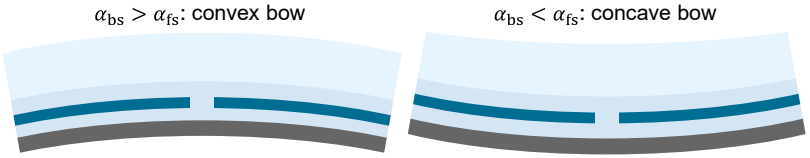


**Figure 4.22:** Sketch of bow after the laminate is cooled down to ambient temperature in lamination induced by the CTE mismatch of front- and backsheet for different CTE ratios.

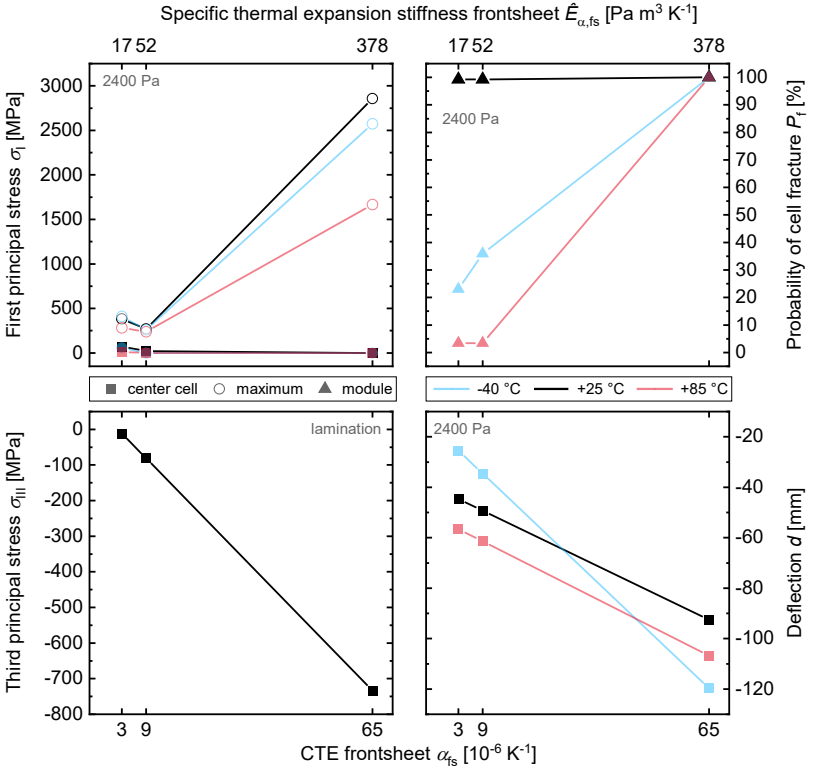


**Figure 4.23:** Results from variation of frontsheet CTE $\alpha_{fs}$ at 2400 Pa push load at -40 °C (blue), +25 °C (black) and +85 °C (red). *Top row: left*: maximum value (open circles) and value between busbars of center cell (filled squares) of the first principal stress $\sigma_I$; *right*: corresponding cell fracture probability (triangles); bottom row: left: third principal stress $\sigma_{III}$ after lamination; *right*: deflection. Please note, bottom ordinates depict CTE $\alpha_{fs}$ and top ordinates the corresponding specific thermal expansion stiffness $\hat{E}_{\alpha,fs}$, both in linear scale.

Since in mechanical load the PV module curvature is also concave, a concave bow after lamination amplifies the deflection $d$ in mechanical load. This is reflected in Figure 4.23 by the much larger deflection $d$ for the CTE of $65\times10^{-6}$ $K^{-1}$. At -40 °C the larger temperature difference further increases the temperature induced concave bow, which amplifies this effect. Accordingly, the -40 °C curve crosses the other temperature curves.

However, the higher deflection does not affect the center cell first principal stress $\sigma_{\mathrm{I}}$ because the magnitude of the third principal stress $\sigma_{\mathrm{III}}$ after lamination also increases for increasing frontsheet CTE $\alpha_{\mathrm{fs}}$. For the lowest CTE ($3\times10^{-6}$ $K^{-1}$), which matches the solar cell CTE of $2.6\times10^{-6}$ $K^{-1}$ well, the third principal stress $\sigma_{\mathrm{III}}$ after lamination is almost negligible. Therefore, in mechanical load a slight first principal stress $\sigma_{\mathrm{I}}$ is observable. Due to the CTE matching of frontsheet and solar cell, the solar cell is almost unaffected by the contraction of the frontsheet and accordingly the backsheet contraction dominates. This is reflected by the direction of the first principal stress $\sigma_{\mathrm{I}}$ depicted in Figure 4.24. After soldering, the principal stress directions are in the cell plane only. After lamination, the orientation changes towards the backsheet for the lowest frontsheet CTE ($3\times10^{-6}$ $K^{-1}$). Increasing the frontsheet CTE to $9\times10^{-6}$ $K^{-1}$, changes the orientation towards the frontsheet. Accordingly, the influence of the frontsheet dominates which leads to a slight decrease of the maximum first principal stress $\sigma_{\mathrm{I,max}}$. Further increasing the frontsheet CTE to $65\times10^{-6}$ $K^{-1}$, the solar cells are further compressed and pushed together. This leads to a bending of the ribbon in the cell gap and a strong local deformation of the solar cell. This together with the strong deflection in mechanical load leads to the strong increase of the maximum first principal stress $\sigma_{\mathrm{I,max}}$ for high frontsheet CTEs.

Due to the high maximum first principal stress $\sigma_{\mathrm{I,max}}$, the cell fracture probability is 100 % for all frontsheet CTE's. Only for -40 °C and 85 °C it decreases for lower CTE's due to the effects explained above in Section 4.5.2.

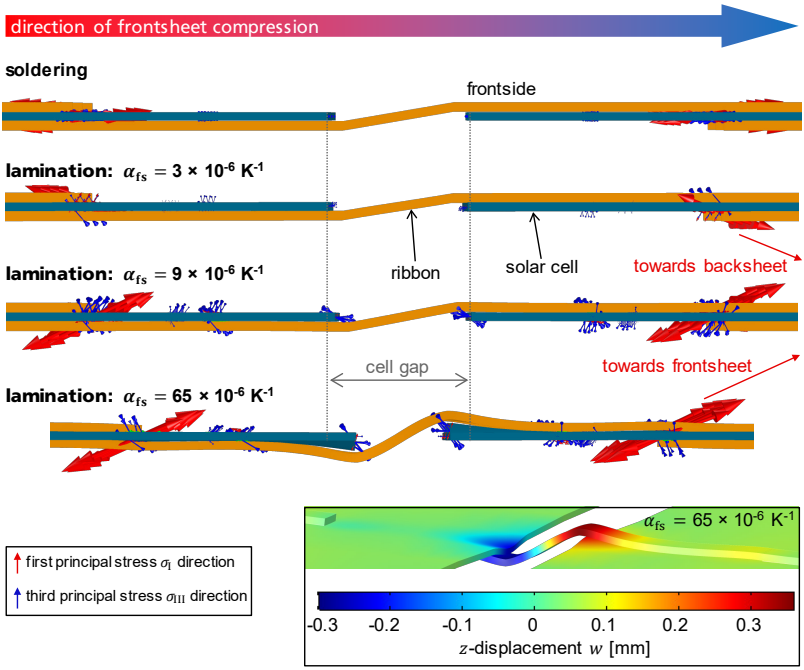


**Figure 4.24**: Direction of the first (red arrows) and third (blue arrows) principal stress after soldering (top) and after lamination for the three different frontsheet CTEs. The length of the arrows is not to scale. Deformation of cell and ribbon is to scale. *Bottom right*: local deformation of solar cell and ribbon in cell gap for the frontsheet CTE of 65×10$^{-6}$ K$^{-1}$.

## Backsheet CTE

The CTE of the backsheet has a very similar influence on the solar cell as the CTE of the frontsheet, but due to the lower height much smaller. Figure 4.25 shows the results for three different CTE's, which cover the range between soda-lime glass and polycarbonate.

The center cell first principal stress $\sigma_I$ decreases for increasing CTE due to the increasing magnitude of the third principal stress $\sigma_{III}$ after lamination. Additionally, the deflection decreases because the opposed convex bow after lamination increases with increasing CTE. As for the frontsheet, the maximum first principal stress $\sigma_{I,max}$ increases with the CTE increase due to the stronger compression after lamination. Finally, the cell fracture probability $P_f$ is 100 % for all CTE's and is only reduced by the change in temperature.

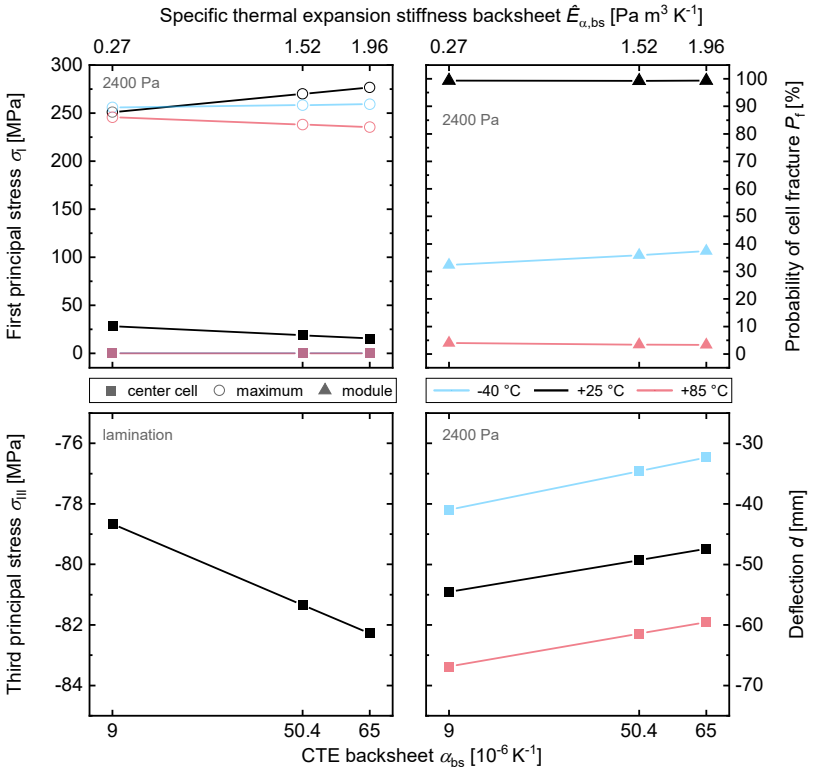


**Figure 4.25:** Results from the variation of backsheet CTE $\alpha_{bs}$ at 2400 Pa push load at -40 °C (blue), +25 °C (black) and +85 °C (red). *Top row: left*: maximum value (open circles) and value between the busbars of the center cell (filled squares) of the first principal stress $\sigma_I$; *right*: corresponding probability of cell fracture (triangles); *bottom row: left*: third principal stress $\sigma_{III}$ after lamination; *right*: deflection. Please note, that the bottom ordinates depict CTE $\alpha_{bs}$ and the top ordinates the corresponding specific thermal expansion stiffness $\hat{E}_{\alpha,bs}$, both in linear scale.

### Backsheet Young's Modulus

Figure 4.26 shows the results of the variation of the backsheet Young's modulus $E_{bs}$. The chosen values cover the range between extremely soft and stiff backsheets.

The magnitude of the third principal stress $\sigma_{III}$ after lamination increases for stiffer backsheets and the mechanical load deflection $d$ decreases due to the stronger convex curvature after lamination and higher bending resistance.

Therefore, the center cell first principal stress $\sigma_{\mathrm{I}}$ decreases with increasing Young's modulus $E_{\mathrm{bs}}$.

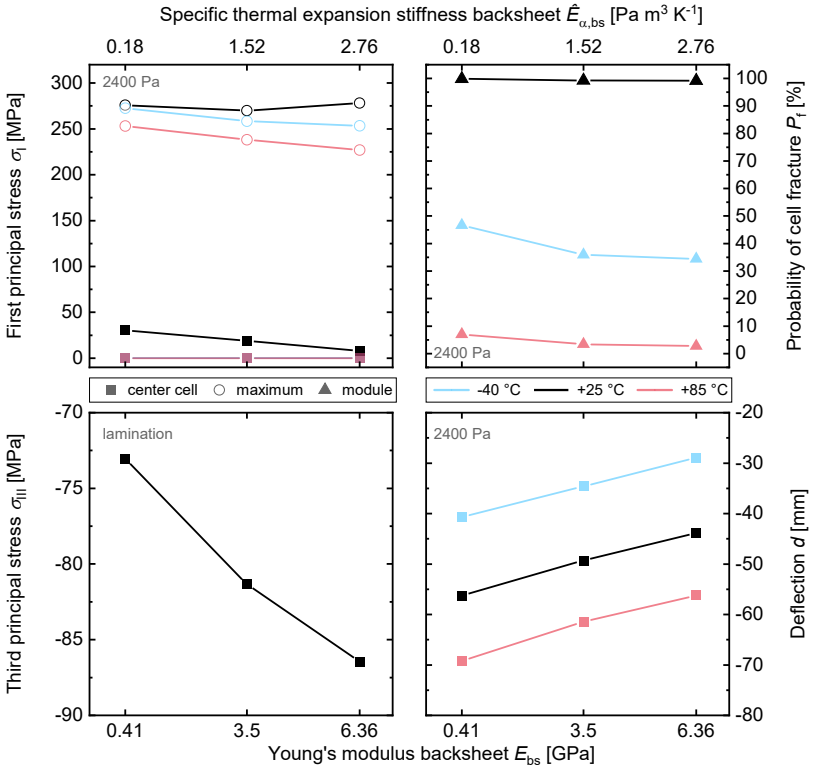


**Figure 4.26:** Results from the variation of backsheet Young's modulus $E_{\mathrm{bs}}$ 2400 Pa push load at -40 °C (blue), +25 °C (black) and +85 °C (red). *Top row: left*: maximum value (open circles) and value between the busbars of the center cell (filled squares) of the first principal stress $\sigma_{\mathrm{I}}$; *right*: corresponding probability of cell fracture (triangles); *bottom row: left*: third principal stress $\sigma_{\mathrm{III}}$ after lamination; *right*: deflection. Please note, that the bottom ordinates depict Young's modulus $E_{\mathrm{bs}}$ and the top ordinates the corresponding specific thermal expansion stiffness $\hat{E}_{\alpha,\mathrm{bs}}$, both in linear scale.

The maximum first principal stress $\sigma_{\mathrm{I,max}}$ shows a similar behavior as in the variation of the frontsheet CTE. For the lowest backsheet Young's modulus $E_{\mathrm{bs}}$ ($\hat{E}_{\alpha,\mathrm{bs}} < \hat{E}_{\alpha,\mathrm{c}} < \hat{E}_{\alpha,\mathrm{r}}$) the maximum first principal stress $\sigma_{\mathrm{I,max}}$ is dominated by the ribbon-solar cell interaction. Increasing the backsheet Young's modulus $E_{\mathrm{bs}}$ to 3.5 GPa increases the impact on the solar cell ($\hat{E}_{\alpha,\mathrm{bs}} \approx \hat{E}_{\alpha,\mathrm{c}} < \hat{E}_{\alpha,\mathrm{r}}$),

which increases the solar cells compression by the backsheet and in turn decreases the relative compression by the ribbon, accordingly the maximum first principal stress $\sigma_{\mathrm{I,max}}$ is slightly reduced. Further increasing the backsheet Young's modulus $E_{\mathrm{bs}}$ ($\hat{E}_{\alpha,\mathrm{bs}} > \hat{E}_{\alpha,\mathrm{c}} < \hat{E}_{\alpha,\mathrm{r}}$) the backsheets contraction amplifies the ribbons contraction, i.e. the maximum first principal stress $\sigma_{\mathrm{I,max}}$ in the solar cell increases again. At +85 °C the coupling of the backsheet to the solar cell and front glass is generally weak, so that the influence of the backsheet is small for all Young's moduli and therefore the stress is mainly influenced by the stronger deflection for softer backsheets.

At -40 °C, the encapsulants specific thermal expansion stiffness $\hat{E}_{\alpha,\mathrm{e}}$ (3.71 Pa m$^3$ K$^{-1}$) is larger than the backsheets ($\hat{E}_{\alpha,\mathrm{e}} > \hat{E}_{\alpha,\mathrm{bs}}$). Accordingly, the backsheet has a minor influence on the solar cell and again the dominating effect is again the deflection.

#### 4.6.1.3 Symmetric Setup

Using a symmetric PV module setup, i.e. having the same front- and backsheet, changes the thermomechanics of the solar cell fundamentally. In a symmetrical setup, the solar cells are in the neutral axis of the laminate, while in a glass-foil setup, the solar cells are in the tensile range at push load. Figure 4.27 shows the variation of the front- and backsheet height (1 mm, 2 mm and 3.2 mm) for two symmetrical setups with soda-lime glass and polycarbonate (PC).

Due to the position of the solar cells in the neutral axis, the first principal stress $\sigma_{\mathrm{I}}$ between the busbars of the center cell is negligible for all heights and both materials. In fact, due to the high magnitude of the third principal stress $\sigma_{\mathrm{III}}$ after lamination, the dominating stress is compressive even at 5400 Pa push load (Appendix C.1, Figure C.6.20). Since the maximum first principal stress $\sigma_{\mathrm{I,max}}$ arises mainly from the interaction of the ribbon with the solar cell, it is non-zero. For soda-lime glass, the value is only slightly dependent on the height, similarly to the third principal stress $\sigma_{\mathrm{III}}$ after lamination. The specific thermal expansion stiffness $\hat{E}_{\alpha}$ is even for 1 mm 10 times higher than the one of the solar cell and three times higher than the one of the ribbon. Therefore, a change from 1 mm to 3.2 mm has only a marginal impact. Whereas the specific thermal expansion stiffness $\hat{E}_{\alpha}$ of polycarbonate at 1 mm is only about twice the value of the solar cell and therefore the height has an influence. The higher specific thermal expansion stiffness $\hat{E}_{\alpha}$ of soda-lime glass compared to polycarbonate originates from the much higher Young's modulus $E$ although the CTE is much smaller, which is also reflected in the much stronger increase of deflection $d$.

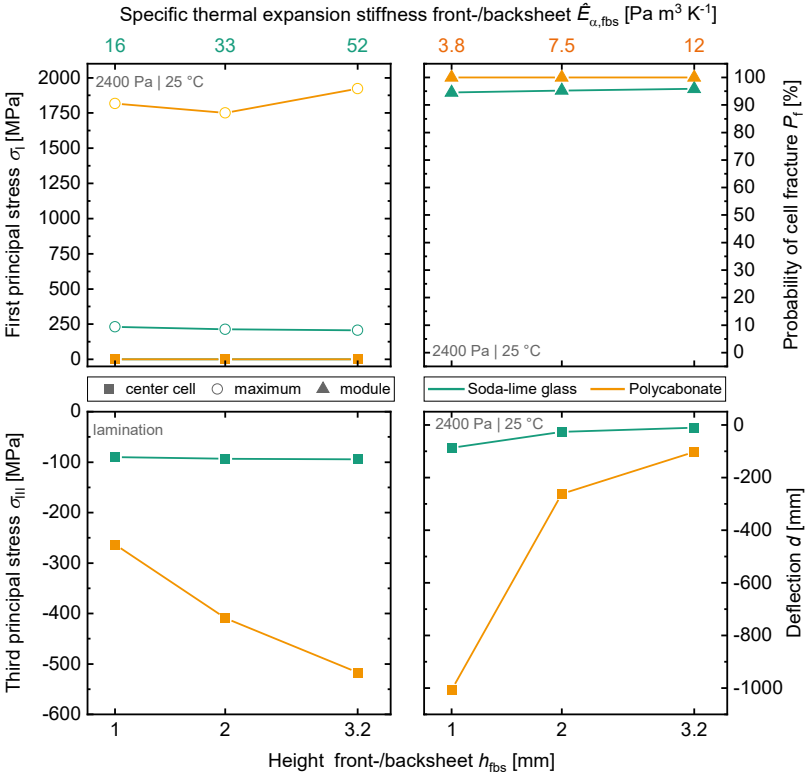


**Figure 4.27:** Results from the variation of front-/backsheet height $h_\mathrm{fbs}$ of a symmetric module setup at 2400 Pa push load at +25 °C for soda-lime glass (green) and polycarbonate (orange). *Top row: left*: maximum value (open) and value between the busbars of the center cell (filled) of the first principal stress $\sigma_\mathrm{I}$; *right*: corresponding probability of cell fracture (triangles); *bottom row: left*: third principal stress $\sigma_\mathrm{III}$ after lamination; *right*: deflection. Please note that for clarity, the results for -40 °C and +85 °C are depicted in separate Figures in Appendix C.1 (Figure C.6.8 and Figure C.6.9). Please note, that the bottom ordinates and the top ordinates the corresponding specific thermal expansion stiffness $\hat{E}_{\alpha,\mathrm{fbs}}$ of glass (left, green) and polycarbonate (right, orange).

At 1 mm, the maximum first principal stress $\sigma_{\mathrm{I,max}}$ is amplified by the huge deflection, accordingly it decreases slightly at 2 mm although the contraction from the back-/frontsheet increases. Please note, that for Polycarbonate, due to its low stiffness, the assumption of geometric linearity overestimates the deflection and stress stronger than for soda-lime glass. For 3.2 mm the deflection decreases further and the dominating effect on the maximum first principal stress $\sigma_{\mathrm{I,max}}$ is the contraction after lamination. Both materials specific thermal expansion

stiffness $\hat{E}_{\alpha}$ values are larger than the ribbons value ($\hat{E}_{\alpha,\mathrm{g}} > \hat{E}_{\alpha,\mathrm{PC}} > \hat{E}_{\alpha,\mathrm{r}}$) but the CTE of soda-lime glass is smaller than the ribbons while the polycarbonates is larger ($\alpha_{\mathrm{g}} < \alpha_{\mathrm{r}} < \alpha_{\mathrm{PC}}$). Therefore, soda-lime glass reduces the ribbons contraction, while polycarbonate increases it. Accordingly, the maximum first principal stress $\sigma_{\mathrm{I,max}}$ for polycarbonate increases, while for soda-lime glass it decreases slightly. For this reason, the maximum first principal stress $\sigma_{\mathrm{I,max}}$ is overall much higher for polycarbonate than for soda-lime glass. Accordingly, the cell fracture probability $P_{\mathrm{f}}$ of soda-lime glass is lower, while for polycarbonate it is 100 % for all heights.

## 4.6.2 Encapsulant

### 4.6.2.1 Young's modulus

The sensitivity study of the encapsulants Young's modulus $E_{\mathrm{e}}$ in Figure 4.29 investigates on one hand the behavior for a fixed Young's modulus with values of EVA's Young's modulus from -40 °C until 150 °C. On the other hand it compares two different encapsulants (EVA and TPO, see Figure 3.13) with a strongly temperature dependent Young's modulus.

Firstly, the fixed Young's moduli are discussed: At 150 °C, EVA is extremely soft with a specific thermal expansion stiffness $\hat{E}_{\alpha,\mathrm{e}}$ for the solar cell area of 0.0006 Pa m$^3$ K$^{-1}$. Accordingly, its capability of strain absorption is high. With increasing Young's modulus, the specific thermal expansion stiffness $\hat{E}_{\alpha,\mathrm{e}}$ increases to 0.03 Pa m$^3$ K$^{-1}$ at +25 °C and becomes 3.7 Pa m$^3$ K$^{-1}$ at -40 °C, which is more than twice the value of the solar cell (1.5 Pa m$^3$ K$^{-1}$). The magnitude of the third principal stress $\sigma_{\mathrm{III}}$ after lamination reflects this by increasing strongly with increasing Young's modulus $E_{\mathrm{e}}$. Similarly, the deflection after mechanical load decreases with increasing Young's modulus $E_{\mathrm{e}}$. The center cell first principal stress $\sigma_{\mathrm{I}}$, which is influenced by these two, should decrease accordingly. However, it first slightly increases and then decreases again. To better understand this behavior, the compressive stress after lamination is neglected as well as the decreasing deflection. For this purpose, the FEM simulation is modified to have the same deflection for all Young's moduli and the lamination stress tensor is not transferred. Figure 4.28, shows the result of this simulation. The largest strain in the encapsulant is shear strain in yz-direction $\tau_{\mathrm{yz}}$, it strongly decreases with increasing Young's modulus $E_{\mathrm{e}}$ of the encapsulant. As the strain decreases, it absorbs less bending strain. Accordingly, the solar cell is exposed to more bending strain and the first principal stress $\sigma_{\mathrm{I}}$ increases in the same manner as the shear

strain $\tau_{yz}$ in the encapsulant decreases. Now, taking the compressive lamination stress and the lower deflection at -40 °C into account, results in a decrease of the first principal stress $\sigma_I$ towards -40 °C and accordingly in the curve in Figure 4.29.

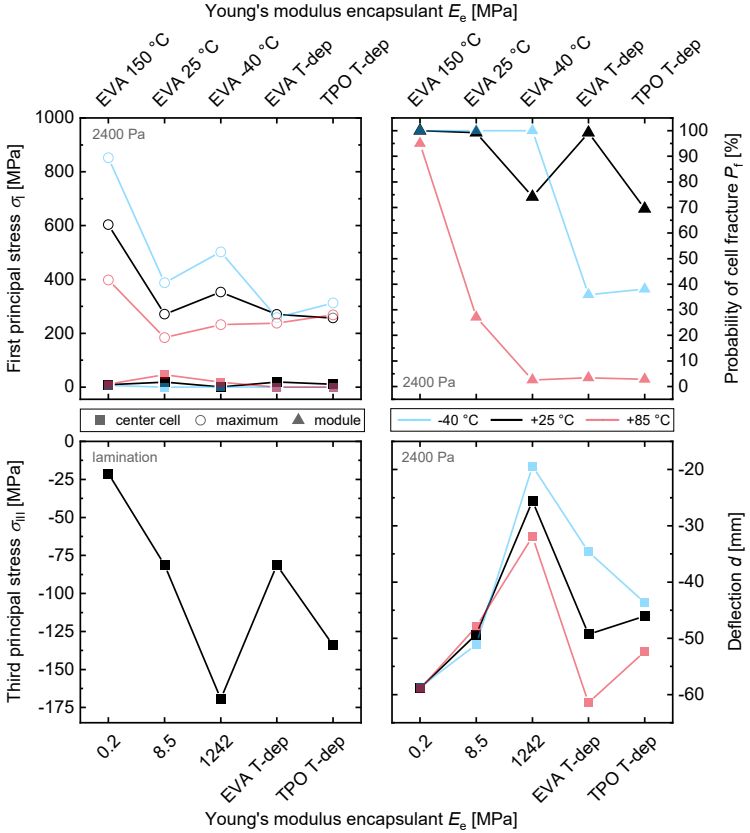


**Figure 4.28:** Results from the variation of encapsulant Young's modulus $E_e$ 2400 Pa push load at -40 °C (blue), +25 °C (black) and +85 °C (red). *Top row: left*: maximum value (open circles) and value between the busbars of the center cell (filled squares) of the first principal stress $\sigma_I$; *right*: corresponding probability of cell fracture (triangles); *bottom row: left*: third principal stress $\sigma_{III}$ after lamination; *right*: deflection.

The strain absorption capability of the encapsulant also dominates the maximum first principal stress $\sigma_{I,max}$: for a low Young's modulus, the solar cell and ribbon contraction is almost uncoupled from the other layers. The larger the encapsulants Young's modulus becomes, the stronger becomes the coupling to the

frontglass, which CTE is about half the CTE of the ribbon and therefore reduces the contraction of the ribbon and accordingly the stress. When the Young's moduls further increases and the encapsulants specific thermal expansion stiffness $\hat{E}_{\alpha,\mathrm{e}}$ surpasses the one of the solar cell and at the same time becomes close to the ribbon value ($\hat{E}_{\alpha,\mathrm{c}} < \hat{E}_{\alpha,\mathrm{e}} \leq \hat{E}_{\alpha,\mathrm{r}}$), both become additionally compressed by the much larger CTE of the encapsulant. Accordingly, the maximum first principal stress $\sigma_{\mathrm{I,max}}$ increases again.

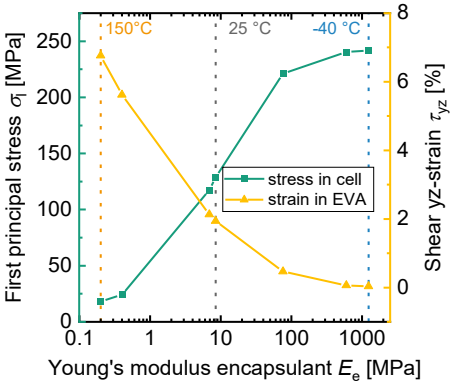


**Figure 4.29**: First principal stress $\sigma_\mathrm{I}$ between the busbars of the center cell (green) and the shear strain in $yz$-direction $\tau_{yz}$ within the EVA (yellow) above the solar cell for different Young's moduli of the encapsulant at mechanical load.

The cell fracture probability $P_\mathrm{f}$ does not follow the maximum first principal stress $\sigma_{\mathrm{I,max}}$, because the stronger compressive stress for higher Young's moduli leads to lower effective area values, which results in the lowest value for the highest Young's modulus.

Finally, the result of the two temperature dependent Young's moduli reflect the results of the fixed values. The higher Young's modulus for temperatures above -25 °C of the TPO (see Figure 3.13) yields a higher compressive stress after lamination and lower tensile stress in mechanical load. This underlines that due to the multiple influences on the thermomechanics, a higher Young's modulus $E_\mathrm{e}$ reduces the cell fracture probability.

#### 4.6.2.2 Height

Figure 4.30 shows the results of the encapsulant height variation between 250 µm and 800 µm. The magnitude of the third principal stress $\sigma_{\mathrm{III}}$ after lamination decreases with increasing encapsulant thickness. Also, the gradient of the

third principal stress $\sigma_{III}$ decreases for thicker encapsulants. This implies that for a very thin encapsulant the encapsulant couples the solar cell strongly to the front- and backsheet and the thicker the encapsulant becomes, the weaker becomes the coupling. The lower compressive stress after lamination of thicker encapsulants is also the reason for the increase of the center cell first principal stress $\sigma_I$ for thicker encapsulants, despite the slight decrease in deflection. The deflection decrease originates from the weaker coupling of the front glass to the backsheet and additionally the laminate becomes thicker and accordingly the bending resistance increases.

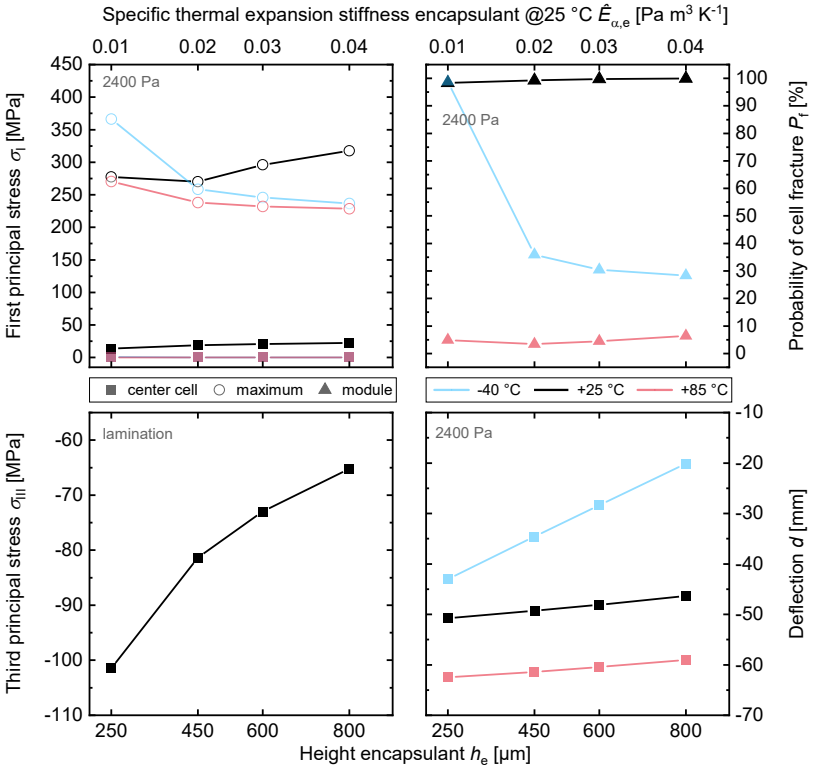


**Figure 4.30:** Results from the variation of encapsulant height $h_e$ 2400 Pa push load at -40 °C (blue), +25 °C (black) and +85 °C (red). *Top row: left*: maximum value (open circles) and value between the busbars of the center cell (filled squares) of the first principal stress $\sigma_I$; *right*: corresponding probability of cell fracture (triangles); *bottom row: left*: third principal stress $\sigma_{III}$ after lamination; *right*: deflection. Please note, that the bottom ordinates depict height $h_e$ and the top ordinates the corresponding specific thermal expansion stiffness $\hat{E}_{\alpha,e}$.

The maximum first principal stress $\sigma_{\mathrm{I,max}}$ shows a different behavior. For 250 µm thick encapsulant, there is only 50 µm encapsulant between the 200 µm thick ribbon and the front-/backsheet. Accordingly, the higher CTE of the backsheet additionally contracts the ribbon which increases the maximum first principal stress $\sigma_{\mathrm{I,max}}$. Contrarily, the frontglass hinders the contraction of the ribbon. For thicker encapsulant, the encapsulant absorbs more strain and so the coupling between the front-/backsheet and the ribbon becomes weaker. Therefore, the maximum first principal stress $\sigma_{\mathrm{I,max}}$ first decreases slightly from 250 µm thickness to 450 µm and then increases again because the ribbon contraction is less influenced by the front-/backsheet.

At -40 °C the encapsulant becomes very stiff which changes the thermomechanics. Firstly, the deflection decreases stronger with increasing encapsulant thickness, because the overall stiffness of the PV module increases. Secondly, the specific thermal expansion stiffness $\hat{E}_{\alpha,\mathrm{e}}$ of the encapsulant increases. At 250 µm height it is with 2.1 Pa m$^3$ K$^{-1}$ slightly higher than the 1.5 Pa m$^3$ K$^{-1}$ of the solar cell. With increasing height of the encapsulant also the specific thermal expansion stiffness $\hat{E}_{\alpha,\mathrm{e}}$ increases and so the impact on the solar cell. Since the CTE of the encapsulant is about 10 times the one of the solar cell, it becomes compressed. This in turn reduces the maximum first principal stress $\sigma_{\mathrm{I,max}}$. Finally, the cell fracture probability $P_{\mathrm{f}}$ follows the trend of the maximum first principal stress $\sigma_{\mathrm{I,max}}$ and decreases strongly at -40 °C. At +25 °C it slightly increases, however since the value is already for 250 µm thick EVA 98 %, the increase is not significant

At 85 °C the encapsulant is very soft for which reason, the coupling of the solar cell and ribbon to the front-/backsheet is only for 250 µm relevant, where the ribbon contraction is amplified by the backsheet contraction. Above the maximum first principal stress $\sigma_{\mathrm{I,max}}$ slightly decreases following the deflection decrease.

### 4.6.3 Solar Cell Height

Figure 4.31 shows the results of the solar cell variation from 80 µm to 180 µm, which increases the specific thermal expansion stiffness $\hat{E}_{\alpha,\mathrm{c}}$ from 0.7 to 1.5 Pa m$^3$ K$^{-1}$. Accordingly, the magnitude of the third principal stress $\sigma_{\mathrm{III}}$ after lamination decreases with increasing height. However, this has a minor effect on the center cell first principal stress $\sigma_{\mathrm{I}}$. Also the deflection decreases just minimally, because of the low specific thermal expansion stiffness $\hat{E}_{\alpha,\mathrm{c}}$ compared to the one

of glass ($\hat{E}_{\alpha,c} \ll \hat{E}_{\alpha,fs}$). The increasing specific thermal expansion stiffness $\hat{E}_{\alpha,c}$ is also the reason for the decrease of the maximum first principal stress $\sigma_{I,max}$, because the impact of the ribbon on the cell becomes lower. Taken with respect to the ribbon joint area, the specific thermal expansion stiffness $\hat{E}_{\alpha,c}$ increases from 0.006 to 0.014 Pa m$^3$ K$^{-1}$, which is about a fourth of the ribbons value of 0.05 Pa m$^3$ K$^{-1}$. This is only partly reflected in the cell fracture probability, which first decreases slightly for 120 µm but then increases again, because of the lower compressive stress after lamination, the tensile stress level is higher and accordingly the effective area as well.

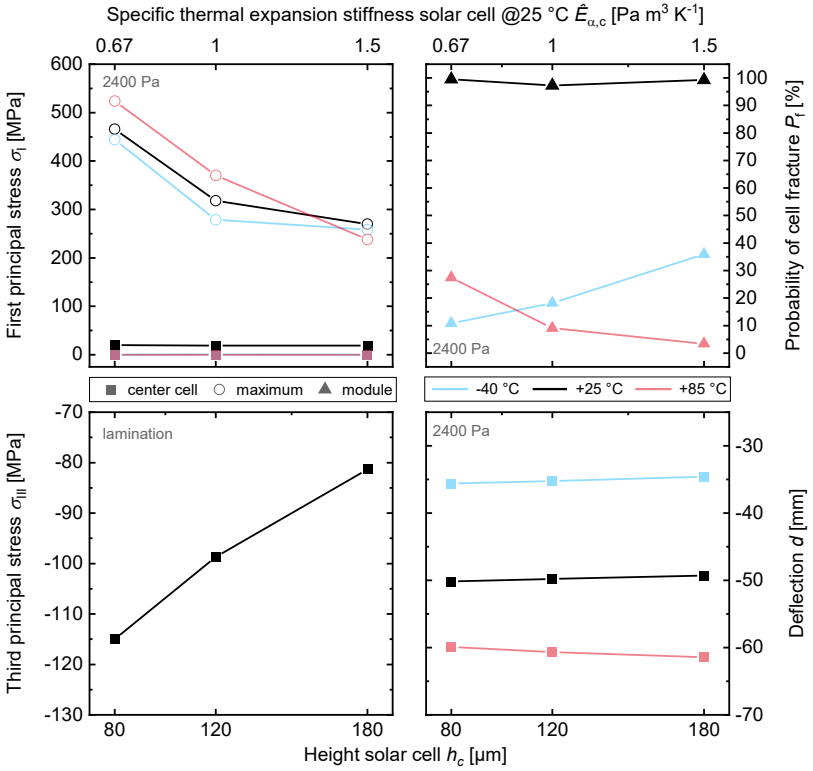


**Figure 4.31:** Results from the variation of solar cell height $h_c$ 2400 Pa push load at -40 °C (blue), +25 °C (black) and +85 °C (red). *Top row: left*: maximum value (open circles) and value between the busbars of the center cell (filled squares) of the first principal stress $\sigma_I$; *right*: corresponding probability of cell fracture (triangles); *bottom row: left*: third principal stress $\sigma_{III}$ after lamination; *right*: deflection. Please note, that the bottom ordinates and the top ordinates the corresponding specific thermal expansion stiffness $\hat{E}_{\alpha,c}$.

### 4.6.4 Mounting Structure

In the performed variation of the frame material, depicted in Figure 4.32, the frame geometry is unchanged and only the material is varied. The strongest influence of the frame material is on the deflection. With steel having the lowest deflection followed by Aluminum and wood, which follows their Young's moduli (see Table 3.9).

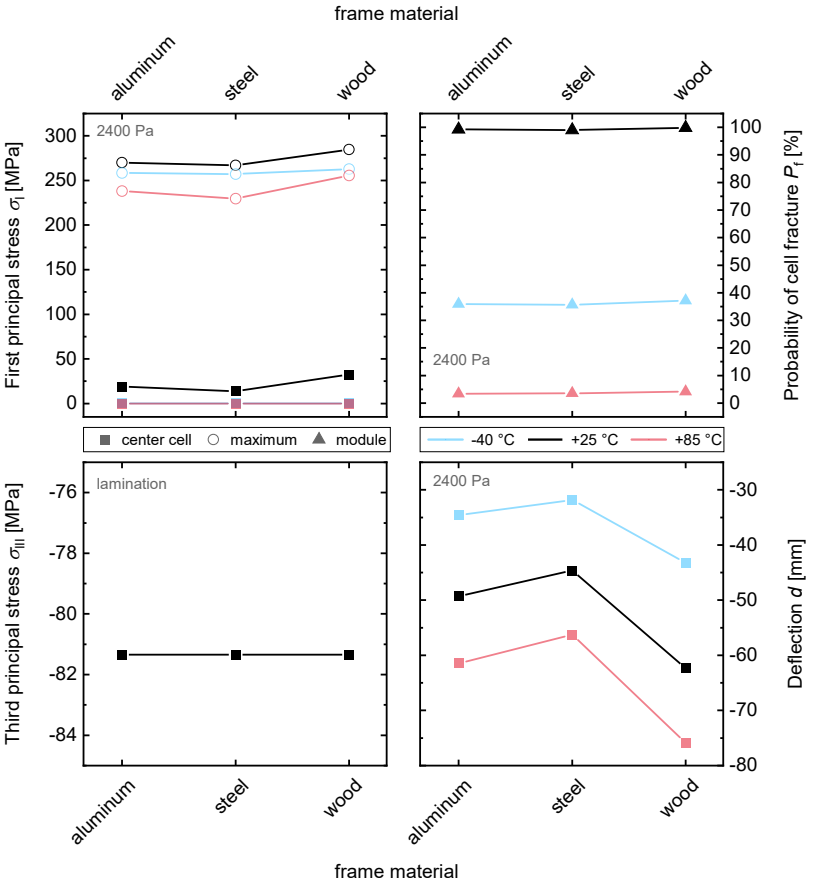


**Figure 4.32:** Results from the variation of frame material 2400 Pa push load at -40 °C (blue), +25 °C (black) and +85 °C (red). *Top row: left*: maximum value (open circles) and value between the busbars of the center cell (filled squares) of the first principal stress $\sigma_I$; *right*: corresponding probability of cell fracture (triangles); *bottom row: left*: third principal stress $\sigma_{III}$ after lamination; *right*: deflection.

Since the third principal stress $\sigma_{\mathrm{III}}$ after lamination is independent of the frame, the center cell first principal stress $\sigma_{\mathrm{I}}$ directly depends on the deflection. With a higher deflection leading to a higher stress and the same for the maximum first principal stress $\sigma_{\mathrm{I,max}}$. However, the impact on the cell fracture probability $P_{\mathrm{f}}$ is minimal and it is almost 100 % for all frames.

## 4.6.5 Module Dimension & Aspect Ratio

Please note, that due to the reasons explained in the Section 3.3.2.4 the metallization and ribbons are neglected in the simulations in this Subsection. This leads to much lower stress and effective area values. Accordingly, the cell fracture probabilities are lower compared to the ones in the sections before and might not reflect the real fracture behavior, which is strongly influenced by the interconnection. The results at 25 °C, which are published in the *IEEE Journal of Photovoltaics* [Bein20b], are shown below. The results at -40 °C and +85 °C are depicted in Figure C.6.10 to Figure C.6.15 in Appendix C.1.

### 4.6.5.1 Number of Cells / Module Size

Figure 4.33 shows the results of the cell number variation from 60 to 140 cells. The magnitude of the third principal stress $\sigma_{\mathrm{III}}$ after lamination for glass-foil modules increases slightly for increasing cell number. The slight dependence of the cell number originates from the increase in module size with the number of added cells times the cell gap.

Due to the CTE mismatch of the front glass and backsheet, glass-foil modules exhibit a small convex bow after lamination (see Figure 4.22), which adds up to the above mentioned stress originating from the compression of the solar cells by the front- and backsheet. Moreover, the bow increases with an increasing module size and hence the stress from the bow. For six strings the difference is very small and hardly visible. For an increasing number of strings, the bow becomes more prominent and hence the difference in the compressive stress becomes more significant.

Since the glass-glass module stack is vertically symmetric, it doesn't exhibit a bow after lamination and hence there is no dependence of the number of cells. However, it shows a higher compressive stress. This higher compressive stress relates to the higher specific thermal expansion stiffness $\hat{E}_{\alpha}$ of glass compared to backsheet. While the glass has a value of 3725 Pa $m^3$ $K^{-1}$, the backsheet has a much lower value of 102 Pa $m^3$ $K^{-1}$.

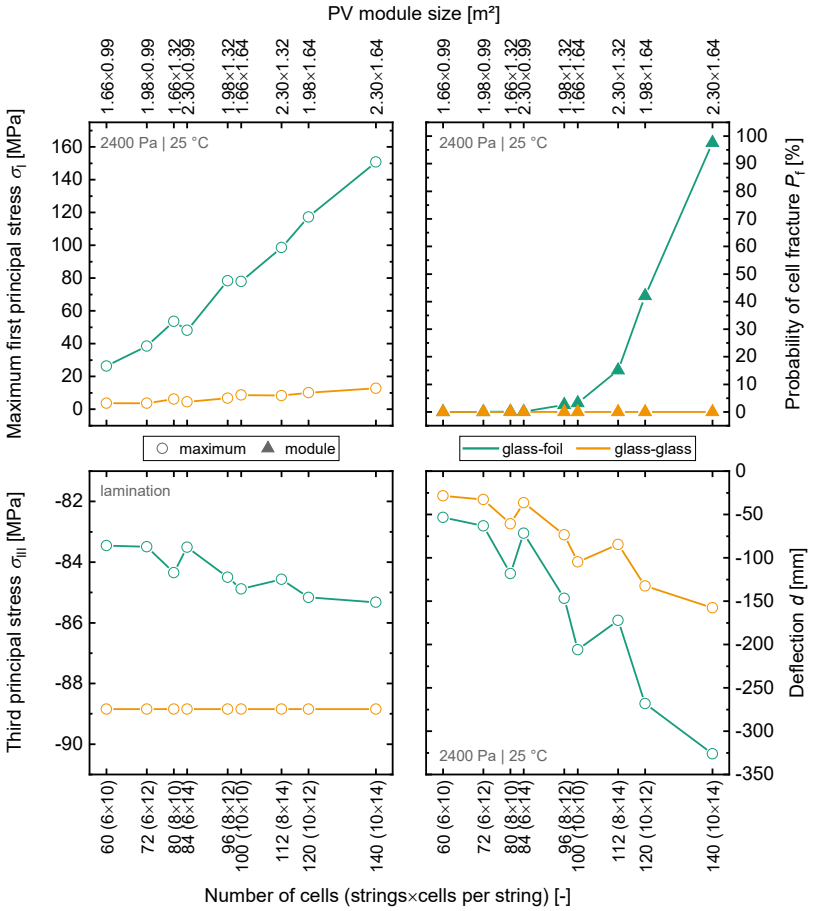


**Figure 4.33:** Results from the variation of the number of cells within a PV module at 2400 Pa push load and 25 °C for glass-foil (green) and glass-glass modules (orange). *Top row: left*: maximum first principal stress $\sigma_I$; *right*: corresponding probability of cell fracture; *bottom row: left*: third principal stress $\sigma_{III}$ after lamination; *right*: deflection. Modified after [Bein20b].

The deflection during mechanical load increases with the module size for both glass-foil and glass-glass modules. As the compressive stress after lamination changes minimally (for glass-glass not significantly), the deflection dominates the first principal stress $\sigma_I$. For glass-foil modules both, the deflection $d$ and the first principal stress $\sigma_I$ increase strongly, which however effects the cell fracture probability only for more than 84 solar cells. Before it is negligible due

to the low first principal stress $\sigma_{\mathrm{I}}$. This shows, that the mounting has to be adapted for modules with a large area. As shown in [Bein16], the chosen mounting structure has a huge influence on the stress in solar cells.

Comparing the different number of strings, e.g. the stress for 80 cells (8 strings with 10 cells) and 84 cells (6 strings with 14 cells) shown in Figure 4.34, shows that adding extra cells to existing strings is thermomechanically more beneficial than adding an extra string. Besides the stronger change of the aspect ratio, the reason is the mounting on the long side of the module. Adding an extra string increases the width of the module without further support, which changes the deflection and curvature. Further, comparing modules with 96 cells (8 strings with 12 cells) to 100 cells (10 strings with 10 cells) as shown in Figure 4.34 reveals, that a quadratic module shape increases the number of cells with high tensile stress. Both have an almost identical maximum first principal stress $\sigma_{\mathrm{I}}$ but the more quadratic module with 100 cells has a higher effective area $A_{\mathrm{eff}}$ and hence a higher cell fracture probability $P_{\mathrm{f}}$.

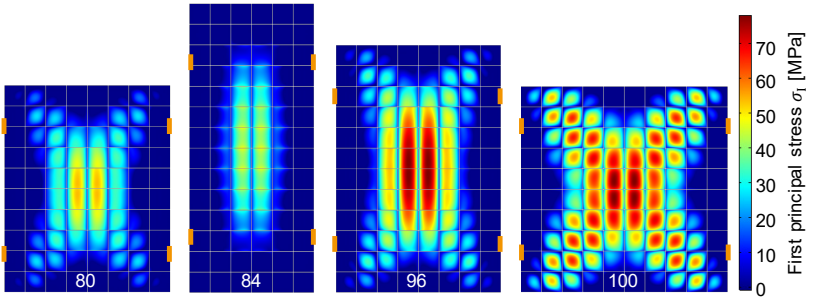


**Figure 4.34**: First principal stress $\sigma_{\mathrm{I}}$ on the backside of the solar cells for modules with a similar number of cells but a different number of strings. The orange rectangle indicates the position of the frame mounting. [Bein20b]

Due to the symmetric setup of glass-glass modules, the solar cells are in the neutral axis [Gabo16]. Accordingly, the dominating stress is the residual compressive stress from lamination and the cell fracture probability $P_{\mathrm{f}}$ is negligible, as is reported before, e.g. [Gabo16], even for the modules with a high number of cells.

#### 4.6.5.2 Cell Size

Figure 4.35 shows the results of the solar cell variation from 156.0 mm to 161.75 mm. The magnitude of the third principal stress $\sigma_{\mathrm{III}}$ after lamination in the glass-foil configuration slightly increases, which originates on the one hand

from the increase of the module size as described above and on the other hand from the larger cell size itself. Since the cell is larger, also the cell compression by the front- and backsheet is larger. The latter also applies to glass-glass modules. Here, the increase is slightly larger due to the higher specific thermal expansion stiffness $\hat{E}_{\alpha,\mathrm{fs}}$ of the glass compared to backsheet.

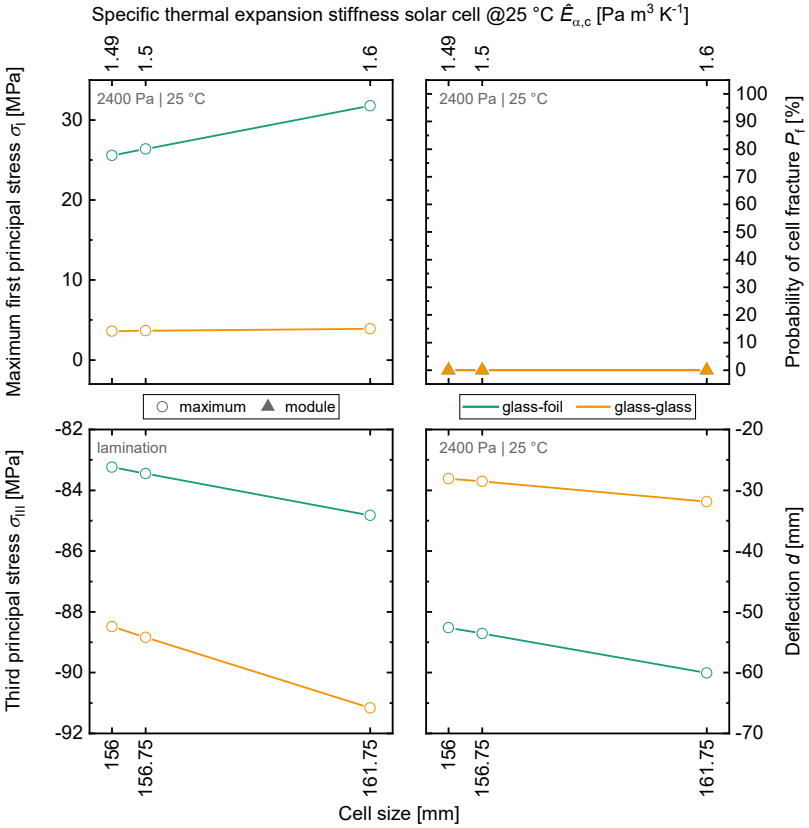


**Figure 4.35**: Results from the variation of cell size at 2400 Pa push load and 25 °C for glass-foil (green) and glass-glass modules (orange). *Top row: left*: maximum first principal stress $\sigma_I$; *right*: corresponding probability of cell fracture; *bottom row: left*: third principal stress $\sigma_{III}$ after lamination; *right*: deflection. Please note, that the bottom ordinates depict cell size and the top ordinates the corresponding specific thermal expansion stiffness $\hat{E}_{\alpha,c}$. Modified after [Bein20b].

With the increase in module size, deflection increases and consequently first principal stress $\sigma_I$. However, for the glass-glass configuration the first principal

stress $\sigma_{\mathrm{I}}$ does not increase significantly, due to the solar cells being in the neutral axis. All stress values correspond to a negligible cell fracture probability $P_{\mathrm{f}}$.

### 4.6.5.3 Cell Format

Figure 4.36 shows the results of the solar cell format variation from full to quarter cells. The magnitude of the third principal stress $\sigma_{\mathrm{III}}$ after lamination in the glass-foil configuration decreases due to the decrease of the cell length, as described above. The same applies to glass-glass modules. Again, due to the higher specific thermal expansion stiffness $\hat{E}_{\alpha}$, the dependence is stronger.

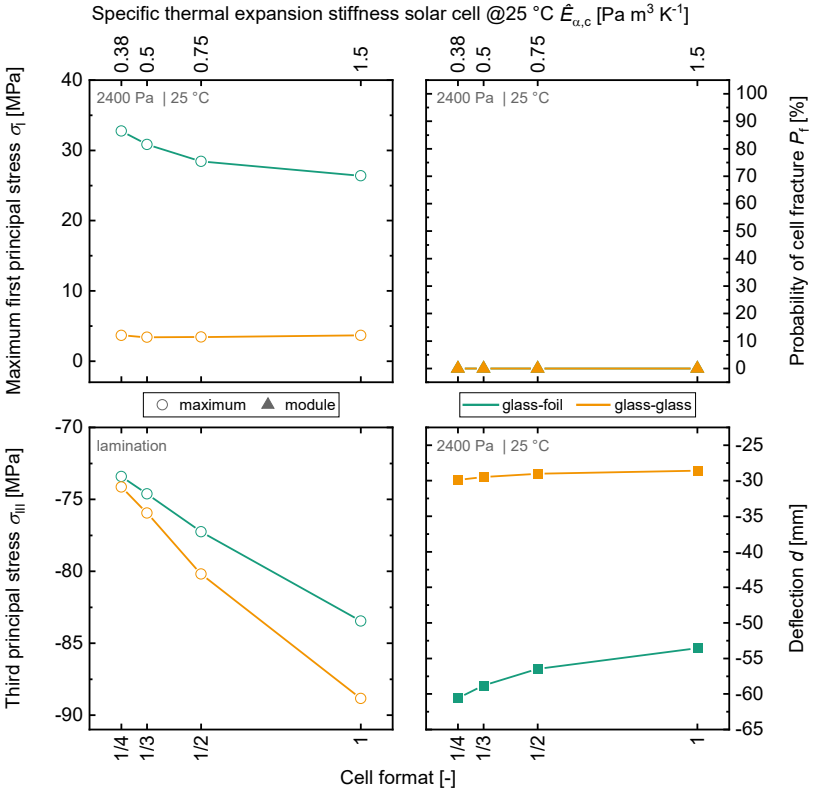


**Figure 4.36**: Results from the variation of cell format at 2400 Pa push load and 25 °C for glass-foil (green) and glass-glass modules (orange). *Top row: left*: maximum first principal stress $\sigma_{\mathrm{I}}$; *right*: corresponding probability of cell fracture; *bottom row: left*: third principal stress $\sigma_{\mathrm{III}}$ after lamination; *right*: deflection. Please note, that the bottom ordinates depict cell format and the top ordinates the corresponding specific thermal expansion stiffness $\hat{E}_{\alpha,c}$. Modified after [Bein20b].

Due to the additional cell gaps, the module size increases for smaller cell formats, accordingly, the deflection in mechanical load increases. This combined with the lower compressive stress after lamination leads to an increase of the first principal stress $\sigma_{\mathrm{I}}$ for smaller cell formats. However, all stress values correspond to negligible cell fracture probabilities $P_{\mathrm{f}}$.

For glass-glass modules the deflection increases less, hence the increase in tensile stress is lower. Therefore, a second effect appears: The solar cell follows the curvature of the PV module. Consequently, a cut solar cell with a shorter length is less bowed by the PV module's deflection. Thus, the tensile stress slightly reduces with decreasing cell format. For glass-glass modules this effect is slightly stronger than the influence of the PV module size, which leads to a very slight decrease of tensile stress.

# 5 Thermomechanical Design Rules

Firstly, the three stress determination methods used within this work are discussed and compared (Section 5.1). Secondly, the influences on the stress within the solar cells are discussed for each different module layer (Section 5.2).

## 5.1 Stress Determination Methods

### 5.1.1 µ-Raman Spectroscopy

For all presented data, the µ-Raman measurements are in good agreement with the FEM simulation and all data could be reproduced. Therefore, the developed measurement procedure with the determined conversion coefficient $\Sigma$, indeed is suitable to measure stress in laminated textured solar cells. In turn, the µ-Raman measurements validate the developed FEM model for a one-cell laminate.

The novelty on the developed measurement procedure compared to the literature is that the procedure is developed to measure on the surface of textured solar cells rather than on the cross-section. Therefore, is takes the surfaces crystal-orientation as well as topology into account. Accordingly, the conversion coefficient $\Sigma$ is also not determined theoretically or on the solar cells' cross-section, as it is done before in the literature, but on its surface. This results in lower a conversion coefficient $\Sigma$ of -(1.19 ± 0.07) rel. $cm^{-1}$/GPa as compared to values measured in the literature between 2…4 rel. $cm^{-1}$/GPa [Luca97, Sara08, Schm10, Wolf96b]. Only one measured value in the same range (1.0 rel. $cm^{-1}$/GPa) [Anas70]) is found in the literature. The obtained value corresponds very well to the 1.21 rel. $cm^{-1}$/GPa value theoretically determined by Ganesan et *al.* [Gane70]. Therefore, it is concluded, that the developed measurement procedure correctly measures the stress within solar cells with textured surfaces.

However, there is still a potential to improve the accuracy of the measurements by actively controlling the sample temperature, hence keeping it constant to avoid a thermal drift. The used temperature correction only captures the thermal drift on distinct locations but not the overall drift. Another impact on the accuracy is the number of Raman spectra measured per stress value. In the point and line scan measurements, 1,000 spectra are taken, while for the area scans only 10 to shorten the measurement time. Comparing the results, it is concluded,

that 10 spectra are sufficient to get a qualitative mapping. However, for an accurate quantitative mapping more spectra are needed, which increases the measurement time significantly. Consequently, then also the thermal drift might increase, hence an active temperature control is essential for stress mappings with a high accuracy.

The advantage of the µ-Raman spectroscopy is that it is contactless, non-destructive and no special sample preparation is needed. Compared to other non-invasive methods this allows a wider use. For example IR photoelasticity used by Wong *et al.* and Zheng *et al.* [Wong97, Zhen02] is limited to IR-transparent materials. X-ray topography used by Meng *et al.* [Meng16, Meng18] is limited to processes involving solar cell bending. X-ray µ-diffraction used by the group of Budiman *et al.* [Budi14, Hand17, Tipp17, Tipp19] requires a synchrotron X-ray source and is limited to measurements through the backsheet due to a limited penetration depth. Like these methods, µ-Raman spectroscopy needs an optical path to the sample. This is not always the case, which limits the application. Another drawback is the strong sensitivity of the Raman peak to factors like temperature and doping concentration of the solar cell. These factors shift the Raman peak in the same order of magnitude as the stress. Hence, they must be known very well and kept constant during a measurement to obtain absolute values. Without knowing these factors, µ-Raman spectroscopy is still capable of measuring stress qualitatively.

In this work, only excitation lasers with 532 nm or lower wavelengths are available. These have a very low penetration depth in Silicon and therefore the surface topology plays an important role. By using an excitation laser with a wavelength higher than about 1200 nm within the near infrared spectrum, higher penetration depths might be achieved which could improve the method further.

### 5.1.2 Solar Cell Integrated Stress Sensor

The presented data show, that a locally highly doped area within a solar cell can be used as a piezoresistive stress sensor. This allows for the first time an in-situ and non-invasive measurement of the stress within a PV module directly in the solar cell without the need of an attached probe. This proof-of-concept can be utilized as a starting point for further development and still many improvements can be done. As an example: the resistance depends on the temperature, even for the high charge carrier concentration of $5\times10^{19}$ $cm^{-3}$ (see appendix A.1). The only way to handle this dependence is by a temperature calibration of the sensor.

In this work, all measurements are done at constant ambient temperature, therefore the temperature dependence can be neglected within this work.

Another improvement to be done is the guard ring, which has not been functional (see appendix A.2), i.e. the stress sensor is sensitive to irradiation. In this work, all measurements are done either in the dark, or indoor at constant artificial illumination. Hence, the sensors resistance is measured before the measurement in unloaded state. Since the stress is calculated from the resistance change the irradiation influence can be neglected. This is the case for the most research applications, which allows the application of the sensors in research and development. Differently is the situation in the field with changing irradiation. Possible strategies to handle the irradiation dependence are either by improving the guard-ring, or by an irradiation calibration. The first one is the preferred method, because it removes the irradiation influence completely and correlations to the temperature calibration are avoided.

The same longitudinal sensitivity $S_\sigma$ of the wafer stripes and the *SenSoCell* shows that the sensor production is reproducible. On the other hand, the *SenSoCell* production has also shown, that the production is challenging, although the sensor itself is relatively simple. The challenge is to keep the positioning precision, which is needed for the small sensor size and the metallization alignment, over the full wafer size. Especially for larger wafer sizes, the current tools available at *Fraunhofer ISE* reach their precision limit. To overcome this, the sensing area could be increased, which might come with a decrease of the accuracy, which has to be investigated.

Overall, the integration of sensing parts into solar cell wafers as well as the integration of *SenSoCells* into PV modules are successful. The sensors resolve the stress within the PV module, which enabled the first validation of a thermomechanical PV module FEM model according to the stress in the solar cell.

### 5.1.3 Finite Element Model

The finite element method allows a much deeper and broader analysis of the thermomechanical effects of the PV module than the experimental methods above do. For example it is possible to resolve the stress within the solar cell in full detail and to determine the full stress tensor rather than only single or mixed components. Also, extensive parameter variations could not be done experimentally. This makes it possible to reveal phenomena, which cannot be explained without FEM simulation. For instance how the stress after lamination compen-

sates the stress in mechanical load (Figure 4.18) can only be fully shown by simulating the mechanical load without initial stress from lamination. Another example is the temperature influence (Section 4.5.2): FEM modelling allows to separately simulate the influence of the changing material properties and the thermal expansion, which is not possible experimentally.

However, as most simulations, FEM simulations come with approximations which might not reflect the real behavior. Therefore, each approximation must be taken with care and, if possible, be verified. The validation experiments (Section 4.3.2) showed, that the used geometric linear approximation has a large deviation to the measurements especially for high loads. A geometric non-linear approach allows a more realistic simulation. However, this approach is associated with a drastic increase in needed memory and even more in computational time. In order to identify the impact of design parameters, however the geometric linear approximation is sufficient. Therefore, the linear approach is chosen in favor for a broader sensitivity study. In consequence, the obtained results overestimate the real values strongly. Accordingly, the obtained absolute values are used to compare one parameter set to another.

The obtained maximum first principal stress $\sigma_{\mathrm{I,max}}$ values are much larger than the first principal stress $\sigma_{\mathrm{I}}$ in the center of the cells and dominate the cell fracture probability $P_{\mathrm{f}}$ in all results. The reason is the singularity around the busbars due to the geometrical shape and the differences in material properties. The investigation of the singularity (Section 4.3.1) showed that the chosen approach - to exclude in the evaluation of the maximum first principal stress $\sigma_{\mathrm{I,max}}$ the stress within 50 µm around the busbar - reduces the stress exaggeration but does not remove the singularity completely. Therefore, the obtained maximum stress $\sigma_{\mathrm{I,max}}$ and accordingly the cell fracture probability $P_{\mathrm{f}}$ represent the non-realistic rectangular busbar and ribbon geometry, which is the upper limit of a realistic geometry with round edges. Nonetheless, within the parameter sensitivity study, the values are comparable and allow relative conclusions about the thermomechanical behavior.

Another approximation, which can have a large influence, is the material model of the encapsulant. Eitner *et al.* [Eitn11a, Eitn11b] showed, that a linear elastic material model does not correctly simulate the cell gap change in a thermal cycling test. However, in this work, the findings of the validation experiments suggest, that the temperature dependent Young's modulus is a good approximation for the mechanical load simulation. However, due to the frame torsion and the resulting deviation at higher loads, this has to be further investigated.

## 5.2 Influences on Stress

The analysis of the simulated stress within the solar cells of the reference PV module configuration reveals that there are two major influences:

1. The mismatch of the thermal expansion when exposed to temperature differences.
2. The curvature of the module and cells when exposed to mechanical loads.

The first one is responsible for the compressive stress of the solar cells after lamination as well as high tensile stress at the end of the ribbon, which dominates the cell fracture probability $P_f$. Both findings are in accordance with findings in the literature, e.g. Either *et al.* found the stress in the solar cells after lamination and subsequent cooling to -40 °C to be compressive [Eitn11a, Eitn11b, Eitn11c]. They have not included ribbons in the FEM model, which is done by Dietrich *et al.* [Diet10], who found the largest tensile stress at the end of the ribbon. However, they do not mention how they handled the singularities occurring at the very same positions. Although measures are taken in this present work, to reduce the influence of the singularities at the busbar and ribbon corners, the stress exaggeration dominated the maximum first principal stress $\sigma_{I,max}$ as shown in Section 4.3. However, it is known, that the regions around the busbar and especially at its end are prone to solar cell cracks [Lai14, Rend19]. Therefore, the amplitude of the stress around the busbar might not reflect the stress quantitatively correct but qualitatively it does. Consequently, the simulated maximum first principal stress $\sigma_{I,max}$ values are overestimated and accordingly the probability of cell fracture as well. Since no other work treating singularities in PV modules were found, this has to be verified by future works.

The second one is responsible that the solar cell in the corner of the PV module with a conventional frame exposed to mechanical load shows tensile stress although the deflection is minimal (see Figure 4.18 and Figure 4.19). For different mounting solutions, like frameless modulus with laminate clamps it could be shown that the highest tensile stress even occurs at the position of the largest curvature instead of the largest deflection [Bein16]. These findings correlate to the findings of Gabor *et al.* [Gabo16].

For both, the material properties play a crucial role. In the following, these influences are discussed in detail for each PV module layer and design rules will be derived, which are also summarized in Section 5.3.

### 5.2.1 Encapsulant

The encapsulant connects the solar cells with the front- and backsheet, which makes it a crucial module component and the thermomechanics of the PV module is strongly influenced by its properties. Since most of the industrial encapsulants have temperature dependent properties, in this work two frequently used encapsulant types with temperature dependent Young's moduli are investigated. The values change in the order of four magnitudes (Figure 3.13) within the temperature range of a PV module. Additionally, the large temperature difference of 190 K from the lamination temperature to -40 °C induces high thermal stresses which overlay with the impact of the changing Young's modulus. Accordingly, the thermomechanics at high and low temperature differ and are discussed separately in the following.

#### Above Room Temperature

High temperatures refer to temperatures around 85 °C, the upper temperature in the thermal cycling test within the IEC 61215 [Inte16] test sequence. Around this temperature, the encapsulants exhibit a low Young's modulus. Therefore, the coupling of the solar cell to the front- and backsheet is relatively weak and the coupling of the solar cell to the ribbon dominates the stress within the solar cell. This arises from the different contraction of the ribbon and the solar cell, which mainly comes from the cooling process after soldering and lamination. At lamination temperature, there is just a low stress level remaining from the soldering process. Just when the encapsulant starts to connect the solar cells to the front- and backsheet the lamination stress starts. From that moment, the maximum stress in the solar cells is a composition of solar cell-ribbon interaction and the solar cell-front-/backsheet interaction. The latter one hinders the first one depending on the strength of the coupling. The strain absorption capacity of the encapsulant is larger for low Young's moduli (Figure 4.28), therefore the coupling is stronger for higher Young's moduli, which results in a lower maximum stress. This coincides with a higher accumulated plastic work within the solder during a TC cycle, simulated by Lindholm *et al.* [Lind20]. If the Young's modulus is too large ($E_{\alpha,\mathrm{e}} \approx E_{\alpha,\mathrm{c}}$), the stress increases again due to the high CTE of the encapsulant in the cell-encapsulant interaction, as shown in Figure 5.1.

So, two points, which reduce the stress in solar cells, can be concluded:

1. A sharp melting point of the encapsulant with a sudden increase of the Young's modulus $E_\mathrm{e}$ below it.

2. The encapsulants specific thermal expansion stiffness $\hat{E}_{\alpha,\mathrm{e}}$ should be between the ribbon $\hat{E}_{\alpha,\mathrm{r}}$ and solar cell $\hat{E}_{\alpha,\mathrm{c}}$ value: $\hat{E}_{\alpha,\mathrm{r}} < \hat{E}_{\alpha,\mathrm{e}} < \hat{E}_{\alpha,\mathrm{c}}$.

These points are an extension of the design rule by Carroll *et al.* [Carr76] recommending thermally soft encapsulant, i.e. encapsulants with a low thermal expansion stiffness $E_\alpha$.

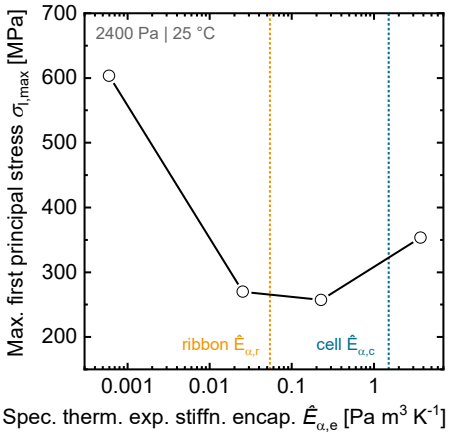


**Figure 5.1:** Maximum first principal stress $\sigma_{\mathrm{I,max}}$ in solar cells at 2400 Pa push load and +25 °C versus the specific thermal expansion stiffness of the encapsulant $\hat{E}_{\alpha,\mathrm{e}}$, the dotted lines indicate the corresponding value of the ribbon (yellow) and solar cell (blue).

### Below Room Temperature

At room temperature, the encapsulant is in a solid state connecting the solar cells to the front- and backsheet. Also, the thermal stress from cooling increases due to the larger temperature difference. Accordingly, the influence of the encapsulant properties increase. When reaching lower temperatures, the thermal stress further increases. At the same time the Young's modulus increases, reducing the deflection in the mechanical load, which correlates with the experimental findings of Mühlhöfer *et al.* [Mülh13]. They found more cracks at low temperatures, which confirms the findings of Mickiewicz *et al.* [Mick11]. Both conclude that the lower strain absorption of the encapsulant is responsible, which is also implied by Figure 4.28. However, the stress temperature dependence in Figure 4.20 shows that also without applied mechanical load, the maximum stress $\sigma_{\mathrm{I,max}}$ increases, so the dominating effect is thermal stress from the solar cell-ribbon interaction. The mechanical load further increases the stress value, which is the reason, why this effect is less critical in thermal cycling without mechanical load.

Another effect, which is only revealed by the FEM simulation: the stress and therefore the crack probability reduces again below -30 °C to values below the ones at room temperature in case of EVA. For the POE the difference is less strong. The reason is the steeper increase of the Young's modulus of EVA at the glass transition temperature. Due to this it keeps its strain absorption capability to lower temperatures and at the same time increases the coupling of the solar cells to the encapsulant and front- and backsheet. The following point can be concluded for stress reduction in solar cells:

3. A sharp glass transition of the encapsulant with a sudden increase of the Young's modulus $E_{\mathrm{e}}$.

The encapsulants height has a similar impact as its Young's modulus. It defines the coupling of the solar cells to the front- and backsheet. If the coupling is too weak, the stress increases, therefore thinner encapsulants are beneficial. However, there is a limit: when there is too little encapsulant between the ribbon and the front- and backsheet. The conclusion is:

4. Thin encapsulants reduce the stress, given that there is sufficient material between the ribbon and the front- and backsheet.

However, this holds only if the stress from the solar cell-ribbon interaction dominates the cell fracture probability. In this work, this stress is overestimated by singularities due to the rectangular busbar and ribbon shape. For lower stress overestimation, other interactions might be relevant, like the displacement of the cells and the corresponding stretching of the ribbon in the cell gap.

### 5.2.2 Front- and Backsheet

In the previous Section, it was shown that the coupling of the solar cell to the front- and backsheet is crucial for the thermomechanics of the PV module. So, the next question rises about the influence of the front- and backsheet.

In the asymmetric glass-foil module design, the glass sheet is mechanically the dominating layer, with by far the highest specific thermal expansion stiffness $\hat{E}_{\alpha,\mathrm{g}}$ (52 Pa m$^3$ K$^{-1}$). Therefore, its properties determine the PV modules deflection in mechanical load. The results revealed that there is a thickness of glass around 3 mm, above which a further increase is less effective.

5. At least one stiff layer is needed with a minimum thickness. For soda-lime glass this is around 3 mm.

The large difference of the specific thermal expansion stiffness $\hat{E}_{\alpha,}$ to the solar cells value of 1.5 Pa $m^3$ $K^{-1}$ is also the reason why the glass' height has almost no influence on the thermal stress in the solar cell. Differently, the frontsheet CTE strongly influences the thermal stress. For CTE values lower than the CTE of the ribbon the thermal stress in the solar cells decreases. Much larger CTE values lead to extremely critical stresses and cell fracture probabilities. To visualize this, the relative specific thermal expansion stiffness $\hat{E}_{\alpha,\mathrm{rel}}$ is introduced. It is the specific thermal expansion stiffness but instead of the CTE the difference of the CTE to the ribbons values is used:

$$\hat{E}_{\alpha,\mathrm{rel}} = E \cdot (\alpha - \alpha_{\mathrm{r}}) \cdot A_{\mathrm{j}} \cdot h \tag{59}$$

Figure 5.2 shows the maximum first principal stress $\sigma_{\mathrm{I,max}}$ in the solar cells versus the relative specific thermal expansion stiffness of the backsheet $\hat{E}_{\alpha,\mathrm{rel,bs}}$ relative to the ribbons CTE ($17 \cdot 10^{-6}$ $K^{-1}$). The backsheet values are chosen instead of the frontsheet values, because more variations are done, which gives a better visualization. The backsheet has the same impact as the frontsheet, even for glass-foil modules the impact is just smaller. This correlates to the findings of Krämer *et al.* [Krae15] that the stress in solder bonds during thermal cycling is higher in glass-glass modules than in glass-foil modules.

However, a CTE larger than the solar cell is beneficial, because the thermal compressive stress after lamination decreases the tensile stress in mechanical load:

6. The CTE of stiff layers (e.g. front- and backsheet) should have a value between the one of the solar cell and the ribbon: $\alpha_{\mathrm{c}} < \alpha < \alpha_{\mathrm{r}}$.

Another effect of the front and backsheet CTE is the direction of the curvature due to thermal strain (Figure 4.22). Since critical high push loads mostly occur due to a heavy accumulation of snow and ice, i.e. at low temperatures, the bow from the thermal strain is opposed to the bow from the snow load and therefore reducing it. Figure 5.2 clearly shows the decrease of the center cell first principal stress $\sigma_{\mathrm{I}}$ with an increasing relative specific thermal expansion stiffness of the backsheet $\hat{E}_{\alpha,\mathrm{rel,bs}}$ relative to the frontsheet CTE:

7. A larger CTE of the backsheet is advantageous with regard to push loads: $\alpha_{\mathrm{bs}} > \alpha_{\mathrm{fs}}$.

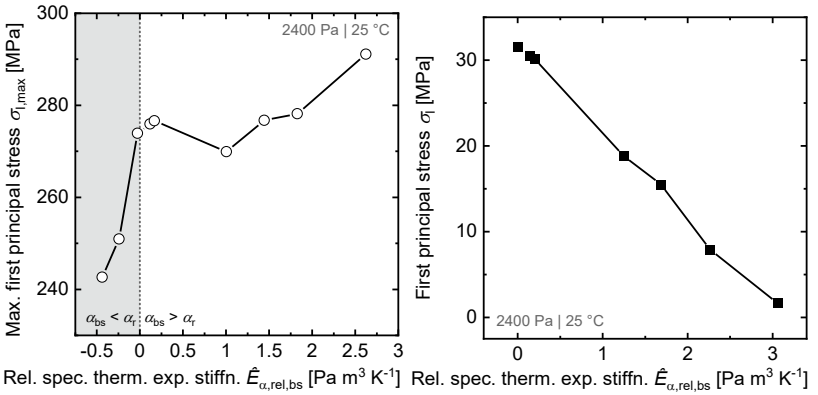


**Figure 5.2:** *Left:* Simulated maximum first principal stress $\sigma_{\mathrm{I,max}}$ in solar cells at 2400 Pa push load and +25 °C versus the relative specific thermal expansion stiffness of the backsheet $\hat{E}_{\alpha,\mathrm{rel,bs}}$ relative to the ribbons CTE. *Right:* Simulated first principal stress $\sigma_{\mathrm{I}}$ between the busbars of the center cell at 2400 Pa push load and +25 °C versus the relative specific thermal expansion stiffness of the backsheet $\hat{E}_{\alpha,\mathrm{rel,bs}}$ relative to the frontsheet CTE.

The results of this work reflect the finding of Gabor *et al.* [Gabo16] that symmetric module designs, e.g. glass-glass modules, are extremely robust against mechanical loads. The reason is that the solar cells are in the neutral axis. Therefore, the dominating stress is thermal stress. As mentioned above, this is larger compared to glass-foil modules. Accordingly, in symmetric designs the material of the front- and backsheet should have a low CTE:

8. Placing the solar cell in the neutral axis, e.g. by a symmetrical module design, for minimal bending stress.
9. Rule 6 is in symmetric module designs more important than for asymmetric designs (glass-foil).

### 5.2.3 Solar Cell

In fact, the possibilities to reduce the stress within the solar cell by modifying it are limited to the size. The material properties are determined by its function as a semiconductor and are predominately the ones of Silicon. However, the size has three different influences.

Firstly, the height. It influences the specific thermal expansion stiffness $\hat{E}_{\alpha,c}$ and hereby the solar cells resistance to external strain. Accordingly, thicker solar cells are exposed to less stress. However, as also shown by Lai *et al.* [Lai13, Lai14], the stress around the ribbon from soldering decreases non-linearly with increasing

cell thickness, while the compressive stress from lamination decreases almost linearly. Since the compressive stress compensates tensile stresses during mechanical load, the cell fracture probability has a minimum around 120 µm cell thicknesses. However, since this minimum strongly depends on the other module materials and especially the ribbons, it is different for each module design.

10. Thicker solar cells are exposed to less stress.

Secondly, the solar cell area. Increasing the solar cell area without adapting the frame, leads to stronger deflection and accordingly higher stresses in the solar cells. Additionally, a string of small solar cells can follow the inhomogeneous frontglass curvature (Figure 4.12 and Figure 4.13) better than a string of large solar cells. To illustrate this, a string of solar cells is compared with a bicycle chain: a solar cell corresponds to a chain element and the interconnectors in the cell gap to the flexible interconnection by pin and roller. Such as the bicycle chains with smaller elements can follow steeper socket curvatures, smaller solar cells can follow steeper inhomogeneous frontglass curvatures. Accordingly, smaller solar cells have a smaller curvature, hence less stress, at the same frontglass curvature.

11. Smaller solar cell edge length decreases stress.

Thirdly, the size effect. The defects in solar cells are statistically distributed [Möll05], i.e. the probability for critical defects increases with the solar cell area. Accordingly, the cell fracture probability increases with increasing solar cell area.

Concluding the size effects, a simple way to reduce the stress and the solar cell fracture probability is to split the solar cells into smaller cells, for example half or third cells, and align the shorter side of the solar cells along the higher curvature. To demonstrate this effect, the FEM simulations of the cell format (Section 4.6.5.3) is extended to simulate half-cells which are oriented with the long edge parallel to the long PV module edge. The resulting first principal stress $\sigma_{\mathrm{I}}$ is compared to half-cells with the long edge along the short PV module edge and full cells as shown in Figure 5.3. While the first principal stress $\sigma_{\mathrm{I}}$ in the mechanical load slightly increases (due to the smaller compressive stress after lamination), when going from full-cells to half-cells, it strongly decreases when aligning the half-cells along the short side of the PV module. Accordingly, the cell fracture probability $P_{\mathrm{f}}$ with the Weibull parameters for full-cells also strongly decreases from 78 % to 3 % at 5400 Pa push load. A similar behavior is observed by Podlowski *et al.* [Podl20] in Mechanical Load Tests on different PV modules with shingled solar cells. Modules with strings aligned along the short side of the PV

module showed much less or no cracks compared to strings aligned along the long side. However, the cell splitting process might induce additional flaws to the splitting edge depending on the technology used [Kaul18]. Kaule *et al.* claim that the thermal laser separation does not influence the fracture probability, therefore this one is recommended for cell splitting.

12. Cut cells: Alignment of the shorter side along the higher curvature reduces stress.

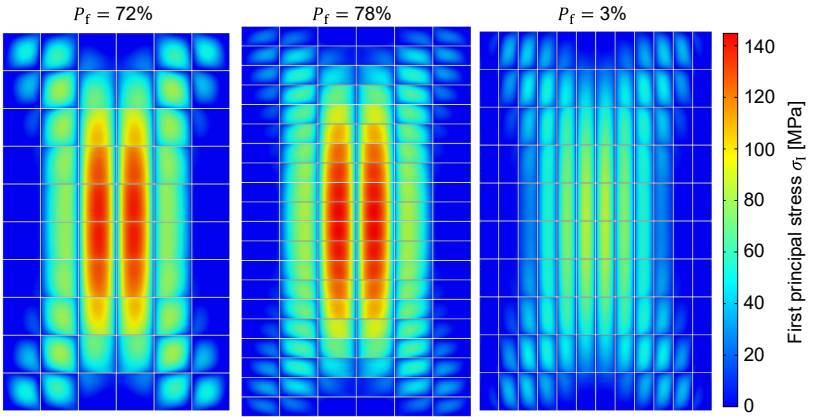


**Figure 5.3**: First principal stress on the back side of the solar cells at 5400 Pa push load with the corresponding cell fracture probability $P_f$ with the Weibull parameters for full-cells. *Left*: full-cells; *Center*: half-cells aligned along the long side of the module*; right*: half-cells aligned along the short side.

### 5.2.4 Mounting Structure and Module Dimension

For glass-foil modules, the frame is an essential module component for the rigidity of the PV module. The shape and dimensions have a crucial role in the deflection and curvature [Gabo16, Schi14, Tumm22]. The results of this work show, that the frames dimension and shape have to be adapted for different materials.

13. The higher the frames stiffness, the better.

Accordingly, it is essential to include the frame as a geometrical component in the FEM simulation rather than as boundary condition as it is a common practice in the literature. For example Dietrich *et al.* used a line mounting [Diet12], and Krämer, Wiese *et al.* [Krae13, Krae15] as well as Li *et al.* [Li19] made the assumption of an ideally stiff frame by placing fixed constraints on the module edges along the entire thickness.

The results of this work show that the frame has to be adapted to larger module areas and aspect ratios. The deflection of the PV module is not constrained in order to study the influence of the module design solely. However, module manufacturers often recommended the use of a rail below the module for high loads. Such a rail limits the deflection to the height of the lower part of the frame and therefore the stress in the solar cells. Other options to reduce the deflections are additional or different mounting positions of the frame to the rack.

14. Smaller module area decreases stress.
15. Frame design has to be adapted to specific module design.

The results also showed that the aspect ratio of the PV in module strongly influences the deflection and hence the stress in the solar cells. Assuming, that due to practical reasons, the mounting of the module takes place only along one side, long modules lead to lower stresses compared to wide modules with a similar number of solar cells, i.e. power.

16. Module aspect ratio: longer modules instead of wider modules (for mounting on long side and non-extreme ratios).

## 5.3 Thermomechanical Design Rules

This Section gathers the thermomechanical design rules derived in Section 5.2. The design rules are clustered according to the respective component. The aim of the design rules is to give a compact overview of the influences on the stress within the solar cells and the PV modules cell fracture probability. Other aspects of the PV module design, such as power efficiency, cost and aesthetics may have opposite requirements. However, this is out of the scope of this work.

The aim of this work is to derive general thermomechanical design rules, with a focus of conventional ribbon interconnected solar cells. Most of the rules are also applicable to other solar cell technologies, such as back-contact or shingle solar cells. However, some rules are very specific to the solar cell and interconnection technology and have to be adapted in future works.

**Table 5.1:** Summary of the derived Thermomechanical design rules clustered by component. The magnitude of the influence on the stress within the solar cells is given in the last column, with increasing magnitude from + to +++.

| Component | Design Rule | Influence |
|---|---|---|
| **Encapsulant** | Sharp melting point with a sudden increase of the Young's modulus $E_\mathrm{e}$ below. | + |
| | The encapsulants specific thermal expansion stiffness $\hat{E}_{\alpha,\mathrm{e}}$ should be between the ribbon $\hat{E}_{\alpha,\mathrm{r}}$ and solar cell $\hat{E}_{\alpha,\mathrm{c}}$ value: $\hat{E}_{\alpha,\mathrm{r}} < \hat{E}_{\alpha,\mathrm{e}} < \hat{E}_{\alpha,\mathrm{c}}$. | ++ |
| | Sharp glass transition with a sudden increase of the Young's modulus $E_\mathrm{e}$. | + |
| | Low thickness, given that there is sufficient material between ribbon and front- and backsheet and that the critical stress originates from the solar cell-ribbon interaction. | + |
| **Front/Back Cover** | At least one stiff layer is needed with a minimum thickness. For soda-lime glass around 3 mm. | ++ |
| | The CTE of stiff layers should have a value between the one of the solar cell and ribbon: $\alpha_\mathrm{c} < \alpha < \alpha_\mathrm{r}$. In symmetric module designs more critical. | +++ |
| | A larger CTE of the backsheet is advantageous for push loads: $\alpha_\mathrm{bs} > \alpha_\mathrm{fs}$. | + |
| | For minimal bending stress: Place the solar cells in the neutral axis, e.g. by a symmetrical module design. | ++ |
| **Solar Cells** | High solar cell thickness. | ++ |
| | Small solar cell edge length. | + |
| | Cut cells: Alignment of the shorter side along the higher curvature. | + |
| **PV Module Size** | Smaller module area decreases stress. | + |
| | Module aspect ratio: longer modules instead of wider modules (for mounting on long side and non-extreme ratios). | + |
| **Frame** | The higher the frames stiffness, the better. | + |
| | Frame design has to be adapted to specific module design. | + |

# 6 Summary and Outlook

There are many and often entangled influences on stress within solar cells, which are summarized in the derived 15 Thermomechanical Design Rules. Additionally, three factors are introduced to characterize PV module materials easily and straightforwardly according to their influence on the thermomechanics.

1. Thermal expansion stiffness $E_\alpha = E \cdot \alpha$ , the product of the Young's modulus $E$ and the coefficient of thermal expansion $\alpha$, first introduced by Carroll et al. [Carr76] but somehow not used since then. It is a measure of how much thermal strain a material can induce.
2. Volumetric thermal expansion stiffness $\bar{E}_\alpha = E_\alpha \cdot V$, which takes the different volume $V$ of the PV module materials into account.
3. Specific thermal expansion stiffness $\hat{E}_\alpha = E_\alpha \cdot A_\mathrm{j} \cdot h$, which takes the joining surface $A_\mathrm{j}$ and the height $h$ of two joined materials into account. It is a measure of how much thermal strain one joining material can induce in the other.

The design rules are derived from a comprehensive parameter sensitivity study using a manifold approach: FEM simulations complemented by two different experimental methods, µ-Raman spectroscopy and solar cell integrated sensors. Both methods are developed within this work. The FEM simulations enabled a wide and in-depth analysis of the PV modules thermomechanics by parameter variations, while the experimental methods validate the FEM simulations. The developed FEM model covers the PV modules geometry in great detail, from the busbar metallization until the frame. The analysis of the parameter sensitivity study results show that some phenomena are only revealed by this multi-scale approach. One example is that the higher stress at temperatures below 0 °C is mainly due to the thermal stress from the solar cell-ribbon interaction, which is amplified by the lower strain absorption capability of the encapsulant as it is assumed by the literature [Mick11, Mülh13].

## 6.1 µ-Raman Spectroscopy

Confocal µ-Raman spectroscopy is successfully applied to measure the stress of laminated solar cells. The new method extends the existing procedures by taking the topology of textured solar cells into account. The texture pyramids cause an inhomogeneous stress distribution on their flanks. Additionally, the different

crystal planes of stress propagation and light scattering influence the Raman signal. The presented results indicate that the procedure covers both influences and is capable of providing a conversion factor $\Sigma$ = -(1.19 ± 0.07) rel. cm$^{-1}$/GPa, which holds for uniaxial and biaxial stress states, as well as the stress originating from the PV module production.

The developed procedure measures the thermomechanical stress in the PV laminate production processes soldering and lamination. The measured stress values are in good accordance with the stress simulated by a FEM model. The simulated stress after lamination agrees within the measurement uncertainty with the measured value. Furthermore, the µ-Raman spectroscopy is capable of measuring stress mappings and hence resolving the stress in great detail, depending on the chosen resolution.

As a further improvement, an active temperature control of the samples is proposed to avoid a temperature-induced shift of the Raman peak. Also, a Raman excitation laser, with a higher penetration depth would decrease the measurement noise.

## 6.2 Solar Cell Integrated Stress Sensor

A new approach for the measurement of stress in laminated solar cells has been developed: a silicon solar cell integrated stress sensor. The advantage of a solar cell integrated sensor is that the stress is measured directly in the solar cell by the solar cell itself.

The sensor is manufactured using only silicon solar cell production processes and utilizes the piezoresistance effect of silicon by high local doping. The sensing part consists of a highly n-doped area. Six different designs with varying aspect ratio $a$ and charge carrier density $N$ are compared. All designs resolve the stress in the test specimens and have sensitivities in the range between -45 %/GPa and -65 %/GPa. The lowest scattering is achieved for the design with $a$ = 10/1, $N = 5 \times 10^{19}$ cm$^{-3}$, which has a sensitivity of (-47.41 ± 0.14) %/GPa.

The concept is successfully transferred on a solar cell wafer which are integrated into a PV module. The in-situ stress measurement during a Mechanical Load Test shows that the sensors are capable of resolving the stress within en-

capsulated solar cells. At the same time the results are the first direct stress measurements of encapsulated solar cells without an external probe and, therefore, the first validation of a thermomechanical FEM simulation according to stress.

Further investigations are needed on the guard-ring, which has not been functional as intended. Within this work, this could be compensated by performing all measurements at constant illumination. However, generally the radiation might change during measurements, especially when applied for in-situ measurements in the field. For such an application also a wireless data transmission and a self-powering approach has to be developed in the future.

For the concept of solar cell integrated sensors a patent is submitted, which is currently pending [Bein18].

## 6.3 FEM Simulation

A three-dimensional thermomechanical FEM model has been developed, which covers the PV module in great detail from busbar to frame. The findings of this work show that in the Mechanical Load Test interconnection and frame have a crucial role on the stress within the solar cells. The busbar and ribbon determine the residual stress after soldering, which show tensile stress at the end of the busbar. Due to their geometry, they are prone to singularities, which overestimate the stress locally. These singularities are investigated thoroughly, with the result that stress within 50 µm around the busbar is not evaluated within this work. However, the obtained stress values are still overestimated also due to the used geometric linear approximation, which is revealed in the validation experiments. In these experiments it is found that the frame parts rotate and translate relative to each other due to the tolerance of the corner connector and presumably plastic deformation of it. This leads to a larger deflection and accordingly larger stress in the solar cells, which could be shown by additionally support the frame corners. Here, the geometric non-linear simulation of the FEM model is in good accordance with the measurements by deviating less than 2.2 mm (7 %) in the deflection, which validates the FEM model. However, the geometric non-linear simulation increases the computational resources immensely. Therefore, the geometric linear approximation is used for the parameter sensitivity study to allow for a systematic parametric study of the PV module thermomechanics.

It is shown that the ribbons play a crucial role in the PV modules thermomechanics. The FEM model will be further improved by splitting the different scales

of the PV module geometry and modelling the ribbons in a sub-model. This allows a much more detailed modelling, such as rounded corners and non-linear material models. Also, the computational effort might decrease by splitting the scales, which in turn allows a geometric non-linear analysis.

The FEM model can be further improved by a more detailed description of the soldering and lamination process. In this work, the cooling down process is simulated for both linear elastically. By implementing a time-dependent study and non-linear material models more realistic process simulations could be achieved. Additionally, the lamination process could be extended by inhomogeneous temperature distributions as well as the applied pressure by the laminator.

Lastly, in this work the residual stress from the solar cell production, like metallization process is not considered at all. Therefore, extending the FEM simulation by the metallization process would improve the results to more realistic values. To obtain reasonable results, exact material models of the used metallization paste play a crucial role.

# Literature


[Alam09] M. O. Alam, H. Lu, C. Bailey and Y. C. Chan, **Finite-Element Simulation of Stress Intensity Factors in Solder Joint Intermetallic Compounds**, *IEEE Transactions on Device and Materials Reliability*, vol. 9, no. 1, pp. 40–48, 2009, 10.1109/TDMR.2008.2010595.

[Anas70] E. Anastassakis, A. Pinczuk, E. Burstein, F. H. Pollak and M. Cardona, **Effect of static uniaxial stress on the Raman spectrum of silicon**, *Solid State Communications*, vol. 8, no. 2, pp. 133–138, 1970, 10.1016/0038-1098(70)90588-0.

[Aßmu17a] M. Aßmus, S. Bergmann, J. Eisenträger, K. Naumenko and H. Altenbach, **Consideration of Non-uniform and Non-orthogonal Mechanical Loads for Structural Analysis of Photovoltaic Composite Structures**, in *STRUCTMAT, vol. 46, Mechanics for materials and technologies*, H. Altenbach *et al,* Basel, Switzerland: Springer International Publishing, 2017, pp. 73–122, 10.1007/978-3-319-56050-2_4.

[Aßmu17b] M. Aßmus, S. Bergmann, K. Naumenko and H. Altenbach, **Mechanical behaviour of photovoltaic composite structures: A parameter study on the influence of geometric dimensions and material properties under static loading**, *Composites Communications*, vol. 5, pp. 23–26, 2017, 10.1016/j.coco.2017.06.003.

[Bagd03] J. Bagdahn, W. N. Sharpe and O. Jadaan, **Fracture strength of polysilicon at stress concentrations**, *Journal of Microelectromechanical Systems*, vol. 12, no. 3, pp. 302–312, 2003, 10.1109/JMEMS.2003.814130.

[Barl09] A. A. Barlian, W.-T. Park, J. R. Mallon, A. J. Rastegar and B. L. Pruitt, **Review: Semiconductor Piezoresistance for Microsystems**, *Proceedings of the IEEE*, vol. 97, no. 3, pp. 513–552, 2009, 10.1109/JPROC.2009.2013612.

[Barr14] J. Barredo, V. Parra, I. Guerrero, A. Fraile and L. Hermanns, **On the mechanical strength of monocrystalline, multicrystalline and quasi-monocrystalline silicon wafers: a four-line bending test study**, *Progress in Photovoltaics: Research and Applications*, vol. 22, no. 12, pp. 1204–1212, 2014, 10.1002/pip.2372.

[Beck15] F. Becker, M. Kuhl, Y. Manoli and O. Paul, **Novel method to operate piezo-FET-based stress sensor offers tenfold increase in sensitivity**, in *Proceedings of the IEEE Sensors 2015,* Busan, South Korea, 2015, pp. 1–4, 10.1109/ICSENS.2015.7370482.

[Beck07] M. Becker, H. Scheel, S. Christiansen and H. P. Strunk, **Grain orientation, texture, and internal stress optically evaluated by micro-Raman spectroscopy**, *Journal of Applied Physics*, vol. 101, no. 6, p. 63531, 2007, 10.1063/1.2434961.

[Bein16] A. J. Beinert, M. Ebert, U. Eitner and J. Aktaa, **Influence of photovoltaic module mounting systems on the thermo-mechanical stresses in solar cells by FEM modelling**, in *Proceedings of the 32nd European Photovoltaic Solar Energy Conference and Exhibition (EU PVSEC),* Munich, Germany, 2016, pp. 1833–1836, 10.4229/EUPVSEC20162016-5BV.1.14.

[Bein18] A. J. Beinert and U. Eitner, Fraunhofer-Gesellschaft zur Förderung der angewandten Forschung e.V, **Solarzelle und Photovoltaikmodul**, Germany, DE102018206155A1, 2019.

[Bein19] A. J. Beinert, A. Büchler, P. Romer, V. Haueisen, L. C. Rendler, M. C. Schubert, M. Heinrich, J. Aktaa and U. Eitner, **Enabling the measurement of thermomechanical stress in solar cells and PV modules by confocal micro-Raman spectroscopy**, *Solar Energy Materials and Solar Cells*, vol. 193, pp. 351–360, 2019, 10.1016/j.solmat.2019.01.028.

[Bein20a] A. J. Beinert, M. Imm, J. Benick, F. Becker, S. Seitz, M. Heinrich, O. Paul, S. W. Glunz, J. Aktaa, U. Eitner and H. Neuhaus, **Silicon solar cell-integrated stress and temperature sensors for photovoltaic modules**, *Progress in Photovoltaics: Research and Applications*, vol. 28, no. 7, pp. 717–724, 2020, 10.1002/pip.3263.

[Bein20b] A. J. Beinert, P. Romer, M. Heinrich, M. Mittag, J. Aktaa and H. Neuhaus, **The Effect of Cell and Module Dimensions on Thermomechanical Stress in PV Modules**, *IEEE Journal of Photovoltaics*, vol. 10, no. 1, pp. 70–77, 2020, 10.1109/JPHOTOV.2019.2949875.

[Bein05] J. Beinert, R. Kübler, H. Kordisch, L. Könczöl, T. Kraft and G. Kleer, **On the characterisation of industrial PV manufacturing lines with respect to silicon fracturing**, in *Proceedings of the 20th European Photovoltaic Solar Energy Conference (EU PVSEC),* Barcelona, Spain, 2005, pp. 1167–1170.

[Bitt91] D. A. Bittle, J. C. Suhling, R. E. Beaty, R. C. Jaeger and R. W. Johnson, **Piezoresistive Stress Sensors for Structural Analysis of Electronic Packages**, *Journal of Electronic Packaging*, vol. 113, no. 3, pp. 203–215, 1991, 10.1115/1.2905397.

[Brig86] A. Briglio, K. Dumas, M. Leipold and A. Morrison, **Flat-Plate Solar Array Project Final Report. Volume III: Silicon sheet: wafers and ribbons**, JPL Publication 86-31, Jet Propulsion Laboratory, Pasadena, CA, USA, 1986.

[Büch17] A. Büchler, A. J. Beinert, S. Kluska, V. Haueisen, P. Romer, F. D. Heinz, M. Glatthaar and M. C. Schubert, **Enabling stress determination on alkaline textured silicon using Raman spectroscopy**, *Energy Procedia*, vol. 124, pp. 18–23, 2017, 10.1016/j.egypro.2017.09.333.

[Budi14] A. S. Budiman, G. Illya, V. Handara, W. A. Caldwell, C. Bonelli, M. Kunz, N. Tamura and D. Verstraeten, **Enabling thin silicon technologies for next generation c-Si solar PV renewable energy systems using synchrotron X-ray microdiffraction as stress and crack mechanism probe**, *Solar Energy Materials and Solar Cells*, vol. 130, pp. 303–308, 2014, 10.1016/j.solmat.2014.07.029.

[Call86] W. Callaghan and McDonald R, **Flat-Plate Solar Array Project final report. Volume I: Executive Summary**, JPL Publication 86-31, Jet Propulsion Laboratory, Pasadena, CA, USA, 1986.

[Carr76] W. Carroll, E. Cuddihy and M. Salama, **Material and Design Considerations of Encapsulants for Photovoltaic Arrays in Terrestrial Applications**, in *Proceedings of the 12th IEEE Photovoltaic Specialists Conference (IEEE PVSC),* Baton Rouge, LA, USA, 1976, pp. 332–339.

[Cudd86] E. Cuddihy, C. Coulbert, Goupta A. and Liang R, **Flat-Plate Solar Array Project Final Report. Volume VII: Module encapsulation**, JPL Publication 86-31, Jet Propulsion Laboratory, Pasadena, CA, USA, 1986.

[Diet10] S. Dietrich, M. Pander, M. Sander, S.-H. Schulze and M. Ebert, **Mechanical and Thermo-Mechanical Assessment of Encapsulated Solar Cells by Finite-Element-Simulation**, in *Proceedings of the SPIE Solar Energy and Technology,* San Diego, California, USA, 2010, 77730F, 10.1117/12.860661.

[Diet12] S. Dietrich, M. Sander, M. Pander and M. Ebert, **Interdependency of mechanical failure rate of encapsulated solar cells and module design parameters**, in *Proceedings of the SPIE Solar Energy + Technology,* San Diego, CA, USA, 2012, 84720P-1-84720P-9, 10.1117/12.929289.

[Diet13a] S. Dietrich, U. Zeller, M. Pander and M. Ebert, **Evaluation of non-uniform mechanical loads on solar modules**, in *Proceedings of the 39th IEEE Photovoltaic Specialists Conference (IEEE PVSC),* Tampa, FL, USA, 2013, pp. 2998–3003, 10.1109/PVSC.2013.6745093.

[Diet13b] S. Dietrich, M. Pander, M. Sander and M. Ebert, **Mechanical Investigations on Metallization Layouts of Solar Cells with Respect to Module Reliability**, *Energy Procedia*, vol. 38, pp. 488–497, 2013, 10.1016/j.egypro.2013.07.308.

[Diet14] S. Dietrich, **Numerische Untersuchungen zur mechanischen Zuverlässigkeit verkapselter Siliziumsolarzellen**, Dissertation, Otto-von-Guericke-Universität Magdeburg, Fakultät für Maschinenbau, Halle (Saale), 2014.

[DIN 17] DIN Deutsches Institut für Normung e. V. (DIN), **Strength testing for photovoltaic wafers**, DIN SPEC 91351, 2017.

[Dola16] A. Dolara, G. C. Lazaroiu, S. Leva, G. Manzolini and L. Votta, **Snail Trails and Cell Microcrack Impact on PV Module Maximum Power and Energy Production**, *IEEE Journal of Photovoltaics*, vol. 6, no. 5, pp. 1269–1277, 2016, 10.1109/JPHOTOV.2016.2576682.

[Doll13] J. C. Doll and B. L. Pruitt, **Piezoresistor Design and Applications**, New York, NY: Springer New York, 2013, 978-1-4614-8516-2.

[Duff94] L. Duffrène, **Comportement viscoélastique d'un verre silico-sodocalcique dans le domaine des températures intermédiaires: approche phénoménologique et modélisation en triaxialité**, Dissertation, Ecole nationale supérieure des mines de Paris, Sciences et Génie des Matériaux, Paris, 1994.

[Edwa83] D. Edwards, G. Heinen, G. Bednarz and W. Schroen, **Test Structure Methodology of IC Package Material Characterization**, *IEEE Transactions on Components, Hybrids, and Manufacturing Technology*, vol. 6, no. 4, pp. 560–567, 1983, 10.1109/TCHMT.1983.1136205.

[Eitn09] U. Eitner, M. Köntges and R. Brendel, **Measuring thermomechanical displacements of solar cells in laminates using digital image correlation**, in *Proceedings of the 34th IEEE Photovoltaic Specialists Conference (IEEE PVSC),* Philadelphia, PA, USA, 2009, pp. 1280–1284, 10.1109/PVSC.2009.5411248.

[Eitn10a] U. Eitner, S. Kajari-Schroeder, M. Köntges and R. Brendel, **Non-Linear Mechanical Properties of Ethylene-Vinyl Acetate (EVA) and its Relevance to Thermomechanics of Photovoltaic Modules**, in *Proceedings of the 5th World Conference on Energy Conversion (WCPEC-5),* Valencia, Spain, 2010, pp. 4366–4368, 10.4229/25thEUPVSEC2010-4AV.3.115.

[Eitn10b] U. Eitner, M. Köntges and R. Brendel, **Use of digital image correlation technique to determine thermomechanical deformations in photovoltaic laminates: Measurements and accuracy**, *Solar Energy Materials and Solar Cells*, vol. 94, no. 8, pp. 1346–1351, 2010, 10.1016/j.solmat.2010.03.028.

[Eitn11a] U. Eitner, S. Kajari-Schroeder, M. Köntges and H. Altenbach, **Thermal stress and strain of solar cells in photovoltaic modules**, in *STRUCTMAT, vol. 15, Shell-like Structures: Non-classical Theories and Applications*, H. Altenbach *et al,* Berlin/Heidelberg: Springer, 2011, 10.1007/978-3-642-21855-2.

[Eitn11b] U. Eitner, M. Pander, S. Kajari-Schroeder, M. Köntges and H. Altenbach, **Thermomechanics of PV Modules Including the Viscoelasticity of EVA**, in *Proceedings of the 26th European Photovoltaic Solar Energy Conference and Exhibition (EU PVSEC),* Hamburg, Germany, 2011, pp. 3267–3269, 10.4229/26thEUPVSEC2011-4EO.3.1.

[Eitn11c] U. Eitner, **Thermomechanics of photovoltaic modules**, Dissertation, Martin-Luther-Universität Halle-Wittenberg, Zentrum für Ingenieurwissenschaften, Halle-Wittenberg, 2011.

[Engl71] A. H. England, **On stress singularities in linear elasticity**, *International Journal of Engineering Science (Int. J. Engng Sci.)*, vol. 9, no. 6, pp. 571–585, 1971, 10.1016/0020-7225(71)90039-5.

[Ferr12] C. Ferrara and D. Philipp, **Why Do Modules Fail?**, *Energy Procedia*, vol. 15, pp. 379–387, 2012, 10.1016/j.egypro.2012.02.046.

[Frau20] Fraunhofer-Institut für Solare Energiesysteme ISE, **Flyerkarte: SenSoCell:** Zuverlässige Messdaten von Solarzellen mit integrierten Sensoren, [Online] Available: https://www.ise.fraunhofer.de/content/dam/ise/de/documents/infomaterial/brochures/photovoltaik/Flyerkarte_SensoCell_final.pdf, Accessed on: 28.08.2021.

[Gabo16] A. M. Gabor, R. Janoch, A. Anselmo, J. L. Lincoln, H. Seigneur and C. Honeker, **Mechanical load testing of solar panels — Beyond certification testing**, in *Proceedings of the 43rd IEEE Photovoltaic Specialists Conference (IEEE PVSC),* Portland, OR, USA, 2016, pp. 3574–3579, 10.1109/PVSC.2016.7750338.

[Gall86] B. Gallagher, P. Alexander and D. Burger, **Flat-Plate Solar Array Project final report. Volume V: Process development**, JPL Publication 86-31, Jet Propulsion Laboratory, Pasadena, CA, USA, 1986.

[Gane70] S. Ganesan, A. Maradudin and J. Oitmaa, **A lattice theory of morphic effects in crystals of the diamond structure**, *Annals of Physics*, vol. 56, no. 2, pp. 556–594, 1970, 10.1016/0003-4916(70)90029-1.

[Gies10] P. Gieschke and O. Paul, **CMOS-integrated Sensor chip for in-plane and out-of-plane shear stress**, *Procedia Engineering*, vol. 5, pp. 1364–1367, 2010, 10.1016/j.proeng.2010.09.368.

[Gies11] P. Gieschke, B. Sbierski and O. Paul, **CMOS-based piezo-FET stress sensors in Wheatstone bridge configuration**, in *Proceedings of the IEEE Sensors 2011,* Limerick, Ireland, 2011, pp. 93–96, 10.1109/ICSENS.2011.6127299.

[Gree88] J. C. Greenwood, **Silicon in mechanical sensors**, *Journal of Physics E: Scientific Instruments*, vol. 21, no. 12, p. 1114, 1988.

[Gros17] D. Gross, W. Hauger, J. Schröder and W. A. Wall, **Technische Mechanik 2***,* 13th ed, Berlin, Heidelberg: Springer Berlin Heidelberg, 2017, 978-3-662-53678-0.

[Gund11a] P. Gundel, M. Drießen, J. Bartsch, U. Jäger, D. Suwito, F. D. Heinz, W. Warta and M. C. Schubert, **Comprehensive Characterization of Advanced Cell Concepts with Sub-Micron Resolution**, *Energy Procedia*, vol. 8, pp. 250–256, 2011, 10.1016/j.egypro.2011.06.132.

[Gund11b] P. Gundel, D. Suwito, U. Jager, F. D. Heinz, W. Warta and M. C. Schubert, **Comprehensive Microscopic Analysis of Laser-Induced High Doping Regions in Silicon**, *Electron Devices, IEEE Transactions on*, vol. 58, no. 9, pp. 2874–2877, 2011, 10.1109/TED.2011.2158649.

[Haas18] F. Haase, J. Kasewieter, S. R. Nabavi, E. Jansen, R. Rolfes and M. Köntges, **Fracture Probability, Crack Patterns, and Crack Widths of Multicrystalline Silicon Solar Cells in PV Modules During Mechanical Loading**, *IEEE Journal of Photovoltaics*, vol. 8, no. 6, pp. 1510–1524, 2018, 10.1109/JPHOTOV.2018.2871338.

[Hand17] V. A. Handara, I. Radchenko, S. K. Tippabhotla, K. R.Narayanan, G. Illya, M. Kunz, N. Tamura and A. S. Budiman, **Probing stress and fracture mechanism in encapsulated thin silicon solar cells by synchrotron X-ray microdiffraction**, *Solar Energy Materials and Solar Cells*, vol. 162, pp. 30–40, 2017, 10.1016/j.solmat.2016.12.028.

[Hart20] J. Y. Hartley, M. Owen-Bellini, T. Truman, A. Maes, E. Elce, A. Ward, T. Khraishi and S. A. Roberts, **Effects of Photovoltaic Module Materials and Design on Module Deformation Under Load**, *IEEE Journal of Photovoltaics*, vol. 10, no. 3, pp. 838–843, 2020, 10.1109/JPHOTOV.2020.2971139.

[Hart07] F. Hartmann and C. Katz, **Structural Analysis with Finite Elements**, Berlin/Heidelberg/New York: Springer, 2007, 13 978-3-540-49698-4.

[Hayn14] W.M. Haynes, Ed, **CRC handbook of chemistry and physics***,* 94th ed, Boca Raton, FL, USA: CRC Press, 2014, 1482208687.

[Hein12] F. D. Heinz, W. Warta and M. C. Schubert, **Optimizing Micro Raman and PL Spectroscopy for Solar Cell Technological Assessment**, *Energy Procedia*, vol. 27, pp. 208–213, 2012, 10.1016/j.egypro.2012.07.053.

[Hein14] F. D. Heinz, M. Breitwieser, P. Gundel, M. König, M. Hörteis, W. Warta and M. C. Schubert, **Microscopic origin of the aluminium assisted spiking effects in n-type silicon solar cells**, *Solar Energy Materials and Solar Cells*, vol. 131, pp. 105–109, 2014, 10.1016/j.solmat.2014.05.036.

[Hirs12] C. Hirschl, M. Granitzer, L. Neumaier, M. Spielberger, W. Mühleisen, M. Kraft, G. Kroupa and J. Schicker, **Combined Experimental and Simulatory Evaluation of Thermal and Mechanical Loads on PV Modules**, in *Proceedings of the 27th European Photovoltaic Solar Energy Conference and Exhibition (EU PVSEC),* Frankfurt, Germany, 2012, pp. 3561–3565, 10.4229/27thEUPVSEC2012-4BV.3.55.

[Hsia19] P.-C. Hsiao, C. Chen, G. Chen, X. Zhang, A. Lennon, Z. Wang, N. Song, Y. Li, Z. Ouyang, C. Hall, C. Zhu, J. Lv and C. Shen, **Comparative Models of Induced Thermomechanical Stress in Silicon Solar Cells Interconnected with Conventional Tabbing and Wire-Based Interconnection Methods**, in *Proceedings of the 46th Photovoltaic Specialists Conference (IEEE PVSC),* Chicago, IL, USA, 2019, pp. 122–125, 10.1109/PVSC40753.2019.8981176.

[Ifju08] P. G. Ifju, **Composite Materials**, in *Springer Handbook of Experimental Solid Mechanics*, W. N. Sharpe. 1st ed, New York: Springer, 2008, pp. 97–124, 10.1007/978-0-387-30877-7_4.

[Inte16] International Electrotechnical Commission (IEC), **Terrestrial photovoltaic (PV) modules – Design qualification and type approval – Part 2: Test procedures**, IEC 61215-2:2016, 2016.

[Inte20] International Electrotechnical Commission (IEC), **Photovoltaic (PV) modules - Non-uniform snow load testing**, IEC 62938:2020, 2020.

[ITRP20] ITRPV, **International Technology Roadmap for Photovoltaic (ITRPV):** 2019 Results, 11th edition, VDMA Photovoltaic Equipment, Frankfurt, Germany, Apr 2020.

[Jaeg94] R. C. Jaeger, J. C. Suhling and R. Ramani, **Errors associated with the design, calibration and application of piezoresistive stress sensors in (100) silicon**, *IEEE Transactions on Components, Packaging, and Manufacturing Technology: Part B*, vol. 17, no. 1, pp. 97–107, 1994, 10.1109/96.296437.

[Jeev12] C. R. Jeevan Doss, M. Kumaravel, B. George and K. V. Jagadeesh, **An innovative method for determining the junction temperature of a photovoltaic cell**, in *IEEE International Instrumentation and Measurement Technology Conference (I2MTC), 2012,* Graz, Austria, 2012, pp. 1847–1850, 10.1109/I2MTC.2012.6229223.

[Jord13] D. C. Jordan and S. R. Kurtz, **Photovoltaic Degradation Rates - an Analytical Review**, *Progress in Photovoltaics: Research and Applications*, vol. 21, no. 1, pp. 12–29, 2013, 10.1002/pip.1182.

[Jord16] D. C. Jordan, S. R. Kurtz, K. VanSant and J. Newmiller, **Compendium of photovoltaic degradation rates**, *Progress in Photovoltaics: Research and Applications*, vol. 24, no. 7, pp. 978–989, 2016, 10.1002/pip.2744.

[Kand82] Y. Kanda, **A graphical representation of the piezoresistance coefficients in silicon**, *IEEE Transactions on Electron Devices*, vol. 29, no. 1, pp. 64–70, 1982, 10.1109/T-ED.1982.20659.

[Kand91] Y. Kanda, **Piezoresistance effect of silicon**, *Sensors and Actuators A*, vol. 28, pp. 83–91, 1991, 10.1016/0924-4247(91)85017-I.

[Kaul14] F. Kaule, W. Wang and S. Schönfelder, **Modeling and testing the mechanical strength of solar cells**, *Solar Energy Materials and Solar Cells*, vol. 120, Part A, pp. 441–447, 2014, 10.1016/j.solmat.2013.06.048.

[Kaul17] F. Kaule, S. Meyer and S. Schönfelder, **Benchmarking Mechanical Strength Data for New Solar Cell Concepts**, in *Proceedings of the 33rd European Photovoltaic Solar Energy Conference and Exhibition (EU PVSEC),* Amsterdam, The Netherlands, 2017, pp. 276–279, 10.4229/EUPVSEC20172017-2AO.5.5.

[Kaul18] F. Kaule, M. Pander, M. Turek, M. Grimm, E. Hofmueller and S. Schönfelder, **Mechanical damage of half-cell cutting technologies in solar cells and module laminates**, *AIP Conference Proceedings*, vol. 1999, pp. 020013-1–020013-9, 2018, 10.1063/1.5049252.

[King97] D. L. King, J. A. Kratochvil and W. E. Boyson, **Temperature coefficients for PV modules and arrays:** Measurement methods, difficulties, and results, in *Proccedings of the 26th IEEE Photovoltaic Specialists Conference (IEEE PVSC),* Anaheim, CA, USA, 1997, pp. 1183–1186, 10.1109/PVSC.1997.654300.

[Klei12] B. Klein, **FEM - Grundlagen und Anwendungen der Finite-Element-Methode im Maschinen- und Fahrzeugbau***,* 9th ed, Wiesbaden, Germany: Vieweg+Teubner Verlag, 2012, 978-3-8348-2134-8.

[Knau15] M. Knausz, G. Oreski, M. Schmidt, P. Guttmann, K. Berger, Y. Voronko, G. Eder, T. Koch and G. Pinter, **Thermal expansion behavior of solar cell encapsulation materials**, *Polymer Testing*, vol. 44, pp. 160–167, 2015, 10.1016/j.polymertesting.2015.04.009.

[Kohn07] C. Kohn, T. Faber, R. Kübler, J. Beinert, G. Kleer, F. Clement, D. Erath, I. Reis, F. Martin and A. Müller, **Analyses of warpage effects induced by passivation and electrode coatings in silicon solar cells**, in *Proceedings of the 22nd European Photovolatic Solar Energy Conference and Exhibition (EU PVSEC),* Milan, Italy, 2007, pp. 1270–1273.

[Kohn09] C. Kohn, R. Kübler, M. Krappitz, G. Kleer, I. Reis, M. Retzlaff, D. Erath and D. Biro, **Influence of the metallization process on the strength of silicon solar cells**, in *Proceedings of the 24th European Photovoltaic Solar Energy Conference and Exhibition (EU PVSEC),* Hamburg, Germany, 2009, 10.4229/24thEUPVSEC2009-2CV.2.4.

[Könt11] M. Köntges, I. Kunze, S. Kajari-Schroeder, X. Breitenmoser and B. Bjørneklett, **The risk of power loss in crystalline silicon based photovoltaic modules due to micro-cracks**, *Solar Energy Materials and Solar Cells*, vol. 95, no. 4, pp. 1131–1137, 2011, 10.1016/j.solmat.2010.10.034.

[Könt16] M. Köntges, S. Altmann, T. Heimberg, U. Jahn and K. A. Berger, **Mean Degradation Rates in PV Systems for Various Kinds of PV Module Failures**, in *Proceedings of the 32nd European Photovoltaic Solar Energy Conference and Exhibition (EU PVSEC),* Munich, Germany, 2016, pp. 1435–1443, 10.4229/EUPVSEC20162016-5DP.1.2.

[Könt17] M. Köntges, G. Oreski, U. Jahn, M. Herz, P. Hacke, Weiss Karl-Anders, G. Razongles, M. Paggi, D. Parlevliet, T. Tanahashi and French, Roger, H, **Assessment of Photovoltaic Module Failures in the Field,** International Energy Agency Photovoltaic Power Systems Programme, IEA-PVPS T13-09:2017, May 2017, [Online] Available: www.iea-pvps.org/key-topics/report-assessment-of-photovoltaic-module-failures-in-the-field-2017, Accessed on: 24.05.2017.

[Koto06] A. Kotousov and Y. T. Lew, **Stress singularities resulting from various boundary conditions in angular corners of plates of arbitrary thickness in extension**, *International Journal of Solids and Structures*, vol. 43, no. 17, pp. 5100–5109, 2006, 10.1016/j.ijsolstr.2005.06.037.

[Krae13] F. Kraemer, S. Wiese, E. Peter and J. Seib, **Mechanical problems of novel back contact solar modules**, *Microelectronics Reliability*, vol. 53, no. 8, pp. 1095–1100, 2013, 10.1016/j.microrel.2013.02.019.

[Krae14] F. Kraemer and S. Wiese, **FEM stress analysis of various solar module concepts under temperature cycling load**, in *Proceedings of the 15th International Conference on Thermal, Mechanical and Multi-Physics Simulation and Experiments in Microelectronics and Microsystems (EuroSimE),* Ghent, Belgium, 2014, pp. 1–8, 10.1109/EuroSimE.2014.6813851.

[Krae15] F. Kraemer and S. Wiese, **Assessment of long term reliability of photovoltaic glass–glass modules vs. glass-back sheet modules subjected to temperature cycles by FE-analysis**, *Microelectronics Reliability*, vol. 55, no. 5, pp. 716–721, 2015, 10.1016/j.microrel.2015.02.007.

[Krau06] S. Krauter, **Solar Electric Power Generation:** Photovoltaic Energy Systems, Berlin Heidelberg New York: Springer-Verlag, 2006, 978-3-540-31345-8.

[Kuch07] H. Kuchling, **Taschenbuch der Physik:** Mit zahlreichen Tabellen, 19th ed, München: Fachbuchverl. Leipzig im Carl-Hanser-Verl, 2007, 978-3-446-41028-2.

[Lai13] C. Lai, C.-H. Su and K. Lin, **Analysis of the thermal stress and warpage induced by soldering in monocrystalline silicon cells**, *Applied Thermal Engineering*, vol. 55, no. 1-2, pp. 7–16, 2013, 10.1016/j.applthermaleng.2013.02.028.

[Lai14] C. Lai, K. Lin and C.-H. Su, **The effects of cracks on the thermal stress induced by soldering in monocrystalline silicon cells**, *Proceedings of the Institution of Mechanical Engineers, Part E: Journal of Process Mechanical Engineering*, vol. 228, no. 2, pp. 127–135, 2014, 10.1177/0954408913487285.

[Lau93] J.H. Lau, Ed, **Thermal Stress and Strain in Microelectronics Packaging**, New York, NY, USA: Van Nostrand Reinhold, 1993, 978-1-4684-7769-6.

[Lee11] Y. Lee and A. A. Tay, **Finite element thermal stress analysis of a solar photovoltaic module**, in *Proceedings of the 37th IEEE Photovoltaic Specialists Conference (IEEE PVSC),* Seattle, WA, 2011, pp. 3179–3184, 10.1109/PVSC.2011.6186616.

[Lee12] Y. Lee and Tay, Andrew A. O, **Finite Element Thermal Analysis of a Solar Photovoltaic Module**, *Energy Procedia*, vol. 15, pp. 413–420, 2012, 10.1016/j.egypro.2012.02.050.

[Lee13] Y. Lee and Tay, Andrew A. O, **Stress Analysis of Silicon Wafer-Based Photovoltaic Modules Under IEC 61215 Mechanical Load Test**, *Energy Procedia*, vol. 33, pp. 265–271, 2013, 10.1016/j.egypro.2013.05.067.

[Leip86] M. Leipold, L. Cheng, T. Daud, A. Mokashi and D. Burger, **Flat-Plate Solar Array Project final report. Volume IV: High-efficiency solar cells**, JPL Publication 86-31, Jet Propulsion Laboratory, Pasadena, CA, USA, 1986.

[Lemk11] B. Lemke, R. Baskaran, S. Ganapathysubramanian and O. Paul, **Experimental Determination of Stress Distributions Under Electroless Nickel Bumps and Correlation to Numerical Models**, *IEEE Sensors Journal*, vol. 11, no. 11, pp. 2711–2717, 2011, 10.1109/JSEN.2011.2157488.

[Levy91] A. Levy, **Thermal Residual Stresses in Ceramic-to-Metal Brazed Joints**, *Journal of the American Ceramic Society*, vol. 74, no. 9, pp. 2141–2147, 1991, 10.1111/j.1151-2916.1991.tb08273.x.

[Li19] G. Li, M. W. Akram, Y. Jin, X. Chen, C. Zhu, A. Ahmad, R. H. Arshad and X. Zhao, **Thermo-mechanical behavior assessment of smart wire connected and busbarPV modules during production, transportation, and subsequent field loading stages**, *Energy*, vol. 168, pp. 931–945, 2019, 10.1016/j.energy.2018.12.002.

[Lind20] D. Lindholm, G. Otnes, H. Fjær, G. Cattaneo, H. Yu Li and S. E. Foss, **Thermomechanical Fatigue of Solder Joint and Interconnect Ribbon: A Comparison Between Glass-Glass and Glass-Foil Modules**, in *Proceedings of the 37th European Photovoltaic Solar Energy Conference and Exhibition (EU PVSEC),* online, 2020, pp. 848–852, 10.4229/EUPVSEC20202020-4CO.1.3.

[Loud64] R. Loudon, **The Raman effect in crystals**, *Advances in Physics*, vol. 13, no. 52, pp. 423–482, 1964, 10.1080/00018736400101051.

[Luca97] G. Lucazeau and L. Abello, **Micro-Raman analysis of residual stresses and phase transformations in crystalline silicon under microindentation**, *Journal of Materials Research*, vol. 12, no. 09, pp. 2262–2273, 1997, 10.1557/JMR.1997.0302.

[Lutw86] R. Lutwack, **Flat-Plate Solar Array Project final Report. Volume II: Silicon material**, JPL Publication 86-31, Jet Propulsion Laboratory, Pasadena, CA, USA, 1986.

[Lyon77] K. G. Lyon, G. L. Salinger, C. A. Swenson and G. K. White, **Linear thermal expansion measurements on silicon from 6 to 340 K**, *Journal of Applied Physics*, vol. 48, no. 3, pp. 865–868, 1977, 10.1063/1.323747.

[Mayl12] W. Mayland, **Untersuchungen zu Spannungssingularitätsordnungen in linear-elastischen und piezoelektrischen Multimaterialkonfigurationen mit der Rand-Finite-Elemente-Methode**, Dissertation, Technische Universität Darmstadt, Institut für Mechanik, Darmstadt, 2012.

[McGu86] P. McGuire and P. Henry, **Flat-Plate Solar Array Project final report. Volume VIII: Project analysis and integration**, JPL Publication, 86-31, Jet Propulsion Laboratory, Pasadena, CA, USA, 1986.

[Meng16] X. Meng, M. Stuckelberger, L. Ding, B. West, A. Jeffries and M. Bertoni, **Characterization of encapsulated solar cells by x-ray topography**, in *Proceedings of the 43rd IEEE Photovoltaic Specialists Conference (IEEE PVSC),* Portland, OR, USA, 2016, pp. 111–114, 10.1109/PVSC.2016.7749559.

[Meng18] X. Meng, M. Stuckelberger, L. Ding, B. West, A. Jeffries and M. Bertoni, **Quantitative Mapping of Deflection and Stress on Encapsulated Silicon Solar Cells**, *IEEE Journal of Photovoltaics*, vol. 8, no. 1, pp. 189–195, 2018, 10.1109/JPHOTOV.2017.2768959.

[Mick11] R. Mickiewicz, B. Li, D. Doble, T. Christian, J. Lloyd, A. Stokes, C. Völker, M. Winter, B. Ketola, A. Norris and N. Shepard, **Effect of Encapsulation Modulus on the Response of PV Modules to Mechanical Stress**, in *Proceedings of the 26th European Photovoltaic Solar Energy Conference and Exhibition (EU PVSEC),* Hamburg, Germany, 2011, pp. 3157–3161, 10.4229/26thEUPVSEC2011-4CO.7.4.

[Möll05] H. J. Möller, C. Funke, M. Rinio and S. Scholz, **Multicrystalline silicon for solar cells**, *Thin Solid Films*, vol. 487, no. 1-2, pp. 179–187, 2005, 10.1016/j.tsf.2005.01.061.

[Mühl15] W. Mühleisen, J. Schicker, L. Neumaier, C. Hirschl, N. Vollert, S. Seufzer, R. Battistutti, M. Pedevilla, J. Scheurer, M. Schwark and T. Fischer, **Stress Measurements in Interconnected Solar Cells with Raman Spectroscopy**, in *Proceedings of the 31st European Photovoltaic Solar Energy Conference and Exhibition (EU PVSEC),* Hamburg, Germany, 2015, pp. 160–163, 10.4229/EUPVSEC20152015-1BV.6.38.

[Mülh13] G. Mülhöfer, H. Berg, C. Ferrara, W. Grzesik and D. Philipp, **Influence of Mechanical Load at Low Temperatures on Cell Defects and Power Degradation at Full Scale PV Modules**, in *Proceedings of the 28th European Photovoltaic Solar Energy Conference and Exhibition (EU PVSEC),* Paris, France, 2013, pp. 2968–2971, 10.4229/28THEUPVSEC2013-4DO.2.2.

[Munz92] D. Munz and Y. Y. Yang, **Stress Singularities at the Interface in Bonded Dissimilar Materials Under Mechanical and Thermal Loading**, *Journal of Applied Mechanics*, vol. 59, no. 4, pp. 857–861, 1992, 10.1115/1.2894053.

[Munz95] D. Munz, M. A. Sckuhr and Y. Yang, **Thermal Stresses in Ceramic-Metal Joints with an Interlayer**, *Journal of the American Ceramic Society*, vol. 78, no. 2, pp. 285–290, 1995, 10.1111/j.1151-2916.1995.tb08798.x.

[Munz01] D. Munz and T. Fett, **Ceramics:** Mechanical properties, failure behaviour, materials selection*,* 1st ed, Berlin | Heidelberg: Springer, 2001, 978-3-642-63580-9.

[Neum16] L. Neumaier, W. Mühleisen, T. Fischer, J. Scheurer, W. Pranger and C. Hirschl, **Contact-Free Raman Spectroscopic Measurement of Residual Stress in Silicon Solar Cells Caused by Stringing**, in *Proceedings of the 32nd European Photovoltaic Solar Energy Conference and Exhibition (EU PVSEC),* Munich, Germany, 2016, pp. 123–126, 10.4229/EUPVSEC20162016-1BV.5.4.

[Owen17a] M. Owen-Bellini, **Thermomechanical degradation mechanisms of silicon photovoltaic modules**, Dissertation, Loughborough University, Mechanical, Electrical and Manufacturing Engineering, Loughborough, 2017.

[Owen17b] M. Owen-Bellini, J. Zhu, T. R. Betts and R. Gottschalg, **Thermo-mechanical stresses of silicon photovoltaic modules**, in *Proceedings of the 13th Photovoltaic Science, Application and Technology Conference (PVSAT-13),* Bangor, UK, 2017, pp. 1–4.

[Pagg13a] M. Paggi, M. Corrado and M. A. Rodriguez, **A multi-physics and multi-scale numerical approach to microcracking and power-loss in photovoltaic modules**, *Composite Structures*, vol. 95, pp. 630–638, 2013, 10.1016/j.compstruct.2012.08.014.

[Pagg13b] M. Paggi and A. Sapora, **Numerical Modelling of Microcracking in PV Modules Induced by Thermo-mechanical Loads**, *Energy Procedia*, vol. 38, pp. 506–515, 2013, 10.1016/j.egypro.2013.07.310.

[Ping09] S. Pingel, Y. Zemen, O. Frank, T. Geipel and J. Berghold, **Mechanical stability of solar cells within solar panels**, in *Proceedings of the 24th European Photovoltaic Solar Energy Conference and Exhibition (EU PVSEC),* Hamburg, Germany, 2009, pp. 3459–3463, 10.4229/24thEUPVSEC2009-4AV.3.49.

[Podl20] L. Podlowski, P. Dörder, S. Heller, M. Gebrelul and S. Wendlandt, **Characterization and Long Term Stability Analysis at Photovoltaic Modules with Shingled Cell Strings**, in *Proceedings of the 37th European Photovoltaic Solar Energy Conference and Exhibition (EU PVSEC),* online, 2020, pp. 1027–1032, 10.4229/EUPVSEC20202020-4AV.1.35.

[Pogu18] V. Pogue, S. N. Melkote and S. Danyluk, **Residual stresses in multi-crystalline silicon photovoltaic wafers due to casting and wire sawing**, *Materials Science in Semiconductor Processing*, vol. 75, pp. 173–182, 2018, 10.1016/j.mssp.2017.11.009.

[Popo11] V. A. Popovich, J. M. Westra, R. A. C. M. M. van Swaaij, M. Janssen, I. J. Bennett and I. M. Richardson, **Raman spectroscopy characterization of residual stress in multicrystalline silicon solar wafers and solar cells: Relation to microstructure, defects and processing conditions**, in *Proceedings of the 37th IEEE Photovoltaic Specialists Conference (IEEE PVSC),* Seattle, WA, USA, 2011, pp. 1668–1673, 10.1109/PVSC.2011.6186276.

[Quas15] V. Quaschning, **Regenerative Energiesysteme:** Technologie - Berechnung - Simulation, Hanser eLibrary, 9th ed, München: Hanser, 2015, 978-3-446-44333-4.

[Rama53] C. V. Raman, **A new radiation**, *Proceedings of the Indian Academy of Sciences - Section A*, vol. 37, no. 3, pp. 333–341, 1953, 10.1007/BF03052651.

[Rend15] L. C. Rendler, J. Walter, T. Geipel, M. Volk, C. Ebert and U. Eitner, **Modelling and verification of mechanical stress induced by soldering of wires for multi busbar interconnection**, in *Proceedings of the 31st European Photovoltaic Solar Energy Conference and Exhibition (EU PVSEC),* Hamburg, Germany, 2015, pp. 84–88, 10.4229/EUPVSEC20152015-1CO.11.2.

[Rend16a] L. C. Rendler, A. Kraft, C. Ebert, S. Wiese and U. Eitner, **Investigation of thermomechanical stress in solar cells with multi busbar interconnection by finite element modeling**, in *Proceedings of the 32nd European Photovoltaic Solar Energy Conference and Exhibition (EU PVSEC),* Munich, Germany, 2016, pp. 94–98, 10.4229/EUPVSEC20162016-1CO.11.2.

[Rend16b] L. C. Rendler, A. Kraft, C. Ebert, U. Eitner and S. Wiese, **Mechanical stress in solar cells with multi busbar interconnection — Parameter study by FEM simulation**, in *Proceedings of the 17th International Conference on Thermal, Mechanical and Multi-Physics Simulation and Experiments in Microelectronics and Microsystems (EuroSimE),* Montpellier, France, 2016, pp. 1–5, 10.1109/EuroSimE.2016.7463325.

[Rend19] L. C. Rendler, P. Romer, A. J. Beinert, J. Walter, S. Stecklum, A. Kraft, U. Eitner and S. Wiese, **Thermomechanical Stress in Solar Cells: Contact Pad Modeling and Reliability Analysis**, *Solar Energy Materials and Solar Cells*, vol. 196, pp. 167–177, 2019, 10.1016/j.solmat.2019.03.041.

[Robe81] R. B. Roberts, **Thermal expansion reference data: silicon 300-850 K**, *Journal of Physics D: Applied Physics*, vol. 14, no. 10, L163-163, 1981, 10.1088/0022-3727/14/10/003.

[Robe82] R. B. Roberts, **Thermal expansion reference data: silicon 80-280K**, *Journal of Physics D: Applied Physics*, vol. 15, no. 9, L119-120, 1982, 10.1088/0022-3727/15/9/004.

[Rodr18] C. D. Rodríguez-Gallegos, M. Bieri, O. Gandhi, J. P. Singh, T. Reindl and S. K. Panda, **Monofacial vs bifacial Si-based PV modules: Which one is more cost-effective?**, *Solar Energy*, vol. 176, pp. 412–438, 2018, 10.1016/j.solener.2018.10.012.

[Roge16] J. Rogelj, M. den Elzen, N. Höhne, T. Fransen, H. Fekete, H. Winkler, R. Schaeffer, F. Sha, K. Riahi and M. Meinshausen, **Paris Agreement climate proposals need a boost to keep warming well below 2 °C**, *Nature*, vol. 534, no. 7609, pp. 631–639, 2016, 10.1038/nature18307.

[Ross86] R. G. Ross, Jr. and M. I. Smokler, **Flat-Plate Solar Array Project final report. Volume VI: Engineering sciences and reliability**, JPL Publication 86-31, Jet Propulsion Laboratory, Pasadena, CA, USA, 1986.

[Röth15] J. Röth, N. Bernhard, C. Belgardt, M. Grimm and F. Kaule, **Thermal Laser Separation (TLS) Dicing Process Study – a New Technology for Cutting Silicon Solar Cells for High-Efficiency Half-Cell Modules**, in *Proceedings of the 31st European Photovoltaic Solar Energy Conference and Exhibition (EU PVSEC),* Hamburg, Germany, 2015, pp. 716–718, 10.4229/EUPVSEC20152015-2AV.3.2.

[Rumb17] J. R. Rumble, **CRC handbook of chemistry and physics**, 98th ed, Boca Raton, FL, USA: CRC Press, 2017, 1498784542.

[Sand13] M. Sander, S. Dietrich, M. Pander, M. Ebert and J. Bagdahn, **Systematic investigation of cracks in encapsulated solar cells after mechanical loading**, *Solar Energy Materials and Solar Cells*, vol. 111, pp. 82–89, 2013, 10.1016/j.solmat.2012.12.031.

[Sara08] G. Sarau, M. Becker, G. Andrä and S. Christiansen, **Residual Stress Measurements in Multicrystalline Silicon Bulk and Thin Film Solar Cells Using Micro-Raman Spectroscopy**, in *Proceedings of the 23rd European Photovoltaic Solar Energy Conference and Exhibition (EU PVSEC),* Valencia, Spain, 2008, pp. 2265–2270, 10.4229/23rdEUPVSEC2008-3AV.1.24.

[Schi14] J. Schicker, C. Hirschl and R. Leidl, **Effect of PV Module Frame Boundaries on Stresses in Solar Cells**, *Journal of Energy Challenges & Mechanics*, vol. 1, no. 3, pp. 155–162, 2014, 10.13140/2.1.3374.1441.

[Schm10] C. V. Schmid, **Schadensmechanismen bei Silizium-Solarzellen und Maßnahmen zur Festigkeitserhöhung**, Dissertation, Karlsruher Institut für Technologie (KIT), KIT-Fakultät für Maschinenbau, Karlsruhe, 2010.

[Schn17] E. J. Schneller, A. M. Gabor, J. Lincoln, R. Janoch, A. Anselmo, J. Walters and H. Seigneur, **Evaluating Solar Cell Fracture as a Function of Module Mechanical Loading Conditions**, in *Proceedings of the 44th IEEE Photovoltaic Specialists Conference (IEEE PVSC),* Washington, DC, USA, 2017, pp. 2897–2901, 10.1109/PVSC.2017.8366463.

[Schö07] S. Schönfelder, A. Bohne and J. Bagdahn, **Comparison of test methods for strength characterization of thin solar wafer**, in *Proceedings of the 22nd European Photovolatic Solar Energy Conference and Exhibition (EU PVSEC),* Milan, Italy, 2007, pp. 1636–1640.

[Shar08] W.N. Sharpe, Ed, **Springer Handbook of Experimental Solid Mechanics**, 1st ed, New York: Springer, 2008, 978-0-387-26883-5.

[Shel18] Shell, **Shell Scenarios Sky:** Meeting the goals of the Paris agreement, Shell International B.V, 2018, [Online] Available: www.shell.com/skyscenario, Accessed on: 2.07.2019.

[Shin18] H. Shin, E. Han, N. Park and D. Kim, **Thermal Residual Stress Analysis of Soldering and Lamination Processes for Fabrication of Crystalline Silicon Photovoltaic Modules**, *Energies*, vol. 11, no. 12, p. 3256, 2018, 10.3390/en11123256.

[Sinc99] G. B. Sinclair, **Logarithmic Stress Singularities Resulting From Various Boundary Conditions in Angular Corners of Plates in Extension**, *Journal of Applied Mechanics*, vol. 66, no. 2, pp. 556–559, 1999, 10.1115/1.2791085.

[Sinc00] G. B. Sinclair, **Logarithmic Stress Singularities Resulting From Various Boundary Conditions in Angular Corners of Plates Under Bending**, *Journal of Applied Mechanics*, vol. 67, no. 1, pp. 219–223, 2000, 10.1115/1.321174.

[Sinc04a] G. B. Sinclair, **Stress singularities in classical elasticity–I: Removal, interpretation, and analysis**, *Applied Mechanics Reviews*, vol. 57, no. 4, pp. 251–298, 2004, 10.1115/1.1762503.

[Sinc04b] G. B. Sinclair, **Stress singularities in classical elasticity—II: Asymptotic identification**, *Applied Mechanics Reviews*, vol. 57, no. 5, pp. 385–439, 2004, 10.1115/1.1767846.

[Smek23] A. Smekal, **Zur Quantentheorie der Dispersion**, *Die Naturwissenschaften*, vol. 11, no. 43, pp. 873–875, 1923, 10.1007/BF01576902.

[Smit54] C. S. Smith, **Piezoresistance Effect in Germanium and Silicon**, *Physical Review*, vol. 94, no. 1, pp. 42–49, 1954, 10.1103/PhysRev.94.42.

[Song18] W. J. R. Song, S. K. Tippabhotla, Tay, A. A. O. and A. S. Budiman, **Numerical Simulation of the Evolution of Stress in Solar Cells During the Entire Manufacturing Cycle of a Conventional Silicon Wafer Based Photovoltaic Laminate**, *IEEE Journal of Photovoltaics*, vol. 8, no. 1, pp. 210–217, 2018, 10.1109/JPHOTOV.2017.2775158.

[Spen81] J. L. Spencer, W. F. Schroen, G. A. Bednarz, J. A. Bryan, T. D. Metzgar, R. D. Cleveland and D. R. Edwards, **New Quantitative Measurements of IC Stress Introduced by Plastic Packages**, in *Proceedings of the 19th International Reliability Physics Symposium,* Las Vegas, NV, USA, 1981, pp. 74–80, 10.1109/IRPS.1981.362977.

[Suga84] K. Suganuma, T. Okamoto, M. Koizljmi and M. Shimada, **Effect of Interlayers in Ceramic-Metal Joints with Thermal Expansion Mismatches**, *Journal of the American Ceramic Society*, vol. 67, no. 12, C-256-C-257, 1984, 10.1111/j.1151-2916.1984.tb19688.x.

[Suhl01] J. C. Suhling and R. C. Jaeger, **Silicon piezoresistive stress sensors and their application in electronic packaging**, *IEEE Sensors Journal*, vol. 1, no. 1, pp. 14–30, 2001, 10.1109/JSEN.2001.923584.

[Suzu18] S. Suzuki, T. Doi, A. Masuda and T. Tanahashi, **Bending cyclic load test for crystalline silicon photovoltaic modules**, *Japanese Journal of Applied Physics*, vol. 57, no. 2S2, 02CE05, 2018, 10.7567/JJAP.57.02CE05.

[Swee93] J. N. Sweet, **Die Stress Measurement Using Piezoresistive Stress Sensors**, in *Thermal Stress and Strain in Microelectronics Packaging*, J. H. Lau, New York, NY, USA: Van Nostrand Reinhold, 1993, pp. 221–271, 10.1007/978-1-4684-7767-2_7.

[Thak12] S. Thakur, A. Kaisare and S. Tonapi, **Thermo-mechanical analysis of a typical solar module: A parametric study**, in *Proceedings of the 13th IEEE Intersociety Conference onThermal and Thermomechanical Phenomena in Electronic Systems (ITherm),* San Diego, CA, USA, 2012, pp. 1255–1263, 10.1109/ITHERM.2012.6231566.

[Tipp17] S. K. Tippabhotla, I. Radchenko, W. Song, G. Illya, V. Handara, M. Kunz, N. Tamura, A. A. Tay and A. S. Budiman, **From cells to laminate: Probing and modeling residual stress evolution in thin silicon photovoltaic modules using synchrotron X-ray micro-diffraction experiments and finite element simulations**, *Progress in Photovoltaics: Research and Applications*, vol. 25, no. 9, pp. 791–809, 2017, 10.1002/pip.2891.

[Tipp19] S. K. Tippabhotla, N. G. Diesta, X. Zhang, S. Sridhara, C. V. Stan, N. Tamura, A. A. Tay and A. S. Budiman, **Thermomechanical residual stress evaluation in multi-crystalline silicon solar cells of photovoltaic modules with different encapsulation polymers using synchrotron X-ray micro-diffraction**, *Solar Energy Materials and Solar Cells*, vol. 193, pp. 387–402, 2019, 10.1016/j.solmat.2019.01.016.

[Trän14] H.-R. Tränkler and L. Reindl, **Sensortechnik**, Berlin, Heidelberg: Springer Berlin Heidelberg, 2014, 978-3-642-29941-4.

[Tumm22] A. Tummalieh, A. J. Beinert, C. Reichel, M. Mittag and H. Neuhaus, **Holistic design improvement of the PV module frame: Mechanical, optoelectrical, cost, and life cycle analysis**, *Progress in Photovoltaics: Research and Applications*, pp. 1–11, 2022, 10.1002/pip.3533.

[Umac16] N. Umachandran and G. TamizhMani, **Effect of spatial temperature uniformity on outdoor photovoltaic module performance characterization**, in *Proceedings of the 43rd IEEE Photovoltaic Specialists Conference (IEEE PVSC),* Portland, OR, USA, 2016, pp. 2731–2737, 10.1109/PVSC.2016.7750148.

[Unit15] United Nations Framework Convention on Climate Change (UNFCCC), **Adoption of the Paris Agreement:** Report No. FCCC/CP/2015/L.9/Rev.1, United Nations Framework Convention on Climate Change (UNFCCC), 2015, [Online] Available: http://unfccc.int/resource/docs/2015/cop21/eng/l09r01.pdf, Accessed on: 4.12.2018.

[Völk06] F. Völklein and T. Zetterer, **Praxiswissen Mikrosystemtechnik:** Grundlagen, Technologien, Anwendungen, 2nd ed, Wiesbaden: Vieweg+Teubner Verlag / GWV Fachverlage, Wiesbaden, 2006, 3-528-13891-2.

[Wagn17] M. Wagner, **Lineare und nichtlineare FEM:** Eine Einführung mit Anwendungen in der Umformsimulation mit LS-DYNA®, Wiesbaden: Springer Fachmedien Wiesbaden, 2017, 978-3-658-17865-9.

[Weib39] W. Weibull, **A Statistical Theory of the Strength of Materials,** Ingeniörsvetenskapsakademiens Hadlingar, vol. 151, Stockholm: Generalstabens Litografiska Anstalts Förlag, 1939.

[Weib51] W. Weibull, **A statistical distribution function of wide applicability**, *Journal of Applied Mechanics*, vol. 18, pp. 293–305, 1951.

[Whit82] J. D. Whitcomb, I. S. Raju and J. G. Goree, **Reliability of the finite element method for calculating free edge stresses in composite laminates**, *Computers & Structures*, vol. 15, no. 1, pp. 23–37, 1982, 10.1016/0045-7949(82)90030-X.

[Wies09] S. Wiese, R. Meier, F. Kraemer and J. Bagdahn, **Constitutive behaviour of copper ribbons used in solar cell assembly processes**, in *Proceedings of the 10th International Conference on Thermal, Mechanical and Multi-Physics Simulation and Experiments in Microelectronics and Microsystems (EuroSimE),* Delft, The Netherlands, 2009, pp. 1–8, 10.1109/ESIME.2009.4938464.

[Wies12] S. Wiese, F. Kraemer, E. Peter and J. Seib, **Mechanical problems of novel back contact solar modules**, in *Proceedings of the 13th IEEE International Conference on Thermal, Mechanical and Multi-Physics Simulation and Experiments in Microelectronics and Microsystems,* Cascais, Portugal, 2012, 1–6, 10.1109/ESimE.2012.6191770.

[Will52] M. L. Williams, **Stress singularities resulting from various boundary conditions in angular corners of plates in extension,** *Journal of Applied Mechanics*, vol. 19, no. 4, pp. 526–528, 1952.

[Wirt16] H. Wirth, K.-A. Weiß and C. Wiesmeier, **Photovoltaic Modules:** Technology and Reliability, Berlin/Boston: De Gruyter, 2016, 978-3-11-034827-9.

[Wolf96a] I. de Wolf, **Micro-Raman spectroscopy to study local mechanical stress in silicon integrated circuits**, *Semiconductor science and technology*, vol. 11, no. 2, p. 139, 1996.

[Wolf96b] I. de Wolf, H. E. Maes and S. K. Jones, **Stress measurements in silicon devices through Raman spectroscopy:** Bridging the gap between theory and experiment, *Journal of Applied Physics*, vol. 79, no. 9, pp. 7148–7156, 1996, 10.1063/1.361485.

[Wong97] S. P. Wong, W. Y. Cheung, N. Ke, M. R. Sajan, W. S. Guo, L. Huang and S. Zhao, **Ir photoelasticity study of stress distribution in silicon under thin film structures**, *Materials Chemistry and Physics*, vol. 51, no. 2, pp. 157–162, 1997, 10.1016/S0254-0584(97)80286-6.

[Zhen02] T. Zheng and S. Danyluk, **Study of Stresses in Thin Silicon Wafers with Near-infraredphase Stepping Photoelasticity**, *Journal of Materials Research*, vol. 17, no. 01, pp. 36–42, 2002, 10.1557/JMR.2002.0008.

# List of Acronyms

| | |
|---|---|
| Al-BSF | Aluminum back-surface-field; solar cell technology |
| BB | busbar |
| CCD | charge-coupled device |
| CMOS | Complementary metal–oxide semiconductor |
| c-Si | monocrystalline silicon |
| CTE | coefficient of thermal expansion |
| DMA | dynamic mechanical analysis, dynamic mechanical analysis |
| DoF | Degree of Freedom |
| EL | Electroluminescence imaging |
| EVA | Ethylene-vinyl acetate |
| FEM | Finite Element Method |
| IML | static inhomogenous mechanical load |
| IR | Infrared: part of the light spectrum with longer wavelengths than the visible light. |
| KOH | potassium hydroxide, used for selective etching of silicon |
| LCOE | levelized cost of electricity: costs of the energy conversion into electricity |
| LSC | laser scribing with cleaving; solar cell splitting technology |
| mc-Si | multicrystalline silicon |
| ML | static homogenous mechanical load |
| NA | numerical aperture |
| Nd:YAG | neodymium-doped yttrium aluminum garnet ($Nd:Y_3Al_5O_{12}$) crystal used in solid-state lasers |
| PC | Polycarbonate |
| PDE | partial differential equation |
| PERC | Passivated Emitter Rear Contact; solar cell technology |
| PET | Polyethylene terephthalate |
| PID | Potential Induced Degradation |

| | |
|---|---|
| Pt100 | Platinum based resistance thermometer with a nominal resistance at 0 °C of 100 Ω. |
| PV | Photovoltaic |
| PVDF | Polyvinylidene difluoride |
| PVF | Polyvinyl fluoride |
| Si | Silicon |
| SWCT | smart wire interconnection technology |
| TC | themal cycling test according to IEC 61215 |
| TLS | thermal laser separation; solar cell splitting technology |
| TPT | trilayer composite of Tedlar-Polyethylene-Tedlar |

# List of Symbols

| Symbol | Typical unit | Description |
|---|---|---|
| $\alpha$ | $10^{-6}$ $K^{-1}$ | coefficient of thermal expansion |
| $\alpha_T$ | $10^{-3}$ $K^{-1}$ | resistance temperature coefficient |
| $\beta_T$ | $10^{-5}$ $K^{-1}$ | second order temperature coefficient |
| $\varepsilon_{ij}$ | - | components of strain tensor |
| $\vec{\kappa}$ | $m^{-1}$ | curvature, defined as the second partial derivative of the deflection: $\vec{\kappa} = \Delta\vec{d}$ |
| $\lambda$ | $cm^{-2}$ | Eigenvalues of the Raman secular equation |
| $\nu$ | - | Poisson's ratio |
| $\boldsymbol{\pi}$ | $GPa^{-1}$ | piezoresistive tensor |
| $\pi_{11,\mathrm{ref}}$ | $GPa^{-1}$ | piezoresistive coefficient at room temperature |
| $\rho$ | Ω mm | specific resistance |
| $\Sigma$ | rel. $cm^{-1}$ $GPa^{-1}$ | conversion coefficient for the conversion of the Raman peak shift into stress |
| $\sigma_0$ | MPa $m^2$ | geometrically independent Weibull scale factor |
| $\sigma_I$ | MPa | first principal stress |
| $\sigma_{II}$ | MPa | second principal stress |
| $\sigma_{III}$ | MPa | third principal stress |
| $\sigma_{ij}$ | MPa | components of stress tensor |
| $\sigma_\theta$ | MPa | characteristic fracture stress |
| $\omega$ | rel. $cm^{-1}$ | Raman wavenumber relative to excitation laser |
| $\omega_{abs}$ | $cm^{-1}$ | wavenumber of absorbed photon |
| $\omega_{em}$ | $cm^{-1}$ | wavenumber of emitted photon |

| Symbol | Typical unit | Description |
|---|---|---|
| $\Omega_{phon}$ | $cm^{-1}$ | wavenumber of excited phonon state |
| | | |
| A | - | aspect ratio |
| $A_{eff}$ | $m^2$ | effective area |
| $A_j$ | $mm^2$ | joining surface of two materials |
| $\boldsymbol{C}$ | MPa | elasticity matrix |
| $\boldsymbol{D}$ | - | differential-operator-matrix |
| $d$ | mm | displacement of PV module |
| $\vec{d}$ | mm | node displacement vector |
| $E$ | MPa | Young's modulus |
| $E_\alpha$ | kPa $K^{-1}$ | thermal expansion stiffness |
| $\hat{E}_{\alpha,\mathrm{rel}}$ | Pa $m^3$ $K^{-1}$ | relative specific thermal expansion stiffness |
| $\hat{E}_\alpha$ | Pa $m^3$ $K^{-1}$ | specific thermal expansion stiffness |
| $\bar{E}_\alpha$ | Pa $m^3$ $K^{-1}$ | volumetric thermal expansion stiffness |
| $f$ | N | vector incorporating all external forces |
| $F_n$ | N | Force equivalent to the surface load $p_{ML}$ normalized to the number of vacuum cups |
| $\boldsymbol{G}$ | - | row matrix |
| $g(x,y)$ | - | geometric stress shape function |
| $h$ | mm | height |
| $\boldsymbol{K}$ | N $m^{-1}$ | element stiffness matrix |
| $l$ | mm | length |
| $L$ | N $m^{-1}$ | lower matrix of the LU factorization |
| $m$ | - | Weibull modulus |

| Symbol | Typical unit | Description |
|---|---|---|
| $N$ | $cm^{-3}$ | charge carrier concentration |
| $P$ | - | dimensionless P-factor |
| $p, q, r$ | $cm^{-2}$ | phonon deformation potentials (material constants) |
| $P_f(\sigma)$ | % | probability of cell fracture |
| $p_{ML}$ | Pa | applied mechanical load |
| $pos_{x,i,j}$ | mm | x-positions of the i, j-vacuum cup |
| $pos_{y,i,j}$ | mm | y-positions of the i, j-vacuum cup |
| $R_{\square}$ | Ω | sheet resistance |
| $R_T$ | Ω | resistance of temperature sensor |
| $R_{T,0}$ | Ω | Nominal resistance at 0°C |
| $r_{vc}$ | mm | radius of the vacuum suction cups of the ML test stand |
| $R_{\sigma,0}$ | Ω | resistance of stress sensor |
| $S_\sigma$ | $GPa^{-1}$ | sensitivity of the stress sensor |
| $S_T$ | $10^{-3}\ K^{-1}$ | sensitivity of the temperature sensor |
| $T$ | °C | temperature |
| $T_{mod}$ | °C | temperature of the module |
| $U$ | - | upper matrix of the LU factorization |
| $V$ | $m^3$ | volume |
| $w$ | mm | width |

# List of Definitions

| | |
|---|---|
| backsheet | layer on the back side of a laminate |
| busbar | metallic contact and current collector of solar cells |
| bending stress | stress originating from the deflection |
| element ratio | ratio of the node distance of two neighoring mesh elements |
| finger | metallic current collector and conductor, perpendicular to busbars and much thinner |
| frontsheet | layer on the front side of a laminate |
| frontglass | glass sheet on the front side of a laminate |
| glass-foil module | PV module with a glass as frontsheet and a polymerbased backsheet foil. |
| glass-glass module | PV module with a glass as front- and backsheet |
| hexahedron | extruded rectangular mesh element |
| laminate | encapsulated solar cells after lamination (without a mounting sstructure) |
| laminate-stress | thermal stress occurring from the CTE mismatch of the laminate materials |
| mechanical stress | stress originating from mechanical loads |
| mounting-stress | thermal stress occurring from the CTE mismatch between the mounting structure and the laminate |
| mounting structure | structure attached to the laminate, which is used for mounting the PV module to a rack. In conventional modules: a frame. |
| prism | extruded triangluar mesh element |
| PV module | laminate with a mounting structure, e.g. frame |
| pyramid | mesh element in the shape of a pyramid with foursided base |
| SenSoCell | solar cell with integreated sensors |
| string | solar cells interconnected in series |
| tetrahedron | mesh element in the shape of a pyramid with triangular base |

| | |
|---|---|
| thermal stress | stress originating from thermal loads, i.e. temperature changes |
| thermomechanical stress | stress originating from combined thermal and mechanical loads |

# Acknowledgements

gefördert durch Cusanuswerk Bischöfliche Studienförderung

Thank you **Prof. Dr. Jarir Aktaa** for supervising me and hence giving me the opportunity to do this dissertation. Thank you for the fruitful discussions and inputs. Thank you to my co-referee, **Prof. Dr. Robert Stieglitz** for your constructive feedback.

Thank you, **Dr. Ulrich Eitner** for supervising me at Fraunhofer ISE. I have learnt a lot from your experience in FEM modelling of PV modules. Thank you, **Martin Heinrich, PhD** for continuing the supervision after Uli left ISE. Thanks to both of you for the regular meetings, fruitful discussions, inputs and proof reading. **Dr. Holger Neuhaus**, thank you for integrating me into and giving me access to the resources of the Module Technology department. Research is always the success of a group, so to **all my colleagues**: thank you for the support, advice, discussions and contribution!

A special thanks to the **Cusanuswerk** for supporting this dissertation with a PhD-scholarship. I have benefited a lot from the yearly graduate schools and other seminars.

**(Mega)Pascal Romer** thank you so much for all the contribution and support in the last years! Without your work this dissertation wouldn't be the same. Thank you for the FEM modelling and simulations you have done. Thank you also for the contribution to the development of µ-Raman spectroscopy. Last but not least, thank you for all the fruitful discussions and proof reading.

Also for the development of the µ-Raman spectroscopy: thank you **Dr. Andreas Büchler** for the fruitful cooperation, the discussions and all the effort you spent!

Thank you, **Mark Imm** for the contribution to the development of the solar cell integrated sensors. This development wouldn't have been successful without the contribution of various people. Thank you, **Dr. Jan Benick** for all the advice and your expertise and **Sonja Seitz** for processing the sensors. Thank you, **Prof. Dr. Oliver Paul** for the good collaboration between IMTEK and Fraunhofer ISE as well as supporting the development with your expertise and granting us access to your laboratories. **Dr. Felix Becker,** thank you for your advice and support in the development and characterization of the sensors.

Thank you, **Christoph Herzog** for your support (even until late night) in the lamination of the validation modules! Thank you **Dominic Röder** for the framing of the modules and glass sheets for the validation. Thank you, **Felix Basler** for your advice regarding the contacting and cabling of the sensor cells. Thank you,

**Heinrich Berg** and **David Hottenrott** for conducting the Mechanical Load Tests (on such short notices).

Thank you, **Nils Klasen** and **Dr.-Ing. Angela De Rose** that I could always rely on your advice, whenever I needed it. I'm very thankful for all the shorter and often longer discussions. Also thank you to **Li Carlos Rendler** and all members of the **iBBB PhD-group** for the constructive discussions in the office or at our seminars.

A big thank you to my wife **Leonie** for believing in me, enduring my moods after long home office days and cheering me up. Finally, a big thank you to **my family** for supporting me in all kinds and believing in me throughout my live. Thank you, **Dr.-Ing. Joachim Beinert** for proof reading and introducing me into the world of solar cell fracture through your work at Fraunhofer IWM.

# List of Publications

## Journal

A. J. Beinert, A. Büchler, P. Romer, V. Haueisen, L. C. Rendler, M. C. Schubert, M. Heinrich, J. Aktaa and U. Eitner, **Enabling the measurement of thermomechanical stress in solar cells and PV modules by confocal micro-Raman spectroscopy**, *Solar Energy Materials and Solar Cells*, vol. 193, pp. 351–360, 2019, 10.1016/j.solmat.2019.01.028.

A. J. Beinert, P. Romer, M. Heinrich, M. Mittag, J. Aktaa and H. Neuhaus, **The Effect of Cell and Module Dimensions on Thermomechanical Stress in PV Modules**, *IEEE Journal of Photovoltaics*, vol. 10, no. 1, pp. 70–77, 2020, 10.1109/JPHOTOV.2019.2949875.

A. J. Beinert, M. Imm, J. Benick, F. Becker, S. Seitz, M. Heinrich, O. Paul, S. W. Glunz, J. Aktaa, U. Eitner and H. Neuhaus, **Silicon solar cell-integrated stress and temperature sensors for photovoltaic modules**, *Progress in Photovoltaics: Research and Applications*, vol. 28, no. 7, pp. 717–724, 2020, 10.1002/pip.3263.

### Co-Authorship

L. C. Rendler, J. Walter, S. Goldenberg, A. J. Beinert, S. Wiese and U. Eitner, **Mechanical and electrical properties of wave-shaped wires for low-stress interconnection of solar cells**, *Solar Energy Materials and Solar Cells*, vol. 176, pp. 204–211, 2018, 10.1016/j.solmat.2017.11.022.

L. C. Rendler, P. Romer, A. J. Beinert, J. Walter, S. Stecklum, A. Kraft, U. Eitner and S. Wiese, **Thermomechanical Stress in Solar Cells: Contact Pad Modeling and Reliability Analysis**, *Solar Energy Materials and Solar Cells*, vol. 196, pp. 167–177, 2019, 10.1016/j.solmat.2019.03.041.

S. Kluska, B. Grübel, G. Cimiotti, C. Schmiga, H. Berg, A. J. Beinert, I. Kubitza, P. Müller and T. Voss, **Plated TOPCon solar cells & modules with reliable fracture stress and soldered module interconnection**, *EPJ Photovoltaics*, vol. 12, 10, 2021, pp. 1-6, 10.1051/epjpv/2021010.

A. Tummalieh, A. J. Beinert, C. Reichel, M. Mittag and H. Neuhaus, **Holistic design improvement of the PV module frame: Mechanical, optoelectrical, cost, and life cycle analysis**, *Progress in Photovoltaics: Research and Applications*, 2022, pp. 1-11, 10.1002/pip.3533.

## Conference

A. J. Beinert, M. Ebert, U. Eitner and J. Aktaa, **Influence of photovoltaic module mounting systems on the thermo-mechanical stresses in solar cells by FEM modelling**, in *Proceedings of the 32nd European Photovoltaic Solar Energy Conference and Exhibition (EU PVSEC)*, Munich, Germany, 2016, pp. 1833–1836, 10.4229/EUPVSEC20162016-5BV.1.14.

A. J. Beinert, R. Leidl, P. Sommeling, U. Eitner and J. Aktaa, **FEM-based development of novel back-contact PV modules with ultra-thin solar cells**, in *Proceedings of the 33rd European Photovoltaic Solar Energy Conference and Exhibition (EU PVSEC)*, Amsterdam, The Netherlands, 2017, pp. 42–47, 10.4229/EUPVSEC20172017-1CO.1.2.

A. J. Beinert, P. Romer, A. Büchler, V. Haueisen, J. Aktaa and U. Eitner, **Thermomechanical stress analysis of PV module production processes by Raman spectroscopy and FEM simulation**, *Energy Procedia*, vol. 124, pp. 464–469, 2017, 10.1016/j.egypro.2017.09.282.

A. J. Beinert, A. Büchler, P. Romer, M. Heinrich, M. C. Schubert, J. Aktaa and U. Eitner, **Stress Mapping by Confocal Raman Spectroscopy on Solar Cells and Modules**, in *Proceedings of the 7th World Conference on Photovoltaic Energy Conversion (WCPEC-7)*, Waikoloa Village, HI, USA, 2018, pp. 3613–3617, 10.1109/PVSC.2018.8547729.

A. J. Beinert, P. Romer, M. Heinrich, M. Mittag, J. Aktaa and H. Neuhaus, **Thermomechanical evaluation of new PV module designs by FEM simulations**, in *Proceedings of the 36th European Photovoltaic Solar Energy Conference and Exhibition (EU PVSEC)*, Marseille, France ,2019, pp. 783–788, 10.4229/EUPVSEC20192019-4BO.11.1.

A. J. Beinert, M. Imm, J. Benick, F. Becker, S. Seitz, M. Heinrich, O. Paul, S. W. Glunz, J. Aktaa, U. Eitner and D. H. Neuhaus, **Enabling the In-Situ Stress and Temperature Measurement by Silicon Solar Cell Integrated Stress and Temperature Sensors for Photovoltaic Modules**, in *Proceedings of the 37th European Photovoltaic Solar Energy Conference and Exhibition (EU PVSEC)*, online, 2020, pp. 38–43, 10.4229/EUPVSEC20202020-1AO.3.4.

A. J. Beinert and A. Mansolin, **Enhancing PV Module Thermomechanical Performance and Reliability by an Innovative Mounting Solution**, in *Proceedings of the 37th European Photovoltaic Solar Energy Conference and Exhibition (EU PVSEC)*, online, 2020, pp. 1096–1099, 10.4229/EUPVSEC20202020-4AV.2.8.

### Co-Authorship

A. Büchler, A. J. Beinert, S. Kluska, V. Haueisen, P. Romer, F. D. Heinz, M. Glatthaar and M. C. Schubert, **Enabling stress determination on alkaline textured silicon using Raman spectroscopy**, *Energy Procedia*, vol. 124, pp. 18–23, 2017, 10.1016/j.egypro.2017.09.333.

M. Mittag, A. J. Beinert, L. C. Rendler, M. Ebert and U. Eitner, **Triangular ribbons for improved module efficiency**, in *Proceedings of the 32nd European Photovoltaic Solar Energy Conference and Exhibition (EU PVSEC)*, Munich, Germany, 2016, pp. 169–172, 10.4229/EUPVSEC20162016-1BV.5.32.

M. Mittag, C. Kutter, S. Hoffmann, P. Romer, A. J. Beinert and T. Zech, **Electrical and thermal modeling of junction boxes**, in *Proceedings of the 33rd European Photovoltaic Solar Energy Conference and Exhibition (EU PVSEC)*, Amsterdam, The Netherlands, 2017, pp. 1501–1506, 10.4229/EUPVSEC20172017-5DO.5.5.

N. Klasen, P. Romer, A. J. Beinert and A. Kraft, **FEM Simulation of Deformations in Strings of Shingled Solar Cells Subjected to Mechanical Reliability Testing**, in *AIP Conference Proceedings 2156*, 2019, 020016-1–020016-11, 10.1063/1.5125881.

A. Pfreundt, D. Yucebas, A. J. Beinert, P. Romer and M. Mittag, **Post-processing thickness variation of PV module materials and its impact on temperature, mechanical stress and power**, in *Proceedings of the 36th European Photovoltaic Solar Energy Conference and Exhibition (EU PVSEC)*, Marseille, France , 2019, pp. 935–940, 10.4229/EUPVSEC20192019-4CO.4.3.

P. Romer, G. Oreski, A. J. Beinert, D. H. Neuhaus and M. Mittag, **More Realistic Consideration of Backsheets Coefficient of Thermal Expansion on Thermomechanics of PV Modules**, in *Proceedings of the 37th European Photovoltaic Solar Energy Conference and Exhibition (EU PVSEC)*, online, 2020, pp. 772–776, 10.4229/EUPVSEC20202020-4BO.11.4.

P. Romer, A. J. Beinert and M. Mittag, **Effects of inhomogeneous snow load on the mechanics of a PV module**, in *Proceedings of the 38th European Photovoltaic Solar Energy Conference and Exhibition (EU PVSEC),* online, 2021, pp. 602 – 606, 10.4229/EUPVSEC20212021-4BO.4.5.

A. Tummalieh, A. J. Beinert, C. Reichel and M. Mittag, **Holistic Design Optimization of the PV Module Frame: CTM, FEM, COO and LCA Analysis**, in *Proceedings of the 38th European Photovoltaic Solar Energy Conference and Exhibition (EU PVSEC),* online, 2021, pp. 540–546, 10.4229/EUPVSEC20212021-4BO.1.5.

J. N. B. Patel, E. Fokuhl, K. S. Prakash, A. Beinert, V. Wesselak, P. Gebhardt and D. Philipp, **Design and Development of Solar Cell Integrated Moisture and Temperature Sensors for Photovoltaic Modules**, in *Proceedings of the 38th European Photovoltaic Solar Energy Conference and Exhibition (EU PVSEC),* online, 2021, pp. 825 – 829, 10.4229/EUPVSEC20212021-4AV.2.16.

M. Heinrich, A. J. Beinert, P. Romer, L. C. Rendler, F. Basler, S. Wendlandt and D. H. Neuhaus, **Approaches for a Lightweight Module with Laminated Materials**, in *Proceedings of the 38th European Photovoltaic Solar Energy Conference and Exhibition (EU PVSEC),* online, 2021, pp. 761–764, 10.4229/EUPVSEC20212021-4AV.1.26.

## Patents

A. J. Beinert and U. Eitner, Fraunhofer-Gesellschaft zur Förderung der angewandten Forschung e.V, **Solarzelle und Photovoltaikmodul**, Germany, DE102018206155A1, 2019.

# Curriculum Vitae

## Personal

| | |
|---|---|
| Name | Andreas Joachim Beinert |

## Academic

| | |
|---|---|
| Oct. 2008 - June 2014 | **Study of Physics** at the Albert Ludwig University of Freiburg, Germany. |
| | **Master of Science** graduation: June 2014.<br>Thesis: „Mechanische Beanspruchung von Glas-Glas PV-Modulen mit frontseitigem Vakuumisolierglas unter Berücksichtigung des Fließverhaltens von Glas". |
| | **Bachelor of Science** graduation: May 2012.<br>Thesis: „Mechanical Investigation on the influence of different soldering procedures and encapsulants on multi-crystalline silicon modules". |
| Sept. 2009 - May 2010 | **Visiting undergraduate student** at the School of Physics and Astronomy at the University of Edinburgh, Scotland. |
| June 2007 | **Abitur** at the Friedrich-Gymnasium, Freiburg i. Br. |

## Professional

| | |
|---|---|
| Since Aug. 2021 | **Head of Team Finite Element Methods** at the Fraunhofer Institute for Solar Energy Systems ISE in Freiburg i. Br., Germany. |
| Mar. 2015 - Dec. 2021 | **Scientist and Doctoral Student** at the Fraunhofer Institute for Solar Energy Systems ISE in Freiburg i. Br., Germany.<br>July 2016 – June 2019: Ph.D.-scholarship from the Cusanuswerk. |
| Nov. 2014 - Feb. 2015 | **Voluntary Service** in the field of solar technology at the Hawassa Children's Center and Vocational Training College in Hawassa, Ethiopia. |

| | |
|---|---|
| Feb. 2013 - Oct. 2014 | **Student Assistant and Master Student** in department PV Module Technology at the Fraunhofer Institute for Solar Energy Systems ISE in Freiburg i. Br., Germany. |
| Sept. 2011 - Feb. 2012 | **Internship and Bachelor Student** in the group Photovoltaic Technology at the Fraunhofer Center for Sustainable Energy Systems CSE in Cambridge, MA, USA. |
| Aug. 2007 - Dec. 2012 | **Student Assistant** in the division Manufacturing Processes at the Fraunhofer Institute for Mechanics of Materials IWM in Freiburg i. Br., Germany. |

# Appendix

# A Solar Cell Integrated Stress Sensor

## A.1 Temperature Dependence

### A.1.1 Method

The temperature dependence of the stress sensors can be separated into two effects [Völk06]:

1. Temperature dependence of the resistance.
2. Temperature dependence of the sensitivity, i.e. of the piezoresistive coefficient.

Therefore, the temperature dependence is investigated with two different experiments described in the two following Sections.

#### A.1.1.1 Temperature Dependence of the Resistance

The temperature dependence of the resistance is expressed by the resistance temperature coefficients $\alpha_T$ and $\beta_T$:

$$R_T(T) = R_{T,\mathrm{ref}}(1 + \alpha_T\, T + \beta_T\, T^2)\,, \tag{60}$$

where $R_{T,\mathrm{ref}}$ is the resistance at a reference temperature. Since the stress sensors are used at room temperature the reference temperature is set to 25 °C.

From each charge carrier density, sensors of the 10/1 aspect ratio design (S.2 and S.5) are tested without external load. Due to a limited availability, four sensors of the $N^+$ and two sensors of the $N^{++}$ profile are used. The samples are placed in a climate chamber and the resistance $R_\sigma$ is measured using an electrical four point probe. The temperature is varied from -40 °C to +160 °C with a heating rate of 0.5 K/min. The relative resistance change $(R_T(T) - R_{T,25\,°\mathrm{C}})/R_{T,25\,°\mathrm{C}}$ is then plotted over the temperature $T$ and fitted with equation (60) to obtain the resistance temperature coefficients.

#### A.1.1.2 Temperature Dependence of the Sensitivity

The resistance change of a piezoresistive sensor depends on the temperature according to equation (17), which is shown again:

$$\Delta R_\sigma = R_\square \frac{l}{w} \pi_{11,ref} P(T,N) \sigma_x . \quad (61)$$

Therefore, the temperature dependence is expressed with the dimensionless factor $P$. To quantify the actual temperature dependence of the sensitivity of the presented stress sensors, from the chosen aspect ratio 10/1 four sensors of each charge carrier density profile are tested. To determine the temperature depended sensitivity, the used bending bridge is placed in a climate chamber. To prevent damage from the bending bridge, the temperature range is limited from 25 °C to 60 °C. Within this range, the sensitivity is determined for five temperatures according to Section 3.2.1.4.

## A.1.2 Results

### A.1.2.1 Temperature Dependence of the Resistance

Figure A.6.1 shows the relative resistance change of each charge carrier density profile for one sensor exemplarily. The solid lines depict 2nd order polynomial fits according to equation (60), the corresponding mean coefficients of all measured sensors are shown in Table A.6.1. Variation S.2 ($N^+$ profile) fits best a quadratic relation, while S.5 ($N^{++}$ profile) shows a strict linear behavior, as can be seen by the vanishing quadratic coefficient in Table A.6.1. However, with a linear resistance coefficient $\alpha_T$ of (-8 ± 3)×$10^{-3}$ %/K, S.2 has an overall lower temperature dependence than S.5 with (155.8 ± 0.4)×$10^{-3}$ %/K. Comparing these values to the stress sensitivities $S_\sigma$ of (61.56 ± 0.09) %/GPa for S.2 and (-47.41 ± 1.4) %/GPa for S.5 reveals that the temperature sensitivity of the resistance is much higher than the stress sensitivity. Therefore, the temperature of the sensor must be known precisely if operated at temperatures different from room temperature.

**Table A.6.1:** Mean linear ($\alpha_T$) and quadratic ($\beta_T$) resistance temperature coefficient of the variations S.2 and S.5.

| Variation | $\alpha_T$ [$10^{-3}$ %/K] | $\beta_T$ [$10^{-3}$ %/K] |
|---|---|---|
| S.2 | -8 ± 3 | 0.4019 ± 0.0009 |
| S.5 | 155.8 ± 0.4 | 0.003 ± 0.004 |

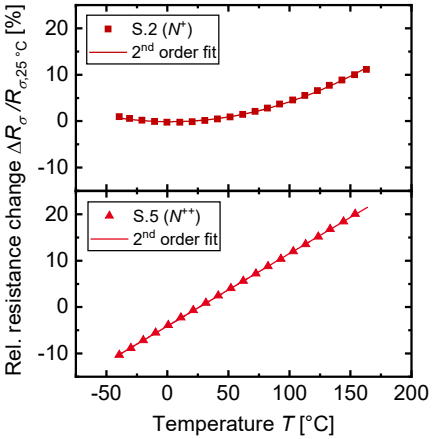


**Figure A.6.1:** Measured change of the resistance relative to the resistance at 25 °C as a function of temperature for the sensor type S.2 (top) and S.5 (bottom). For clarity, not all data points are shown. The lines depict a 2nd order polynomial fit with the mean coefficients of all measured sensors given in Table A.6.1.

### A.1.2.2 Temperature Dependence of the Sensitivity

Figure A.6.2 shows the temperature dependent sensitivity $S_\sigma$ of the variations S.2 ($N^+$ profile) and S.5 ($N^{++}$ profile) for one sensor. The solid lines depict linear fits to the data, the corresponding mean slopes of all measured sensors are shown in Table A.6.2. The temperature dependence of the $N^+$ profile is stronger compared to the $N^{++}$ profile. However, there have been large temperature fluctuations in the measurements of the $N^{++}$ profiles, therefore the uncertainty is relatively high and more measurements should be done in the future.

**Table A.6.2:** Mean slope of the sensitivity $S_\sigma$ over temperature $T$ of the sensor type S.2 and S.5.

| Variation | Slope of sensitivity over temperature [%/GPa/K] |
|---|---|
| S.2 | 0.130 ± 0.002 |
| S.5 | 0.066 ± 0.014 |

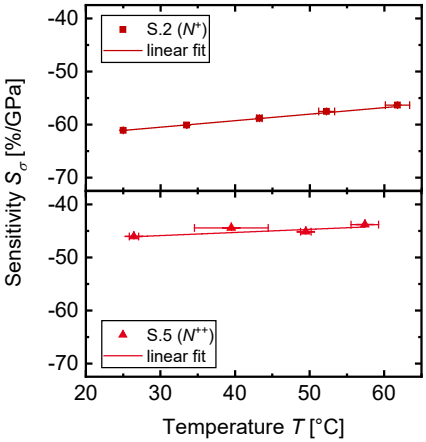


**Figure A.6.2:** Measured sensitivity $S_\sigma$ in dependence of temperature for sensor type S.2 (top) and S.5 (bottom). The lines depict a linear fit to the data with the mean slopes of all measured sensors shown in Table A.6.2.

### A.1.3 Discussion

Both, the resistance $R_\sigma$ and the sensitivity $S_\sigma$ of the piezoresistive stress sensor show a temperature dependence. While the dependence of the sensitivity is rather weak, the temperature dependence of the resistance $R_\sigma$ is strong, especially compared to its stress dependence, i.e. the sensitivity $S_\sigma$. Therefore, the temperature of the sensor must be known precisely for accurate measurements of thermomechanical stress. Since the sensitivity $S_\sigma$ has only a very weak temperature dependence for the chosen $N^{++}$ profile, the influence of the temperature on the measured stress is minimal. Within this work, all measurements are performed at room temperature. Therefore, the temperature influence is negligible. In further works, a more extensive temperature calibration with higher statistical relevenace would be reasonable in order to allow for a broader use of the stress sensor.

## A.2 Irradiance Dependence

### A.2.1 Method

To test the functionality of the guard-ring, from both charge carrier densities four sensors with aspect ratio 10/1 (S.2 and S.5, see Table 3.1) are exposed to 1000 W/m² for 10 s by a LED sun simulator. The measurement is conducted once

with the guard-ring set to ground and once without. The relative difference of the resistance $R_\sigma$ with and without illumination is evaluated and compared for the two guard-ring operation modes.

### A.2.2 Results and Discussion

For the $N^+$ charge carrier density of $1 \times 10^{19}$ (design S.2) the resistance $R_\sigma$ decreases by 15 % when the sensor is illuminated.

Due to the higher charge carrier density of $5 \times 10^{19}$ of the $N^{++}$-profile (design S.5), more electrons are generated by the illumination and hence the resistance $R_\sigma$ decrease is with 24 % stronger.

For both charge carrier densities, there is no significant difference between the two guard-ring operation modes measured. Apparently, the guard-ring does not work or is not well designed. However, all measurements within this work could be done with the sensors being shielded from any illumination or at constant illumination. Therefore, the further investigation of the guard-ring is left for further works.

# B Solar Cell Integrated Temperature Sensor

The PV modules temperature influences not only the reliability but also its performance [King97]. Several methods are proposed to determine the PV module temperature in the past. The most common method is the use of temperature sensors such as thermocouples [Jeev12, King97, Umac16], which are either laminated into or attached to the back side of the PV module. The former has the disadvantage that the PV module setup is modified by the sensor and due to its height, the temperature cannot be assigned to one layer. The latter does not allow an accurate temperature measurement within the PV module [Umac16]. Another approach is infrared (IR) imaging [Jeev12], which is capable of resolving the temperature of solar cells. However, IR imaging for permanent measurements during operation and testing is rather costly and therefore applied occasionally, only. Also the silicon solar cell itself is used as a temperature sensing device by utilizing the temperature dependence of the voltage [Jeev12]. However, since the voltage depends on various factors, the operation conditions, especially the irradiation, need to be determined as well.

Within this work, a temperature sensor, which can be integrated into the silicon solar cell itself is developed along with the solar cell integrated stress sensor (see Section 3.2). Hence, it can measure the solar cell temperature directly without interfering with the PV module setup. Figure B.6.3 a shows a schematic drawing of the proposed design.

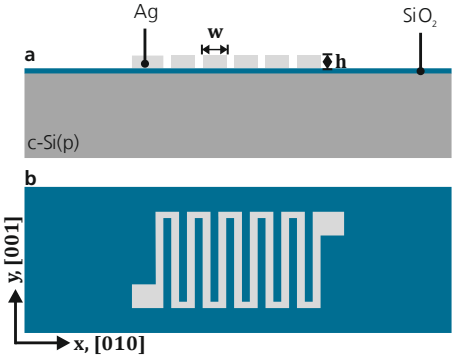


**Figure B.6.3:** Schematic drawing of the resistive temperature sensor. **a:** Cross-sectional view with the metallization insulated from the substrate by silicon oxide. **b:** Top view with the meander like structure of the metallization, not to scale. Modified after [Bein20a].

# B.1 Method and Theory

The temperature sensitivity of the silver used for metallization is utilized to develop a sensor equivalent to a Pt100 resistance thermometer. Accordingly, the designed structure has a nominal resistance $R_{T,0}$ at 0 °C of 100 Ω. The resistance $R_{T,0}$ depends on the specific resistance $\rho$, length $l$, width $w$ and height $h$:

$$R_{T,0} = \rho \frac{l}{h\,w}. \tag{62}$$

In first order approximation, the temperature dependence expressed by equation (60) reduces to:

$$R_T(T) = R_{T,0}(1 + \alpha_T\, T)\,, \tag{63}$$

where $R_{T,0}$ and $\alpha_T$ are defined for 0 °C, and $T$ denotes temperature in °C.

Due to the relatively low specific resistance $\rho$ of silver of about $1.6\times10^{-5}$ Ωmm [Rumb17], the sensor is designed as a meander to allow a small size while achieving a resistance of 100 Ω at reference temperature, The silicon

oxide layer is used as an electrical insulation layer from the sensor cell. The sensors are manufactured on the same solar cell wafer as the stress sensors (see Section 3.2.1.2) at Fraunhofer ISE and the same process as for the stress sensor metallization (Figure B.6.4) is used. This technique is commonly used for contact formation of high-efficiency solar cells.

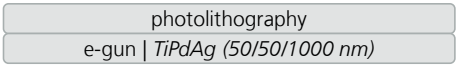


**Figure B.6.4:** Process flow of temperature sensor fabrication. e-gun: electron beam physical vapor deposition, TiPdAg: titanium, palladium, silver. Modified after [Bein20a].

## B.1.1 Characterization

The resistance $R_T$ is measured using an electrical four point probe setup during three temperature cycles in the range of -40…+160 °C for eight different sensors. The actual temperature is measured with at least two type K thermocouples. In each cycle, the temperature is increased in steps of 10 K with a slope of 2 K/min and hold constant for 10 min before measurement to have a stable temperature during the measurement. The measured resistance $R_T$ is plotted versus the temperature (see Figure B.6.5) and finally the sensitivity $S_T$, which is the resistance temperature coefficient $\alpha_T$, is determined by a linear fit:

$$S_T = \alpha_T = \frac{\Delta R_T}{R_{T,0}\,\Delta T}\,. \tag{64}$$

For each cycle, the resistance temperature coefficient $\alpha_T$ is determined for the heating and cooling phase separately. A mean is drawn over all cycles and phases and finally over all eight sensors.

### B.1.1.1 Laminate Integration

One silicon stripe containing three temperature sensors is laminated using above mentioned standard PV laminate setup (see Figure 3.10) with a 20×20 cm$^2$ frontglass of 3 mm height. Next to the sensor stripe, two type K thermocouples are placed. Then the laminated sensor stripe is exposed to 145 temperature cycles between -35 °C and +85 °C with a slope of 8.3 K/min and a holding time at the minimum and maximum temperature of 15 min. Using an electrical four point probe, the resistance is measured each 1.5 min. The 0 °C resistance $R_{T,0}$ and the temperature coefficient $\alpha_t$ are evaluated each 10$^{th}$ cycle.

## B.2 Results and Discussion

The variance of the eight sensors is not significant. Therefore, exemplarily results of Sensor 1 are shown in Figure B.6.5 left. The mean resistance temperature coefficient $\alpha_T$ is (3.557 ± 0.008) $10^{-3}K^{-1}$. The mean value of $R_{T,0}$ is (100.6 ± 0.3) Ω.

Figure B.6.5 right shows the results of the laminated sensor stripe. The relative change of the 0 °C resistance $R_{T,0}$ and of the temperature coefficient $\alpha_t$ each 10th cycle is shown. The results indicate a slight increase of less than 0.5 % of the 0 °C resistance $R_{T,0}$, most likely due to a slight degradation of the solder joint. However, the temperature coefficient $\alpha_t$ does not show this systematic change. A fairly high temperature gradient is chosen during the thermal cycles to minimize the testing time. Consequently, the variability of the temperature coefficient $\alpha_t$ is up to 0.75 %. Since this is still a relatively low value and the temperature gradients occurring in the field are lower, it is concluded, that the sensors are capable to determine the temperature of silicon solar cells within a PV laminate.

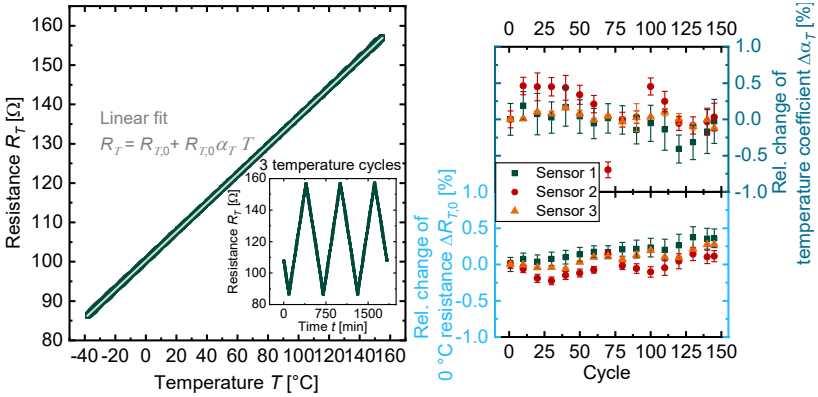


**Figure B.6.5:** *Left:* Temperature dependent resistance $R_T$ of one exemplary temperature sensor. The data represent three temperature cycles shown in the insert. The line is a linear fit. *Right:* Change of 0 °C resistance $R_{T,0}$ (bottom) and the resistance temperature coefficient $\alpha_T$ (top) for three module integrated sensors during 145 thermal cycles. The values are evaluated each 10 cycles, the change is relative to the first cycle.

# C Additional FEM Results

To investigate if the busbars and ribbons need to be included in the FEM model in order to resolve just the deflection $d$ of the PV module in the mechanical load test correctly, a FEM simulation with the busbars and ribbons included is compared to a FEM simulation without busbar and ribbon. Figure C.6.6 shows that the difference in deflection is 0.4%, which is negligible. Therefore, for a reasonable simulation of deflection $d$, busbars and ribbons can be neglected in the FEM model.

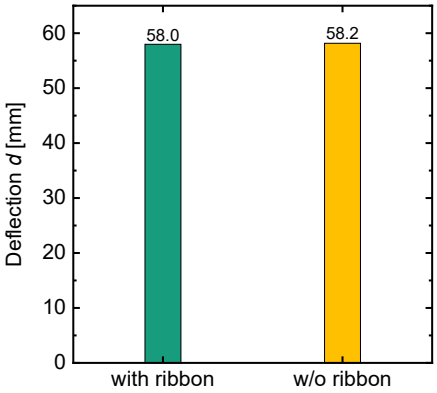


**Figure C.6.6:** Comparison of simulated deflection at 2400 Pa mechanical load with the busbars and ribbon included in the FEM model (green) and without (yellow). The difference of 0.4 % is negligible within the numerical uncertainty.

Figure C.6.7 shows the deflection $d$ and x-curvature $\kappa_x$ as a function of the applied mechanical load on the PV module simulated within the validation experiments. It shows, that the curvature has a steeper gradient than the deflection.

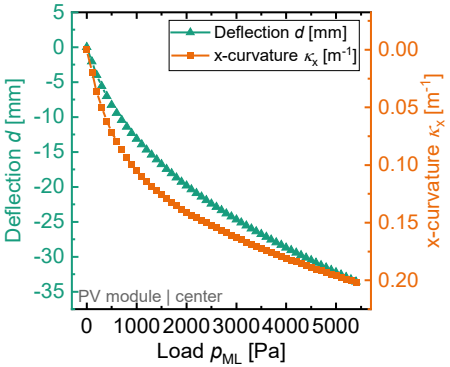


**Figure C.6.7:** Simulated deflection (green, left axis) and curvature along the short edge (orange, right axis) of the geometric non-linear validation FEM simulation.

# C.1 Parameter Sensitivity Study 2400 Pa for other Temperatures

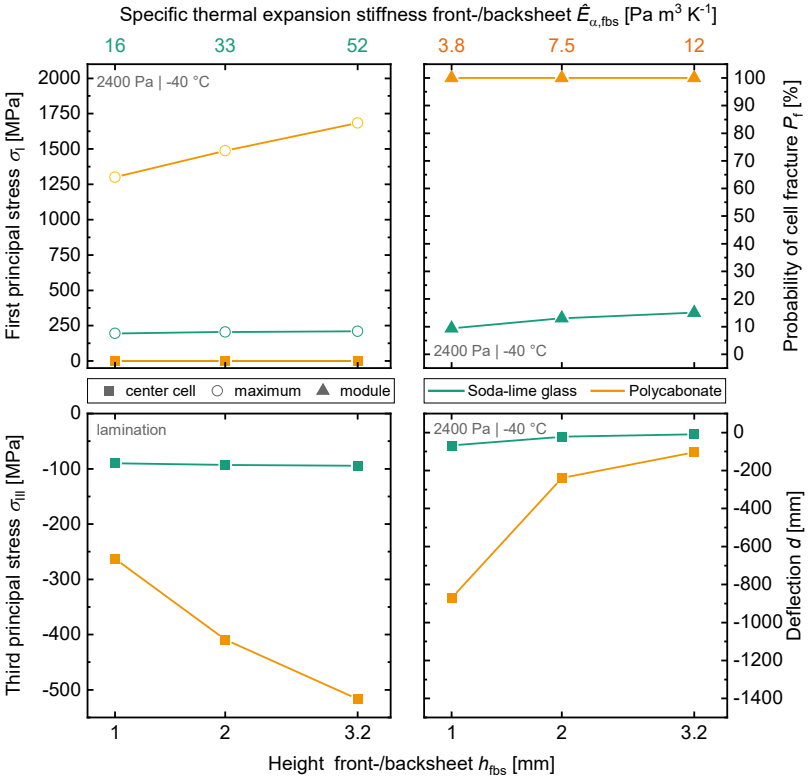


**Figure C.6.8:** Results from the variation of front-/backsheet height $h_{fbs}$ of a symmetric module setup at 2400 Pa push load at -40 °C for soda-lime glass (green) and polycarbonate (orange). *Top row: left*: maximum value (open circles) and value between the busbars of the center cell (closed squares) of the first principal stress $\sigma_I$; *right*: corresponding probability of cell fracture (triangles); *bottom row: left*: third principal stress $\sigma_{III}$ after lamination; *right*: deflection.

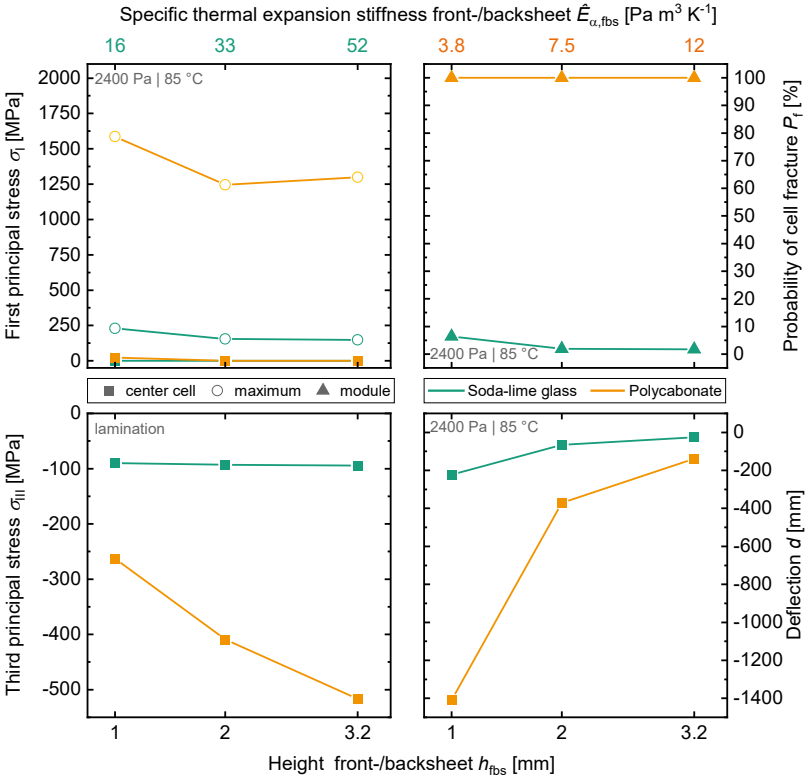


**Figure C.6.9:** Results from the variation of front-/backsheet height $h_{fbs}$ of a symmetric module setup at 2400 Pa push load at +85 °C soda-lime glass (green) and polycarbonate (orange). *Top row: left*: maximum value (open circles) and value between the busbars of the center cell (closed squares) of the first principal stress $\sigma_I$; *right*: corresponding probability of cell fracture (triangles); *bottom row: left*: third principal stress $\sigma_{III}$ after lamination; *right*: deflection.

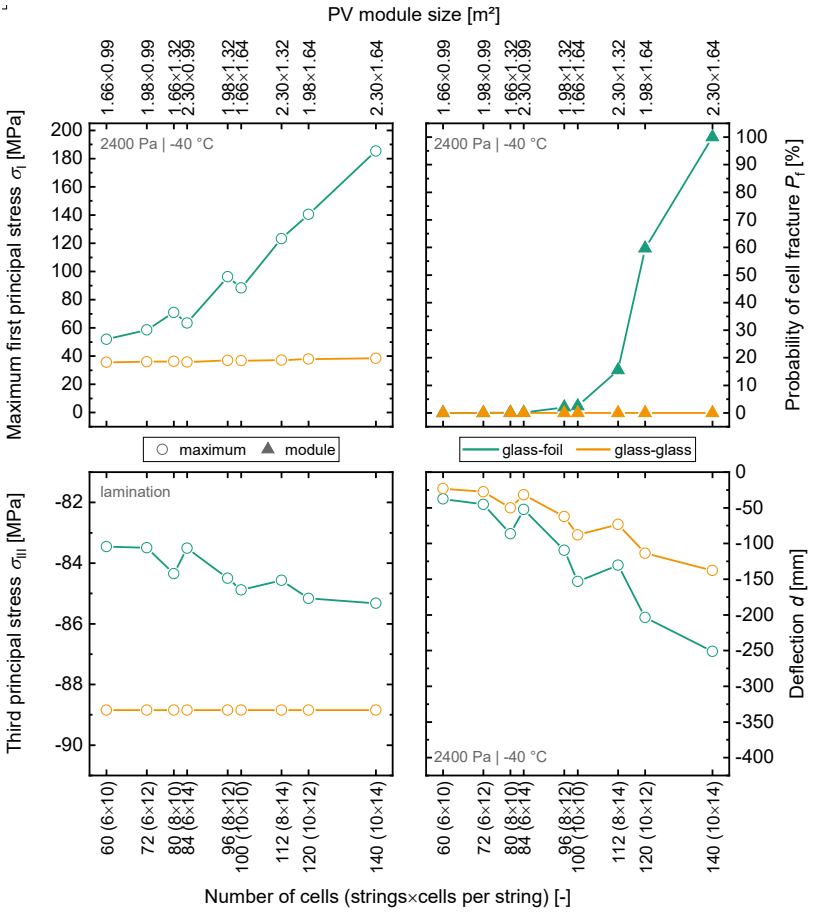


**Figure C.6.10:** Results from the variation of the number of cells within a PV module at 2400 push load and -40 °C for glass-foil (green) and glass-glass modules (orange). *Top row: left*: maximum first principal stress $\sigma_I$; *right*: corresponding probability of cell fracture; *bottom row: left*: third principal stress $\sigma_{III}$ after lamination; *right*: deflection.

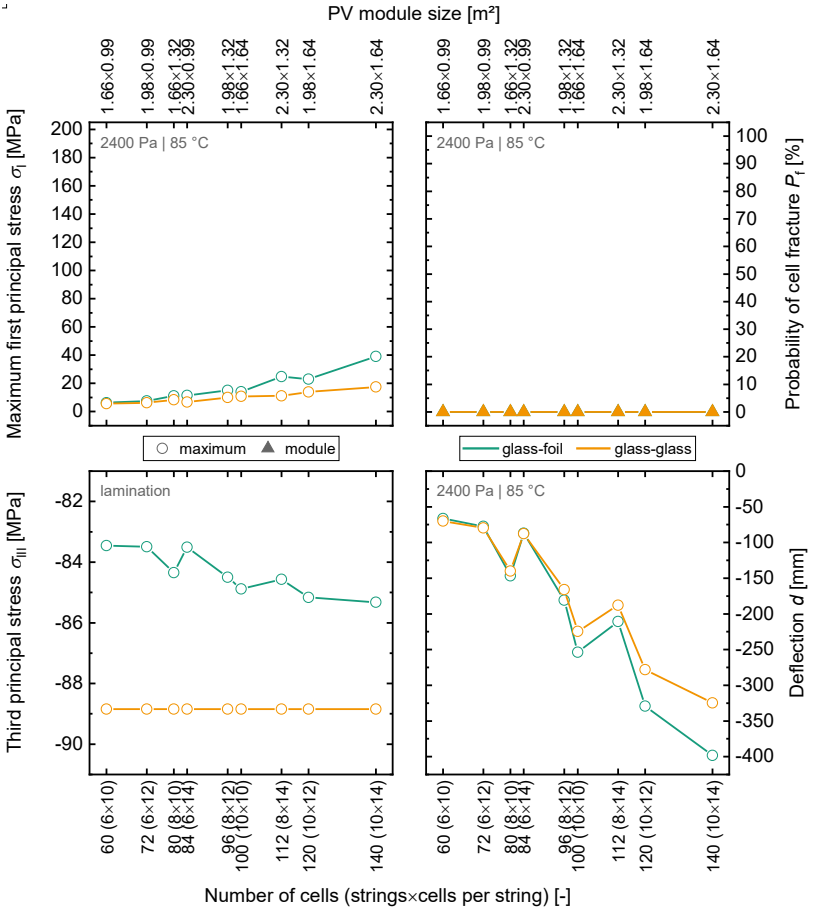


**Figure C.6.11:** Results from the variation of the number of cells within a PV module at 2400 Pa push load and 85 °C glass-foil (green) and glass-glass modules (orange). *Top row: left*: maximum first principal stress $\sigma_I$; *right*: corresponding probability of cell fracture; *bottom row: left*: third principal stress $\sigma_{III}$ after lamination; *right*: deflection.

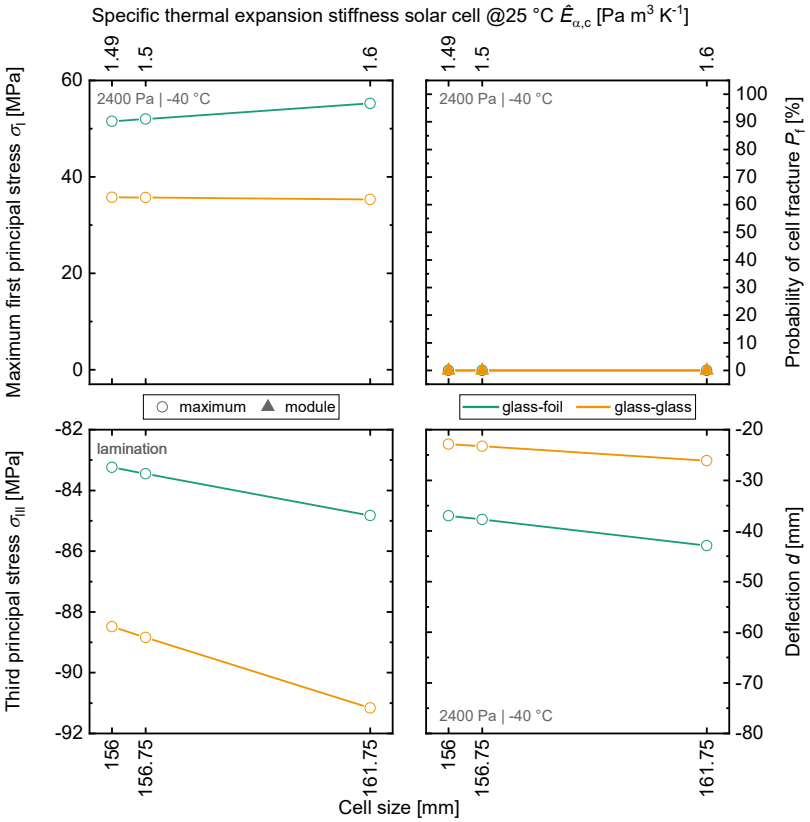


**Figure C.6.12**: Results from the variation of cell size at 2400 Pa push load and -40 °C glass-foil (green) and glass-glass modules (orange). *Top row: left*: maximum first principal stress $\sigma_I$; *right*: corresponding probability of cell fracture; *bottom row: left*: third principal stress $\sigma_{III}$ after lamination; *right*: deflection. Please note, that the bottom ordinates depict cell size and the top ordinates the corresponding specific thermal expansion stiffness $\hat{E}_{\alpha,c}$.

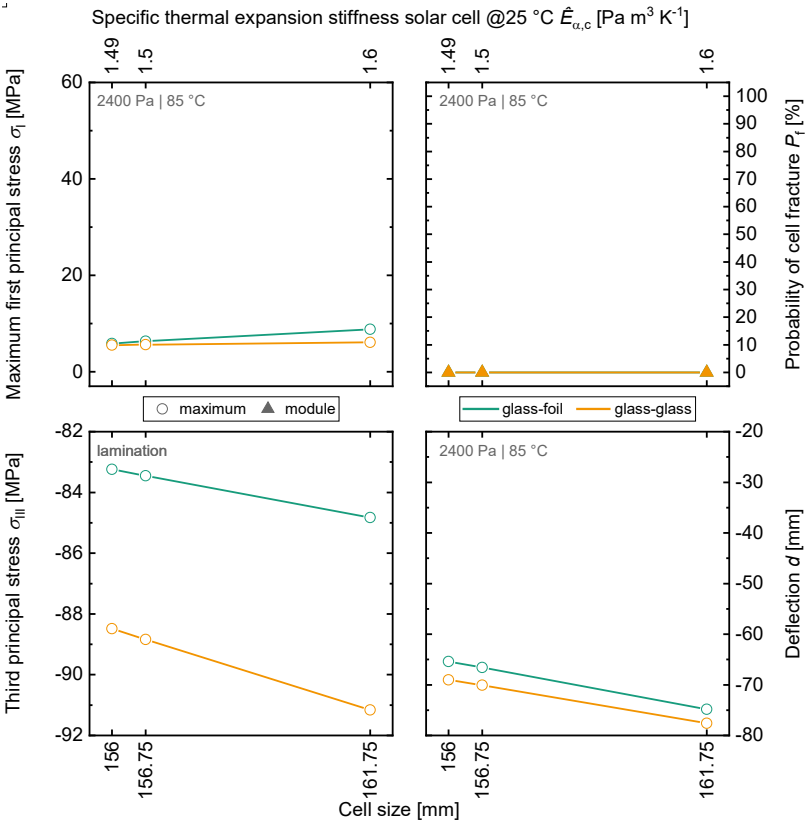


**Figure C.6.13**: Results from the variation of cell size at 2400 Pa push load and 85 °C glass-foil (green) and glass-glass modules (orange). *Top row: left*: maximum first principal stress $\sigma_I$; *right*: corresponding probability of cell fracture; *bottom row: left*: third principal stress $\sigma_{III}$ after lamination; *right*: deflection. Please note, that the bottom ordinates depict cell size and the top ordinates the corresponding specific thermal expansion stiffness $\hat{E}_{\alpha,c}$.

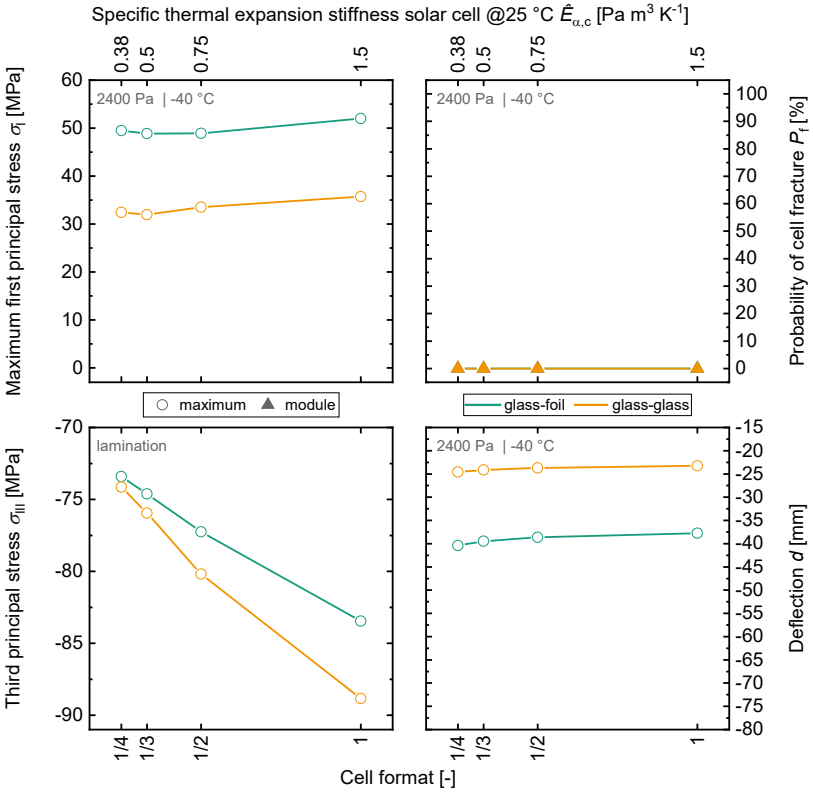


**Figure C.6.14**: Results from the variation of cell format at 2400 Pa push load and -40 °C for glass-foil (green) and glass-glass modules (orange). *Top row: left*: maximum first principal stress $\sigma_I$; *right*: corresponding probability of cell fracture; *bottom row: left*: third principal stress $\sigma_{III}$ after lamination; *right*: deflection. Please note, that the bottom ordinates depict cell format and the top ordinates the corresponding specific thermal expansion stiffness $\hat{E}_{\alpha,c}$.

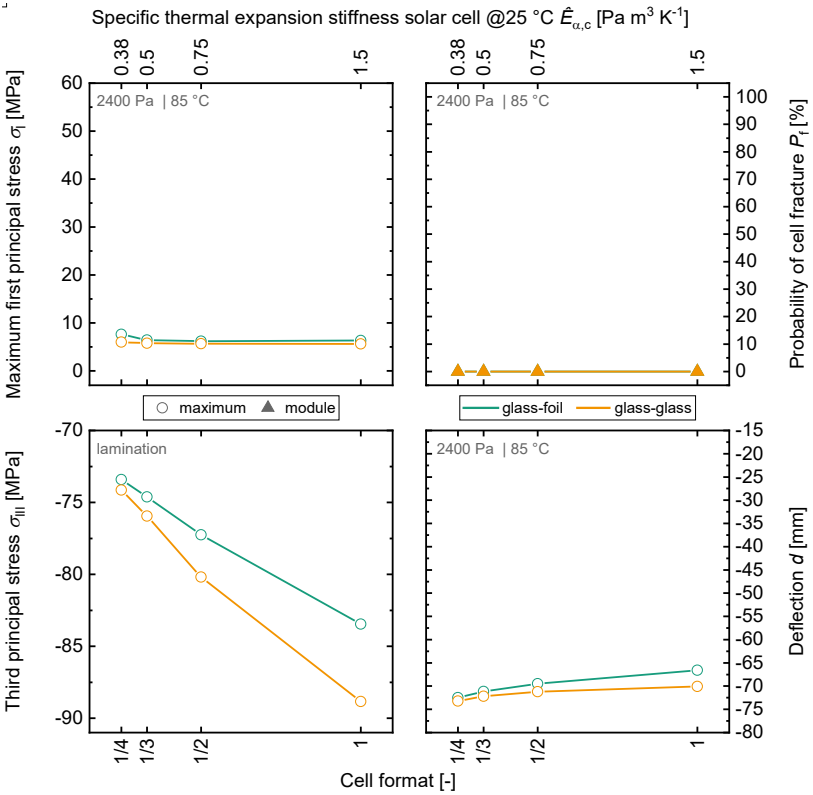


**Figure C.6.15**: Results from the variation of cell format at 2400 Pa push load and 85 °C for glass-foil (green) and glass-glass modules (orange). *Top row: left*: maximum first principal stress $\sigma_I$; *right*: corresponding probability of cell fracture; *bottom row: left*: third principal stress $\sigma_{III}$ after lamination; *right*: deflection. Please note, that the bottom ordinates depict cell format and the top ordinates the corresponding specific thermal expansion stiffness $\hat{E}_{\alpha,c}$.

# C.2 Parameter Sensitivity Study Mechanical Load 5400 Pa

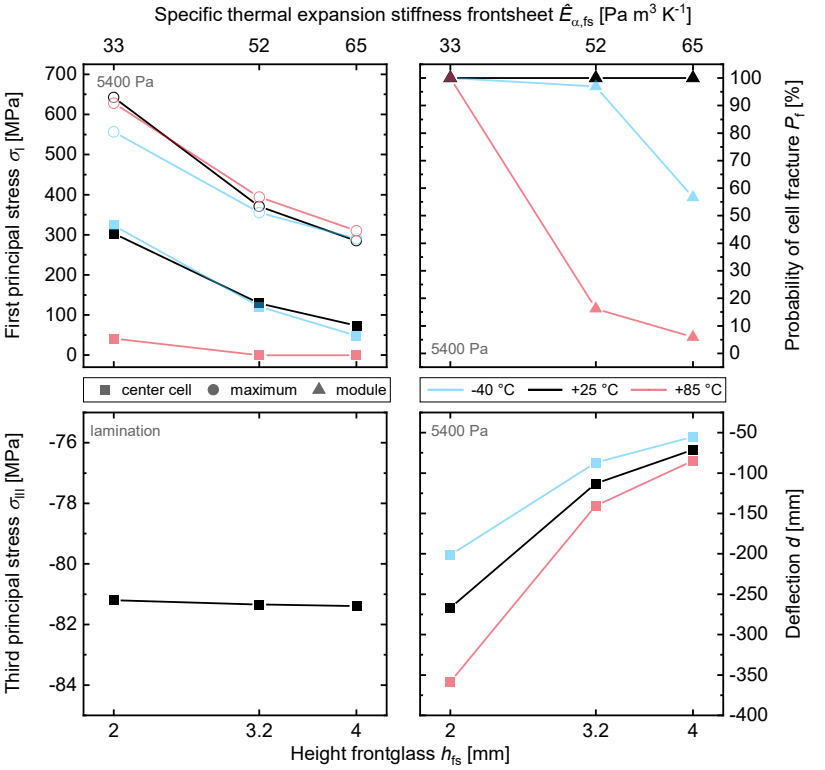


**Figure C.6.16:** Results from the variation of frontglass height $h_{fs}$ at 5400 Pa push load at -40 °C (blue), +25 °C (black) and +85 °C (red). *Top row: left*: maximum value (open circles) and value between the busbars of the center cell (filled squares) of the first principal stress $\sigma_I$; *right*: corresponding probability of cell fracture (triangles); *bottom row: left*: third principal stress $\sigma_{III}$ after lamination; *right*: deflection. Please note, that the bottom ordinates depict height $h_{fs}$ and the top ordinates the corresponding specific thermal expansion stiffness $\hat{E}_{\alpha}$.

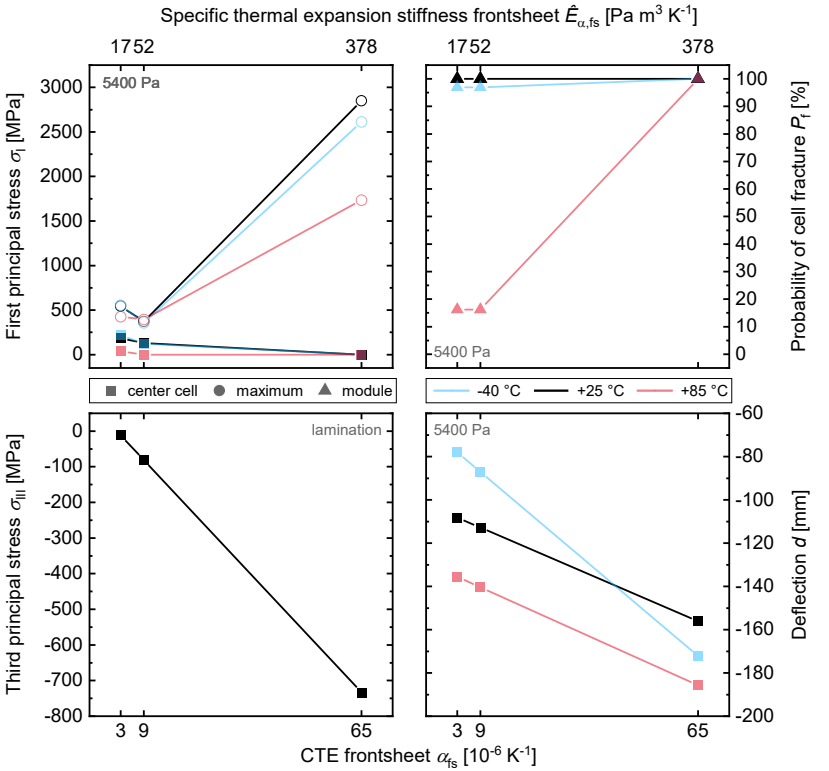


**Figure C.6.17:** Results from the variation of frontsheet CTE $\alpha_{fs}$ at 5400 Pa push load at -40 °C (blue), +25 °C (black) and +85 °C (red). *Top row: left*: maximum value (open circles) and value between the busbars of the center cell (filled squares) of the first principal stress $\sigma_I$; *right*: corresponding probability of cell fracture (triangles); bottom row: left: third principal stress $\sigma_{III}$ after lamination; *right*: deflection. Please note, that the bottom ordinates depict CTE and the top ordinates the corresponding specific thermal expansion stiffness $\hat{E}_{\alpha}$.

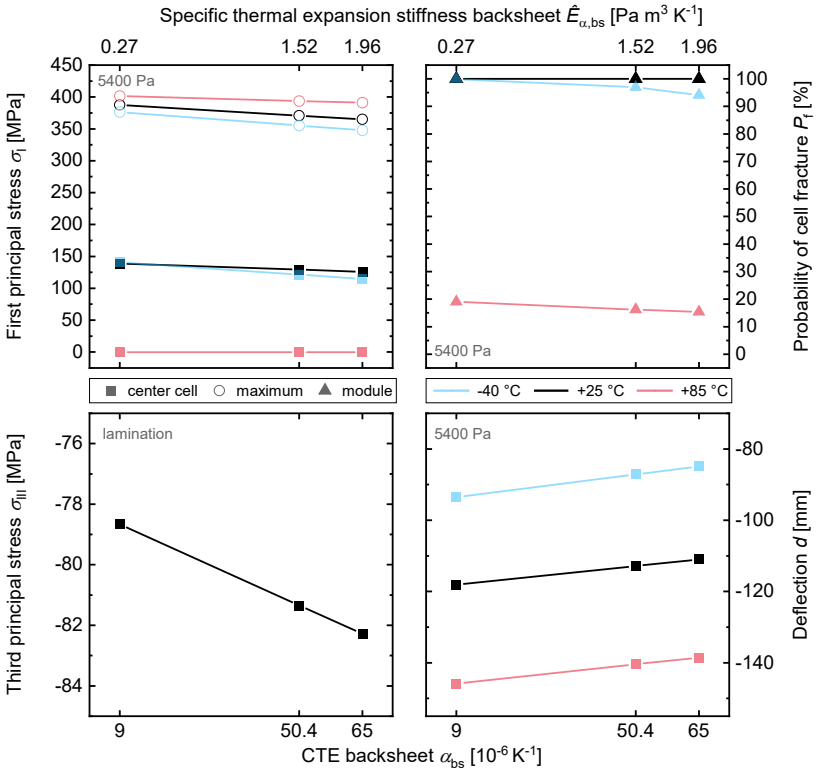


**Figure C.6.18:** Results from the variation of backsheet CTE $\alpha_{bs}$ at 5400 Pa push load at -40 °C (blue), +25 °C (black) and +85 °C (red). *Top row: left*: maximum value (open circles) and value between the busbars of the center cell (filled squares) of the first principal stress $\sigma_I$; *right*: corresponding probability of cell fracture (triangles); *bottom row: left*: third principal stress $\sigma_{III}$ after lamination; *right*: deflection. Please note, that the bottom ordinates depict CTE and the top ordinates the corresponding specific thermal expansion stiffness $\hat{E}_{\alpha}$.

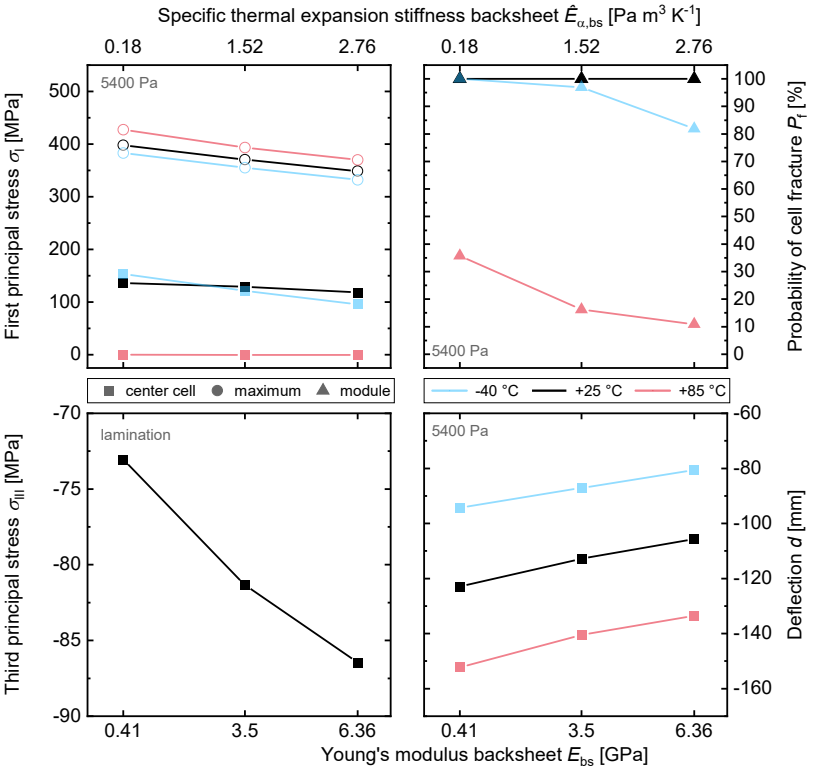


**Figure C.6.19:** Results from the variation of backsheet Young's modulus $E_{bs}$ at 5400 Pa push load at -40 °C (blue), +25 °C (black) and +85 °C (red). *Top row: left*: maximum value (open circles) and value between the busbars of the center cell (filled squares) of the first principal stress $\sigma_I$; *right*: corresponding probability of cell fracture (triangles); *bottom row: left*: third principal stress $\sigma_{III}$ after lamination; *right*: deflection. Please note, that the bottom ordinates depict Young's modulus and the top ordinates the corresponding specific thermal expansion stiffness $\hat{E}_\alpha$.

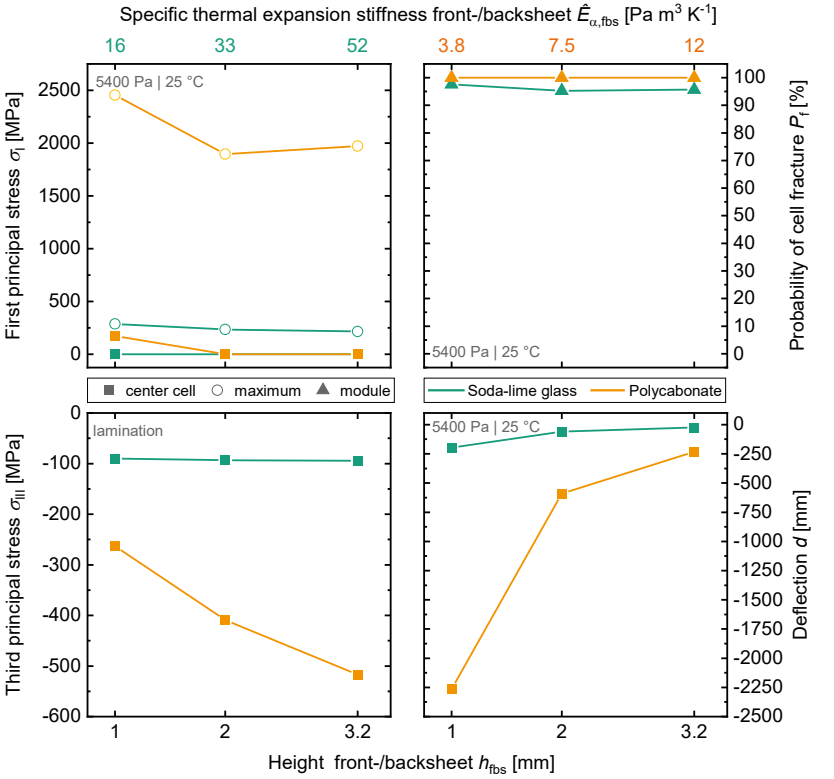


**Figure C.6.20:** Results from the variation of front-/backsheet height $h_{fbs}$ of a symmetric module setup at 5400 Pa push load at +25 °C for soda-lime glass (green) and polycarbonate (orange). *Top row: left*: maximum value (open circles) and value between the busbars of the center cell (closed squares) of the first principal stress $\sigma_I$; *right*: corresponding probability of cell fracture (triangles); *bottom row: left*: third principal stress $\sigma_{III}$ after lamination; *right*: deflection. Please note, that the bottom ordinates depict height $h_{fbs}$ and the top ordinates the corresponding specific thermal expansion stiffness $\hat{E}_\alpha$ for glass (left, green) and polycarbonate (right, orange).

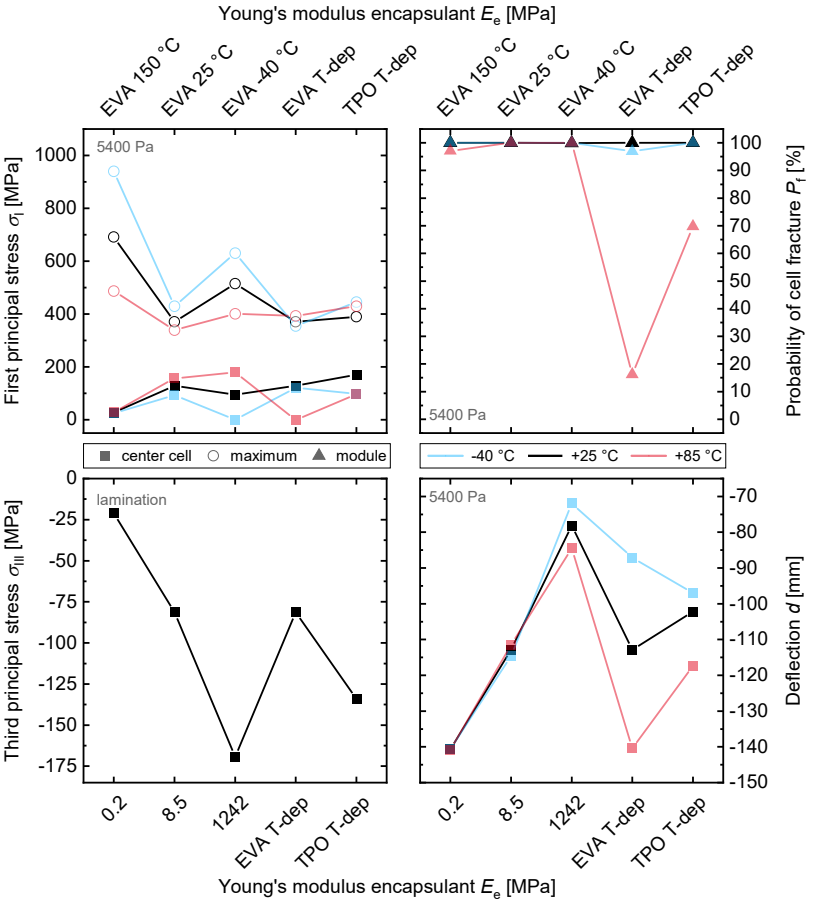


**Figure C.6.21:** Results from the variation of encapsulant Young's modulus $E_e$ at 5400 Pa push load at -40 °C (blue), +25 °C (black) and +85 °C (red). *Top row: left*: maximum value (open circles) and value between the busbars of the center cell (filled squares) of the first principal stress $\sigma_I$; *right*: corresponding probability of cell fracture (triangles); *bottom row: left*: third principal stress $\sigma_{III}$ after lamination; *right*: deflection.

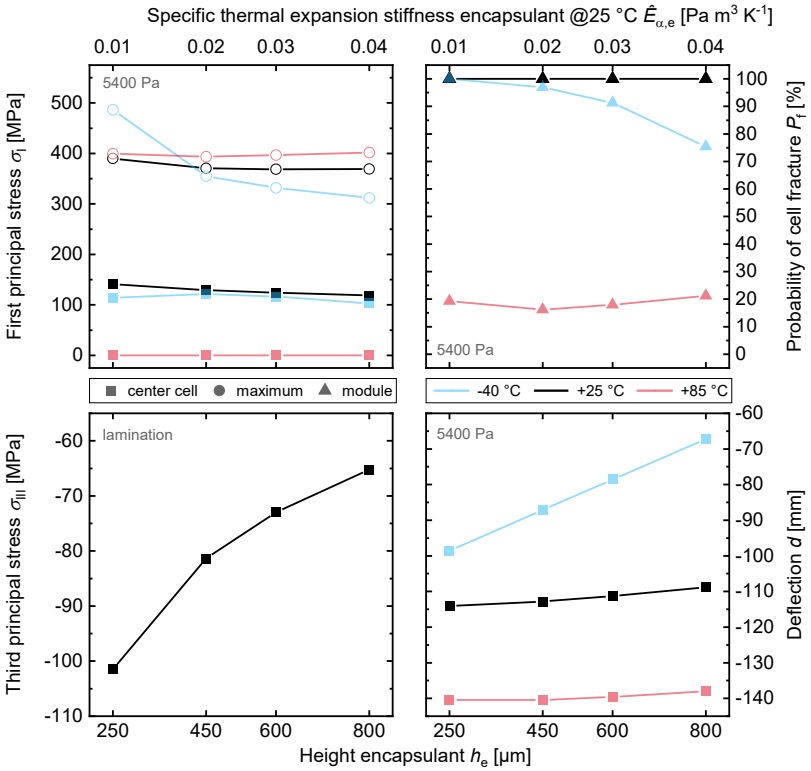


**Figure C.6.22:** Results from the variation of encapsulant height $h_e$ at 5400 Pa push load at -40 °C (blue), +25 °C (black) and +85 °C (red). *Top row: left*: maximum value (open circles) and value between the busbars of the center cell (filled squares) of the first principal stress $\sigma_I$; *right*: corresponding probability of cell fracture (triangles); *bottom row: left*: third principal stress $\sigma_{III}$ after lamination; *right*: deflection. Please note, that the bottom ordinates depict height $h_e$ and the top ordinates the corresponding specific thermal expansion stiffness $\hat{E}_\alpha$.

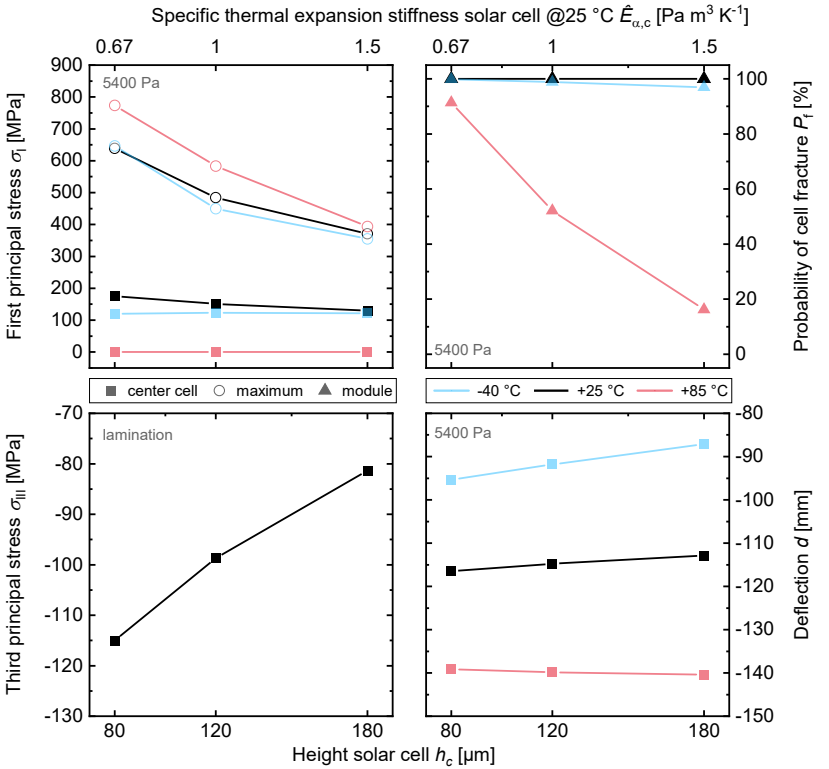


**Figure C.6.23:** Results from the variation of solar cell height $h_c$ at 5400 Pa push load at -40 °C (blue), +25 °C (black) and +85 °C (red). *Top row: left*: maximum value (open circles) and value between the busbars of the center cell (filled squares) of the first principal stress $\sigma_I$; *right*: corresponding probability of cell fracture (triangles); *bottom row: left*: third principal stress $\sigma_{III}$ after lamination; *right*: deflection. Please note, that the bottom ordinates depict height $h_c$ and the top ordinates the corresponding specific thermal expansion stiffness $\hat{E}_\alpha$.

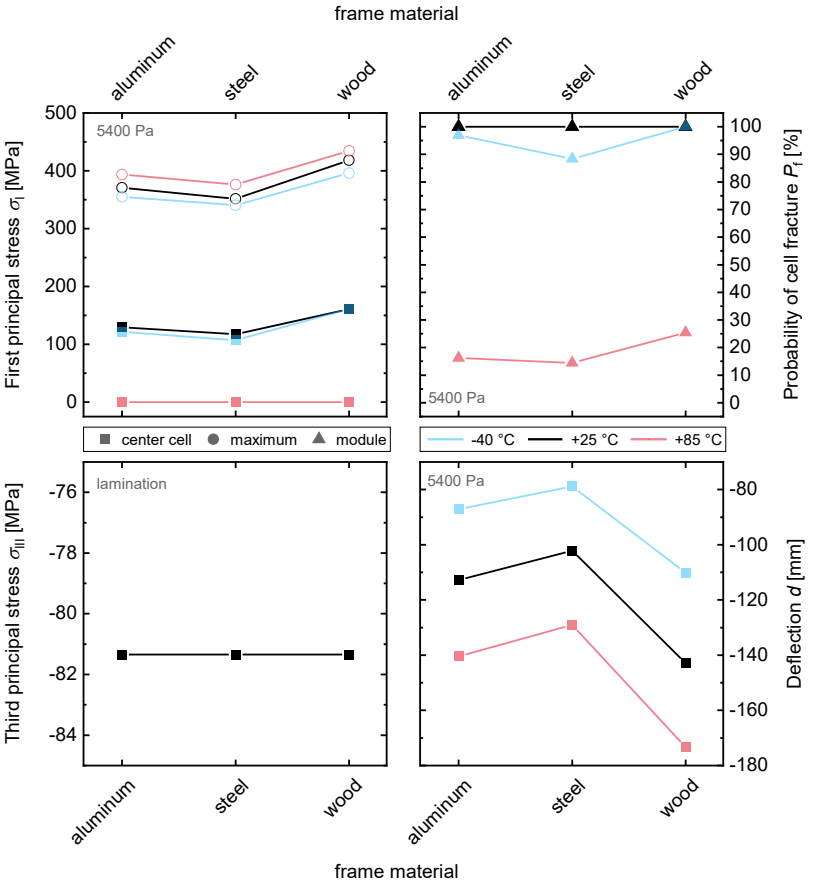


**Figure C.6.24:** Results from the variation of frame material at 5400 Pa push load at -40 °C (blue), +25 °C (black) and +85 °C (red). *Top row: left*: maximum value (open circles) and value between the busbars of the center cell (filled squares) of the first principal stress $\sigma_I$; *right*: corresponding probability of cell fracture (triangles); *bottom row: left*: third principal stress $\sigma_{III}$ after lamination; *right*: deflection.

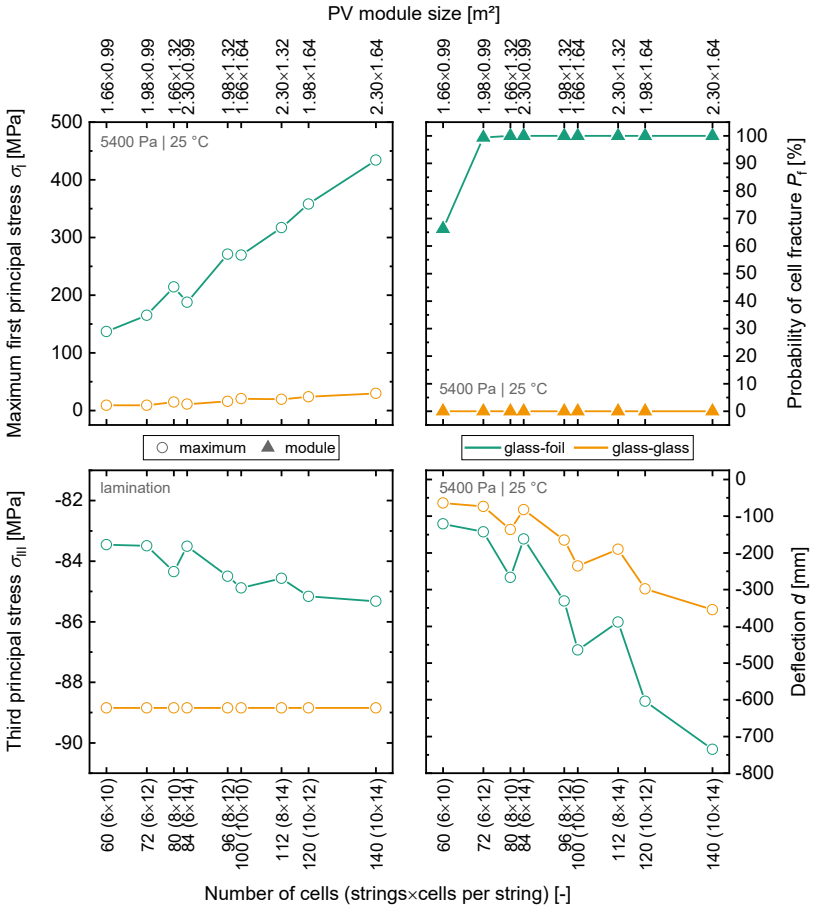


**Figure C.6.25:** Results from the variation of the number of cells within a PV module at 5400 Pa push load for glass-foil (green) and glass-glass modules (orange). *Top row: left*: maximum first principal stress $\sigma_I$; *right*: corresponding probability of cell fracture; *bottom row: left*: third principal stress $\sigma_{III}$ after lamination; *right*: deflection.

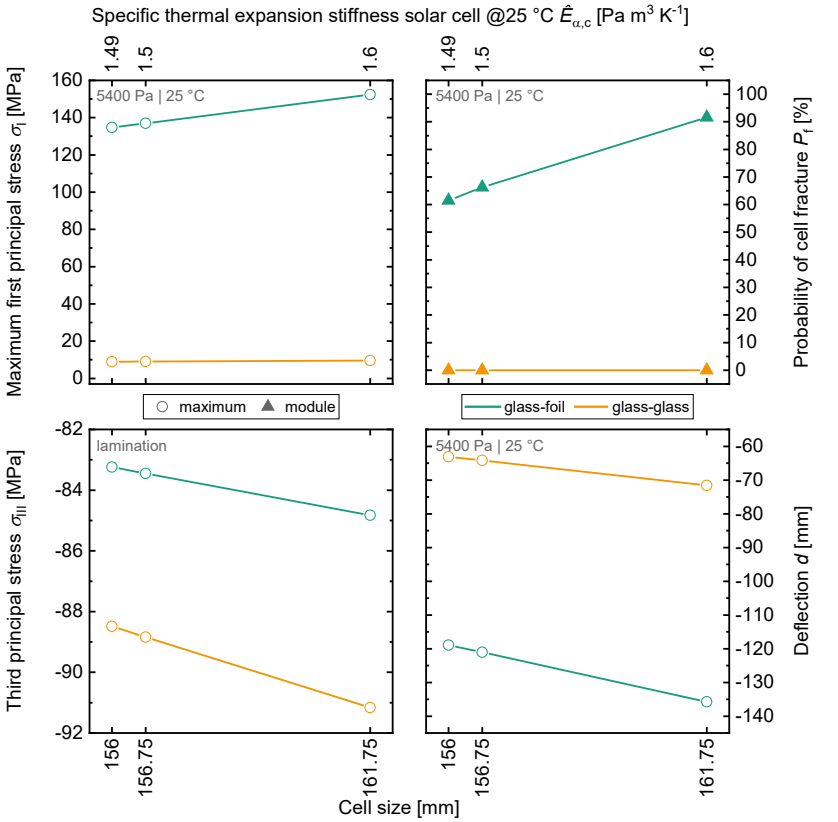


**Figure C.6.26**: Results from the variation of cell size at 5400 Pa push load glass-foil (green) and glass-glass modules (orange). *Top row: left*: maximum first principal stress $\sigma_I$; *right*: corresponding probability of cell fracture; *bottom row: left*: third principal stress $\sigma_{III}$ after lamination; *right*: deflection. Please note, that the bottom ordinates depict cell size and the top ordinates the corresponding specific thermal expansion stiffness $\hat{E}_\alpha$.

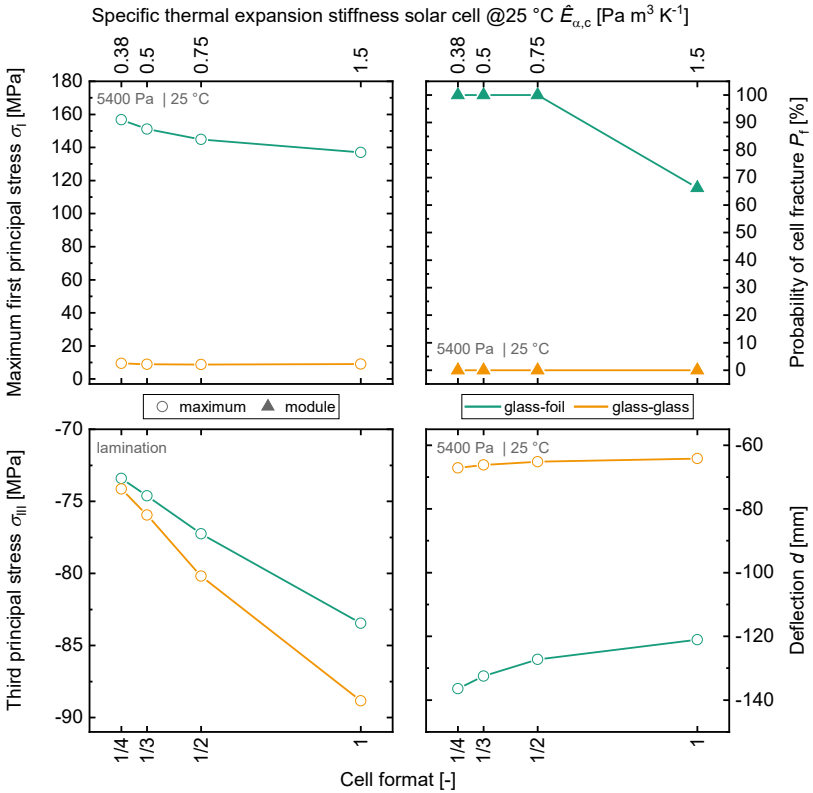


**Figure C.6.27**: Results from the variation of cell format at 5400 Pa push load for glass-foil (green) and glass-glass modules (orange). *Top row: left*: maximum first principal stress $\sigma_I$; *right*: corresponding probability of cell fracture; *bottom row: left*: third principal stress $\sigma_{III}$ after lamination; *right*: deflection. Please note, that the bottom ordinates depict cell format and the top ordinates the corresponding specific thermal expansion stiffness $\hat{E}_\alpha$.

Stress in solar cells plays a crucial role in the reliability of photovoltaic (PV) modules. The influences on stress are as diverse as the number of different materials in a PV module and become more and more complex with the growing variety of PV modules for different applications.

Within this dissertation, a set of 15 thermomechanical design rules is derived to support and accelerate future PV module developments. Three methods are developed and applied:

1. Thermomechanical finite element method simulations of PV module designs (FEM)

2. μ-Raman spectroscopy of laminated solar cells (μ-Raman)

3. Solar cell integrated stress sensors (SenSoCell®)

Furthermore, the concept of specific thermal expansion stiffness $\hat{E}_{\alpha} = E \cdot \alpha \cdot A_{j} \cdot h$ is introduced as a measure of how much thermal strain one material can induce in another.

ISBN 978-3-8396-1808-0

Fraunhofer VERLAG